Summer 8-15-2018

Fundamental Controls on the Reactivity of Aluminum Oxide and Hydroxide Surfaces: Contributions of Surface Site Coordination States and Interfacial Water Structure

Tingying Xu
Washington University in St. Louis

WASHINGTON UNIVERSITY IN ST. LOUIS

Division of Earth and Planetary Sciences

Dissertation Examination Committee:
Jeffrey G. Catalano, Chair
John D. Fortner
Daniel E. Giammar
Jill D. Pasteris
Kun Wang

Fundamental Controls on the Reactivity of Aluminum Oxide and Hydroxide Surfaces: Contributions of Surface Site Coordination States and Interfacial Water Structure

by
Tingying Xu

A dissertation presented to
The Graduate School
of Washington University in
partial fulfillment of the
requirements for the degree
of Doctor of Philosophy

August 2018
St. Louis, Missouri

TABLE OF CONTENTS

LIST OF FIGURES

CHAPTER 1

CHAPTER 2

CHAPTER 3

CHAPTER 4

APPENDIX A

LIST OF TABLES

ACKNOWLEDGEMENTS

Pursuit of my doctoral degree in the United States has been both a challenging and rewarding experience. This research would not be possible without the encouragement and support of numerous individuals. I would especially like to thank my advisor, Jeff Catalano, for giving me the opportunity to pursue my Ph. D. in his research group and being an excellent mentor in scientific research. I truly appreciate his encouragement when I encountered hundreds of times of failures in mineral syntheses in the beginning of my research and his step-by-step teaching on synchrotron techniques, especially surface X-ray scattering measurements. Without his guidance and support, I will never be confident enough to overcome countless difficulties I met in learning surface scattering.

I would like to thank rest of my committee members for their thoughtful discussions and valuable suggestions into my research during the past five years. I would also like to thank the U.S. National Science Foundation (NSF) Environmental Chemical Sciences program through award no. CHE-1505532 and Washington University in St. Louis to financially support my research.

A major portion of my research was conducted at the Advanced Photon Source and SLAC National Accelerator Laboratory. I would like to thank Ryan Davis and Dale Brewe for their beamline support during my EXAFS data collection. Many thanks go to Peter Eng and Joanne Stubbs for their generous support in my surface scattering experiments. I truly appreciate their customized setup prior each of our beamtime that made our life much easier when collecting the surface scattering data.

I would like to thank my wonderful group members in the Aqueous Geochemistry and Mineralogy Laboratory, both past and present, for their invaluable help and support along the

way. Special acknowledgement is due to Elaine Flynn, Lyndsay Troyer, and Nyssa Crompton for their company in the lab preparing samples and at the beamtime collecting data.

I am deeply thankful to my family, especially my parents who strongly supported me mentally and financially and provided me continuous love and understanding as I pursue my Ph.D. degree in Washington University. Although we are physically distant, our bonds are strengthened during my doctoral studies. Finally, I would like to give my special thanks to my husband, Wenlei Chen, for his support in countless ways. We have been through a lot of unexpected and difficult times as we moved from China to the U.S. for our Ph. D. studies. I appreciated his patience in encouraging me and dragging me back to normal when I went dark for days or months. I also appreciated his critical comments on my research which largely improved the quality of my work. I am extremely grateful that he is always standing by me with positive thinking and cheering me up during those hard times.

Tingying Xu

Washington University in St. Louis

August 2018

ABSTRACT OF THE DISSERTATION

Fundamental Controls on the Reactivity of Aluminum Oxide and Hydroxide Surfaces:
Contributions of Surface Site Coordination States and Interfacial Water Structure

by
Tingying Xu
Doctor of Philosophy in Earth and Planetary Sciences
Washington University in St. Louis, 2018
Professor Jeffrey G. Catalano, Chair

Chemical reactions at mineral-water interfaces are of great importance in many geological and environmental processes. Essential to many of these is adsorption because it directly controls contaminant fate and nutrient availability, promotes the nucleation and growth of minerals, initiates surface redox reactions, and plays a crucial role in carbon cycling and sequestration. These reactions occur at mineral surface sites having multiple possible coordination states that interact with both adsorbates and water. While general ion adsorption mechanisms and surface charging behaviors are well established, the roles of individual surface functional group types and water in affecting the structure and reactivity of the interfacial region have not been systematically investigated. Previous studies suggest that surface functional groups in different coordination environments differ in their charge states, proton affinities, and kinetics of oxygen exchange with water. This indicates that these groups may also have different reactivities toward adsorbates and may induce distinct structural arrangements of water near mineral surfaces. This latter role for charged surface groups further suggests that adsorbates, which act as new charged surface sites, potentially may alter the structure of water near surfaces. Such restructuring of interfacial water may contribute to the energetics of many important reactions at environmental interfaces, but this remains unclear currently. Thus, a direct

relationship between surface reactions (involving various surface functional groups and adsorbates) and interfacial water properties needs to be established.

Aluminum (hydr)oxides, as important reactive and widespread minerals in nature and in engineered systems, play significant roles in many geological and environmental processes. Surfaces of these minerals are especially important due to their ability to control the degradation and transformation of contaminants in soils and sediments and affect the composition of natural waters and geochemical element cycling. Gibbsite, the most common form of aluminum hydroxide found in nature, and its rarer polymorph bayerite, display substantially different morphologies dominated by distinct crystallographic planes. Corundum, as the only thermodynamically stable form of aluminum oxide, has been widely investigated as a proxy for aluminum hydroxide mineral surfaces and surfaces of other phases, such as the edges of Al-rich smectites and the aluminol surface of kaolinite. This study is focused on these minerals because they can serve as model analogues for understanding the surface reactivity of other naturally abundant Al-bearing minerals in soils and sediments due to the similarity in functional groups exposed on their surfaces and for studying fundamental geochemical reactions at interfaces.

The main objective of this dissertation is to determine how surface site coordination states on aluminum (hydr)oxide mineral surfaces affect ion adsorption mechanisms, interfacial water structure, and the feedback between these. Arsenate is employed as the probe adsorbate because of its environmental relevance and its uptake over a wide pH range. This research specifically seeks to (1) identify the effects of surface site coordination on macroscopic arsenate adsorption and its binding mechanisms on synthetic gibbsite and bayerite particles; (2) determine how ionic strength affects arsenate adsorption on gibbsite and bayerite; (3) characterize the response of interfacial water structure to pH variations and arsenate adsorption on corundum

(001) surfaces; and (4) compare the response of interfacial water structure to pH variations and arsenate adsorption on corundum (012) and (001) surfaces.

Synthetic gibbsite and bayerite have distinct particle morphologies, exposing different types of functional groups. Gibbsite platelets expose large (001) basal surfaces terminated predominantly by $>Al_2O$ groups, whereas bayerite microrods display mainly edge surfaces dominated by >AlO groups. Macroscopic adsorption isotherms at a single ionic strength show that gibbsite adsorbs less arsenate per unit surface area than bayerite at pH 4 and 7 and suggest that two surface complexes form on each mineral. Arsenate adsorption decreases with increasing ionic strength on both minerals, with a larger effect at pH 4 than pH 7. The observed pH-dependence corresponds with a substantial decrease in surface charge, as indicated by ζ-potential measurements. At a single ionic strength, similar electrokinetic behavior is observed at the same relative coverages of arsenate, suggesting that similar reactive surface groups (>AlO) control surface charging on both minerals. Extended X-ray absorption fine structure (EXAFS) spectroscopy shows no variation in arsenate surface speciation on a given mineral with different surface coverage, pH, and ionic strength. While bidentate binuclear inner-sphere complexes are the dominant surface species present, EXAFS results find that the number of second shell Al neighbors around arsenate is lower than required for this adsorbate to occur solely as an inner-sphere complex, suggesting that outer-sphere species also occur on both minerals, in greater abundance on gibbsite. Together, these observations reveal that arsenate adsorption mechanisms and capacities vary with mineral morphologies because of the distribution of distinct surface functional groups. These also demonstrate that arsenate displays macroscopic and spectroscopic behavior consistent with the coexistence of inner- and outer-sphere surface complexes.

This dissertation also investigated interfacial water structure near single crystal corundum surfaces. Surface X-ray scattering measurements show that corundum (001) surfaces induce weak spatial ordering of interfacial water that varies little between pH 5 and 9 but is substantially altered by the adsorption of arsenate. In the absence of arsenate, interfacial water ordering near the (012) surfaces is also largely unaffected by pH. This general invariance observed on both surfaces suggest that over the pH range of most natural waters, surface site protonation-deprotonation appears inadequate to induce extensive restructuring of interfacial water. The adsorption of arsenate weakly perturbs interfacial water structure near the (012) surface, in contrast to the substantial restructuring of interfacial water seen near the (001) surface. Arsenate is observed to form coexisting inner- and outer-sphere surface complexes on both surfaces, suggesting that adsorption mechanisms may not control the resulting restructuring of interfacial water. Instead, the different surface functional groups present on the (001) and (012) surfaces, with their distinct charging behaviors, likely drive the response of interfacial water to arsenate adsorption.

This study improves our understanding of the fundamental controls of chemical reactions at environmental interfaces through systematic studies of arsenate adsorption on aluminum hydroxide particles and aluminum oxide single crystals. Arsenate adsorption on aluminum hydroxide surfaces is complicated, with different types of surface complexes forming through reactions at multiple types of functional groups of different reactivities. The complex interactions between arsenate and aluminum hydroxides can be extended to systems with other naturally abundant Al/Fe-bearing minerals and this must be considered when predicting arsenate fate at environmental interfaces. The dynamic response of interfacial water structure to adsorbates observed on different corundum surfaces here suggests a relationship among surface functional

group coordination states, ion adsorption mechanisms, and interfacial water structure. Such adsorbate-induced restructuring of interfacial water indicates that water structure plays an important role in the energetics of interfacial reactions. This study provides new insight into the roles of surface functional group coordination states and interfacial water restructuring in chemical reactions at mineral-water interfaces.

CHAPTER 1

INTRODUCTION

1.1 BACKGROUND

Chemical reactions that occur at mineral-water interfaces are central to many geological and environmental processes, such as mineral precipitation and dissolution, trace metal adsorption and desorption, geochemical cycling of elements, acid mine drainage, natural water compositions, biomineralization, soil formation, and geologic CO_2 sequestration (Al-Abadleh and Grassian, 2003; Björneholm et al., 2016; Brown et al., 1999; Brown and Parks, 2001; Grassian, 2008; Kappler and Straub, 2005; Yanina and Rosso, 2008). Essential to many of these is ion adsorption, a process that directly reduces adsorbates' concentration in aqueous fluids. In soils and aquatic systems, this not only limits the transport of contaminants (Chorover et al., 2007; Koretsky, 2000) but also controls the bioavailability of nutrients (Abat et al., 2012; Chorover and Brusseau, 2008; Ohno and Amirbahman, 2010). Adsorption also plays a critical role in promoting the nucleation and growth of minerals (Benning and Waychunas, 2008), surface-catalyzed redox reactions (Amstaetter et al., 2010; Boland et al., 2011; Elsner et al., 2004), and microbial- or ligand-promoted dissolution of oxide minerals (Kraemer, 2004, 2005; Rechard et al., 2007; Shi et al., 2013). Knowledge of the fundamental controls on these interfacial reactions is needed to predict important processes occurring in geological and environmental systems.

In many natural systems, the surfaces of metal oxide minerals are the principal sites for adsorption reactions to occur (Al-Abadleh and Grassian, 2003; Brown et al., 1999; Brown and

Parks, 2001). Metal oxide surfaces contain an array of surface sites composed of oxygen surface functional groups in multiple coordination states to the underlying metal atoms (Al-Abadleh and Grassian, 2003). Surface complexation models have clearly assumed that charge states and proton affinities of these surface functional groups are directly related to the coordination states of oxygen (Hiemstra and Van Riemsdijk, 1999; Hiemstra et al., 1989; Hiemstra et al., 1996; Venema et al., 1998). In addition, surface functional groups show a difference in the kinetics of oxygen exchange rates between surface sites and water molecules, with a slow and fast exchange rate observed for doubly and singly coordinated oxygen groups, respectively (Casey and Phillips, 2001; Casey et al., 2000; Casey and Rosenqvist, 2004; Phillips et al., 2003). These distinct behaviors of surface functional groups in various coordination environments suggest that they may also have different reactivity towards adsorbates, but this has not been investigated experimentally to date.

The interface between metal oxides and water where adsorption reactions occur is not an abrupt transition between a highly ordered solid and completely random liquid, but is instead a chemical and structural transition zone where surface functional groups interact with both adsorbates and water molecules. When in aqueous solutions, metal oxide surfaces can obtain charge either from protonation or deprotonation of various surface functional groups or the adsorption of a charged species from the solution onto the surface (Kallay et al., 2010; Sherman, 2009; Sposito, 1998). This charge development generates a local electrostatic potential at the interface that plays an important role in driving interfacial reactions. In the absence of adsorbate, the electrostatic potential from the charging of surface functional groups affects the orientation of water molecules through their dipole moments (Lützenkirchen et al., 2010; Toney et al., 1994; Zhang et al., 2008). These effects induce spatial ordering of interfacial water, with the degree of

water ordering depending on the charge states of surface functional groups, which is ultimately controlled by mineral surface structure (Catalano, 2010; Catalano, 2011; Catalano et al., 2009; Catalano et al., 2006; Cheng et al., 2001; Fenter et al., 2003; Fenter and Sturchio, 2004; Ghose et al., 2010; Zhang et al., 2007). Under environmental conditions, this picture becomes more complicated because of the variability in the chemistry of natural fluids, such as the presence of adsorbates and the wide range of possible pH values. Previous experimental and theoretical studies clearly show that interfacial water structure responds to chemical changes at the interfaces (Kerisit et al., 2006; Sung et al., 2011; Zhang et al., 2008) and can also affect ion adsorption processes (Catalano et al., 2008). The adsorption of a charged ion and changes in solution pH that affect surface site charging behaviors result in different electrostatic potentials at the interface, which may in turn affect interfacial water structure. If interfacial water restructuring does occur upon variations in chemical conditions, such a change may affect the thermodynamics of interfacial reactions enthalpically or entropically. However, how the interactions among different surface functional groups, adsorbates, and water molecules impact interfacial reaction energetics are currently unclear.

While the general ion adsorption mechanisms and surface charging behavior of metal oxide-water interfaces have been well established, the roles of individual surface functional group type and interfacial water in affecting the structure and reactivity of the interfacial region have not yet been systematically understood at a fundamental, molecular level. This dissertation seeks to resolve these uncertainties in the fundamental controls on the chemical reactivity of metal oxide-water interfaces and establish a possible relationship between surface adsorption reactions and interfacial water properties through a series of systematic studies. Aluminum (hydr)oxides, gibbsite [γ-$Al(OH)_3$], bayerite [α-$Al(OH)_3$], and corundum(α-Al_2O_3), are important

reactive and widespread minerals in nature and in engineered systems, are chosen as the main substrates. Surfaces of these minerals are especially important due to their ability to control the fate of contaminants in soils and sediments and affect the composition of natural waters and geochemical element cycling. These minerals can also serve as model analogues to study the surface reactivity of other naturally abundant Al/Fe-bearing minerals because of the similarity in the types of surface functional groups exposed (Al-Abadleh and Grassian, 2003). Arsenate ($H_nAsO_4^{3-n}$) is employed as the probe adsorbate because of its environmental relevance (Jain and Ali, 2000; Smedley and Kinniburgh, 2002) and its well-established adsorption mechanisms on metal oxide surfaces (Arai et al., 2001; Catalano et al., 2008; Foster et al., 1998; Kappen and Webb, 2013; Ladeira et al., 2001), including its substantial uptake over a wide pH range (unlike many cations). Macroscopic, spectroscopic, and scattering studies of arsenate adsorption on synthetic aluminum hydroxide powders and aluminum oxide single crystals are utilized together to systematically understand surface functional group reactivity and interfacial water restructuring at the aluminum (hydr)oxide-water interface.

1.2 CRYSTAL AND SURFACE STRUCTURE OF ALUMINUM HYDROXIDE AND OXIDE MINERALS

Two aluminum hydroxide polymorphs, gibbsite and bayerite, and aluminum oxide, corundum, are selected as the solid substrates for this study. Gibbsite is the thermodynamically stable crystalline form of aluminum hydroxide under environmental conditions while bayerite is known as the product of synthesis and is rarely found in nature (Digne et al., 2002; Gale et al., 2001). These two minerals are composed of the same basic structure: layers of $Al(OH)_6$ octahedral sheets stacking in different sequences, with hydrogen-bonding as the main contributor

to cohesion among layers (Figure 1.1) (Welfers and Misra, 1987). Gibbsite and bayerite display distinct particle morphologies dominated by different crystallographic planes. During crystal formation, gibbsite is well developed in the *a* and *b* directions but limited in the *c* direction. This results in thin, flat hexagonal platelets that are mainly composed of basal planes. In contrast, bayerite crystals have strong growth in the *c* direction but limited growth in the *a* and *b* directions. They often appear as prisms or rods that are dominated by edge planes. Corundum, occurring naturally as a metamorphic and igneous mineral, is the only thermodynamically stable form of aluminum oxide (Welfers and Misra, 1987). It has a structure consisting of hexagonal close packed oxygen atoms with Al^{3+} ions sitting in two-thirds of the octahedral sites to maintain charge balance (Figure 1.1) (Welfers and Misra, 1987).

Despite the differences in bulk structure, the surface terminations of specific crystallographic planes are similar for gibbsite/bayerite and corundum. The (001) basal surfaces of gibbsite/bayerite and corundum are terminated solely in doubly coordinated functional groups (>Al_2O) (Figure 1.1). In contrast, non-basal surfaces of these minerals are terminated by different types of functional groups, with (110) or (100) edge surfaces of gibbsite and bayerite only terminated by singly coordinated functional groups (>AlO) and (012) planes of corundum terminated by both >AlO and triply coordinated functional groups (>Al_3O) (Figure 1.1). This similarity allows direct comparison of the reactivity of individual surface functional group types at aluminum (hydr)oxide-water interfaces using both synthetic monodispersed gibbsite/bayerite powders and large singly crystals of corundum oriented to various crystallographic planes.

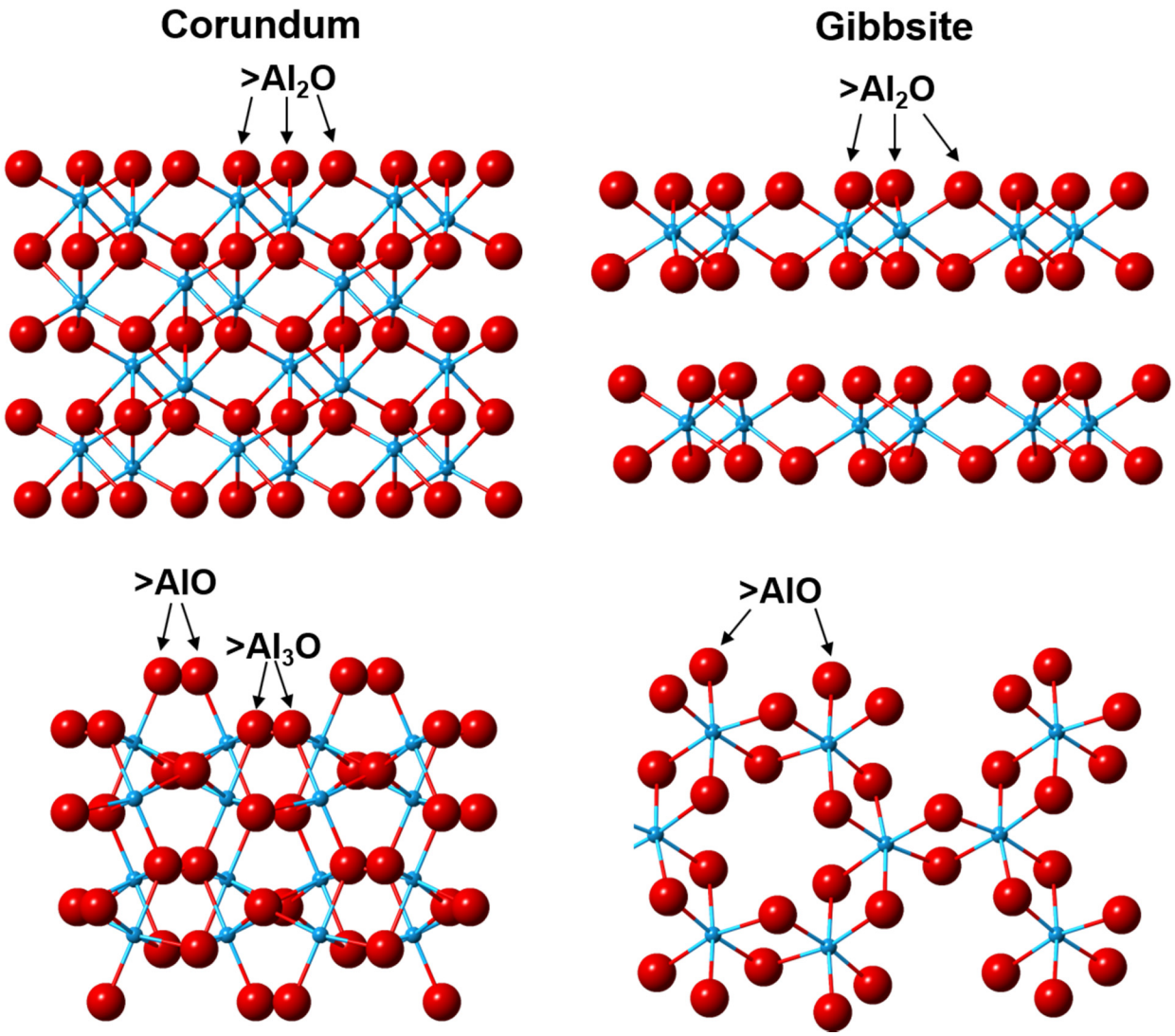

Figure 1.1. Structures of corundum (left) and gibbsite (right). The top two images are the surface structures of (001) basal surfaces of corundum and gibbsite. The bottom two images are the surface structures of non-basal surfaces of corundum and gibbsite, with the left being the (012) surface of corundum and right being edge (110) or (100) surfaces of gibbsite. The blue and red spheres represent Al and O atoms, respectively. H atoms are not included in the gibbsite structures for clarity. Also shown are the singly (>AlO), doubly (>Al_2O), and triply (>Al_3O) coordinated functional groups exposed on these surfaces. Bayerite surface terminations are the same as gibbsite.

1.3 CHARGE STATES OF SURFACE FUNCTIONAL GROUPS

Three types of oxygen surface functional groups, >AlO, >Al_2O, and >Al_3O, are expected at aluminum (hydr)oxide-water interfaces (Figure 1.1). Thermodynamic models together with Pauling bond valence rules clearly demonstrate that the protonation and deprotonation of these functional groups and thus their charge states are primarily controlled by the coordination states of oxygen and the contacting solution pH (Bickmore et al., 2004; Hiemstra et al., 1989; Hiemstra et al., 1996; Hiemstra et al., 1999). Singly and triply coordinated functional groups can deprotonate from >$AlOH_2^{+0.5}$ to >$AlOH^{-0.5}$ at weakly alkaline conditions ($9.9 < pK_a < 11$), from >$AlOH^{-0.5}$ to >$AlO^{-1.5}$ at high pH ($pK_a \sim 11.9$), or from >$Al_3OH^{+0.5}$ to >$Al_3O^{-0.5}$ at pH ~5.9 (Bickmore et al., 2004; Hiemstra et al., 1999). Doubly coordinated functional groups can deprotonated to >Al_2O^- at high pH ($pK_{a2} \sim 12$) and protonate to >$Al_2OH_2^+$ at low pH ($pK_{a1} \sim 0$) (Bickmore et al., 2004; Hiemstra et al., 1999). Therefore, singly and triply coordinated functional groups are usually charged under typical pH conditions of natural waters while doubly coordinated functional groups are essentially charge neutral over a wide pH range.

1.4 SOLUBILITY OF ALUMINUM HYDROXIDE AND OXIDE MINERALS

The solubility of aluminum (hydr)oxide minerals is controlled by temperature and pH. Gibbsite is the example aluminum hydroxide mineral discussed here due to the similarity in crystal structure compared to bayerite. According to the solubility curves for gibbsite and corundum at room temperature (Figure 1.2), solubilities for both minerals are small in the pH range of most natural waters, typically spanning from 4 to 9. The experiments conducted in this study are at pH 4 and 7 for gibbsite and bayerite particles and at pH 5, 7, and 9 for corundum single crystals. A broader pH range is not examined because the solubilities of gibbsite and

corundum increase below pH 4 and above pH 9. This could potentially generate Al^{3+} ions at low pH and $Al(OH)_4^-$ ions at high pH, which may not only re-adsorb to mineral surfaces, affecting arsenate adsorption, but also alter the interfacial water structure near the surfaces that we aim to investigate.

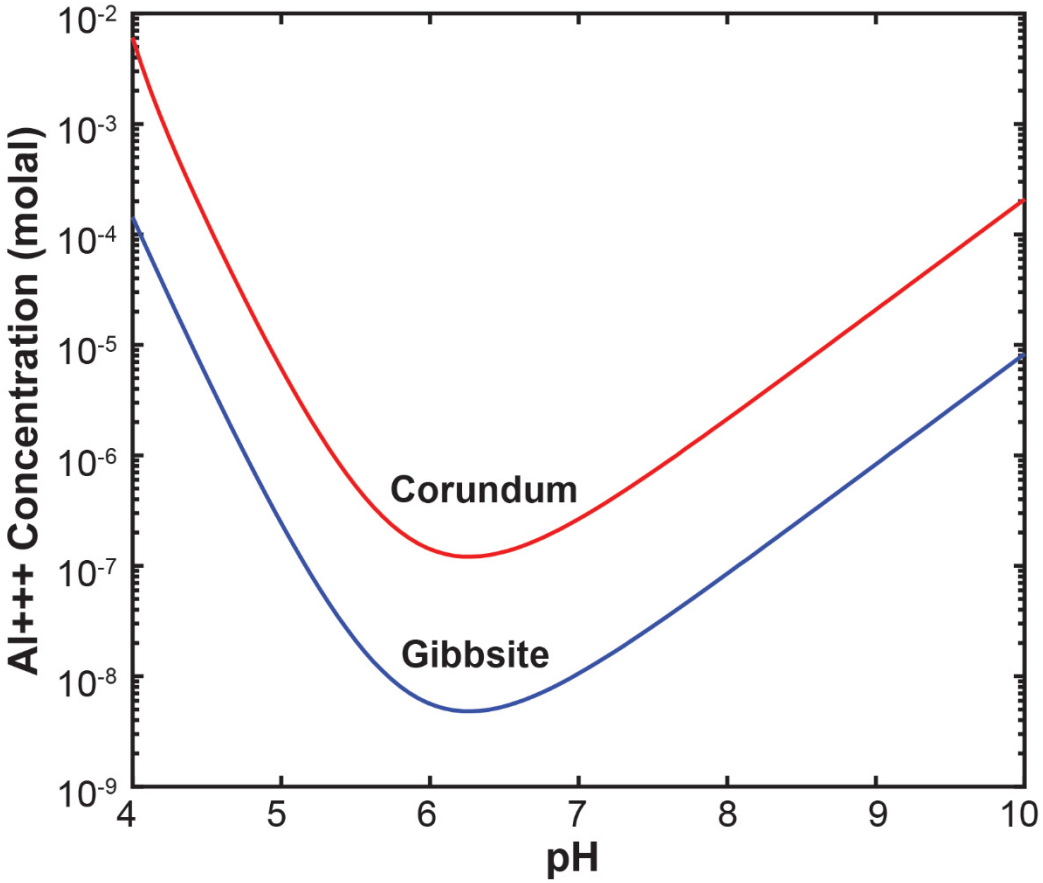

Figure 1.2. Solubility curves of gibbsite and gibbsite in 0.01 molal NaCl. Calculations are performed in The Geochemist's Workbench (Bethke, 2007) using the Lawrence Livermore National Laboratory thermochemical database V8 R6 (Delany and Lundeen, 1990).

1.5 ARSENATE GEOCHEMISTRY IN AQUEOUS SYSTEMS

Arsenic may exist in the −3, 0, +3, and +5 oxidation states with the dominant chemical forms present in most aqueous systems being inorganic species (Stollenwerk, 2003). The toxicity and mobility of arsenic is controlled by its aqueous speciation. According to the Eh-pH diagram of arsenic (Figure 1.3), As(V) and As(III) are the most common oxidation states present in soils and natural waters. As(III) is found under reducing conditions, and As(V) is thus chosen as the probe in this study because of its stability in near-surface environments. In aqueous systems, As(V) occurs as the oxoanion, arsenate, whose degree of protonation is controlled by pH (Nordstrom and Archer, 2003) According to arsenate speciation diagram (Figure 1.4) and its pK_a values of pK_a^1 = 2.30, pK_a^2 = 6.99, and pK_a^3 = 11.80 (Nordstrom and Archer, 2003), $H_2AsO_4^-$ is the predominant species between pH 2.30 to 6.99 while $HAsO_4^{2-}$ is the predominant species between pH 6.99 and 11.80. These calculations thus predict that $H_2AsO_4^-$ and $HAsO_4^{2-}$ are dominant arsenate species in most natural waters at typical environmental pH values of 4 to 9.

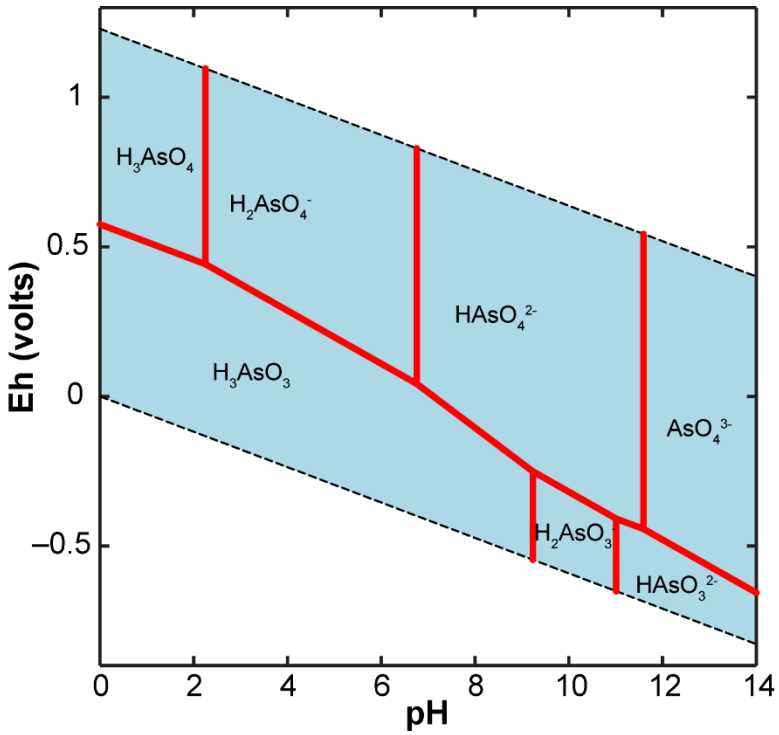

Figure 1.3. The Eh-pH diagram for arsenic at 25°C, with an activity of 10^{-3}.

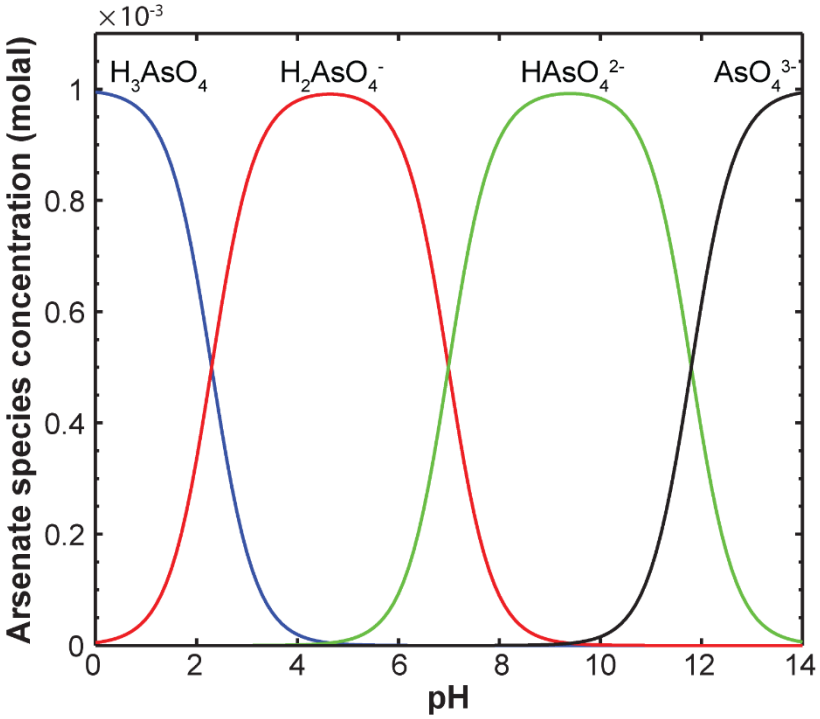

Figure 1.4. Arsenate speciation diagram at 25°C, with total arsenic concentration of 10^{-3} molal.

1.6 ARSENATE ADSORPTION MECHANISMS

Arsenate has been found to adsorb to a variety of mineral surfaces, especially to aluminum and iron oxides/hydroxides, (e.g., Arai et al., 2001; Davis and Kent, 1990; Foster et al., 1998; Goldberg, 1986; Manning et al., 1998; Waychunas et al., 1993). Both macroscopic and spectroscopic studies have been used to investigate arsenate adsorption mechanisms on the surfaces of specific aluminum or iron (hydr)oxide minerals, (e.g., Arai et al., 2001; Catalano et al., 2008; Fendorf et al., 1997; Foster et al., 1998; Goldberg and Johnston, 2001; Manceau, 1995; Myneni et al., 1998; Waychunas et al., 1993). Arsenate has been primarily interpreted to undergo surface complexation by forming inner-sphere complexes, yet recent research suggests outer-sphere species may also be important. Most previous spectroscopic studies of arsenate adsorption mechanisms on aluminum/iron (hydr)oxide mineral surface have identifies the formation of inner-sphere arsenate complexes in a bridging bidentate geometry (Arai et al., 2001; Arai et al., 2003; Farquhar et al., 2002; Fendorf et al., 1997; Foster et al., 1998; Goldberg and Johnston, 2001; Jia et al., 2007; Ladeira et al., 2001; Lumsdon et al., 1984; Manceau, 1995; Myneni et al., 1998; Sherman and Randall, 2003; Sun and Doner, 1996; Waychunas et al., 1993). Inner-sphere complexation represents a ligand-exchange reaction, in which arsenate directly binds to specific mineral surface sites. Although not widely recognized, outer-sphere arsenate complexation may also exist on aluminum/iron (hydr)oxide mineral surfaces. Such complexation occurs when arsenate binds to surface functional groups via electrostatic interaction or hydrogen-bonding, and thus no direct chemical bonds form between arsenate and mineral surface sites. Two previous studies have suggested the possibility of the occurrence of such complexes on metal oxides (Catalano et al., 2007; Fukushi and Sverjensky, 2007) and one study has directly observed the simultaneous occurrence of both inner- and outer-sphere arsenate complexes on corundum and

hematite single crystal surfaces (Catalano et al., 2008). While the transferability of such processes on highly-idealized single crystal surfaces to particles representative of natural sorbents is unknown, these results suggest that the dual adsorption mechanism is likely plausible for arsenate at environmental interfaces.

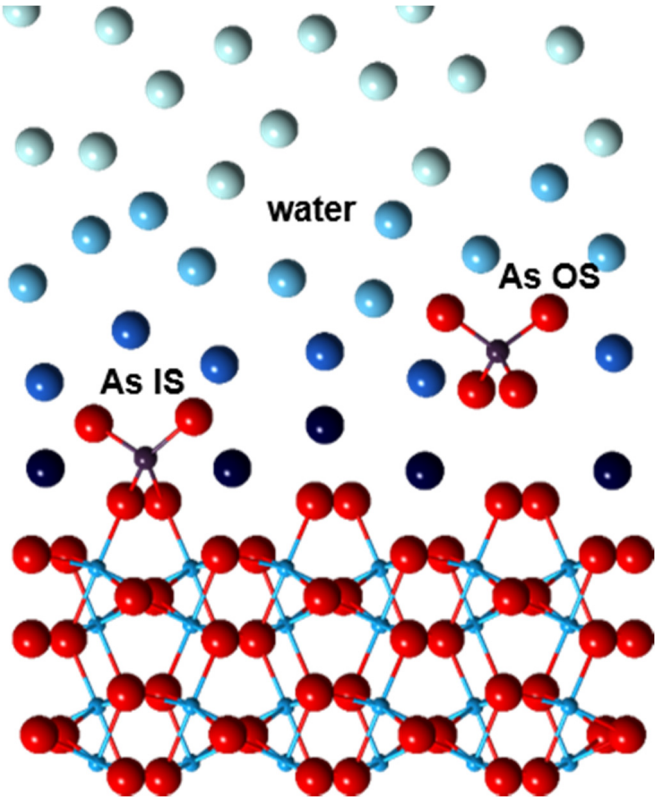

Figure 1.5. Schematic of arsenate adsorption mechanisms, presenting the coexistence of the inner-sphere (IS) and outer-sphere (OS) arsenate species at corundum-water interfaces. Blue, purple, and red balls represent Al, As, and O atoms, respectively.

1.7 RESEARCH OBJECTIVES

The goal of this research is to investigate how surface site coordination state and interfacial water structure affects adsorption reactions at aluminum (hydr)oxide-water interfaces, how adsorbates alter the structure of water near these mineral surfaces, and the feedback between ion adsorption and interfacial water restructuring on mineral surface reactivity. This dissertation consists of four specific research projects, outlined in the following chapters:

CHAPTER 2: Impacts of surface site coordination on arsenate adsorption: macroscopic uptake and binding mechanisms on aluminum hydroxide surfaces (Xu, T., Catalano, J.G.)

This chapter consists of a detailed analysis of the adsorption behavior of arsenate on two aluminum hydroxide polymorphs with distinct particle morphologies, gibbsite and bayerite, at pH 4 and 7. These minerals display surface functional groups in a series of coordination states, each of which differ in their adsorption affinities for arsenate. The distribution of functional group types varies among distinct surfaces of aluminum hydroxides and we thus hypothesize that arsenate adsorption behavior and mechanisms will show a dependence on particle morphologies. Gibbsite exposes large basal surfaces terminated predominantly by $>Al_2O$ groups whereas bayerite displays mainly edge surfaces dominated by >AlO groups. The effects of particle morphologies on arsenate macroscopic adsorption behavior at pH 4 and 7, as well as the effects of arsenate adsorption on the surface charging behavior of gibbsite and bayerite are investigated. To elucidate if arsenate adsorption mechanisms differ between the two minerals, extended X-ray absorption fine structure (EXAFS) spectroscopic measurements on a series of arsenate adsorbed samples at pH 4 and 7 are conducted. Macroscopic adsorption studies show that gibbsite adsorbs less arsenate per unit surface area that bayerite at both pH conditions. EXAFS spectroscopy

identifies the same arsenate inner-sphere surface complexes on both minerals regardless of pH and arsenate coverage. Outer-sphere arsenate species may also occur on both minerals with a greater abundance on gibbsite according to the EXAFS results. These demonstrate that macroscopic and molecule-scale arsenate adsorption behavior, including adsorption reactivity, capacity, and mechanisms, vary with particle morphologies because of the distribution of distinct surface functional groups.

CHAPTER 3: Effects of ionic strength on arsenate adsorption at aluminum hydroxide-water interfaces (Xu, T., Catalano, J.G.)

In this chapter, the effects of ionic strength on arsenate adsorption on gibbsite and bayerite surfaces are examined. The ionic strength-dependence of the macroscopic adsorption behavior and molecular-scale surface speciation of arsenate bound to gibbsite and bayerite are explored with batch adsorption experiments and EXAFS measurements. Arsenate adsorption isotherm experiments show that the uptake of arsenate onto both minerals does display a strong dependence on ionic strength, a clear macroscopic signature indicating the presence of outer-sphere arsenate species. Together with the EXAFS results, arsenate displays macroscopic and molecular-scale behavior consistent with the coexistence of inner- and outer-sphere complexes. This demonstrates that outer-sphere complexation can be responsible for strong adsorption of ions and suggests that environments experiencing an increase in salt content may induce arsenic release to water.

CHAPTER 4: Response of interfacial water to arsenate adsorption on corundum (001) surfaces: effects of pH and adsorbate surface coverage (Xu, T., Stubbs, J.E., Eng, P.J., Catalano, J.G.)

In this chapter, the effects of pH and ion adsorption on the interfacial water structure at mineral-water interfaces are investigated using surface X-ray scattering methods, including non-resonant X-ray reflectivity (XR) and resonant anomalous X-ray reflectivity (RAXR). Arsenate is used as the probe adsorbate and the single-crystal corundum (001) surface is used as the main substrate. The surface of corundum (001) is terminated by $>Al_2O$ groups that are neutrally-charged over a wide pH range. XR results show that interfacial water displays weak ordering that is largely unaffected by pH in the absence of arsenate, suggesting surface charging alone is inadequate to induce extensive structural changes in interfacial water on this surface. In the presence of arsenate, interfacial water structure is determined after isolating the adsorbed arsenate component using RAXR analysis. Our results show that interfacial water undergoes substantial restructuring upon arsenate adsorption, suggesting that charged surface complexes strongly perturbs interactions of water molecules on the corundum (001) surface. Such an adsorbate-induced restructuring of interfacial water suggests that water structure plays an important role in the energetics of chemical reactions at mineral-water interfaces.

CHAPTER 5: Comparative response of interfacial water structure to pH variations and arsenate adsorption on corundum (012) and (001) surfaces (Xu, T., Stubbs, J.E., Eng, P.J., Catalano, J.G.)

Chapter 5 is a comparative study of interfacial water properties near corundum (001) and (012) surfaces. Chapter 4 has shown that the (001) surface with neutrally charged functional

groups induces weak ordering of interfacial water that varies little between pH 5 and 9 but is substantially altered by the adsorption of arsenate. The (012) surface with functional groups in different coordination states that are always charged induces strong interfacial water ordering and is thus predicted to show a different water structure response to variations in chemical conditions than the (001) surface. Surface X-ray scattering measurements under similar experimental conditions as Chapter 4 reveal that interfacial water structure above the corundum (012) surfaces is largely unperturbed by pH changes and arsenate adsorption. These observations are then compared to water behavior obtained in Chapter 4 on corundum (001) surfaces to gain a systematic understanding of the fundamental controls on water structure at corundum-water interfaces. The results of this research suggest that the different surface functional groups present on the (001) and (012) surfaces with their distinct charging behavior likely drive the distinct responses of interfacial water to arsenate adsorption.

1.8 REFERENCES

Abat, M., McLaughlin, M.J., Kirby, J.K. and Stacey, S.P. (2012) Adsorption and desorption of copper and zinc in tropical peat soils of Sarawak, Malaysia. *Geoderma* **175**, 58-63.

Al-Abadleh, H.A. and Grassian, V.H. (2003) Oxide surfaces as environmental interfaces. *Surf. Sci. Rep.* **52**, 63-161.

Amstaetter, K., Borch, T., Larese-Casanova, P. and Kappler, A. (2010) Redox transformation of arsenic by Fe(II)-activated goethite (α-FeOOH). *Environ. Sci. Technol.* **44**, 102-108.

Arai, Y., Elzinga, E.J. and Sparks, D.L. (2001) X-ray absorption spectroscopic investigation of arsenite and arsenate adsorption at the aluminum oxide-water interface. *J. Colloid Interface Sci.* **235**, 80-88.

Arai, Y., Lanzirotti, A., Sutton, S., Davis, J.A. and Sparks, D.L. (2003) Arsenic speciation and reactivity in poultry litter. *Environ. Sci. Technol.* **37**, 4083-4090.

Benning, L.G. and Waychunas, G.A. (2008) Nucleation, Growth, and Aggregation of Mineral Phases: Mechanisms and Kinetic, in: Brantley, S.L., Kubichi, J.D., White, A.F. (Eds.), *Kinetics of Water-Rock Interaction*. Springer, Newyork, pp. 259-333.

Bethke, C.M. (2007) Geochemical and Biogeochemical Reaction Modeling, Cambridge University Press: New York.

Bickmore, B.R., Tadanier, C.J., Rosso, K.M., Monn, W.D. and Eggett, D.L. (2004) Bond-valence methods for pKa prediction: critical reanalysis and a new approach. *Geochim. Cosmochim. Acta* **68**, 2025-2042.

Björneholm, O., Hansen, M.H., Hodgson, A., Liu, L.-M., Limmer, D.T., Michaelides, A., Pedevilla, P., Rossmeisl, J., Shen, H., Tocci, G., Tyrode, E., Walz, M.-M., Werner, J. and Buhm, H. (2016) Water at interfaces. *Chem. Rev.* **116**, 7698-7726.

Boland, D.D., Collins, R.N., Payne, T.E. and Waite, T.D. (2011) Effect of amorphous Fe(III) oxide transformation on the Fe(II)-mediated reduction of U(VI). *Environ. Sci. Technol.* **45**, 1327-1333.

Brown, G.E., Jr., Henrich, V.E., Casey, W.H., Clark, D.L., Eggleston, C., Felmy, A., Goodman, D.W., Gratzel, M., Maciel, G., McCarthy, M.I., Nealson, K.H., Sverjensky, D.A., Toney, M.F. and Zachara, J.M. (1999) Metal oxide surfaces and their interactions with aqueous solutions and microbial organisms. *Chem. Rev.* **99**, 77-174.

Brown, G.E., Jr. and Parks, G.A. (2001) Sorption of trace elements on mineral surfaces: Modern perspectives from spectroscopic studies, and comments on sorption in the marine environment. *Int. Geol. Rev.* **43**, 963-1073.

Casey, W.H. and Phillips, B.L. (2001) Kinetics of oxygen exchange between sites in the $GaO_4Al_{12}(OH)_{24}(H_2O)_{12}^{7+}$(aq) molecule and aqueous solution. *Geochim. Cosmochim. Acta* **65**, 705-714.

Casey, W.H., Phillips, B.L., Karlsson, M., Nordin, J.P., Sullivan, D.L. and Neugebauer-Crawford, S. (2000) Rates and mechanisms of oxygen exchanges between sites in the $AlO_4Al_{12}(OH)_{24}(H_2O)_{12}^{7+}$(aq) complex and water: Implications for mineral surface chemistry. *Geochim. Cosmochim. Acta* **64**, 2951-2964.

Casey, W.H. and Rosenqvist, J. (2004) The flux of oxygen from the basal surface of gibbsite at equilibrium. *Geochim. Cosmochim. Acta* **68**, 3547-3555.

Catalano, J.G. (2010) Relaxations and interfacial water ordering at the corundum (110) surface. *J. Phys. Chem. C* **114**, 6624-6630.

Catalano, J.G. (2011) Weak interfacial water ordering on isostructural hematite and corundum (001) surfaces. *Geochim. Cosmochim. Acta* **75**, 2062-2071.

Catalano, J.G., Fenter, P. and Park, C. (2009) Water ordering and surface relaxations at the hematite (110)-water interface. *Geochim. Cosmochim. Acta* **73**, 2242-2251.

Catalano, J.G., Park, C., Fenter, P. and Zhang, Z. (2008) Simultaneous inner- and outer-sphere arsenate complexation on corundum and hematite. *Geochim. Cosmochim. Acta* **72**, 1986-2004.

Catalano, J.G., Park, C., Zhang, Z. and Fenter, P. (2006) Termination and water adsorption at the α-Al_2O_3 (012)-aqueous solution interface. *Langmuir* **22**, 4668-4673.

Catalano, J.G., Zhang, Z., Park, C., Fenter, P. and Bedzyk, M.J. (2007) Bridging arsenate surface complexes on the hematite (012) surface. *Geochim. Cosmochim. Acta* **71**, 1883-1897.

Cheng, L., Fenter, P., Nagy, K.L., Schlegel, M.L. and Sturchio, N.C. (2001) Molecular-scale density oscillations in water adjacent to a mica surface. *Phys. Rev. Lett.* **87**, 156103.

Chorover, J. and Brusseau, M.L. (2008) Kinetics of Sorption–Desorption: Mechanisms and Kinetic, in: Brantley, S.L., Kubichi, J.D., White, A.F. (Eds.), *Kinetics of Water-Rock Interaction*. Springer, Newyork, pp. 109-149.

Chorover, J., Kretzschmar, R., Garcia-Pichel, F. and Sparks, D.L. (2007) Soil biogeochemical processes within the Critical Zone. *ELEMENTS* **3**, 321-326.

Davis, J.A. and Kent, D.B. (1990) Surdace complexation modeling in aqueous geochemistry. *Rev. Mineral.* **23**, 178-244.

Delany, J.M. and Lundeen, S.R. (1990) The LLNL thermochemical database. *Lawrence Livermore National Laboratory*, p.150.

Digne, M., Sautet, P., Raybaud, P., Toulhoat, H. and Artacho, E. (2002) Structure and stability of aluminum hydroxides: a theoretical study. *J. Phys. Chem.* **106**, 5155-5162.

Elsner, M., Schwarzenbach, R.P. and Haderlein, S.B. (2004) Reactivity of Fe(II)-bearing minerals toward reductive transformation of organic contaminants. *Environ. Sci. Technol.* **38**, 799-807.

Farquhar, M.L., Charnock, J.M., Livens, F.R. and Vaughan, D.J. (2002) Mechanisms of arsenic uptake from aqueous solution by interaction with goethite, lepidocrocite, mackinawite, and pyrite: an X-ray absorption spectroscopy study. *Environ. Sci. Technol.* **36**, 1757-1762.

Fendorf, S., Eick, M.J., Grossl, P. and Sparks, D.L. (1997) Arsenate and chromate retention mechanisms on goethite. 1. Surface structure. *Environ. Sci. Technol.* **31**, 315-320.

Fenter, P., Cheng, L., Park, C., Zhang, Z. and Sturchio, N.C. (2003) Structure of the orthoclase (001)- and (010)-water interfaces by high-resolution X-ray reflectivity. *Geochim. Cosmochim. Acta* **67**, 4267-4275.

Fenter, P. and Sturchio, N.C. (2004) Mineral-water interfacial structures revealed by synchrotron X-ray scattering. *Prog. Surf. Sci.* **77**, 171-258.

Foster, A.L., Brown, G.E., Jr., Tingle, T.N. and Parks, G.A. (1998) Quantitative arsenic speciation in mine tailings using X-ray absorption spectroscopy. *Am. Mineral.* **83**, 553-568.

Fukushi, K. and Sverjensky, D.A. (2007) A predictive model (ETLM) for arsenate adsorption and surface speciation on oxides consistent with spectroscopic and theoretical molecular evidence. *Geochim. Cosmochim. Acta* **71**, 3717-3745.

Gale, J.D., Rohl, A.L., Milman, V. and Warren, M.C. (2001) An *ab initio* study of the structure and properties of aluminum hydroxide: gibbsite and bayerite. *J. Phys. Chem. B* **105**, 10236-10242.

Ghose, S.K., Waychunas, G.A., Trainor, T.P. and Eng, P.J. (2010) Hydrated goethite (α-FeOOH) (100) interface structure: ordered water and surface functional groups. *Geochim. Cosmochim. Acta* **74**, 1943-1953.

Goldberg, S. (1986) Chemical modeling of arsenate adsorption on aluminum and iron oxide minerals. *Soil Sci. Soc. Am. J.* **50**, 1154-1157.

Goldberg, S. and Johnston, C.T. (2001) Mechanisms of arsenic adsorption on amorphous oxides evaluated using macroscopic measurements, vibrational spectroscopy, and surface complexation modeling. *J. Colloid Interface Sci.* **234**, 204-216.

Grassian, V.H. (2008) Surface science of complex environmental interfaces: Oxide and carbonate surfaces in dynamic equilibrium with water vapor. *Surf. Sci. Rep.* **602**, 2955-2962.

Hiemstra, T. and Van Riemsdijk, W.H. (1999) Surface structural ion adsorption modeling of competitive binding of oxyanions by metal (hydr)oxides. *J. Colloid Interface Sci.* **210**, 182-193.

Hiemstra, T., Van Riemsdijk, W.H. and Bolt, G.H. (1989) Multisite proton adsorption modeling at the solid/solution interface of (hydr)oxides: a new approach I. Model description and evaluation of intrinsic reaction constants. *J. Colloid Interface Sci.* **133**, 91-104.

Hiemstra, T., Venema, P. and Van Riemsdijk, W.H. (1996) Intrinsic proton affinity of reactive surface groups of metal (hydr)oxides: The bond valence principle. *J. Colloid Interface Sci.* **184**, 680-692.

Hiemstra, T., Yong, H. and Van Riemsdijk, W.H. (1999) Interfacial charging phenomena of aluminum (hydr)oxides. *Langmuir* **15**, 5942-5955.

Jain, C.K. and Ali, I. (2000) Arsenic: occurrence, toxicity and speciation techniques. *Water Res.* **34**, 4304-4312.

Jia, Y.F., Xu, L.Y., Wang, X. and Demopoulos, G.P. (2007) Infrared spectroscopic and X-ray diffraction characterization of the nature of adsorbed arsenate on ferrihydrite. *Geochim. Cosmochim. Acta* **71**, 1643-1654.

Kallay, N., Preočanin, T., Kovačević, D., Lützenkirchen, J. and Chibowski, E. (2010) Electrostatic potentials at solid/liquid interfaces. *Croat. Chem. Acta* **83**, 357-370.

Kappen, P. and Webb, J. (2013) An EXAFS study of arsenic bonding on amorphous aluminum hydroxide. *Appl. Geochem.* **31**, 79-83.

Kappler, A. and Straub, K.L. (2005) Geomicrobiological cycling of iron. *Rev. Mineral. Geochem.* **59**, 85-108.

Kerisit, S., Ilton, E.S. and Parker, S.C. (2006) Molecular dynamics simulations of electrolyte solutions ate the (100) goethite surface. *J. Phys. Chem. B* **110**, 20491-20501.

Koretsky, C. (2000) The significance of surface complexation reactions in hydrologic systems: a geochemist's perspective. *J. Hydrol.* **230**, 127-171.

Kraemer, S.M. (2004) Iron oxide dissolution and solubility in the presence of siderophores. *Aquat. Sci.* **66**, 3-18.

Kraemer, S.M. (2005) Siderophores and the dissolution of iron-bearing minerals in marine systems. *Rev. Mineral. Geochem.* **59**, 53-84.

Ladeira, A.C.Q., Ciminelli, V.S.T., Duarte, H.A., Alives, M.C.M. and Ramos, A.Y. (2001) Mechanism of anion retention from EXAFS and density functional calculations: Arsenic(V) adsorbed on gibbsite. *Geochim. Cosmochim. Acta* **65**, 1211-1217.

Lumsdon, D.G., Fraser, A.R., Russell, J.D. and Livesey, N.T. (1984) New infrared band assignments for the arsenate ion adsorbed on synthetic goethite (α-FeOOH). *J. Soil Sci.* **35**, 381-386.

Lützenkirchen, J., Zimmermann, R., Preocanin, T., Filby, A., Kupcik, T., Küttner, D., Abdelmonem, A., Schild, D., Rabung, T., Plaschke, M., Brandenstein, F., Werner, C. and Geckeis, H. (2010) An attempt to explain bimodal behaviour of the sapphire c-plane electrolyte interface. *Adv. Colloid Interface Sci.* **157**, 61-74.

Manceau, A. (1995) The mechanism of anion adsorption on iron oxides: evidence for the bonding of arsenate tetrahedra on free $Fe(O,OH)_6$ edges. *Geochim. Cosmochim. Acta* **59**, 3647-3653.

Manning, B.A., Fedorf, S.E. and Goldberg, S. (1998) Surface structures and stability of arsenic(III) on goethite: spectroscopy evidence for inner-sphere complexes. *Environ. Sci. Technol.* **32**, 2383-2388.

Myneni, S.C.B., Traina, S.J., Waychunas, G.A. and Logan, T.J. (1998) Experimental and theoretical vibrational spectroscopic evaluation of arsenate coordination in aqueous solutions, solids, and at mineral-water interfaces. *Geochim. Cosmochim. Acta* **62**, 3285-3300.

Nordstrom, D.K. and Archer, D.G. (2003) Arsenic thermodynamic data and environmental geochemistry, in: Welch, A.H., Stollenwerk, K.G. (Eds.), *Arsenic in Ground Water: Geochemistry and Occurrence*. Kluwer Academic Publishers, Dordrecht.

Ohno, T. and Amirbahman, A. (2010) Phosphorus availability in boreal forest soils: A geochemical andnutrient uptake modeling approach. *Geoderma* **155**, 46-54.

Phillips, B.L., Lee, A.P. and Casey, W.H. (2003) Rates of oxygen exchange between the $Al_2O_8Al_{28}(OH)_{56}(H_2O)_{26}^{18+}$(aq) ($Al_{30}$) molecule and aqueous solution. *Geochim. Cosmochim. Acta* **67**, 2725-2733.

Rechard, P., Kretzchmar, R. and Kraemer, S.M. (2007) Dissolution mechanisms of goethite in the presence of siderophores and organic acids. *Geochim. Cosmochim. Acta* **71**, 5635-5650.

Sherman, D.M. (2009) Surface complexation modeling: Mineral fuid equilbria at the molecular scale. *Rev. Mineral. Geochem.* **70**, 181-205.

Sherman, D.M. and Randall, S.R. (2003) Surface complexation of arsenic(V) to iron(III) (hydr)oxides: Structural mechanism from ab initio molecular geometries and EXAFS spectroscopy. *Geochim. Cosmochim. Acta* **67**, 4223-4230.

Shi, Z., Zachara, J.M., Wang, Z., Shi, L. and Fredrickson, J.K. (2013) Reductive dissolution of goethite and hematite by reduced flavins. *Geochim. Cosmochim. Acta* **121**, 139-154.

Smedley, P.L. and Kinniburgh, D.G. (2002) A review of the source, behavior and distribution of arsenic in natural waters. *Appl. Geochem.* **17**, 517-568.

Sposito, G. (1998) On Points of Zero Charge. *Environ. Sci. Technol.* **32**, 2815-2819.

Stollenwerk, K.G. (2003) Geochemical processes controlling transport of arsenic in groundwater: A review of adsorption, in: Welch, A.H., Stollenwerk, K.G. (Eds.), *Arsenic in ground water: Geochemistry and Occurrence*. Kluwer Academic Publisher, Boston, pp. 67-100.

Sun, X. and Doner, H.E. (1996) An investigation of arsenate and arsenite bonding structures on goethite by FTIR. *Soil Sci.* **161**, 865-872.

Sung, J., Zhang, L.N., Tian, C.S., Shen, Y.R. and Waychunas, G.A. (2011) Effect of pH on the water/α-Al_2O_3 (1-102) interface structure studied by sum-frequency vibrational spectroscopy. *J. Phys. Chem. C* **115**, 13887-13893.

Toney, M.F., Howard, J.N., Richer, J., Borges, G.L., Gordon, J.G., Melroy, O.R., Wiesler, D.G., Yee, D. and Sorensen, L.B. (1994) Voltage-dependent ordering of water molecules at an electrode-electrolyte interface. *Nature* **368**, 444-446.

Venema, P., Hiemstra, T., Weidler, P.G. and van Riemsdijk, W.H. (1998) Intrinsic proton affinity of reactive surface groups of metal (hydr)oxides: Application to iron (hydr)oxides. *J. Colloid Interface Sci.* **198**, 282-295.

Waychunas, G.A., Rea, B.A., Fuller, C.C. and Davis, J.A. (1993) Surface chemistry of ferrihydrite: Part 1. EXAFS studies of the geometry of coprecipitated and adsorbed arsenate. *Geochim. Cosmochim. Acta* **57**, 2251-2269.

Welfers, K. and Misra, C. (1987) Oxides and hydroxides of aluminum. *Alcoa Technical Paper* **19**, 10-18.

Yanina, S.V. and Rosso, K.M. (2008) Linked reactivity at mineral-water interfaces through bulk crystal conduction. *Science* **320**, 218-222.

Zhang, L., Tian, C., Waychunas, G.A. and Shen, Y.R. (2008) Structures and charging of α-alumina (0001)/water interfaces studied by sum-frenqueny vibrational spectroscopy. *J. Am. Chem. Soc.* **130**, 7686-7694.

Zhang, Z., Fenter, P., Sturchio, N.C., Bedzyk, M.J., Machesky, M.L. and Wesolowski, D.J. (2007) Structure of rutile TiO_2 (110) in water and 1 molal Rb^+ at pH 12: inter-relationship among surface charge, interfacial hydration structure, and substrate structural displacements. *Surf. Sci.* **601**, 1129-1143.

CHAPTER 2

IMPACTS OF SURFACE SITE COORDINATION ON ARSENATE ADSORPTION: MACROSCOPIC UPTAKE AND BINDING MECHANISMS ON ALUMINUM HYDROXIDE SURFACES

Published as:
Xu, T. and Catalano, J.G. Impacts of surface site coordination on arsenate adsorption: macroscopic uptake and binding mechanisms on aluminum hydroxide surfaces. *Langmuir*, 2016, 32, 13261-13269.

2.1 ABSTRACT

Aluminum hydroxides play important roles in regulating the fate and transport of contaminants and nutrients in soils and aquatic systems. Like many metal oxides, these minerals display surface functional groups in a series of coordination states, each of which may differ in its affinity for adsorbates. The distribution of functional group types varies among distinct surfaces of aluminum hydroxides, and we thus hypothesize that the adsorption behavior and mechanisms will show a dependence on particle morphology. To test this hypothesis, we investigate arsenate adsorption on two aluminum hydroxide polymorphs with distinct particle morphologies, gibbsite [γ-$Al(OH)_3$] and bayerite [α-$Al(OH)_3$], at pH 4 and 7. Synthetic gibbsite platelets expose large (001) basal surfaces predicted to be terminated by doubly coordinated functional groups (>Al_2OH). In contrast, synthetic bayerite microrods display mainly edge surfaces (parallel to the c-axis) containing abundant singly coordinated functional groups (>$AlOH_2$). Macroscopic adsorption studies show that gibbsite adsorbs less arsenate per unit surface area than bayerite at both pH values and suggest that two surface complexes form on each material. Similar electrokinetic behavior is displayed at the same relative coverages of arsenate, suggesting that similar reactive surface groups (>$AlOH_2$) control the surface charging on both particles. EXAFS spectroscopy shows that there is no variation in arsenate surface speciation on a given mineral with surface coverage or pH. Whereas bidentate binuclear inner-sphere species are the dominant complexes present, the EXAFS result suggests that outer-sphere species also occur on both minerals, with a greater abundance on gibbsite. This binding mode likely involves adsorption to >Al_2OH sites, which have a slow ligand exchange rate that inhibits inner-sphere binding. These results demonstrate that adsorption mechanisms and capacity, even

when normalized for specific surface area, vary with metal oxide particle morphology because of the distribution of distinct functional groups.

2.2 INTRODUCTION

Chemical reactions at metal oxide surfaces are of great importance in many environmental and industrial processes, such as contaminant and nutrient transportation, crystal growth and dissolution, surface redox reactions, and corrosion and catalysis science (Al-Abadleh and Grassian, 2003; Brown et al., 1999; Grassian, 2008; Kappler and Straub, 2005; Kraemer, 2005; Sherman, 2009). These reactions predominantly occur at surface functional groups, which exist in multiple coordination states on the surface (Hiemstra et al., 1989). As common and highly reactive environmental adsorbents, aluminum hydroxide minerals are of particular interest because they not only play an important role in contaminant sequestration and nutrient release in soils and aquatic systems but also serve as a model system for understanding the surface reactivity of other naturally abundant Al-bearing minerals because of the similarity in functional groups exposed on their surfaces (Al-Abadleh and Grassian, 2003; Hiemstra et al., 1999).

The surface reactivity of aluminum hydroxide minerals under environmental conditions is primarily determined by the ability of surface functional groups to interact with both adsorbates and water (Hiemstra and Van Riemsdijk, 1996; Hiemstra et al., 1999). Aluminum hydroxide surfaces are terminated in either singly ($>AlOH_2$) or doubly ($>Al_2OH$) coordinated functional groups (Sherman, 2009). Models of surface complexation often explicitly assume that charge states and proton affinities of surface functional groups are directly related to the coordination state of oxygen (Hiemstra and Van Riemsdijk, 1996; Hiemstra et al., 1989; Hiemstra et al., 1999). Singly coordinated groups deprotonate from $>AlOH_2^{1/2+}$ to $>AlOH^{1/2-}$at weakly alkaline conditions ($pK_a \sim 9$) (Hiemstra et al., 1999). $>Al_2OH$ groups are fully charge-satisfied under neutral conditions, with deprotonation to $>Al_2O^-$ occurring at high pH ($pK_{a2} \sim 12$) and protonation to $>Al_2OH_2^+$ occurring at low pH ($pK_{a1} \sim 0$) (Hiemstra et al., 1999). Most surface

complexation models consider adsorbate binding only to >$AlOH_2$ sites, with >Al_2OH groups limited to protonation-deprotonation reactions (Fukushi and Sverjensky, 2007; Gan and Franks, 2006; Hiemstra and Van Riemsdijk, 1996; Rosenqvist et al., 2002). Although steric constraints and the slow water-exchange rates of >Al_2OH groups (Casey and Phillips, 2001; Casey et al., 2000; Casey and Rosenqvist, 2004) suggest that this may be a valid assumption, the reactivity of such groups towards adsorbates has not been evaluated experimentally to date.

>$AlOH_2$ and >Al_2OH functional groups occur in substantially different site densities and distributions on distinct terminations of aluminum hydroxide surfaces (Bickmore et al., 2004). Basal (001) surfaces of aluminum hydroxides are predicted to be terminated exclusively in >Al_2OH groups with a structure nearly identical to that determined for the (001) plane of corundum (α-Al_2O_3) (Catalano, 2010; Catalano, 2011; Catalano et al., 2007; Eng et al., 2000; Welfers and Misra, 1987). Prior work has shown that the corundum (001) surface is relatively inert, and similar behavior is expected for aluminum hydroxide basal surfaces (Lützenkirchen et al., 2010). In contrast, other surfaces of aluminum hydroxides are terminated in >$AlOH_2$ groups, which are known to readily bind adsorbates (Catalano et al., 2008). Together, these observations imply that aluminum hydroxide minerals will show variations in reactivity toward adsorbates as a function of particle morphology, specifically the relative area of basal and non-basal surfaces.

This hypothesized morphology-reactivity relationship is tested in the present study by exploring the macroscopic adsorption behavior and molecular-scale surface speciation of arsenate ($H_nAsO_4^{3-n}$) on aluminum hydroxide polymorphs gibbsite [γ-$Al(OH)_3$] and bayerite [α-$Al(OH)_3$]. Arsenate is employed as a probe adsorbate because of its environmental relevance and its uptake over a wide pH range (unlike cation adsorbates) (Jain and Ali, 2000; Smedley and Kinniburgh, 2002). In aqueous solutions, arsenate forms oxoanions whose degree of protonation

is controlled by the pH. The pK_a values of arsenate (pK_1 = 2.30, pK_2 = 6.99, and pK_3 = 11.8) predict that the predominant arsenate aqueous species at typical environmental pH values of 4 to 8 would be $H_2AsO_4^-$ and $HAsO_4^{2-}$. The gibbsite particles have a platelet morphology dominated by basal surfaces, and the bayerite particles have a different morphology, exposing predominantly edge surfaces and relatively few basal surfaces. Arsenate adsorption isotherms at pH 4 and 7 explored the morphological effects on macroscopic adsorption behavior. Zeta-potential (ζ) measurements determined the effects of arsenate adsorption on the surface charging behavior of gibbsite and bayerite. Extended X-ray absorption fine structure (EXAFS) spectroscopy characterized arsenate adsorption mechanisms on each mineral surface at low, medium, and high surface coverages at both pH 4 and 7. These macroscopic and molecular scale studies were integrated to assess the effects of surface site coordination on arsenate adsorption on aluminum hydroxides surfaces.

2.3 MATERIALS AND METHODS

2.3.1 Mineral Synthesis and Characterization

Gibbsite platelets were prepared by the dropwise titration of a 10 wt.% ammonia solution into a vigorously stirred solution of 0.13 M $Al(NO_3)_3$ at room temperature until pH 5 was reached, followed by aging in a closed polypropylene bottle at 98 °C for 10 days (Shen et al., 2006). Bayerite microrods were synthesized following modified procedures outlined by Lefevre et al. (Lefevre and Fedoroff, 2002). Initially, 400 mL of a 10^{-3} M NaOH solution was heated in a closed 1 L polypropylene bottle at 70°C in a water bath under an Ar(g) headspace to eliminate CO_2. Next, 100 mL of a 0.1 M alkaline aluminum nitrate solution with an OH/Al ratio of 5 made by mixing $Al(NO_3)_3 \cdot 9H_2O$ and NaOH pellets was added slowly at a flow rate of 40 mL/h to pH 9.8. The pH of the suspension was monitored, and 0.5 mL increments of 0.2 M HNO_3 were

intermittently injected to maintain a value of ~ 9.8. After the complete addition of the alkaline aluminum nitrate solution, the pH was brought to 8 by adding 0.2 M HNO_3. The precipitate was then aged in the mother liquid overnight at room temperature. Both solids were washed repeatedly in deionized water (>18.2 MΩ·cm) to remove excess electrolytes. The resulting wet pastes were resuspended in deionized water and stored in polypropylene bottles for further use.

A portion of each mineral suspension was dried in a convection oven at 55°C for characterization. Powder X-ray diffraction (XRD) patterns (Figure A2.1 and A2.2) were collected to confirm the formation of gibbsite and bayerite and the absence of impurities (Bruker D8 Advance X-ray diffractometer, Cu Kα radiation). Crystal morphologies and particle sizes were examined using a scanning electron microscope (SEM) operated at 5 kV for gibbsite and 15 kV for bayerite (JEOL JSM-7001F Field Emission SEM). Brunauer-Emmett-Teller (BET) specific surface areas of the synthetic gibbsite and bayerite were 21.8 and 23.4 m^2/g, respectively (N_2 adsorption, Quantachrome Instruments Autosorb-1).

2.3.2 Macroscopic Arsenate Adsorption Isotherms

Arsenate adsorption isotherms were measured at pH 4 and 7 on both minerals. In the final volumes, all samples contained 4 g/L gibbsite or bayerite, 0.01 M $NaNO_3$ to buffer the ionic strength, a pH buffer of 0.001 M 3-(*N*-morpholino) propanesulfonic acid hemisodium salt (MOPS) at pH 7 (no buffer was used at pH 4), and arsenate at desired concentrations. The initial loading of arsenate varied from 10 µM to 600 µM, added from a $Na_2HAsO_4 \cdot 7H_2O$ solution. The pH value of each sample was adjusted to 4 or 7 with 1.0 M NaOH or HNO_3. All samples were placed on end-over-end rotators and mixed for 24 h at room temperature. Preliminary experiments showed that this time was sufficient to achieve equilibrium with respect to arsenate

adsorbed to mineral particles. During the reaction time, the pH of the samples varied by less than ± 0.1 pH unit from the target values. At the end of the reaction period the samples were centrifuged, and the supernatant was decanted, filtered (0.22 μm, MCE), and acidified to 2% HNO_3 (trace metal grade). Dissolved arsenate concentrations were determined by inductively coupled-plasma mass spectrometry (ICP-MS, PerkinElmer ELAN DRCII). Arsenate adsorption was calculated by the difference between the known total and the measured dissolved arsenate concentrations.

2.3.3 ζ-Potential Analysis

ζ-potential analysis was performed to study the effect of arsenate adsorption on the surface charge properties of both gibbsite and bayerite. Suspensions were prepared in the same way as the batch adsorption samples at pH 4 and 7. The initial loadings of low (20 and 60 μM), moderate (100 and 180 μM), and high (300 and 400 μM) arsenate were chosen according to the adsorption isotherm curves. Two samples with no arsenate were prepared to be the blank references. At the end of the adsorption reaction periods, 1 mL suspensions were withdrawn with syringes and injected into a ζ-potential analyzer (Zetasizer Nano, ZS Malvern, Southborough, MA). Each measurement was made in triplicate; unused portions of each sample were then filtered, acidified, and analyzed in the same way as were for the batch adsorption samples.

2.3.4 Extended X-ray Absorption Fine Structure Spectroscopy

The coordination environment of arsenate adsorbed to gibbsite and bayerite was investigated with extended X-ray adsorption fine structure (EXAFS) spectroscopy. Separate batch adsorption experiments were conducted in scaled-up reactors (50 mL centrifuge tubes) to

prepare fresh samples with sufficient mass for EXAFS measurements. Three samples for each mineral at both pH 4 and 7 were collected from batch adsorption experiments with initial loadings of low (40 μM), moderate (120 μM), and high (400 μM) arsenate (Table 2.1). All samples were centrifuged and loaded as wet pastes into polycarbonate sample holders sealed with Kapton tape. Samples were then transported to the Advanced Photon Source (APS) at Argonne National Laboratory to obtain As K-edge EXAFS spectra at APS beamline 20-BM-B (Heald, 2011; Heald et al., 1999). Incident beam optics consisted of a Si (111) double crystal monochromator, a Pt-coated Si toroidal focusing mirror, and a Rh-coated Si harmonic rejection mirror. Fluorescence yield spectra were measured using a 13-element energy dispersive Ge detector. Energy was calibrated using a Au metal foil, with the first inflection point in the Au L_{III}-edge set to 11919 eV.

EXAFS data were processed using the Athena (Ravel and Newville, 2005) and SixPack (Webb, 2005) interfaces to IFEFFIT (Newville, 2001). Phase-shift and backscattering amplitude functions for structural analysis of the EXAFS spectra were calculated using FEFF 7.02 (Ankudinov and Rehr, 1997) from the crystal structure of mansfieldite, $AlAsO_4 \cdot 2H_2O$ (Harrison, 2000). The amplitude reduction factor, S_0^2, was fixed to 1.0 for fitting. All spectra for each mineral were fitted using a single starting structural model consisting of As-O and As-Al single scattering paths and three multiple scattering paths: a triangular As-O-O path, a collinear As-O-As-O path, and a non-collinear As-O-As-O path. The parameters for these paths were determined from geometric considerations (Mikutta et al., 2010). For the As-Al single scattering path, the Debye-Waller factor, σ^2, was fixed to 0.006 to reduce correlations during fitting.

Table 2.1. Conditions for the adsorption samples analyzed by EXAFS spectroscopy.

Sample	Mineral	pH	$[AsO_4^{3-}]_{init}$ (μM)	$[AsO_4^{3-}]_{final}$ (μM)	Γ_{As} (μmol/m^2)
G1	4 g/L gibbsite	7.0	40	0.43	0.45
G2	4 g/L gibbsite	7.0	120	41	0.91
G3	4 g/L gibbsite	7.0	400	312	1.01
G4	4 g/L gibbsite	4.0	40	0.21	0.46
G5	4 g/L gibbsite	4.0	120	30	1.03
G6	4 g/L gibbsite	4.0	400	275	1.44
B1	4 g/L bayerite	7.0	40	0.09	0.69
B2	4 g/L bayerite	7.0	120	20	1.71
B3	4 g/L bayerite	7.0	400	275	2.14
B4	4 g/L bayerite	4.0	40	4.0	0.62
B5	4 g/L bayerite	4.0	120	17	1.78
B6	4 g/L bayerite	4.0	400	220	3.10

2.4 RESULTS

2.4.1 Characteristics of Synthetic Gibbsite and Bayerite

The two particle types used in this study display substantially different morphologies. SEM imaging of the synthetic gibbsite (Figure 2.1A) reveals uniform hexagonal platelets enclosed by the (001), (110), and (100) planes. With an average thickness of 40 nm and a width in the range of 0.6 to 1 μm, gibbsite is dominated by the basal (001) planes, representing about 91% of the total surface area. SEM imaging of the synthetic bayerite shows a distinct morphology, occurring as 3 to 10 μm long rods with flat irregular bases (Figure 2.1B). On bayerite, the edge (110) and (100) planes represent 94% of the total surface area, and the remaining areas are predominantly represented by the basal (001) planes.

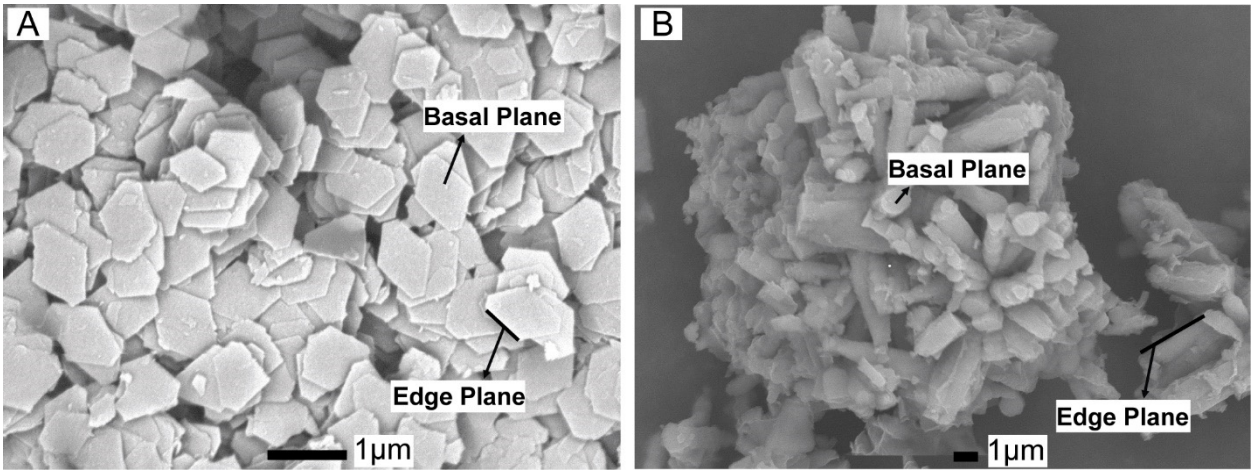

Figure 2.1. SEM images of the synthetic (A) gibbsite and (B) bayerite used in the study.

Gibbsite and bayerite are composed of the same basic structure layers of $Al(OH)_6$ octahedral sheets (Welfers and Misra, 1987). The layers are arranged in an AB-BA-AB sequence in gibbsite but in an AB-AB-AB sequence in bayerite. Despite the differences in their layer stacking, the surface terminations of various crystallographic planes are similar for these two minerals. Basal surfaces of gibbsite and bayerite, referred as the (001) planes, are terminated solely by $>Al_2OH$ groups, whereas the edge surfaces of gibbsite and bayerite, referred as the (110) or (100) planes, are terminated by $>AlOH_2$ groups (Figure 2.2). Considering the differences in particle morphologies, the surface of synthetic gibbsite is thus dominated by $>Al_2OH$ sites associated with the (001) plane and the surface of synthetic bayerite is dominantly terminated by $>AlOH_2$ sites of the (110) and (100) planes. In addition to having distinct distributions among aluminum hydroxide surfaces, $>Al_2OH$ and $>AlOH_2$ groups on basal and non-basal surfaces of gibbsite and bayerite also have different site densities, assuming ideal surface terminations, with a density of 13.6 sites/nm^2 for the $>Al_2OH$ group on basal surfaces and a density of 8.1 sites/nm^2 for $>AlOH_2$ groups on edge surfaces. The site densities were calculated using the crystal structure of gibbsite from Saalfeld and Wedde (1974). The synthetic

particles used here may differ from idealized morphology-dependent site distributions because of surface defects, such as steps on basal surfaces that display >$AlOH_2$ sites.

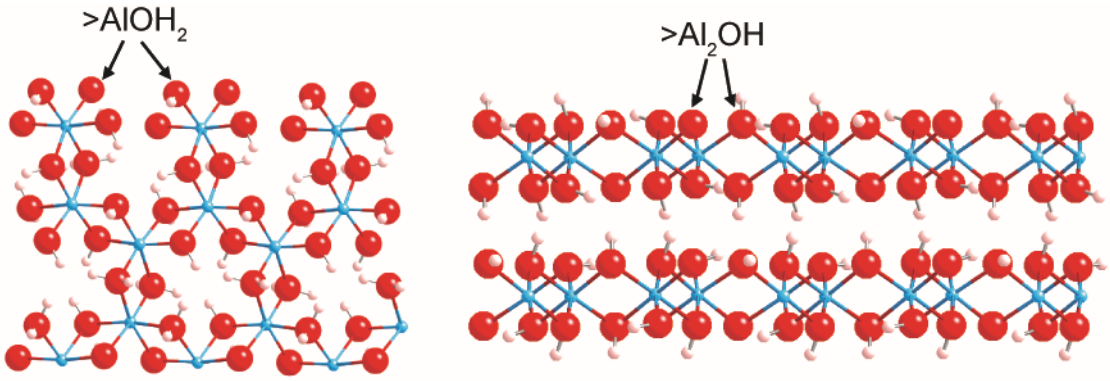

Figure 2.2. Structures of gibbsite viewed down the c-axis (left) and a-axis (right). Surface structures of the gibbsite (left) edge (110) or (100) surfaces and (right) basal (001) surfaces, with the labels indicating the different surface functional group coordination states present. Atom positions are determined from the crystal structure of gibbsite (Balan et al., 2006). Bayerite surface terminations are the same for gibbsite.

2.4.2 Macroscopic Arsenate Adsorption

The macroscopic adsorption of arsenate onto gibbsite and bayerite at pH 4 and 7 shows similar trends. For each mineral, more arsenate is observed to be adsorbed at pH 4 than at pH 7 (Figure 2.3), consistent with known oxoanion adsorption behavior (Brown and Parks, 2001). At each pH, more arsenate is observed to adsorb onto bayerite per unit surface area (BET normalized) than onto gibbsite (Figure 2.3). These differences are unlikely to result from aggregation effects during particle drying for BET measurements. SEM shows that gibbsite platelets have greater aggregations, aligning, and stacking during drying. If this affects the BET measurement, then the gibbsite surface area would be underestimated, leading to overestimated surface-area-normalized arsenate adsorption on gibbsite. The distinct arsenate binding capacity of these minerals is thus not an experimental artifact.

The macroscopic arsenate adsorption data for both minerals at both pH values were then fitted using Langmuir isotherms with co-optimized maximum adsorption capacity parameters ($\Gamma_{i,max}$) and affinity constants (K_i):

$$\Gamma_{ads} = \sum_{i=1}^{n} \frac{K_i \Gamma_{i,max} C_{(ads)}}{1 + K_i C_{(ads)}} \qquad (1)$$

where Γ_{ads} is the amount of adsorbate adsorbed and $C_{(ads)}$ is the final adsorbate concentration in solution. The adsorption data is poorly fitted using a single site Langmuir isotherm (n = 1 in Eq.1) for both gibbsite and bayerite (Figure A2.3). The single isotherms overestimate adsorption at low arsenate concentrations and underestimate uptake at higher concentrations. To better reproduce the data for both minerals, adsorption curves are then fitted using a dual Langmuir model (n = 2 in Eq.1) (Figure 2.3). The substantial improvement in this dual Langmuir fit suggests that at least two types of surface complexes have formed during the arsenate adsorption process.

The total Γ_{max} values of bayerite are larger than those of gibbsite at both pH values (Table 2.2). However, the difference in total Γ_{max} and the ratio of $\Gamma_{1,max}$ to $\Gamma_{2,max}$ for both surfaces do not vary in proportion to the basal and non-basal surface areas estimated from SEM, showing a lack of correlation with particle morphology. In addition, the K values for the two isotherm components are similar on both minerals at a given pH. There is thus no readily apparent relationship between particle morphology and either binding affinity or the relative capacity for different surface species.

Table 2.2. Fitting parameters for arsenate dual Langmuir isotherms.

Mineral	Γ_{max} (µmol/m^2)	K (L/µmol)	R-factor [a]
Gibbsite pH 4			
Langmuir_1	1.05 ± 0.03	2.1 ± 0.3	
Langmuir_2	0.9 ± 0.1	0.003 ± 0.001	
Total	2.0 ± 0.1		0.019
Gibbsite pH 7			
Langmuir_1	0.65 ± 0.05	29 ± 11	
Langmuir_2	0.52 ± 0.05	0.04 ± 0.02	
Total	1.17 ± 0.07		0.028
Bayerite pH 4			
Langmuir_1	1.85 ± 0.08	2.4 ± 0.4	
Langmuir_2	2.7 ± 0.4	0.004 ± 0.001	
Total	4.6 ± 0.4		0.025
Bayerite pH 7			
Langmuir_1	1.05 ± 0.07	18 ± 7	
Langmuir_2	1.05 ± 0.08	0.021 ± 0.007	
Total	2.1 ± 0.1		0.036

[a] Goodness-of-fit parameter. The R-factor is the sum of the differences between the data and the model fit at each data point divided by the sum of the data at each corresponding point. It represents the mean misfit between the data and the fit. Smaller R-factor values reflect better fits.

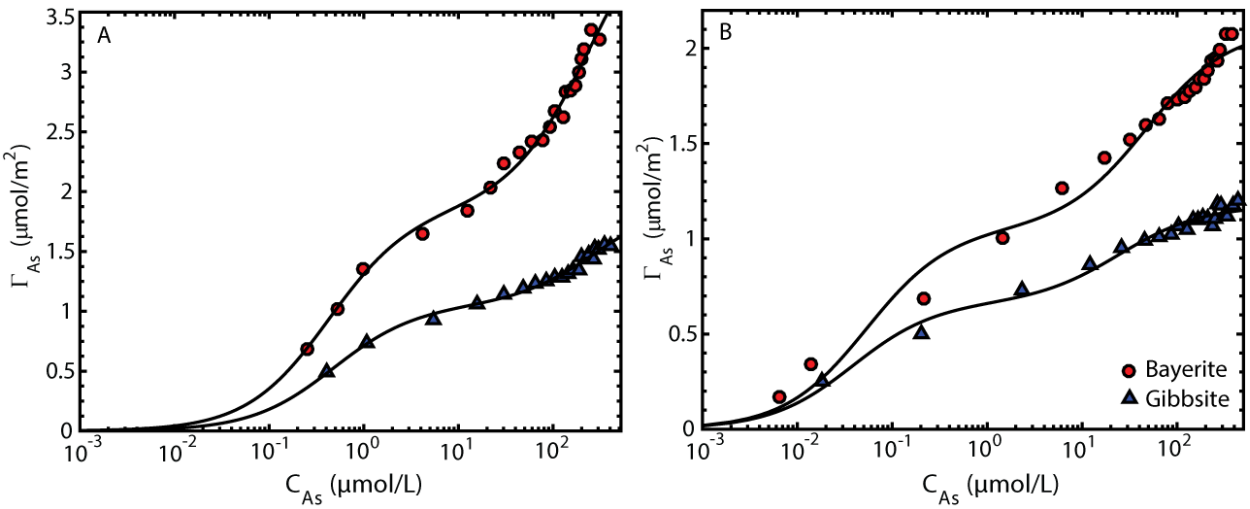

Figure 2.3. Arsenate adsorption isotherm on gibbsite and bayerite at (A) pH 4 and (B) pH 7. Lines represent dual Langmuir isotherm fits to the data.

2.4.3 Arsenate Adsorption Effect on Surface Charge Properties

ζ-potential measurements were made to evaluate how the differences in macroscopic uptake affect surface charging. Gibbsite and bayerite mineral suspensions have positive ζ-potential values at both pH 4 and 7, indicating positive surface charge in the absence of arsenate (Figure 2.4). This observation is consistent with previous studies of aluminum hydroxides (Adekola et al., 2011; Bickmore et al., 2004; Gan and Franks, 2006; Hiemstra et al., 1999; Rosenqvist et al., 2002), although the magnitude of the ζ-potential is larger in the present work. Arsenate adsorption shifts the ζ-potential to less positive values, as expected for anion adsorption. At the maximum arsenate surface coverage at each pH value, the ζ-potentials are similar for both minerals (27 to 32 mV at pH 4 and -5 to -10 mV at pH 7). In addition, at the first plateaus in the adsorption isotherms (pH 4: ~1.0 μmol/m^2 on gibbsite, ~1.9 μmol/m^2 on bayerite, pH 7: ~0.6 μmol/m^2 on gibbsite, ~1.1 μmol/m^2 on bayerite) the ζ-potentials are also similar between the two minerals at a given pH. The comparable electrokinetic response from arsenate surface coverages at the same relative location along the isotherm suggests that similar surface functional groups on both particles control the observed surface charging.

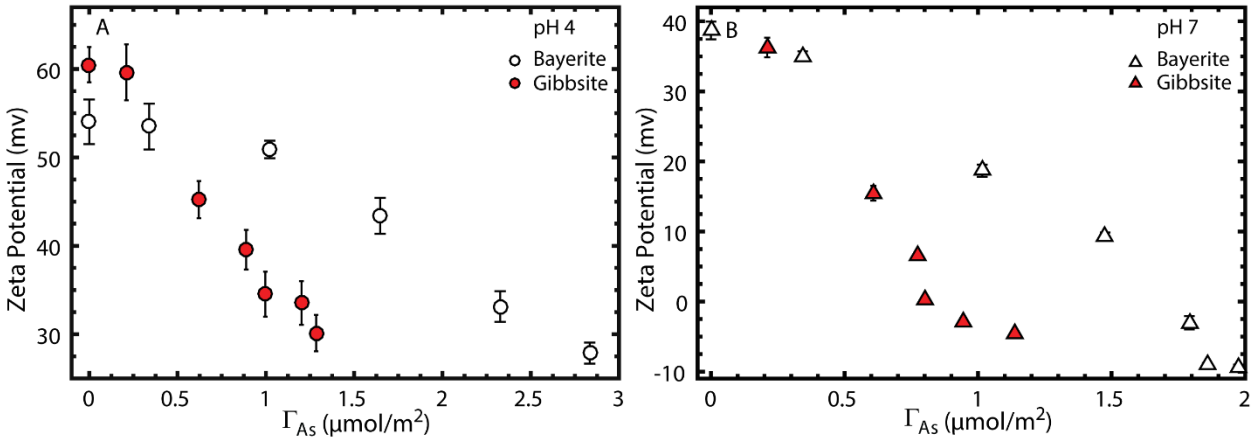

Figure 2.4. ζ-potential of gibbsite and bayerite as a function of adsorbed arsenate at pH 4 (A) and pH 7 (B).

2.4.4 Arsenate Adsorption Mechanisms

Arsenic surface speciation for a series of adsorption samples (Table 2.1) was characterized using EXAFS spectroscopy to determine the effect of particle morphology on arsenate binding mechanisms. The macroscopic behavior described above suggests that similar reactive sites control arsenate binding on both minerals. These should produce similar arsenic coordination environments, which can be assessed using in situ spectroscopic measurements. Conditions are selected where the final sample conditions produce low, medium, and high arsenate coverages associated with different proportions of the two isotherm components.

Different experimental conditions (i.e., pH, arsenate coverage, and mineral adsorbent) do not produce any distinctive visual patterns in the EXAFS spectra (Figure 2.5A, D). No change in arsenate surface speciation was observed with increasing arsenate coverage, as would be expected from the isotherm data. Fourier transform magnitudes for all samples have two features that are attributed to As-O and As-Al shells (Figure 2.5B, E). Structural model fitting of the spectra yields interatomic distances of ~1.69 Å for the As-O shell and ~3.2 Å for the As-Al shell (Table 2.3), in good agreement with structural parameters determined by other researchers (Arai et al., 2001; Foster et al., 1998; Kappen and Webb, 2013; Ladeira et al., 2001). In addition, this As-Al distance indicates that arsenate forms bidentate binuclear inner-sphere surface complexes (Arai et al., 2001; Foster et al., 1998; Kappen and Webb, 2013; Ladeira et al., 2001).

For both minerals, the coordination number for the Al neighbor associated with the inner-sphere complex is less than 2 (Table 2.3), with the value expected for arsenate adsorbed solely as a bidentate binuclear species. This may indicate the presence of other types of surface complexes (e.g., monodentate inner-sphere complexes or outer-sphere complexes). Past studies of arsenate adsorption on Al (oxyhydr)oxides have suggested that monodentate complexation may occur at

low arsenate coverage with an As-Al distance range of 3.5 Å to 3.6 Å (Arai et al., 2001; Kappen and Webb, 2013; Ladeira et al., 2001). Attempts to fit an additional Al neighbor corresponding to a monodentate binding model did not improve the quality of the fit and resulted in a coordination number for this longer Al shell within an error of zero for all arsenate coverages studied. This indicates that monodentate species are not a significant contributor to arsenate surface speciation on these minerals. Prior resonant anomalous X-ray reflectivity studies of arsenate adsorbed to corundum (012) surfaces demonstrated the coexistence of inner- and outer-sphere arsenate species (Catalano et al., 2008). The As-Al distances for such complexes are >5 Å (Catalano et al., 2008), too long to be directly observed by EXAFS spectroscopy. Although such species cannot be unambiguously identified in the present study, the low coordination number for the Al shell at ~3.2 Å and the lack of other inner-sphere species suggest that outer-sphere complexes are also present.

Structural model fitting parameters were further evaluated to assess possible differences in arsenate surface speciation on the two minerals. Arsenate adsorbed on gibbsite displayed a systematically smaller number of Al neighbors than did bayerite (Figure 2.6A, B), although the uncertainties in individual measurements were large. We performed a t-test to statistically evaluate whether the set of Al coordination numbers for arsenate adsorbed to gibbsite differed from the set for bayerite. The resulting test-statistic, $t_{calc} = 8.414$, corresponds to a confidence level of 99.9% and a *p*-value of 0.001, providing strong evidence that the mean Al coordination number for gibbsite is significantly different from that for bayerite. These results suggest that arsenate surface complexation mechanisms differ between the two mineral absorbents. The lower Al coordination number on gibbsite indicates a larger proportion of outer-sphere complexes or more disordered surface species. Similar statistical tests performed on the distances to Al

neighbors yield t_{calc} = 1.93, corresponding to a confidence level of 90% and a *p*-value of 0.1, proving that the distances to Al neighbors are statistically invariant for the two minerals (Figure 2.6C, D).

Table 2.3. As K-edge EXAFS fitting parameters.

Sample	Path	CN[a]	R(Å)[b]	σ^2 (Å^2)[c]	R-factor[d]	χ_v^{2} [d]
G1	As-O	4	1.693(4)	0.0018(2)	0.016	47.7
	As-Al	0.9(7)[e]	3.20(5)	0.006		
G2	As-O	4	1.693(5)	0.0018(2)	0.019	33.71
	As-Al	0.8(7)	3.19(6)	0.006		
G3	As-O	4	1.694(5)	0.0019(2)	0.020	37.01
	As-Al	0.9(7)	3.21(5)	0.006		
G4	As-O	4	1.694(4)	0.0018(2)	0.017	62.28
	As-Al	0.8(7)	3.20(6)	0.006		
G5	As-O	4	1.695(4)	0.0019(2)	0.017	30.78
	As-Al	0.9(7)	3.21(5)	0.006		
G6	As-O	4	1.694(5)	0.0021(2)	0.020	47.15
	As-Al	0.9(7)	3.23(5)	0.006		
B1	As-O	4	1.696(4)	0.0017(2)	0.017	84.95
	As-Al	1.4(7)	3.21(3)	0.006		
B2	As-O	4	1.693(5)	0.0020(2)	0.019	87.17
	As-Al	1.2(7)	3.20(4)	0.006		
B3	As-O	4	1.693(4)	0.0021(2)	0.016	46.78
	As-Al	1.4(6)	3.19(3)	0.006		
B4	As-O	4	1.694(4)	0.0017(2)	0.014	41.01
	As-Al	1.3(6)	3.19(3)	0.006		
B5	As-O	4	1.694(3)	0.0018(2)	0.010	48.68
	As-Al	1.3(5)	3.20(3)	0.006		
B6	As-O	4	1.694(3)	0.0020(2)	0.010	54.72
	As-Al	1.2(5)	3.20(3)	0.006		

[a] Coordination number. [b] Interatomic distance. [c] Debye-Waller factor. [d] Goodness-of-fit parameters (Kelly et al., 2008). [e] The estimated standard deviations are listed in parentheses, representing the errors in the last digit. Parameters with no listed uncertainties were fixed in the analyses.

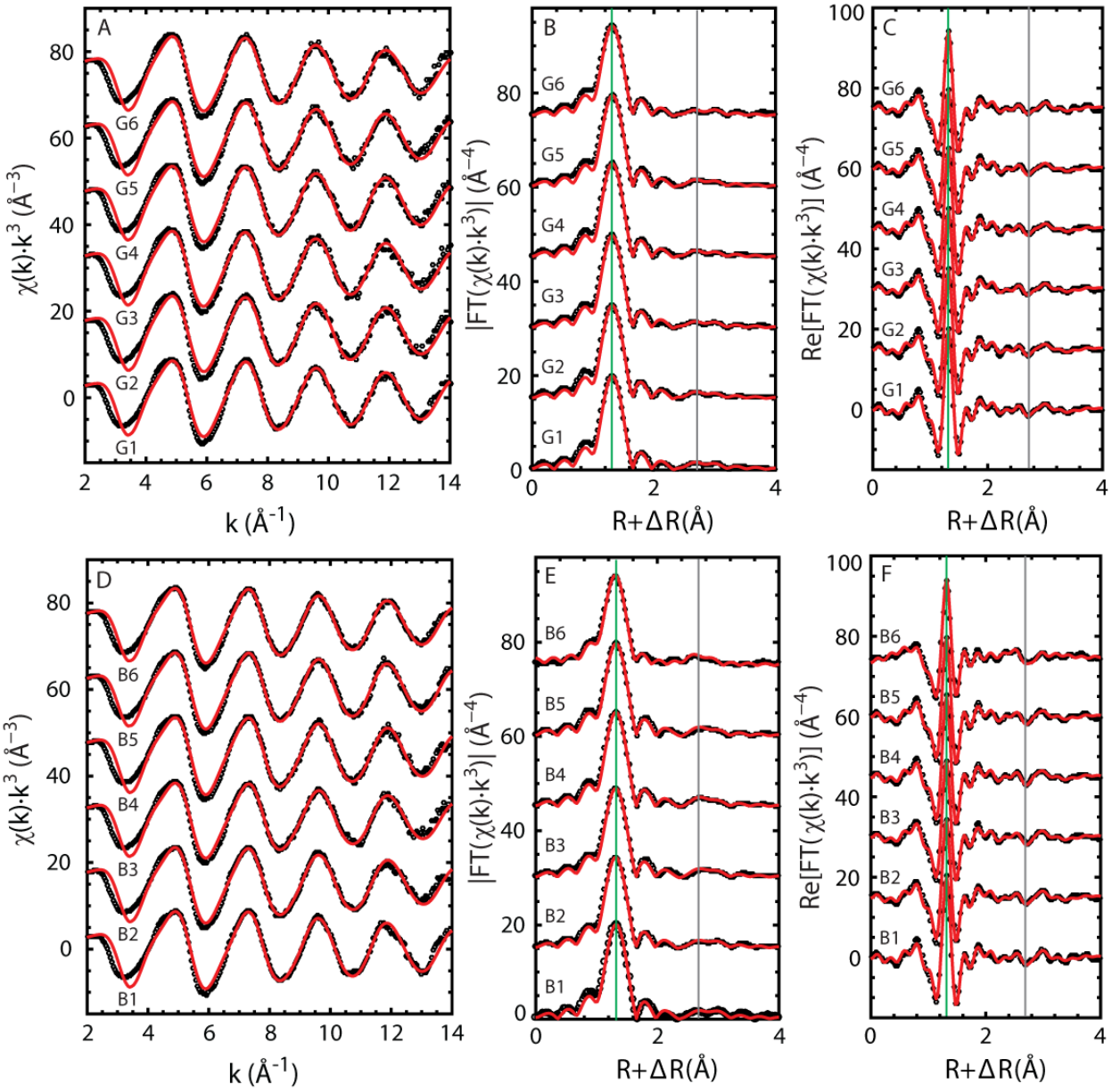

Figure 2.5. Data (dotted) and structural fits (solid) to the As K-edge spectra (A, D), Fourier transform magnitudes (B, E), and real components of the Fourier transforms (C, F) of the series of adsorption samples. Green lines indicate the location of As-O shells and gray lines indicate the location of As-Al shells. Detailed sample information is provided in Table 2.1.

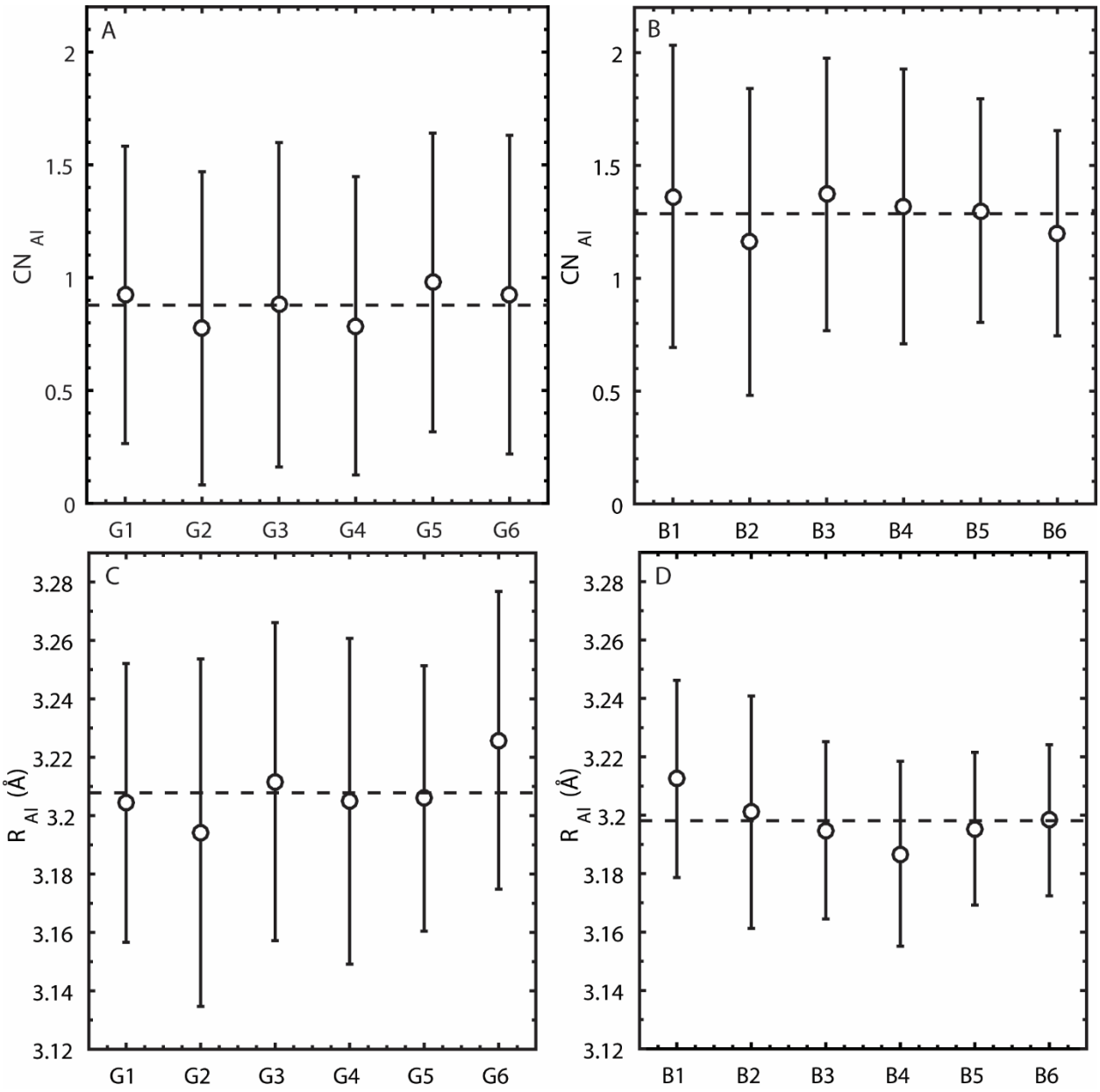

Figure 2.6. EXAFS-derived coordination number of the second-shell Al atoms (CN_{Al}) (A, B) and As-Al interatomic distances (R_{Al}) (C, D) for the series of adsorption samples. Also plotted are the mean values for each group (dashed). Detailed sample information is provided in Table 2.1, and the full fitting parameters are summed in Table 2.3.

2.5 DISCUSSION

2.5.1 Particle Morphology Effects on Arsenate Adsorption

This study demonstrates that the morphology of aluminum hydroxides affects the binding capacity of these minerals as well as the distribution between inner- and outer-sphere arsenate adsorption. Adsorption isotherms show that gibbsite with predominantly basal surfaces terminated by $>Al_2OH$ groups adsorbs less arsenate per unit surface area than bayerite with abundant edge surfaces bound by $>AlOH_2$ groups. The greater arsenate adsorption observed on bayerite is likely the result of morphology differences that produce more $>AlOH_2$ sites on this mineral than on gibbsite. However, defects, such as steps, must be present on the gibbsite (001) surface to provide extra $>AlOH_2$ sites, as the observed morphology differences suggest that far fewer of these sites should be present on gibbsite than indicated by arsenate adsorption if the particles had ideal surface terminations. AFM imaging (Figure A2.4) confirms that the gibbsite (001) surface contains abundant 1.0 to 1.4 nm steps, providing an addition source of $>AlOH_2$ sites. Besides the total amount of arsenate adsorbed, arsenate uptake behaves similarly on gibbsite and bayerite in isotherm experiments, indicating that arsenate binding primarily happens at the same site on both minerals, forming the same surface complexes. ζ-potential measurements show that the ζ-potentials reach the same values at the same relative arsenate surface coverage (i.e., fraction of maximum coverage) on both minerals, suggesting that $>AlOH_2$ groups control surface charging on the particles used in this study. The macroscopic results in this study, including the adsorbate geometry, similar isotherms, and surface charging behavior, suggest that adsorbates bind primarily at similar reactive sites (i.e., $>AlOH_2$ sites) on both minerals.

EXAFS spectroscopy of selected samples identifies the presence of the same arsenate surface complexes, inner-sphere bidentate binuclear surface complexes, on both minerals,

regardless of pH and arsenate coverage. Other types of surface complexes that lack EXAFS-detectable Al neighbors, likely outer-sphere species, are also present on both minerals, in a greater abundance on gibbsite. A previous study has already observed outer-sphere arsenate coadsorbs with inner-sphere arsenate on single crystal surfaces such as corundum and hematite (Catalano et al., 2008). Those surfaces expose similar functional groups, singly and doubly coordinated hydroxyl groups, compared to aluminum hydroxide particles used in this work. Thus, EXAFS results in this study suggest that outer-sphere arsenate complexes are present on mineral particles, not just on single crystals, although their observation in the present case is indirect and thus not unambiguous. The presence of such species is unexpected because prior studies of outer-sphere complexation have not observed a substantial dependence on ionic strength (Antelo et al., 2005; Arai et al., 2001; Goldberg and Johnston, 2001), a classical indicator of such an adsorption mechanism. However, variations in adsorption with ionic strength will be weak when the surface potential is small or the percent adsorption is large, and neutral surface complexes will display no dependence on ionic strength. If such complexes are present, then inner- and outer-sphere arsenate species maintain an approximately constant proportion along the adsorption isotherm because the coordination numbers of As-Al obtained from the EXAFS fittings do not vary with the arsenate surface coverage. This is in agreement with measurements of arsenate adsorption on corundum and hematite single crystal surfaces (Catalano et al., 2008). The greater proportion of outer-sphere complexes on gibbsite than on bayerite suggests that these species may be associated with $>Al_2OH$ groups, where inner-sphere binding is inhibited by the slow ligand exchange.

2.5.2 Implications for Adsorption Process

The present study demonstrates that particle morphology quantitatively alters the surface-area-normalized binding capacity of adsorbates. It shows that oxide or hydroxide minerals such as gibbsite and bayerite do not have a constant reactive surface site density, an assumption of surface complexation models (Sahai and Sverjensky, 1997), but instead have densities of available binding sites that vary with particle shape. Nucleation and growth processes, which determine the morphology of aluminum hydroxides, can thus control the surface-area-normalized binding capacity. Therefore, the number of adsorbates bound to aluminum hydroxide minerals will greatly depend on the initial formation conditions of these minerals. In addition, the distinct surface-area-normalized adsorption capacities for the aluminum hydroxide polymorphs studied here may not extend to all adsorbates. Arsenate binding requires ligand exchange, and the exchange rates of both $>Al_2OH$ groups and the oxoligands on arsenate are exceptionally slow (Casey and Phillips, 2001; Casey et al., 2000; Phillips et al., 2000; Phillips et al., 2003; Rosenqvist et al., 2002). Adsorbates with rapid water exchange rates, such as divalent cations, may be able to form inner-sphere complexes with $>Al_2OH$ sites, yielding different total binding capacities for these minerals (Casey et al., 2000; Wehrli et al., 1990).

2.6 CONCLUSIONS

This study demonstrates the differences in arsenate adsorption involving surface hydroxyl groups in various coordination states on aluminum hydroxides. Similar isotherms and electrokinetic behavior observed in macroscopic experiments suggest that the adsorbate mainly binds at a single type of reactive site, $>AlOH_2$ groups, on both minerals by forming the same type of surface complexes and that these sites control the surface charge properties of the sorbent particles. Adsorption isotherm experiments on both minerals also suggest that surface defects,

such as steps, should be present on the synthetic gibbsite basal surfaces to provide extra >$AlOH_2$ groups for arsenate. The same binding mechanisms operate on both minerals but the distribution between inner- and outer-sphere arsenate species differs.

Although thermodynamic adsorption models have largely assumed that singly coordinated functional groups are highly reactive and doubly coordinated groups are relatively inert, this has generally lacked direct experimental confirmation. Our work, therefore, supports the idea that singly coordinated functional groups, such as >$AlOH_2$ groups, are reactive and have a high affinity for adsorbates such as arsenate. This is in agreement with the observations for similar functional groups exposed on iron oxyhydroxide minerals (Ding et al., 2012; Song and Boily, 2012). In addition, the greater proportion of outer-sphere arsenate observed on gibbsite may result from binding at >Al_2OH groups on basal surfaces, where slow ligand exchange would inhibit inner-sphere binding. This indicates that basal surfaces of gibbsite terminated by >Al_2OH groups are also reactive to adsorbates but the formation of inner-sphere species is controlled by ligand exchange rates and thus is kinetically inhibited in many cases. In summary, our findings illustrate that arsenate adsorption on aluminum hydroxides is complex, with different types of surface complexes forming through reactions at multiple functional groups of different reactivity.

2.7 ACKNOWLEDGEMENTS

This research was supported by the U.S. National Science Foundation (NSF) Environmental Chemical Sciences Program (award no. CHE-1505532). ICP-MS and ζ-potential analyses were conducted at the Nano Research Facility at Washington University in St. Louis, supported by the NSF through award no. ECS-00335765. Use of the Bruker D8 Advance XRD at Washington University in St. Louis is made possible at NSF through award no. EAR-1161543.

SEM imaging was carried out at the Institute for Materials Science and Engineering at Washington University in St. Louis. Specific surface area measurements were performed at Jens Environmental Molecular and Nanoscale Analysis Laboratory at Washington University in St. Louis. EXAFS spectra were collected at beamline 20-BM-B at the Advanced Photon Source, an Office of Science User Facility operated for the U.S. Department of Energy (DOE) Office of Science by Argonne National Laboratory, which is supported by the U.S. DOE under contract no. DE-AC02-06CH11357. The authors thank Dale Brewe for beamline support and Sanmathi Chavalmane for assistance operating the ICP-MS.

2.8 APPENDIX

AFM Imaging of Gibbsite Basal Planes

Atomic force microscopy (AFM) imaging was conducted to investigate the abundance of steps on the gibbsite basal (001) surface. Gibbsite particles in deionized water were deposited on a glass slide that had been cleaned with HLPC-grade acetone, HPLC-grade methanol, and deionized water. A drop of HPLC-grade methanol was added to change the wetting of the surface and to promote evaporation. The sample was dried at ambient temperature in a vacuum desiccator for 15 minutes. The glass slide was then mounted in an Agilent Technologies model 5500 AFM operating in contact mode with a silicon nitride probe (Veeco NP-S; cantilever B with a nominal spring constant of 0.12 N/m). All images were collected in air.

Imaging reveals that most particles contain step structures on the basal surface (Figure A2.4). Higher-resolution images on the basal plane of a single particle reveal a step-and-terrace morphology. Observed step heights were generally 1.0 or 1.4 nm, corresponding to thickness of 2 and 3 $Al(OH)_3$ sheets, respectively. Terraces showed a wide range of widths, with an average step spacing of 41±16 nm.

Table A2.1. Fitting parameters for arsenate single Langmuir isotherms.

Mineral	Γ_{max} (µmol/m^2)	K (L/µmol)	R-factor [a]
Gibbsite pH 4	1.37 ± 0.04	0.8 ± 0.2	0.092
Gibbsite pH 7	1.08 ± 0.02	3 ± 1	0.077
Bayerite pH 4	2.8 ± 0.1	0.6 ± 0.2	0.13
Bayerite pH 7	1.83 ± 0.05	0.8 ± 0.3	0.098

[a] Goodness-of-fit parameter. The R-factor is the sum of the differences between the data and the model fit at each data point divided by the sum of the data at each corresponding point.

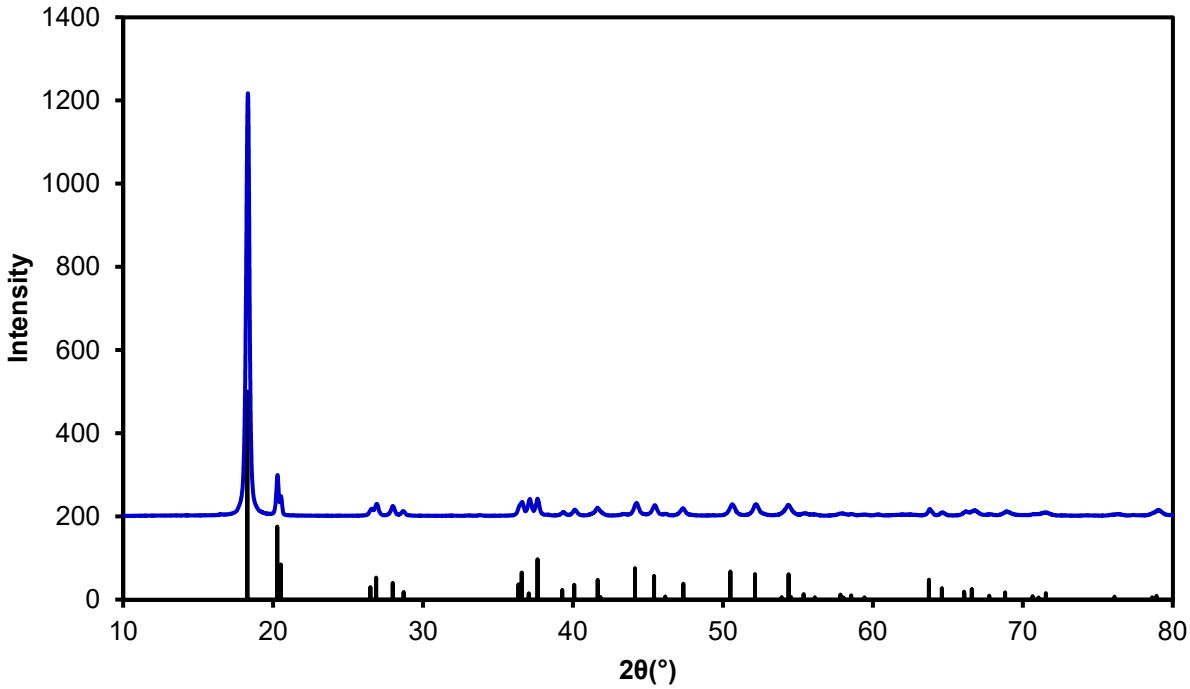

Figure A2.1. Powder XRD patterns of the synthetic gibbsite. Black sticks indicate the positions and intensities of diffraction lines calculated from the crystal structure of Balan et al., (2006) (Balan et al., 2006).

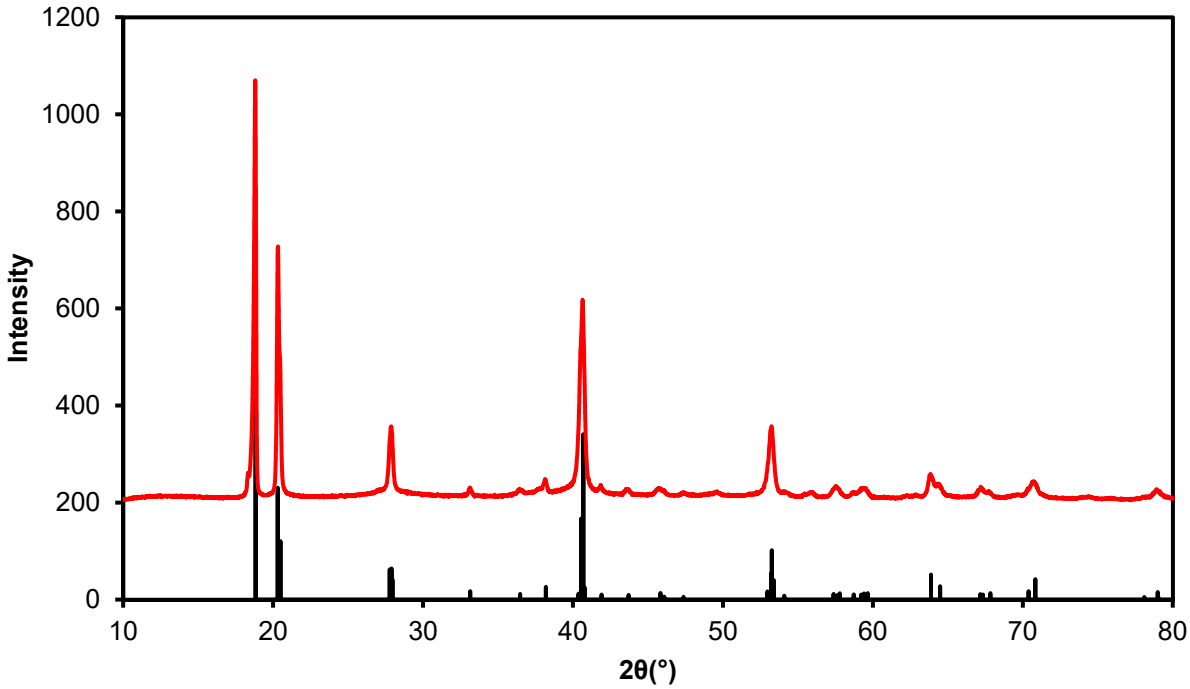

Figure A2.2. Powder XRD patterns of the synthetic bayerite. Black sticks indicate the positions and intensities of diffraction lines calculated from the crystal structure of Balan et al., (2008) (Balan et al., 2008).

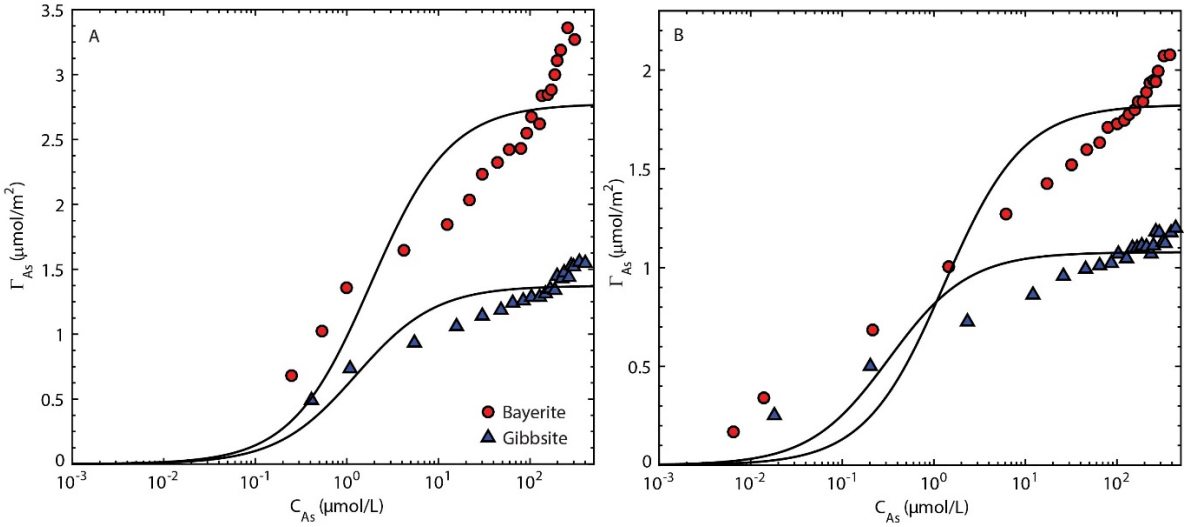

Figure A2.3. Single Langmuir isotherm fits (black lines) to arsenate uptake on gibbsite and bayerite at (A) pH 4 and (B) pH 7.

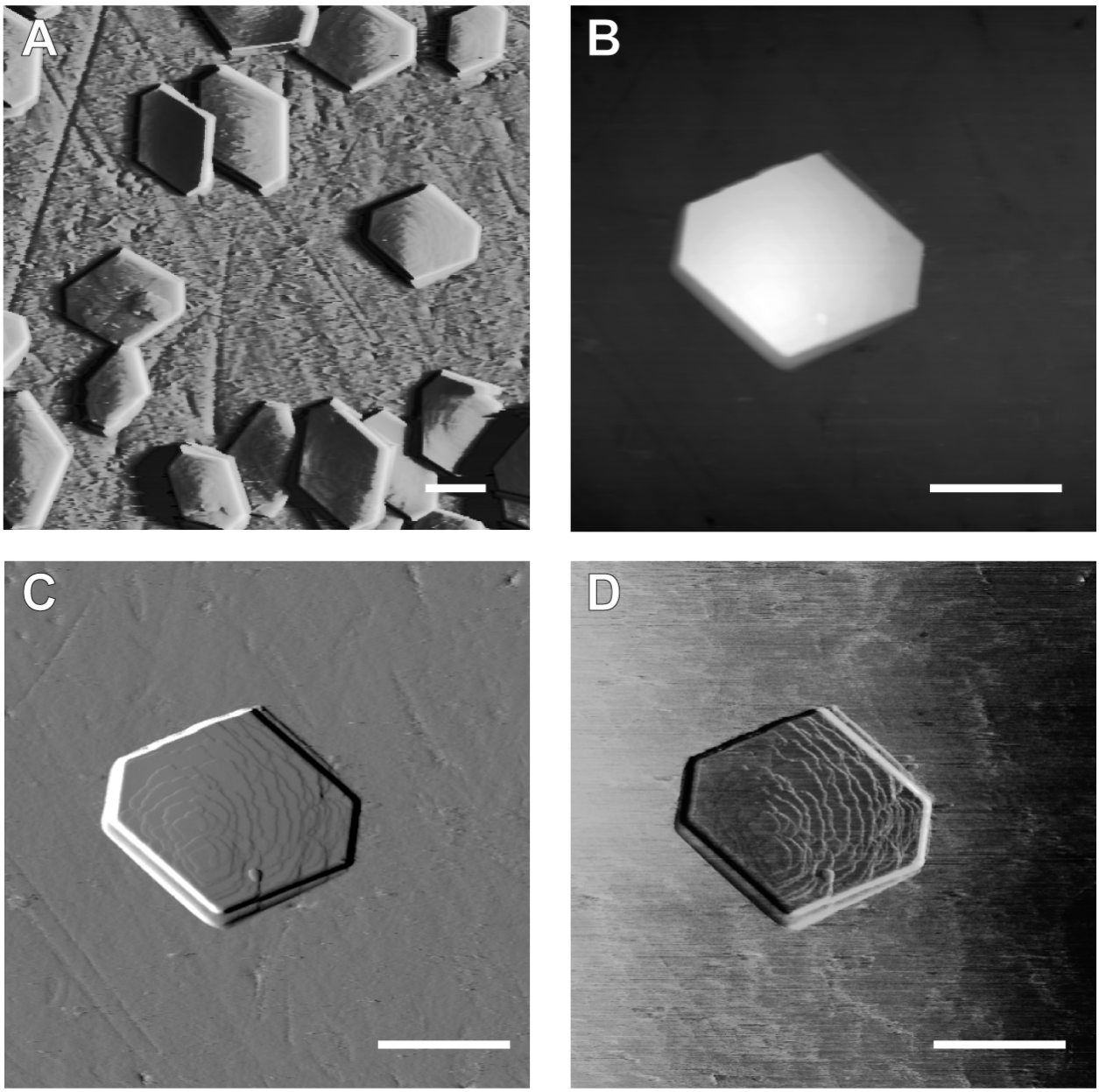

Figure A2.4. Contact mode images of the basal planes of gibbsite plates. (A) Deflection image of multiple particles; contrast was enhanced to more clearly display the occurrence of steps. Height (B), deflection (C), and lateral force (D) images of a single particle. Scale bar in all images is 500 nm.

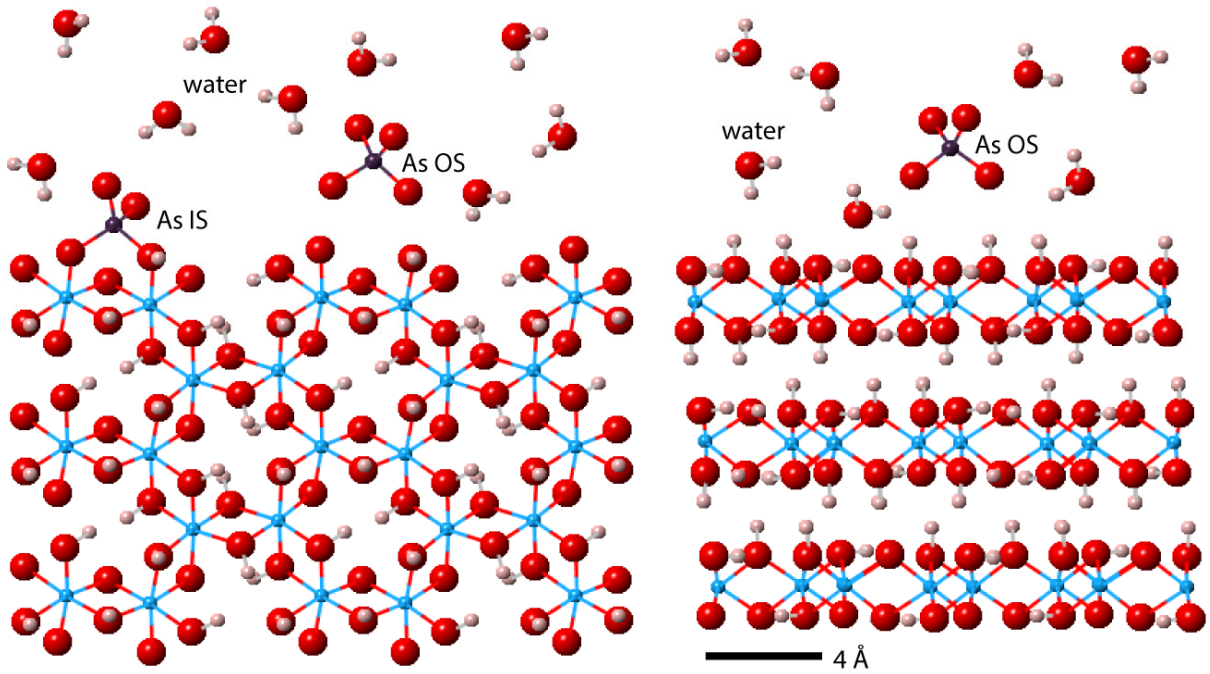

Figure A2.5. Schematic of arsenate adsorption mechanism, the coexisting of inner- and outer-sphere arsenate species, at aluminum hydroxide-water interfaces. Blue, purple, red, and pink balls represent Al, As, O, and H atoms, respectively.

2.9 REFERENCES

Adekola, F., Fedoroff, M., Geckeis, H., Kupcik, T., Lefevre, G., Lutzenkirchen, J., Plaschke, M., Preocanin, T., Rabung, T. and Schild, D. (2011) Characterization of acid-base properties of two gibbsite samples in the context of literature results. *J. Colloid Interface Sci.* **354**, 306-317.

Al-Abadleh, H.A. and Grassian, V.H. (2003) Oxide surfaces as environmental interfaces. *Surf. Sci. Rep.* **52**, 63-161.

Ankudinov, A.L. and Rehr, J.J. (1997) Relativistic calculations of independent X-ray absorption spectra. *Phys. Rev. B* **56**, 1712-1715.

Antelo, J., Avena, M., Fiol, S., Lopez, R. and Arce, F. (2005) Effects of pH and ionic strength on the adsorption of phosphate and arsenate at the goethite-water interface. *J. Colloid Interface Sci.* **285**, 476-486.

Arai, Y., Elzinga, E.J. and Sparks, D.L. (2001) X-ray absorption spectroscopic investigation of arsenite and arsenate adsorption at the aluminum oxide-water interface. *J. Colloid Interface Sci.* **235**, 80-88.

Balan, E., Blanchard, M., Hochepied, J.-F. and Lazzeri, M. (2008) Surface modes in the infrared spectrum of hydrous minerals: the OH stretching modes of bayerite. *Phys. Chem. Miner.* **35**, 279-385.

Balan, E., Lazzeri, M., Morin, G. and Mauri, F. (2006) First-principles study of the OH-stretching modes of gibbsite. *Am. Mineral.* **91**, 115-119.

Bickmore, B.R., Tadanier, C.J., Rosso, K.M., Monn, W.D. and Eggett, D.L. (2004) Bond-valence methods for pKa prediction: critical reanalysis and a new approach. *Geochim. Cosmochim. Acta* **68**, 2025-2042.

Brown, G.E., Henrich, V.E., Casey, W.H., Clark, D.L., Eggleston, C., Felmy, A., Goodman, D.W., Gratzel, M., Maciel, G., McCarthy, M.I., Nealson, K.H., Sverjensky, D.A., Toney, M.F. and Zachara, J.M. (1999) Metal oxide surfaces and their interactions with aqueous solutions and microbial organisms. *Chem. Rev.* **99**, 77-174.

Brown, G.E. and Parks, G.A. (2001) Sorption of trace elements on mineral surfaces: Modern perspectives from spectroscopic studies, and comments on sorption in the marine environment. *Int. Geol. Rev.* **43**, 963-1073.

Casey, W.H. and Phillips, B.L. (2001) Kinetics of oxygen exchange between sites in the $GaO_4Al_{12}(OH)_{24}(H_2O)_{12}^{7+}$(aq) molecule and aqueous solution. *Geochim. Cosmochim. Acta* **2001**, 705-714.

Casey, W.H., Phillips, B.L., Karlsson, M., Nordin, J.P., Sullivan, D.L. and Neugebauer-Crawford, S. (2000) Rates and mechanisms of oxygen exchanges between sites in the $AlO_4Al_{12}(OH)_{24}(H_2O)_{12}^{7+}$(aq) complex and water: Implications for mineral surface chemistry. *Geochim. Cosmochim. Acta* **64**, 2951-2964.

Casey, W.H. and Rosenqvist, J. (2004) The flux of oxygen from the basal surface of gibbsite at equilibrium. *Geochim. Cosmochim. Acta* **68**, 3547-3555.

Catalano, J.G. (2010) Relaxations and interfacial water ordering at the corundum (110) surface. *J. Phys. Chem. C* **114**, 6624-6630.

Catalano, J.G. (2011) Weak interfacial water ordering on isostructural hematite and corundum (001) surfaces. *Geochim. Cosmochim. Acta* **75**, 2062-2071.

Catalano, J.G., Fenter, P. and Park, C. (2007) Interfacial water structure on the (012) surface of hematite: Ordering and reactivity in comparison with corundum. *Geochim. Cosmochim. Acta* **71**, 5313-5324.

Catalano, J.G., Park, C., Fenter, P. and Zhang, Z. (2008) Simultaneous inner- and outer-sphere arsenate complexation on corundum and hematite. *Geochim. Cosmochim. Acta* **72**, 1986-2004.

Ding, X., Song, X. and Boily, J.-F. (2012) Identification of fluoride and phosphate binding sites at FeOOH surfaces. *J. Phys. Chem. C* **116**, 21939-21947.

Eng, P.J., Trainor, T.P., Brown, G.E., Waychunas, G.A., Newville, M., Sutton, S. and River, M.L. (2000) Structure of the hydrated α-Al_2O_3 (0001) surface. *Science* **288**, 1029-1033.

Foster, A.L., Brown, G.E., Tingle, T.N. and Parks, G.A. (1998) Quantitative arsenic speciation in mine tailings using X-ray absorption spectroscopy. *Am. Mineral.* **83**, 553-568.

Fukushi, K. and Sverjensky, D.A. (2007) A predictive model (ETLM) for arsenate adsorption and surface speciation on oxides consistent with spectroscopic and theoretical molecular evidence. *Geochim. Cosmochim. Acta* **71**, 3717-3745.

Gan, Y. and Franks, G.V. (2006) Charging behavior of the gibbsite (001) surface in NaCl solution investigated by AFM colloidal probe technique. *Langmuir* **22**, 6087-6092.

Goldberg, S. and Johnston, C.T. (2001) Mechanisms of arsenic adsorption on amorphous oxides evaluated using macroscopic measurements, vibrational spectroscopy, and surface complexation modeling. *J. Colloid Interface Sci.* **234**, 204-216.

Grassian, V.H. (2008) Surface science of complex environmental interfaces: Oxide and carbonate surfaces in dynamic equilibrium with water vapor. *Surf. Sci. Rep.* **602**, 2955-2962.

Harrison, W.T.A. (2000) Synthetic mansfieldite, $AlAsO_4 \cdot 2H_2O$. *Acta Cryst.* **56**, 421.

Heald, S.M. (2011) Optics upgrades at the APS beamline 20-BM. *Nucl. Instr. Meth. Phys. Res.* **649**, 128-130.

Heald, S.M., Brewe, D.L., Stern, E.A., Kin, K.H., Brown, F.C., Jiang, D.T., Crozier, E.D. and Gordon, R.A. (1999) XAFS and micro-XAFS at the PNC-CAT beamlines. *J. Synchrotron Rad.* **6**, 347-349.

Hiemstra, T. and Van Riemsdijk, W.H. (1996) A surface structural approach to ion adsorption: the charge distribution (CD) model. *J. Colloid Interface Sci.* **179**, 488-508.

Hiemstra, T., Van Riemsdijk, W.H. and Bolt, G.H. (1989) Multisite proton adsorption modeling at the solid/solution interface of (hydr)oxides: a new approach I. Model description and evaluation of intrinsic reaction constants. *J. Colloid Interface Sci.* **133**, 91-104.

Hiemstra, T., Yong, H. and Van Riemsdijk, W.H. (1999) Interfacial charging phenomena of aluminum (hydr)oxides. *Langmuir* **15**, 5942-5955.

Jain, C.K. and Ali, I. (2000) Arsenic: occurrence, toxicity and speciation techniques. *Water Res.* **34**, 4304-4312.

Kappen, P. and Webb, J. (2013) An EXAFS study of arsenic bonding on amorphous aluminum hydroxide. *Appl. Geochem.* **31**, 79-83.

Kappler, A. and Straub, K.L. (2005) Geomicrobiological cycling of iron. *Rev. Mineral. Geochem.* **59**, 85-108.

Kelly, S.D., Hesterberg, D. and Ravel, B. (2008) Analysis of soils and minerals using X-ray absorption spectroscopy. *Methods of Soil Analysis Part 5 - Mineralogical Methods*, 387-463.

Kraemer, S.M. (2005) Siderophores and the dissolution of iron-bearing minerals in marine systems. *Rev. Mineral. Geochem.* **59**, 53-84.

Ladeira, A.C.Q., Ciminelli, V.S.T., Duarte, H.A., Alives, M.C.M. and Ramos, A.Y. (2001) Mechanism of anion retention from EXAFS and density functional calculations: Arsenic(V) adsorbed on gibbsite. *Geochim. Cosmochim. Acta* **65**, 1211-1217.

Lefevre, G. and Fedoroff, M. (2002) Synthesis of bayerite [β-$Al(OH)_3$] microrods by neutralization of alyminate ions at constant pH. *Materials Letters* **56**, 978-983.

Lützenkirchen, J., Zimmermann, R., Preocanin, T., Filby, A., Kupcik, T., Küttner, D., Abdelmonem, A., Schild, D., Rabung, T., Plaschke, M., Brandenstein, F., Werner, C. and Geckeis, H. (2010) An attempt to explain bimodal behaviour of the sapphire c-plane electrolyte interface. *Adv. Colloid Interface Sci.* **157**, 61-74.

Mikutta, C., Frommer, J., Voegelin, A., Kaegi, R. and Kretzschmar, R. (2010) Effect of citrate on the local Fe coordination in ferrihydrite, arsenate binding, and ternary arsenate complex formation. *Geochim. Cosmochim. Acta* **74**, 5574-5592.

Newville, M. (2001) IFEFFIT: Interactive EXAFS analysis and FEFF fitting. *J. Synchrotron Rad.* **8**, 322-324.

Phillips, B.L., Casey, W.H. and Karlsson, M. (2000) Bonding and reactivity at oxide mineral surfaces from model aqueous complexes. *Nature* **404**, 379-382.

Phillips, B.L., Lee, A.P. and Casey, W.H. (2003) Rates of oxygen exchange between the $Al_2O_8Al_{28}(OH)_{56}(H_2O)_{26}^{18+}$(aq) ($Al_{30}$) molecule and aqueous solution. *Geochim. Cosmochim. Acta* **67**, 2725-2733.

Ravel, B. and Newville, M. (2005) ATHENA, ARTEMIS, HEPHAESTUS: Data analysis for X-ray absorption spectroscopy using IFEFFIT. *J. Synchrotron Rad.* **12**, 537-541.

Rosenqvist, J., Persson, P. and Sjoberg, S. (2002) Protonation and charging of nanosized gibbsite [α-$Al(OH)_3$] particles in aqueous suspension. *Langmuir* **18**, 4598-4604.

Saalfeld, H. and Wedde, H. (1974) Refinement of the crystal structure of gibbsite, $Al(OH)_3$. *Z. Kristallogr.* **139**, 129-135.

Sahai, N. and Sverjensky, D.A. (1997) Evaluation of internally consistent parameters for the triple-layer model by the systematic analysis of oxide surface titration data. *Geochim. Cosmochim. Acta* **61**, 2801-2826.

Shen, S., Chow, P.S., Chen, F., Feng, S. and Tan, R.B.H. (2006) Synthesis of submicron gibbsite platelets by organic-free hydrothermal crystallization process. *J. Cryst. Growth* **292**, 136-142.

Sherman, D.M. (2009) Surface complexation modeling: Mineral fuid equilbria at the molecular scale. *Rev. Mineral. Geochem.* **70**, 181-205.

Smedley, P.L. and Kinniburgh, D.G. (2002) A review of the source, behavior and distribution of arsenic in natural waters. *Appl. Geochem.* **17**, 517-568.

Song, X. and Boily, J.F. (2012) Structural control on OH site availability and reactivity at iron oxyhydroxide particle surfaces. *Phys. Chem. Chem. Phys.* **14**, 2579-2586.

Webb, S.M. (2005) SixPack: A graphical user interface for XAS analysis using IFEFFIT. *Phys. Scr.* **115**, 1011-1014.

Wehrli, B., Wieland, E. and Furrer, G. (1990) Chemical mechanisms in the dissolution kinetics of minerals: The aspect of active sites. *Aquat. Sci.* **52**, 3-31.

Welfers, K. and Misra, C. (1987) Oxides and hydroxides of aluminum. *Alcoa Technical Paper* **19**, 10-18.

CHAPTER 3

EFFECTS OF IONIC STRENGTH ON ARSENATE ADSORPTION AT ALUMINUM HYDROXIDE-WATER INTERFACES

Published as:
Xu, T. and Catalano, J.G. Effects of ionic strength on arsenate adsorption at aluminum hydroxide-water interfaces. *Soil Systems*, 2018, 2, 1.

3.1 ABSTRACT

Adsorption processes at mineral-water interfaces control the fate and transport of arsenic in soils and aquatic systems. Mechanistic and thermodynamic models to describe this phenomenon only consider inner-sphere complexes but recent observation of the simultaneous adsorption of inner- and outer-sphere arsenate on single crystal surfaces complicates this picture. In this study, we investigate the ionic strength-dependence of the macroscopic adsorption behavior and molecular-scale surface speciation of arsenate bound to gibbsite and bayerite. Arsenate adsorption decreases with increasing ionic strength on both minerals, with a larger effect at pH 4 than pH 7. The observed pH-dependence corresponds with a substantial decrease in surface charge at pH 7, as indicated by ζ-potential measurements. Extended X-ray absorption fine structure (EXAFS) spectroscopy finds that the number of second shell Al neighbors around arsenate is lower than that required for arsenate to occur solely as an inner-sphere surface complex. Together, these observations demonstrate that arsenate displays macroscopic and molecular-scale behavior consistent with the co-occurrence of inner- and outer-sphere surface complexes. This demonstrates that outer-sphere species can be responsible for strong adsorption of ions and suggests that environments experiencing an increase in salt content may induce arsenic release to water, especially under weakly acidic conditions.

3.2 INTRODUCTION

Adsorption is a critical control on the occurrence and fate of arsenic in soils and aquatic systems (Arai et al., 2003; Foster et al., 1998; Jain and Ali, 2000; Mandal and Suzuki, 2003; Smedley and Kinniburgh, 2002) and is utilized to remove this toxic element during water treatment (Chwirka et al., 2000; Garelick et al., 2005). Arsenate ($H_xAsO_4^{x-3}$), the common form of arsenic under oxidizing conditions, strongly adsorbs to many mineral surfaces, especially to aluminum and iron (oxyhydr)oxides (Arai et al., 2001; Arai et al., 2003; Foster et al., 1998; Goldberg and Johnston, 2001). The macroscopic uptake of this oxoanion onto oxide minerals has not been observed to display a dependence on ionic strength in prior studies (Antelo et al., 2005; Arai et al., 2001; Goldberg and Johnston, 2001), indicating a lack of outer-sphere complexes (Hayes et al., 1988). Previous spectroscopic studies have widely observed that arsenate forms inner-sphere surface complexes on mineral surfaces (Arai et al., 2001; Arai et al., 2003; Fendorf et al., 1997; Goldberg and Johnston, 2001; Manceau, 1995; Myneni et al., 1998; Sun and Doner, 1996; Waychunas et al., 1993). Surface complexation models for arsenate adsorption predict the partitioning of this oxoanion between water and mineral surfaces using only such complexes (Dixit and Hering, 2003; Goldberg, 1986; Goldberg and Johnston, 2001; Hiemstra and Van Riemsdijk, 1999). A description of arsenate adsorption behavior based solely on an inner-sphere (ligand exchange) binding mechanism was thus established over the last few decades that is widely accepted today.

This picture became more complicated when the simultaneous occurrence of both inner- and outer-sphere arsenate surface complexes was observed on aluminum and iron oxide single crystal surfaces (Catalano et al., 2008). While the transferability of processes on such highly-idealized surfaces to particles representative of natural and engineered sorbents is uncertain, a re-

evaluation of past observations is warranted. Detection of inner-sphere complexes using extended X-ray absorption fine structure (EXAFS) spectroscopy does not preclude co-existing outer-sphere species, as the latter lack diagnostic features in EXAFS spectra (Catalano et al., 2008). Hydrogen bonding of outer-sphere molecules to surface functional groups may yield infrared (IR) spectra of arsenate similar to what would be expected for inner-sphere species (Myneni et al., 1998). Furthermore, macroscopic uptake of arsenate will not display a dependence on ionic strength where outer-sphere complexes are neutrally-charged or when the surface potential is near zero. Prior work with mineral powders thus often cannot unambiguously rule out the co-occurrence of outer- and inner-sphere arsenate surface complexes.

Our recent work investigating binding site effects on arsenate adsorption to $Al(OH)_3$ polymorphs, gibbsite and bayerite, observed a lower coordination number of second-shell Al neighbors for gibbsite, indicating an additional surface species was present (Xu and Catalano, 2016). Other inner-sphere binding configurations were not present, suggesting co-occurring outer-sphere arsenate species. This molecular-scale picture conflicts with previous macroscopic studies that have not observed ionic strength-dependent arsenate adsorption behavior on aluminum and iron oxides (Antelo et al., 2005; Arai et al., 2001; Goldberg and Johnston, 2001). Antelo et al. (2005) did not detect observable changes in arsenate adsorption isotherms for goethite between 0.01 and 0.1 M KNO_3 fluids. Goldberg and Johnston (2001) observed a possible increase in adsorption with increasing ionic strength in adsorption edge measurements on amorphous iron oxide but saw no ionic strength dependence on amorphous aluminum oxide. Arai et al. (2001) observed no ionic strength effect on arsenate adsorption to γ-Al_2O_3, but their data contains substantial scatter and high percentages of arsenate adsorption at low pH, making detection of ionic strength effects difficult. In all cases, a substantial fraction clearly occurs as

inner-sphere species based on many past spectroscopic studies (Arai et al., 2001; Arai et al., 2003; Fendorf et al., 1997; Goldberg and Johnston, 2001; Lumsdon et al., 1984; Manceau, 1995; Myneni et al., 1998; Sun and Doner, 1996; Waychunas et al., 1993) and the ionic strength-dependence of macroscopic adsorption would be smaller in magnitude than for an ion that binds solely as an outer-sphere species. Exploration of the ionic strength dependence of arsenate adsorption to aluminum hydroxides is thus warranted given the contrasting past results.

In this study, we seek to determine whether macroscopic arsenate adsorption onto aluminum hydroxides displays a dependence on ionic strength that is consistent with our recent molecular-scale observations suggesting that inner- and outer-sphere species co-occur. Both gibbsite and bayerite are studied because they differ in morphology and thus have distinct distributions of surface functional group types (Hiemstra et al., 1999) that may lead to a distinct ionic strength-dependence of arsenate adsorption. Adsorption isotherms were measured on both minerals at pH 4 and 7 with ionic strength of 0.001, 0.01, 0.1, and 0.5 M $NaNO_3$. ζ-potential measurements assessed the sign and relative magnitude of gibbsite and bayerite surface charge in the presence and absence of adsorbed arsenate at the different ionic strength value used for the isotherm measurements. EXAFS spectroscopy characterized arsenate adsorption mechanisms on each mineral surface at low and high arsenate surface coverages at low and high ionic strength at both pH 4 and 7. These macroscopic and molecular-scale studies were integrated to assess the influences of ionic strength on arsenate adsorption on aluminum hydroxide surfaces.

3.3 MATERIALS AND METHODS

3.3.1 Mineral and Reagent Preparation

Gibbsite and bayerite were prepared following previously published syntheses (Xu and Catalano, 2016), modified from the procedures described in Shen et al. (2006) and Lefevre and Fedoroff (2002). After synthesis, gibbsite and bayerite were washed repeatedly in deionized water (>18.2 MΩ·cm) to remove excess electrolytes. Both minerals were resuspended in deionized water and stored in polypropylene bottles. The concentrations of the gibbsite and bayerite mineral suspensions were determined through gravimetric analysis. Both gibbsite and bayerite particles have been previously characterized by Brunauer-Emmett-Teller (BET) analysis, powder X-ray diffraction (XRD), and scanning electron microscope (SEM) (Xu and Catalano, 2016).

Sodium nitrate ($NaNO_3$, Sigma Aldrich St. Louis, MO, USA, ReagentPlus ≥ 99%), 3-(N-morpholino) propanesulfonic acid hemisodium salt (MOPS; Sigma Aldrich, ≥ 99%), and sodium arsenate ($Na_2HAsO_4 \cdot 7H_2O$; Sigma Aldrich, ACS Reagent ≥ 98%) stock solutions were made with deionized water. Two 20 g/L suspensions of gibbsite and bayerite were prepared in deionized water. Experiments conducted at pH 7 used a MOPS solution to buffer pH. All pH adjustments were made using HNO_3 or NaOH solutions.

3.3.2 Macroscopic Arsenate Adsorption Isotherms

Arsenate adsorption onto gibbsite and bayerite at pH 4 and 7 at solution ionic strength of 0.001, 0.01, 0.1, and 0.5 M $NaNO_3$ were investigated by batch adsorption isotherm experiments. Samples contained 4 g/L of gibbsite or bayerite reacted in a solution with an initial arsenate concentration from 10 μM to 500 μM, the desired concentration of $NaNO_3$ (0.001, 0.01, 0.1, and

0.5 M), and, at pH 7, a pH buffer of 0.001 M MOPS, added as the hemisodium salt (no buffer was used at pH 4). It should be noted that the addition of MOPS hemisodium salt increases the ionic strength values to 0.0015, 0.0105, 0.1005, and 0.5005 M for the pH 7 system. For each series of experiment, four mineral-free blanks with 40, 100, 200, and 400 μM arsenate were prepared to assess systematic errors in the initial arsenate concentrations. The samples were rotated on end-over-end rotators for 24 hours at room temperature. During the reaction time, sample pH was checked and adjusted to the target values. At the end of the experiment, the samples were filtered (0.22 μm, MCE; Santa Cruz Biotechnology, Dallas, TX, USA), discarding the first 1 mL of the filtrate, and acidified to 2% HNO_3 (trace metal grade; EMD Millipore, Billerica, MA, USA). The acidified filtrates were diluted appropriately with 2% HNO_3 for inductively coupled-plasma mass spectrometry (ICP-MS, Thermo Scientific iCAP Q, Bremen, Germany) analysis for dissolved arsenate concentrations.

3.3.3 ζ-Potential Analysis

ζ-potential analysis was performed to study the electrokinetic response of gibbsite and bayerite particles to different ionic strength with and without arsenate over the pH range of 3-8. Suspensions were prepared in the same way as the batch adsorption samples with 40 and 400 μM arsenate. Samples with no arsenate were prepared as the blank references. Suspensions (1 mL) were withdrawn with syringes and injected into a ζ-Potential analyzer (Zetasizer Nano ZS, Malvern, Southborough, MA, USA). Each data point is the average of three replicate measurements.

3.3.4 EXAFS Spectroscopic Measurements

The coordination environment of arsenate adsorbed to gibbsite and bayerite at different ionic strength was investigated with EXAFS spectroscopy. Separate batch adsorption experiments were conducted to prepare fresh samples before beamline measurements. Scaled-up reactors (50 mL total volume) were used to prepare samples with sufficient solid mass for EXAFS measurements. Two adsorbed arsenate samples for each mineral at the lowest and highest background electrolyte concentrations (I = 0.001 and 0.5 M $NaNO_3$) at each pH were prepared with initial low (40 μM) and high (400 μM) loading of arsenate (Table 3.1). All samples were centrifuged to separate the supernatant and solid (wet paste). The solids were packed as wet paste into polycarbonate sample holders, sealed with 25 μm Kapton tape, and heat sealed in a polyethylene bag with a damp Kimwipe to prevent drying.

Samples were prepared within 3 days of transport to the Stanford Synchrotron Radiation Lightsource (SSRL) at the SLAC National Accelerator Laboratory for measurements of As K-edge EXAFS spectra at SSRL beamline 4-1. Beamline 4-1 uses a Si (220) double crystal monochromator, which was detuned by 35% to attenuate beam harmonics. Fluorescence yield spectra were measured using a 30-element energy-dispersive Ge detector. Energy was calibrated using a Au metal foil, with the first inflection point in the Au LIII-edge set to 11919 eV.

The Athena interface (Ravel and Newville, 2005) to IFEFFIT (Newville, 2001), together with the SamView component of SixPack (Webb, 2005), were used to average, deadtime correct, and normalize the spectra. The mansfieldite ($AlAsO_4 \cdot 2H_2O$) structure (Harrison, 2000) was used to calculate phase-shift and backscattering amplitude functions for structural analysis of the EXAFS spectra using FEFF 7.02 (Ankudinov and Rehr, 1997). The k^3-weighted EXAFS spectra were fit over a k range of 3.5-12.5 Å and an R range of 0.8-4 Å, with the amplitude reduction

factor (S_0^2) fixed to 1.0. All spectra for each sample were fitted using a single starting structural model consisting of As-O and As-Al single scattering paths and three multiple scattering paths: a triangular As-O-O path, a collinear As-O-As-O path, and a non-collinear As-O-As-O path. The parameters for these paths were determined from geometric considerations (Mikutta et al., 2010). In the model fits, As-O coordination numbers were fixed at 4 and the coordination numbers of As-Al shells were allowed to vary. For the As-Al single scattering path, the Debye-Waller factor, σ^2, was fixed to 0.006 to reduce covariation during fitting.

Table 3.1. Conditions for the adsorption samples analyzed by EXAFS spectroscopy.

Sample	Mineral	pH	Desired I (M $NaNO_3$)	$[AsO_4^{3-}]_{init}$ (µM)	$[AsO_4^{3-}]_{final}$ (µM)	Γ_{As} (µmol/m^2)
G1	4 g/L gibbsite	7.0	0.5	40	10	0.35
G2	4 g/L gibbsite	7.0	0.5	400	338	0.71
G3	4 g/L gibbsite	7.0	0.001	40	2	0.44
G4	4 g/L gibbsite	7.0	0.001	400	329	0.82
G5	4 g/L gibbsite	4.0	0.5	40	9	0.36
G6	4 g/L gibbsite	4.0	0.5	400	312	1.01
G7	4 g/L gibbsite	4.0	0.001	40	1	0.45
G8	4 g/L gibbsite	4.0	0.001	400	278	1.41
B1	4 g/L bayerite	7.0	0.5	40	3	0.63
B2	4 g/L bayerite	7.0	0.5	400	333	1.16
B3	4 g/L bayerite	7.0	0.001	40	2	0.65
B4	4 g/L bayerite	7.0	0.001	400	319	1.39
B5	4 g/L bayerite	4.0	0.5	40	7	0.63
B6	4 g/L bayerite	4.0	0.5	400	329	1.31
B7	4 g/L bayerite	4.0	0.001	40	1	0.71
B8	4 g/L bayerite	4.0	0.001	400	101	1.92

3.4 RESULTS

3.4.1 Properties of Synthesized Materials

The chemical and physical properties of the gibbsite and bayerite used in this research have been previously described (Xu and Catalano, 2016). Briefly, the gibbsite and bayerite used in this study are aluminum hydroxide polymorphs with different morphology. Both mineral particles are enclosed by basal and edge surfaces with a substantially different ratio of these two types of surfaces. Synthetic gibbsite with a platelet morphology and bayerite with a micro-rod morphology were previously estimated to have ~91% of the basal (001) planes, terminated by doubly coordinated (>Al_2OH) functional groups, and ~94% of the edge planes, terminated by singly coordinated (>$AlOH_2$) functional groups, respectively (Xu and Catalano, 2016). The gibbsite and bayerite particles have similar surface areas (21.8 m^2/g and 23.4 m^2/g, respectively) determined by BET analysis (Xu and Catalano, 2016). Both minerals used in this study were previously characterized by XRD and SEM, confirming that they are consistent with the expected products of the published mineral synthesis methods, i.e., single phase, relatively monodispersed particles of the target mineral.

3.4.2 Macroscopic Arsenate Adsorption

The macroscopic arsenate adsorption isotherms on both minerals at each ionic strength show similar trends, with arsenate displaying greater adsorption at low pH and on bayerite versus gibbsite (Figure 3.1), consistent with our prior study (Xu and Catalano, 2016). The macroscopic arsenate adsorption data are then fitted using Langmuir isotherm with co-optimized maximum adsorption capacity parameters ($\Gamma_{max,i}$) and affinity constants (K_i):

$$\Gamma_{ads} = \sum_{i=1}^{n} \frac{K_i \Gamma_{max,i} C_{(ads)}}{1 + K_i C_{(ads)}} \qquad (1)$$

where Γ_{ads} is the amount of adsorbate adsorbed, $C_{(ads)}$ is the final adsorbate concentration in solution, n = 1 for single Langmuir fits involving only one adsorption site, and n = 2 for dual Langmuir fits involving two adsorption sites. The adsorption data are better fitted using the dual Langmuir isotherm model for both gibbsite and bayerite (Figure 3.1 and Figure A3.1). Comparing the fitting parameters in the dual Langmuir model, the total Γ_{max} values ($\Gamma_{max,1}$ + $\Gamma_{max,2}$) of bayerite are larger than those of gibbsite at same pH and same ionic strength (Table 3.2), which could be attributed to the abundance of edge surface sites on bayerite particles displaying stronger adsorption capacity. However, under the same experimental condition, the two components $\Gamma_{max,1}$ and $\Gamma_{max,2}$ do not vary in proportion to the relative areas of basal and edge surface sites on both minerals, suggesting that dual Langmuir behavior is not related to particle morphology but the presence of two different surface complexes (e.g., inner- and outer-sphere species) on both minerals. These macroscopic adsorption behaviors in the present study have also been observed in our previous study (Xu and Catalano, 2016). It should be noted that the very large K_1 value in the dual Langmuir model fit for gibbsite at pH 7 in 0.5 M $NaNO_3$ is likely not determined uniquely because of the lack of adsorption data at very low arsenate concentration. This is reflected in the small value of $\Gamma_{max,1}$ and the large uncertainty in K_1.

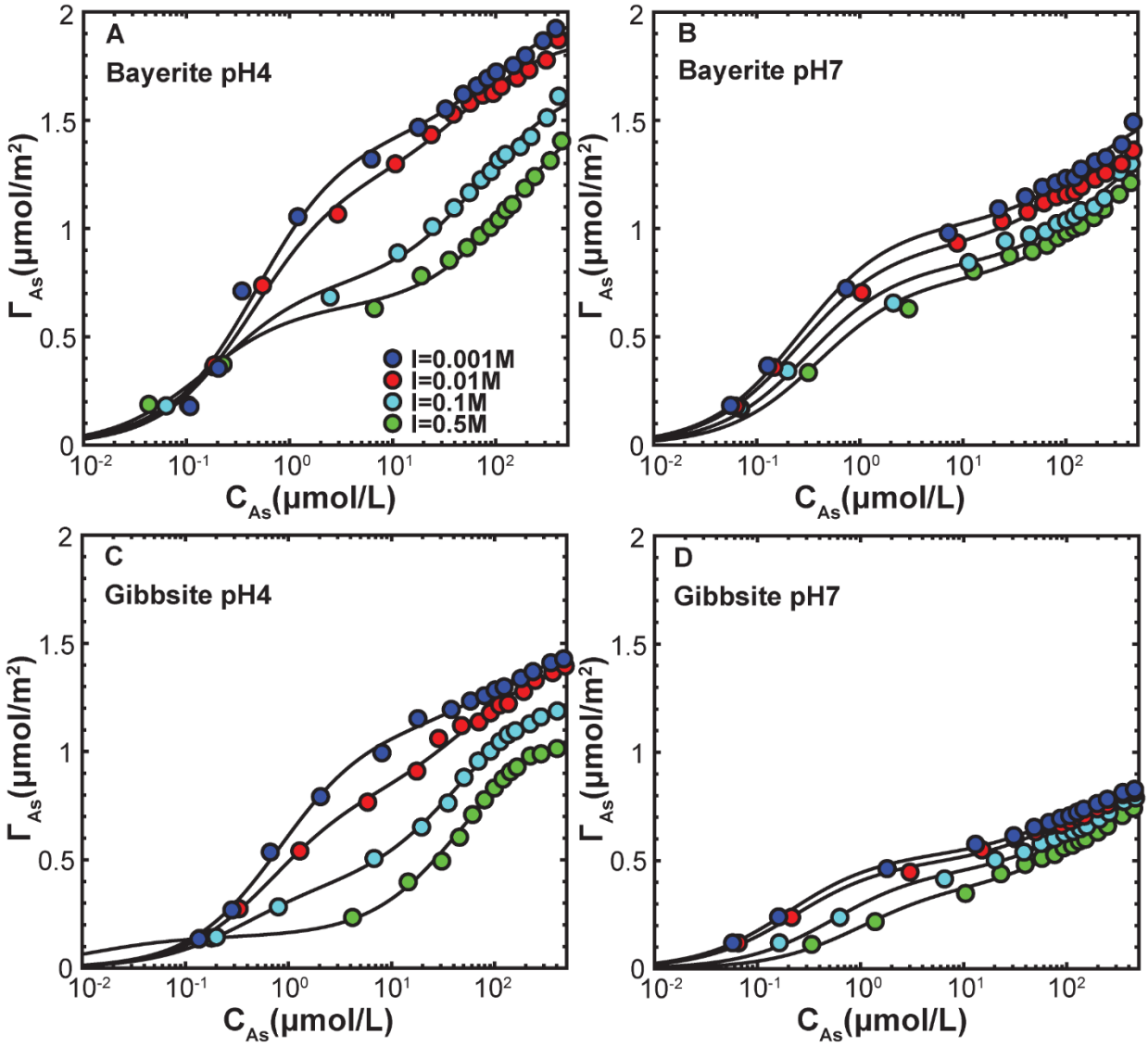

Figure 3.1. Arsenate adsorption isotherms as a function of ionic strength for bayerite at (A) pH 4 and (B) pH 7, on gibbsite at (C) pH 4 and (D) pH 7. Solid lines represent dual Langmuir isotherm fits to the data, with detailed fitting information provided in Table 3.2.

For each mineral, a change in ionic strength has substantial effects on arsenate uptake, with adsorption decreasing as ionic strength increases (Figure 3.1). These ionic strength-dependence effects on arsenate adsorption are larger in magnitude at pH 4 and on bayerite (Figure 3.1). At pH 4 the effect of ionic strength varies with final arsenate concentration (C_{As}): low C_{As} (< 0.3 μmol/L) regions display little variation in uptake with ionic strength, intermediate conditions (0.3 μmol/L< C_{As} < 60 μmol/L) show the greatest ionic strength effect, and high C_{As} (> 60 μmol/L) regions show a weaker ionic strength effect. In contrast, at pH 7 the effect of ionic strength on adsorption appears uniform across all arsenate concentrations. These results display clear macroscopic signatures associated with the presence of outer-sphere species, i.e., a decrease in adsorption with increasing ionic strength. The smaller effect seen at pH 7 may imply such species are of lower abundance under neutral conditions, but the magnitude of ionic strength effects on outer-sphere adsorption varies with the surface potential. If the surface charge is largely neutralized at pH 7 by arsenate adsorption, then little to no effect of ionic strength is expected even if outer-sphere species are present.

Table 3.2. Fitting parameters for dual Langmuir isotherms.

Mineral	pH	I (M)	$\Gamma_{max,1}$ (µmol/m^2)	K_1 (L/µmol)	$\Gamma_{max,2}$ (µmol/m^2)	K_2 (L/µmol)	R-Factor [a]
Bayerite	4	0.5	0.64 ± 0.03	7.23 ± 1.37	0.98 ± 0.05	0.007 ± 0.001	0.020
		0.1	0.75 ± 0.04	4.83 ± 0.89	0.94 ± 0.04	0.014 ± 0.003	0.017
		0.01	1.24 ± 0.06	2.25 ± 0.32	0.65 ± 0.06	0.02 ± 0.007	0.019
		0.001	1.43 ± 0.07	2.11 ± 0.32	0.62 ± 0.09	0.009 ± 0.006	0.022
Bayerite	7	0.5	0.77 ± 0.03	2.54 ± 0.48	0.62 ± 0.08	0.005 ± 0.002	0.021
		0.1	0.83 ± 0.04	3.17 ± 0.65	0.59 ± 0.13	0.004 ± 0.002	0.026
		0.01	0.92 ± 0.30	3.86 ± 0.47	0.51 ± 0.04	0.010 ± 0.003	0.016
		0.001	1.02 ± 0.03	3.87 ± 0.50	0.60 ± 0.07	0.006 ± 0.002	0.020
Gibbsite	4	0.5	0.15 ± 0.03	78 ± 9	0.99 ± 0.03	0.020 ± 0.003	0.022
		0.1	0.39 ± 0.03	2.7 ± 0.6	0.90 ± 0.03	0.023 ± 0.002	0.012
		0.01	0.81 ± 0.05	1.45 ± 0.26	0.63 ± 0.05	0.018 ± 0.005	0.018
		0.001	1.11 ± 0.04	1.21 ± 0.11	0.39 ± 0.04	0.009 ± 0.004	0.013
Gibbsite	7	0.5	0.38 ± 0.02	1.02 ± 0.21	0.47 ± 0.03	0.006 ± 0.002	0.020
		0.1	0.45 ± 0.02	1.85 ± 0.26	0.44 ± 0.03	0.006 ± 0.002	0.018
		0.01	0.49 ± 0.02	4.39 ± 0.62	0.38 ± 0.02	0.011 ± 0.003	0.019
		0.001	0.53 ± 0.01	5.02 ± 0.40	0.36 ± 0.01	0.010 ± 0.002	0.010

[a] Goodness-of-fit parameter. The R-factor is the sum of the differences between the data and the model fit at each data point, divided by the sum of the data at each corresponding point. It represents the mean misfit between the data and the fit. Smaller R-factor values reflect better fits.

3.4.3 Ionic Strength Effect on Surface Charge Properties

ζ-potential measurements were made to evaluate how different background electrolyte concentrations affect surface charging, and thus trends in the surface potential of gibbsite and bayerite particles in the absence and presence of arsenate. Over the pH range studied, gibbsite and bayerite suspensions have positive ζ-potential values in the absence of arsenate (Figure 3.2), consistent with previous studies of aluminum hydroxides with a typical isoelectric point (IEP) around pH 9-10 (Adekola et al., 2011; Gan and Franks, 2006; Hiemstra et al., 1999; Manning and Goldberg, 1996; Rosenqvist et al., 2002). At individual pH conditions, ζ-potential for both minerals decreases with increasing ionic strength (Figure 3.2), consistent with the known effect of counterion screening of surface charge, reducing the potential at the shear plane. After arsenate loading, the ζ-potential values of both minerals shift to more negative values, as expected for anion adsorption. For each mineral system, the ζ-potential value is lower near pH 7 than near pH 4, indicating that the surface potential is also lower at pH 7, and ionic strength-dependence effects on outer-sphere species are thus expected to be substantially greater at pH 4 (Figure 3.2). The ζ-potential appears to always be larger for bayerite than gibbsite in the presence of arsenate below pH 6 (Figure 3.2), indicating that the bayerite systems should display stronger ionic strength effects at acidic conditions. These two features are consistent with the observations in adsorption isotherm experiments in this study. In addition, the IEP differs between the two minerals, occurring near pH 7 for gibbsite at both arsenate coverages, but remaining above pH 8 for bayerite except at the highest arsenate coverage (Figure 3.2).

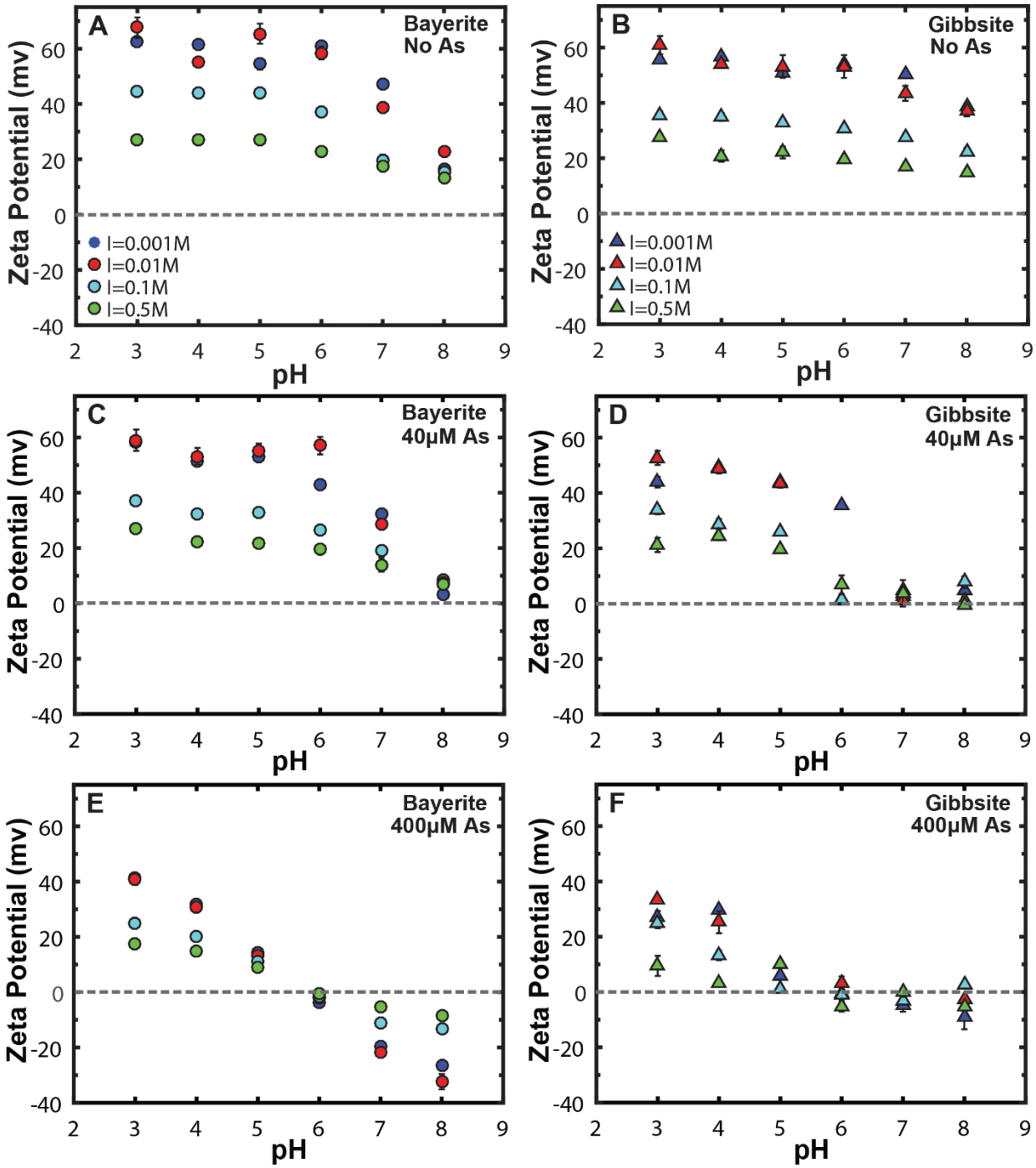

Figure 3.2. ζ-potential as a function of pH for systems with no arsenate on bayerite (A) and gibbsite (B), 40 μM arsenate on bayerite (C) and gibbsite (D), 400 μM arsenate on bayerite (E) and gibbsite (F). The error bars represent the standard deviation of three replicate measurements.

3.4.4 Arsenate Adsorption Mechanisms

Arsenic surface speciation for a series of adsorption samples (Table 3.1) was characterized using EXAFS spectroscopy to determine the effect of ionic strength on arsenate binding mechanisms. Conditions are chosen to explore low and high arsenate surface loading at the highest and lowest electrolyte concentrations, 0.5 and 0.001 M $NaNO_3$. Structural model fits of the EXAFS spectra yield interatomic distances of ~3.2 Å for As-Al shell for all samples regardless of pH, ionic strength, arsenate coverage, and mineral sorbents (Figure 3.3, Table 3.3). This configuration corresponds to a bridging bidentate inner-sphere surface complex, as has been identified in most previous studies (Arai et al., 2001; Foster et al., 1998; Kappen and Webb, 2013; Ladeira et al., 2001; Waychunas et al., 1993). All spectra for each sample were fitted using a single starting structural model consisting of only one Al neighbor corresponding to this bidentate binding configuration. As noted in our prior study (Xu and Catalano, 2016), we also evaluated whether monodentate species are present by adding a second As-Al path at R of 3.5 to 3.6 Å in our initial model. However, this did not improve the quality of fit and resulted in a coordination number for this longer Al shell within an error of zero for all sample studied. This indicates that monodentate inner-sphere species are negligible on these minerals for all conditions examined.

The EXAFS-derived coordination number of Al neighbors associated with the inner-sphere complex on both minerals is less than 2 (Table 3.3), the expected value if all the adsorbed arsenate was in a bridging bidentate geometry. This could indicate the presence of outer-sphere arsenate complexes as other inner-sphere binding configurations were not observed under our experimental conditions (Xu and Catalano, 2016). Also, this coordination number of Al neighbors is lower on average on gibbsite than that on bayerite. It should be noted that Al

coordination numbers obtained from individual samples are not statistically distinguishable because of the large fitting uncertainties. However, statistical tests (t-tests), as applied in the prior study (Xu and Catalano, 2016), showed that the difference in the average Al coordination numbers for two mineral sets is significant. The lower average Al coordination number on gibbsite indicates a greater proportion of outer-sphere complexes. For individual mineral system, similar statistical tests were performed to evaluate if the average Al coordination number of high ionic strength set differs from that of low ionic strength set. t-tests show that average Al coordination numbers are statistically invariant with different ionic strength for both minerals, suggesting that ionic strength has little effect on arsenate surface complexation geometry as well as the distribution of different types of arsenate surface species on gibbsite or bayerite.

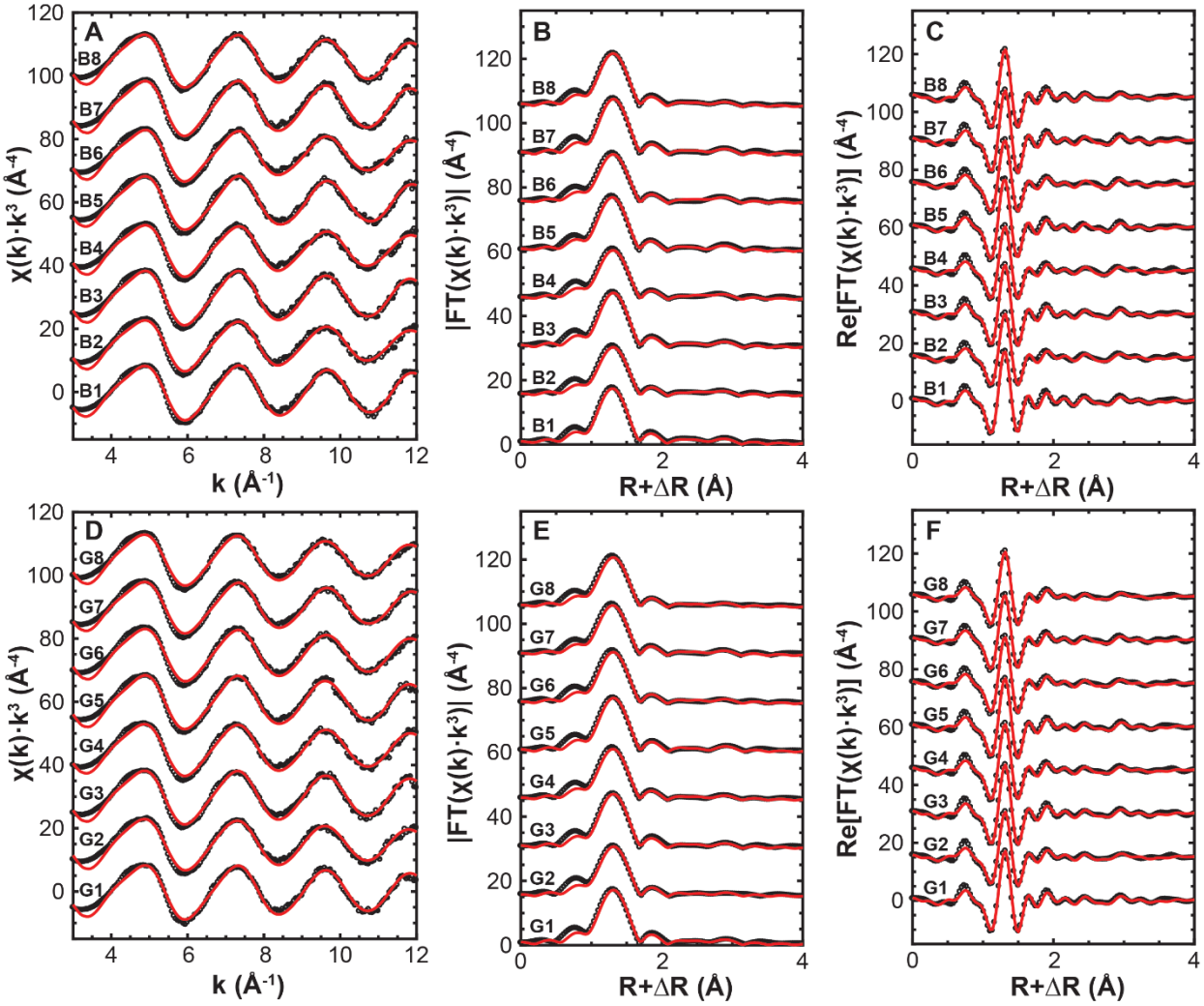

Figure 3.3. Data (dotted) and structural fits (solids) to the As K-edge spectra (A, D), Fourier transform magnitudes (B, E), and real components of the Fourier transforms (C, F) of the series of adsorption samples. Detailed sample information is provided in Table 3.1.

Table 3.3. As K-edge EXAFS fitting parameters

Sample	Path	CN[a]	R (Å)[b]	σ^2 (Å^2)[c]	ΔE_0 (eV)[d]	R-Factor[e]	χ_v^2 [e]
G1	As-O	4	1.696(4)	0.0019(2)	7(1)	0.008	37.70
	As-Al	0.9(5)[f]	3.19(3)	0.006			
G2	As-O	4	1.701(4)	0.0027(2)	8(1)	0.008	26.50
	As-Al	0.6(4)	3.21(5)	0.006			
G3	As-O	4	1.697(4)	0.0020(2)	7(1)	0.008	41.28
	As-Al	0.9(5)	3.19(3)	0.006			
G4	As-O	4	1.694(4)	0.0024(2)	6(1)	0.011	49.88
	As-Al	0.8(5)	3.19(4)	0.006			
G5	As-O	4	1.697(3)	0.0021(3)	8(1)	0.007	20.25
	As-Al	1.1(4)	3.22(3)	0.006			
G6	As-O	4	1.696(5)	0.0024(5)	7(1)	0.013	58.38
	As-Al	0.8(6)	3.19(5)	0.006			
G7	As-O	4	1.690(5)	0.0026(2)	6(1)	0.012	62.78
	As-Al	1.0(5)	3.18(4)	0.006			
G8	As-O	4	1.698(5)	0.0027(2)	7(1)	0.012	32.16
	As-Al	0.7(5)	3.21(5)	0.006			
B1	As-O	4	1.686(4)	0.0018(2)	5(1)	0.009	42.92
	As-Al	1.2(5)	3.18(3)	0.006			
B2	As-O	4	1.697(5)	0.0028(5)	7(1)	0.013	27.54
	As-Al	1.1(5)	3.17(3)	0.006			
B3	As-O	4	1.696(4)	0.0019(2)	7(1)	0.007	34.56
	As-Al	1.2(4)	3.20(3)	0.006			
B4	As-O	4	1.696(5)	0.0027(3)	7(1)	0.013	73.71
	As-Al	1.2(5)	3.17(3)	0.006			
B5	As-O	4	1.686(5)	0.0020(2)	5(1)	0.011	56.60
	As-Al	1.2(6)	3.19(3)	0.006			
B6	As-O	4	1.695(5)	0.0028(2)	7(1)	0.012	75.51
	As-Al	1.4(5)	3.18(3)	0.006			
B7	As-O	4	1.697(4)	0.0018(2)	7(1)	0.007	37.21
	As-Al	1.2(5)	3.19(3)	0.006			
B8	As-O	4	1.694(3)	0.0021(2)	6(1)	0.006	20.21
	As-Al	1.1(4)	3.18(3)	0.006			

[a] Coordination number. [b] Interatomic distance. [c] Debye-Waller factor. [d] Difference in the threshold Fermi level between the data and theory. [e] Goodness-of-fit parameters (Kelly et al., 2008). [f] The estimated standard deviations are listed in parentheses, representing the errors in the last digit.

3.5 DISCUSSION

3.5.1 Implications for Arsenate Adsorption Mechanisms

Our macroscopic and spectroscopic measurements on aluminum hydroxide powders, together with the previous surface scattering study of arsenate adsorbed on aluminum and iron oxide single crystal surfaces (Catalano et al., 2008), now provide a generally self-consistent description of arsenate adsorption, indicating that inner- and outer-sphere arsenate species co-adsorb over a wide range of surface coverages and pH. Arsenate adsorption does show the classical dependence on ionic strength, with a substantial effect when the surface potential is large and a negligible effect when the surface potential is near zero. All of these observations are the expected macroscopic behaviors when outer-sphere arsenate surface complexes are present.

However, these results also reveal unexpected observations. The decrease in arsenate adsorption with increasing ionic strength in the isotherms is expected to reduce the fraction of adsorbed arsenate that occurs as an outer-sphere complex, but no clear trend in the coordination number of second shell Al neighbors with increasing ionic strength was observed in EXAFS spectroscopy. This may be because the uncertainty in EXAFS-derived coordination numbers (typically ± 0.5) is too large to observe the expected trends with the number of analyses available. Alternatively, other aspects of the adsorption process may be affected by ionic strength in ways that do not substantially change the balance of inner- and outer-sphere species. For example, a prior study using the extended triple-layer model suggested a possible reaction stoichiometry involving both inner- and outer-sphere arsenate species in a ratio independent of pH and surface coverage and only sensitive to the activity of water (Fukushi and Sverjensky, 2007). Alternatively, if applying a charge distribution model then inner-sphere complexes have two O ligands extending to the β-plane, producing an ionic strength-dependence on macroscopic

uptake (Hiemstra and Van Riemsdijk, 1999). While this would be weaker in magnitude than for outer-sphere species, the reduction in surface coverage combined with the EXAFS fitting uncertainties may be adequate to explain the apparent lack of change in the distribution of arsenate surface species. More broadly, the ratio of inner- to outer-sphere arsenate species appears to be stable across a wide range of surface coverages (Catalano et al., 2008; Xu and Catalano, 2016), pH values (Xu and Catalano, 2016), and salt contents. Reaction stoichiometries that reproduce this phenomenon need to be investigated in future refinements of surface complexation models.

A separate feature of note in the results is an apparent correlation of the dual Langmuir model fitting parameters (i.e., K and Γ_{max} values) and ionic strength (Table 3.2). $\Gamma_{max,1}$ values decrease with increasing ionic strength for both minerals at both pH conditions, with a weaker variation at pH 7 (Figure A3.2A). K_1 values show distinct behaviors at the two pH values studied, increasing with increasing ionic strength at pH 4 but decrease at pH 7 (Figure A3.2C). In contrast, $\Gamma_{max,2}$ and K_2 values display little variation as ionic strength changes for all conditions (Figure A3.2B, D). If the distinct strong and weak correlations of K_1 and K_2 with ionic strength originated from K_1 attributed to inner-sphere adsorption and K_2 attributed to outer-sphere adsorption, a change in the population of inner- and outer-sphere species with increasing ionic strength and arsenate surface coverage should occur. However, as noted above this is not observed in our EXAFS results. The origin of the effects of ionic strength on the dual Langmuir isotherm components is thus uncertain. Many factors can induce variations in K values, including changes in activity coefficients for the dissolved species, surface site competition with electrolyte ions, Na-AsO_4 complexation in solution, and changes in surface potential as ionic strength and arsenate surface coverage increases. Thus, the observed trends in K with ionic

strength are most likely attributed to multiple origins instead of a single origin. The smaller difference in $\Gamma_{max,1}$ seen at pH 7 compared to pH 4 may be dominantly controlled by the difference in surface potential (large surface potential at pH 4 and small to zero one at pH 7) but also may be affected by changes in solution speciation and Na^+ and NO_3^- interactions with mineral surfaces. However, the spectroscopic results clearly rule out the strongly (Langmuir isotherm 1) and weakly (Langmuir isotherm 2) bound arsenate species corresponding to inner- and outer-sphere complexes. The coexistence of such species is surprisingly unrelated to the apparent adsorption isotherm behavior. Surface complexation models are needed to identify the aspects of the observed variations in uptake behaviors with increasing ionic strength that are induced by activity corrections, solution complexation, surface site competition, and surface potential changes.

3.5.2 Implications for Arsenate in the Environment

The strong adsorption of arsenate to many aluminum and iron (hydro)oxide minerals widely observed in past studies (Arai et al., 2001; Fendorf et al., 1997; Goldberg and Johnston, 2001; Manceau, 1995; Waychunas et al., 1993) has traditionally been attributed to solely inner-sphere surface complexes. However, the co-adsorption of inner- and outer-sphere arsenate species indicates that the latter species are partially responsible for this strong adsorption behavior. While such species appear to have high affinity for the mineral surface, they are expected to be more kinetically labile because of their adsorption-desorption does not involve ligand exchange. This suggests that they may desorb more rapidly from mineral surfaces than inner-sphere species, although experimental confirmation is needed as desorption of outer-sphere species was recently shown to be the rate-limiting step in overall Rb^+ desorption on muscovite

(Lee et al., 2017). Past macroscopic kinetic studies for arsenate have often observed two-stage (i.e., fast and slow) desorption from powder substrates (Arai and Spark, 2002; O'Reilly et al., 2001; Pigna et al., 2006; Quaghebeur et al., 2005) and the fast component may be attributable to the outer-sphere species suggested in the current work. Arsenate adsorption behavior is thus more complex than previously recognized, with inner- and outer-sphere surface complexes displaying similar adsorption affinities and co-occurring over a wide range of conditions.

The present work highlights a clear relationship between ionic strength and arsenate adsorption behavior on aluminum hydroxides that may affect arsenate mobility in natural systems under various geochemical conditions. A diverse set of environments can generate an increase in ionic strength: suspended particles in rivers entering the ocean, saltwater intrusion into an aquifer, brines released during hydrocarbon exploration or geologic CO_2 sequestration, and soils and streams exposed to road salt. Arsenate desorption from particles may thus occur in all cases, although the present work suggests it would be most substantial under weakly acidic conditions, such as in soils, and may be negligible in neutral to alkaline groundwater and seawater. The present work thus identifies an unrecognized process to potentially mobilize arsenic in environmental and geological systems.

3.6 ACKNOWLEDGEMENTS

This research was supported by the U.S. National Science Foundation (NSF) Environmental Chemical Sciences program through award No. CHE-1505532. ζ-potential analyses were conducted at the Nano Research Facility at Washington University in St. Louis, supported by the NSF through award No. ECS-00335765. EXAFS spectra were collected at beamline 4-1 at the SSRL, operated by SLAC National Accelerator Laboratory with support

from the U.S. Department of Energy (DOE) Office of Science through Contract No. DE-AC02-76SF00515. The authors would like to thank Ryan Davis for beamline support.

3.7 APPENDIX

Table A3.1. Fitting parameters for single Langmuir isotherms

Mineral	Ionic Strength (mol/L)	Γ_{max} (µmol/m^2)	K (L/µmol)	R-factor[a]
Bayerite pH 4	0.5	1.24 ± 0.08	0.09 ± 0.04	0.12
Bayerite pH 4	0.1	1.39 ± 0.07	0.20 ± 0.08	0.11
Bayerite pH 4	0.01	1.65 ± 0.05	0.98 ± 0.26	0.074
Bayerite pH 4	0.001	1.71 ± 0.04	1.34 ± 0.29	0.067
Bayerite pH 7	0.5	1.03 ± 0.04	0.62 ± 0.26	0.094
Bayerite pH 7	0.1	1.09 ± 0.04	0.85 ± 0.38	0.096
Bayerite pH 7	0.01	1.18 ± 0.03	1.71 ± 0.55	0.077
Bayerite pH 7	0.001	1.26 ± 0.04	2.02 ± 0.66	0.079
Gibbsite pH 4	0.5	1.09 ± 0.04	0.032 ± 0.005	0.043
Gibbsite pH 4	0.1	1.19 ± 0.02	0.07 ± 0.04	0.065
Gibbsite pH 4	0.01	1.26 ± 0.04	0.35 ± 0.10	0.086
Gibbsite pH 4	0.001	1.31 ± 0.03	0.77 ± 0.13	0.054
Gibbsite pH 7	0.5	0.66 ± 0.03	0.092 ± 0.03	0.091
Gibbsite pH 7	0.1	0.69 ± 0.03	0.22 ± 0.09	0.099
Gibbsite pH 7	0.01	0.71 ± 0.03	0.72 ± 0.09	0.097
Gibbsite pH 7	0.001	0.72 ± 0.02	1.51 ± 0.02	0.095

[a] Goodness-of-fit parameter. The R-factor is the sum of the differences between the data and the fit at each data point, divided by the sum of the data at each corresponding point. Smaller R-factor values reflect better fits.

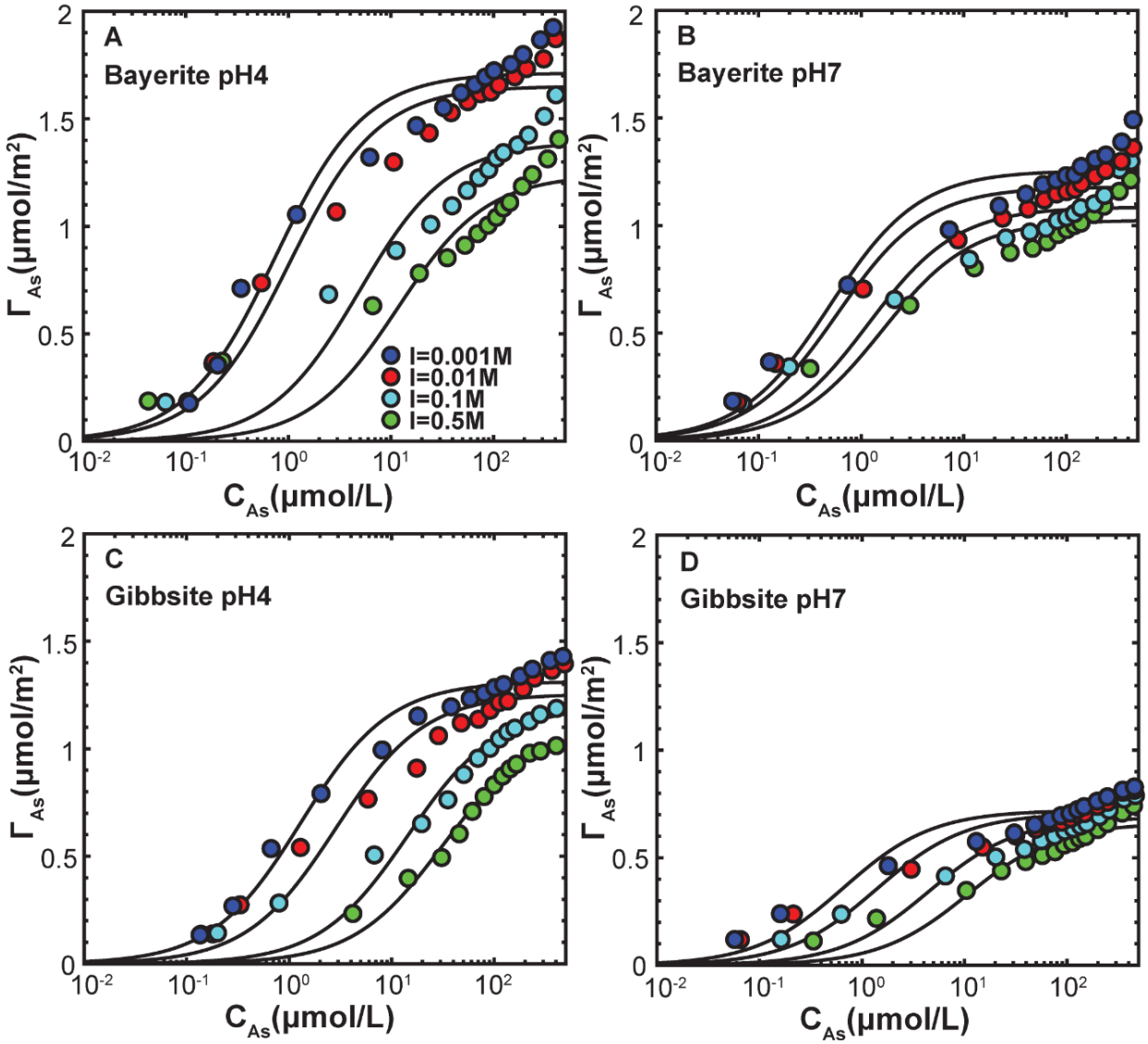

Figure A3.1. Single Langmuir isotherm fits (black lines) to arsenate adsorption in different ionic strength on bayerite (A) pH 4 and (B) pH 7, on gibbsite at (C) pH 4 and (D) pH 7. Detailed fitting parameters are summed in Table A3.1.

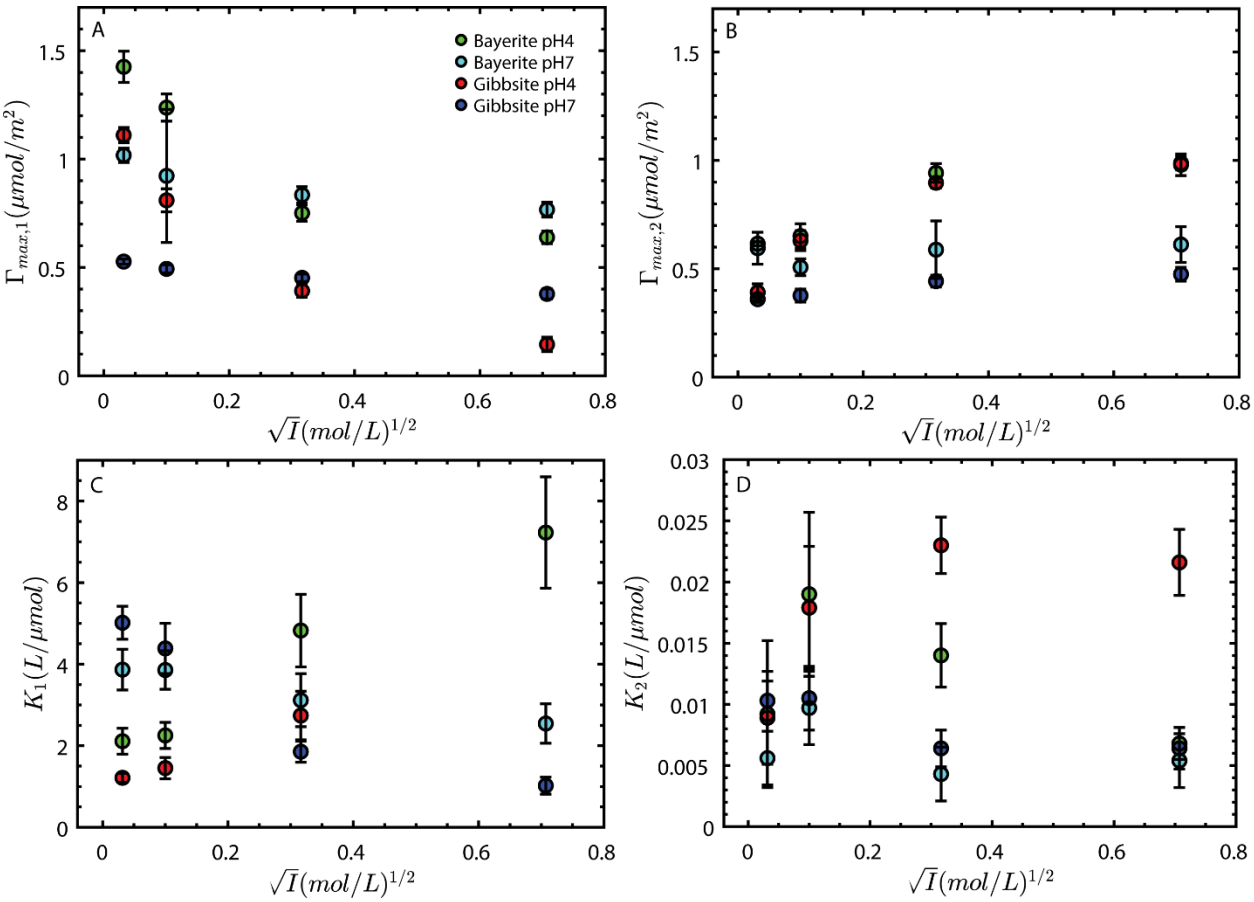

Figure A3.2. Correlations of Dual Langmuir fitting parameters (A) $\Gamma_{max,1}$, (B) $\Gamma_{max,2}$, (C) K_1 and (D) K_2 versus square root of ionic strength.

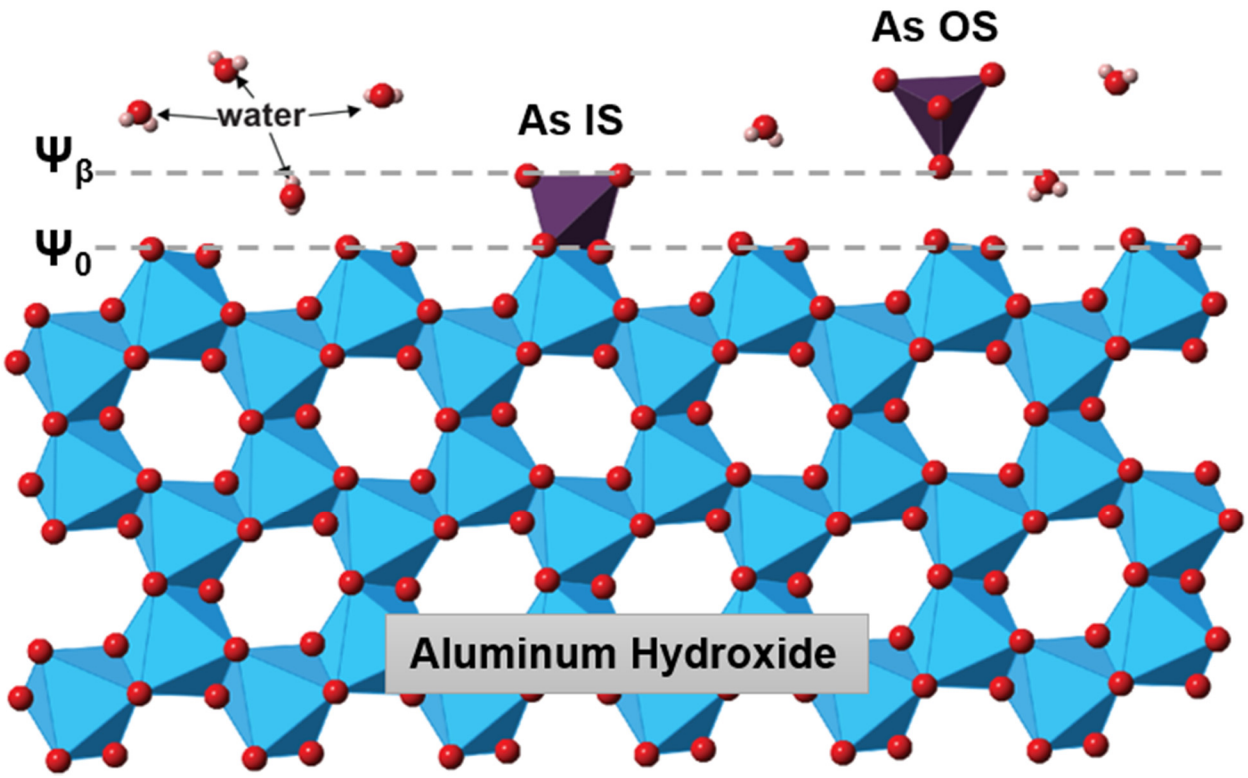

Figure A3.3. Schematic of arsenate adsorption mechanism at aluminum hydroxide-water interfaces, with the coexisting of inner-sphere and outer-sphere arsenate surface complexes. Inner-sphere arsenate species directly bind to aluminum hydroxide surfaces and are related to the surface potential at 0-plane (ψ_0). Outer-sphere arsenate species form farther away from the surface and are related to the surface potential at β-plane (ψ_β).

3.8 REFERENCES

Adekola, F., Fedoroff, M., Geckeis, H., Kupcik, T., Lefevre, G., Lutzenkirchen, J., Plaschke, M., Preocanin, T., Rabung, T. and Schild, D. (2011) Characterization of acid-base properties of two gibbsite samples in the context of literature results. *J. Colloid Interface Sci.* **354**, 306-317.

Ankudinov, A.L. and Rehr, J.J. (1997) Relativistic calculations of independent X-ray absorption spectra. *Phys. Rev. B* **56**, 1712-1715.

Antelo, J., Avena, M., Fiol, S., Lopez, R. and Arce, F. (2005) Effects of pH and ionic strength on the adsorption of phosphate and arsenate at the goethite-water interface. *J. Colloid Interface Sci.* **285**, 476-486.

Arai, Y., Elzinga, E.J. and Sparks, D.L. (2001) X-ray absorption spectroscopic investigation of arsenite and arsenate adsorption at the aluminum oxide-water interface. *J. Colloid Interface Sci.* **235**, 80-88.

Arai, Y., Lanzirotti, A., Sutton, S., Davis, J.A. and Sparks, D.L. (2003) Arsenic speciation and reactivity in poultry litter. *Environ. Sci. Technol.* **37**, 4083-4090.

Arai, Y. and Spark, D.L. (2002) Residence time effects on arsenate surface speciation at the aluminum oxide-water interface. *Soil Sci.* **167**, 303-314.

Catalano, J.G., Park, C., Fenter, P. and Zhang, Z. (2008) Simultaneous inner- and outer-sphere arsenate complexation on corundum and hematite. *Geochim. Cosmochim. Acta* **72**, 1986-2004.

Chwirka, J.D., Thomson, B.M. and Stomp, J.M. (2000) Removing arsenic from groundwater. *J. Am. Water Works Assoc.* **92**, 79-88.

Dixit, S. and Hering, J.G. (2003) Comparison of arsenic(V) and arsenic(III) sorption onto iron oxide minerals: implications for arsenic mobility. *Environ. Sci. Technol.* **37**, 4182-2189.

Fendorf, S., Eick, M.J., Grossl, P. and Sparks, D.L. (1997) Arsenate and chromate retention mechanisms on goethite. 1. Surface structure. *Environ. Sci. Technol.* **31**, 315-320.

Foster, A.L., Brown, G.E., Tingle, T.N. and Parks, G.A. (1998) Quantitative arsenic speciation in mine tailings using X-ray absorption spectroscopy. *Am. Mineral.* **83**, 553-568.

Fukushi, K. and Sverjensky, D.A. (2007) A predictive model (ETLM) for arsenate adsorption and surface speciation on oxides consistent with spectroscopic and theoretical molecular evidence. *Geochim. Cosmochim. Acta* **71**, 3717-3745.

Gan, Y. and Franks, G.V. (2006) Charging behavior of the gibbsite (001) surface in NaCl solution investigated by AFM colloidal probe technique. *Langmuir* **22**, 6087-6092.

Garelick, H., Dybowska, A., Valsami-Jones, E. and Priest, N.D. (2005) Remediation technologies for arsenic contaminated drinking waters. *J. Soils Sediments* **5**, 182-190.

Goldberg, S. (1986) Chemical modeling of arsenate adsorption on aluminum and iron oxide minerals. *Soil Sci. Soc. Am. J.* **50**, 1154-1157.

Goldberg, S. and Johnston, C.T. (2001) Mechanisms of arsenic adsorption on amorphous oxides evaluated using macroscopic measurements, vibrational spectroscopy, and surface complexation modeling. *J. Colloid Interface Sci.* **234**, 204-216.

Harrison, W.T.A. (2000) Synthetic mansfieldite, $AlAsO_4 \cdot 2H_2O$. *Acta Cryst.* **56**, 421.

Hayes, K.F., Papelis, C. and Leckie, J.O. (1988) Modeling ionic strength effects of anion adsorption at hydrous oxide/solution interface. *J. Colloid Interface Sci.* **125**, 717-726.

Hiemstra, T. and Van Riemsdijk, W.H. (1999) Surface structural ion adsorption modeling of competitive binding of oxyanions by metal (hydr)oxides. *J. Colloid Interface Sci.* **210**, 182-193.

Hiemstra, T., Yong, H. and Van Riemsdijk, W.H. (1999) Interfacial charging phenomena of aluminum (hydr)oxides. *Langmuir* **15**, 5942-5955.

Jain, C.K. and Ali, I. (2000) Arsenic: occurrence, toxicity and speciation techniques. *Water Res.* **34**, 4304-4312.

Kappen, P. and Webb, J. (2013) An EXAFS study of arsenic bonding on amorphous aluminum hydroxide. *Appl. Geochem.* **31**, 79-83.

Ladeira, A.C.Q., Ciminelli, V.S.T., Duarte, H.A., Alives, M.C.M. and Ramos, A.Y. (2001) Mechanism of anion retention from EXAFS and density functional calculations: Arsenic(V) adsorbed on gibbsite. *Geochim. Cosmochim. Acta* **65**, 1211-1217.

Lee, S.S., Fenter, P., Nagy, K.L. and Sturchio, N.C. (2017) Real-time observation of cation exchange kinetics and dynamics at the muscovite-water interface. *Nat. Commun.* **8**, 15826.

Lefevre, G. and Fedoroff, M. (2002) Synthesis of bayerite [β-$Al(OH)_3$] microrods by neutralization of alyminate ions at constant pH. *Materials Letters* **56**, 978-983.

Lumsdon, D.G., Fraser, A.R., Russell, J.D. and Livesey, N.T. (1984) New infrared band assignments for the arsenate ion adsorbed on synthetic goethite (α-FeOOH). *J. Soil Sci.* **35**, 381-386.

Manceau, A. (1995) The mechanism of anion adsorption on iron oxides: evidence for the bonding of arsenate tetrahedra on free $Fe(O,OH)_6$ edges. *Geochim. Cosmochim. Acta* **59**, 3647-3653.

Mandal, B.K. and Suzuki, K.T. (2003) Arsenic round the world: a review. *Talanta* **58**, 201-235.

Manning, B.A. and Goldberg, S. (1996) Modeling Competitive Adsorption of Arsenate with Phosphate and Molybdate on Oxide Minerals. *Soil Sci. Soc. Am. J.* **60**, 121.

Mikutta, C., Frommer, J., Voegelin, A., Kaegi, R. and Kretzschmar, R. (2010) Effect of citrate on the local Fe coordination in ferrihydrite, arsenate binding, and ternary arsenate complex formation. *Geochim. Cosmochim. Acta* **74**, 5574-5592.

Myneni, S.C.B., Traina, S.J., Waychunas, G.A. and Logan, T.J. (1998) Experimental and theoretical vibrational spectroscopic evaluation of arsenate coordination in aqueous solutions, solids, and at mineral-water interfaces. *Geochim. Cosmochim. Acta* **62**, 3285-3300.

Newville, M. (2001) IFEFFIT: Interactive EXAFS analysis and FEFF fitting. *J. Synchrotron Rad.* **8**, 322-324.

O'Reilly, S.E., Strawn, D.G. and Sparks, D.L. (2001) Residence time effects on arsenate adsorption/desorption mechanisms on goethite. *Soil Sci. Soc. Am. J.* **65**, 67-77.

Pigna, M., Krishnamurti, G.S.R. and Violante, A. (2006) Kinetics of arsenate sorption-desorption from metal oxides: effect of residence time. *Soil Sci. Soc. Am. J.* **70**, 2017-2027.

Quaghebeur, M., Rate, A., Rengel, Z. and Hinz, C. (2005) Desorption kinetics of arsenate from kaolinite as influenced by pH. *J. Environ. Qual.* **34**, 479-486.

Ravel, B. and Newville, M. (2005) ATHENA, ARTEMIS, HEPHAESTUS: Data analysis for X-ray absorption spectroscopy using IFEFFIT. *J. Synchrotron Rad.* **12**, 537-541.

Rosenqvist, J., Persson, P. and Sjoberg, S. (2002) Protonation and charging of nanosized gibbsite [α-$Al(OH)_3$] particles in aqueous suspension. *Langmuir* **18**, 4598-4604.

Shen, S., Chow, P.S., Chen, F., Feng, S. and Tan, R.B.H. (2006) Synthesis of submicron gibbsite platelets by organic-free hydrothermal crystallization process. *J. Cryst. Growth* **292**, 136-142.

Smedley, P.L. and Kinniburgh, D.G. (2002) A review of the source, behavior and distribution of arsenic in natural waters. *Appl. Geochem.* **17**, 517-568.

Sun, X. and Doner, H.E. (1996) An investigation of arsenate and arsenite bonding structures on goethite by FTIR. *Soil Sci.* **161**, 865-872.

Waychunas, G.A., Rea, B.A., Fuller, C.C. and Davis, J.A. (1993) Surface chemistry of ferrihydrite: Part 1. EXAFS studies of the geometry of coprecipitated and adsorbed arsenate. *Geochim. Cosmochim. Acta* **57**, 2251-2269.

Webb, S.M. (2005) SixPack: A graphical user interface for XAS analysis using IFEFFIT. *Phys. Scr.* **115**, 1011-1014.

Xu, T. and Catalano, J.G. (2016) Impacts of surface site coordination on arsenate adsorption: Macroscopic uptake and binding mechanisms on aluminum hydroxide surfaces. *Langmuir* **32**, 13261-13269.

CHAPTER 4

RESPONSE OF INTERFACIAL WATER TO ARSENATE ADSORPTION ON CORUNDUM (001) SURFACES: EFFECTS OF PH AND ADSORBATE SURFACE COVERAGE

Submitted to *Geochimica et Cosmochimica Acta* as:
Xu, T., Stubbs, J.E., Eng, P.J., and Catalano, J.G. (2018) Response of interfacial water to arsenate adsorption on corundum (001) surfaces: Effect of pH and adsorbate surface coverage.

4.1 ABSTRACT

The interaction of water with metal oxide mineral surfaces affects chemical reactions that are important to many natural processes. Previous studies demonstrate that the various functional groups on mineral surfaces control ion adsorption as well as the ordering of interfacial water, but the effect of water structure on the reactivity and dynamics of interfacial reactions has not been systematically investigated. In this study, surface X-ray scattering measurements on corundum (001) surfaces with and without arsenate over a range of pH conditions have been used to determine the response of interfacial water structure to arsenate adsorption. In the absence of arsenate, the structure of interfacial water near this surface varies little over the pH range of 5 to 9, suggesting that surface charging from protonation-deprotonation under the conditions studied is inadequate to induce extensive restructuring. In contrast, interfacial water undergoes substantial restructuring upon arsenate adsorption, indicating that charged surface complexes substantially perturb the arrangement and order of interfacial water on this surface. The overall interfacial water structure also varies proportionally with arsenate surface coverage, with adsorbed water layers moving closer to the surface and the extended layering of interfacial water showing reduced positional disorder as arsenate surface coverage increases. Systematic variations in interfacial water properties with increasing arsenate concentration at each pH value are consistent with the coexistence of two distinct water structures (in the absence and presence of adsorbed arsenate) that vary in proportion with adsorbate surface coverage. These observations demonstrate that the adsorption of arsenate alters the structure of interfacial water near corundum (001) surfaces, possibly through the modification of the charge state of surface sites or by providing new sites to which water may hydrogen bond. Such adsorbate-induced

restructuring of interfacial water may contribute to the energetics of chemical reactions at mineral-water interfaces.

4.2 INTRODUCTION

The interaction of water with metal oxide mineral surfaces affects chemical reactions that are crucial to a broad range of natural processes (Al-Abadleh and Grassian, 2003; Björneholm et al., 2016; Brown et al., 1999; Rubasinghegea and Grassian, 2013). Essential to many of these processes are adsorption reactions because they are major controlling factors in the fate and transport of contaminants and nutrients in soils and aquatic systems (Brown and Parks, 2001; Chorover and Brusseau, 2008), an important initial step for mineral growth and dissolution (Benning and Waychunas, 2008) and surface electron transfer reactions (Yanina and Rosso, 2008) and also a significant contributor to the global carbon cycle and CO_2 sequestration (Hamm et al., 2013; Kaszuba et al., 2013). These reactions occur at the mineral-fluid interface, a chemical and structural transition zone in which surface functional groups in multiple coordination environments interact with both adsorbates and water molecules. An improved understanding of the fundamental controls on adsorption reactions at mineral-water interfaces is needed to better predict important processes occurring in geological and environmental systems.

Among various substrates, surfaces of corundum (α-Al_2O_3) have received particular attention as proxies for many naturally occurring Al-bearing minerals, such as aluminum hydroxides and aluminosilicate clays, because of similarities in the types of functional groups exposed on their surfaces (Al-Abadleh and Grassian, 2003; Brown et al., 1999). It is difficult to investigate the molecular-scale properties of the interfacial regions of common particulate or polycrystalline materials such as gibbsite and boehmite using currently available analytical methods. Corundum single crystals are thus ideal model systems for the fundamental study of mineral-water interfacial reactions (Catalano, 2010; Catalano et al., 2006; Eng et al., 2000; Lützenkirchen, 2013; Lützenkirchen et al., 2010; Trainor et al., 2002).

The general adsorption mechanisms and surface charging behavior of corundum-water interfaces have been extensively investigated, but the role of interfacial water in affecting the structure and reactivity of interfacial regions has not yet been systematically understood at the fundamental molecular level. Previous experimental and theoretical studies have explored the structure and ordering of water near a series of surfaces of corundum and its isostructural iron oxide hematite with variable terminations (Argyris et al., 2011; Catalano, 2010; Catalano, 2011; Catalano et al., 2007, 2009; Catalano et al., 2006; Flörsheimer et al., 2008; Gaigeot et al., 2012; Hass et al., 1998; Huang et al., 2014; Kerisit, 2011; Ma et al., 2016; Sung et al., 2012; Sung et al., 2011; Tuladhar et al., 2016; Tuladhar et al., 2017; Zhang et al., 2008). These studies have found that the structure of interfacial water layers is primarily controlled by mineral surface structures. (001) surfaces of these minerals are terminated by doubly coordinated functional groups that are charge neutral over a wide pH range (Boily et al., 2011; Chatman et al., 2013; Hiemstra et al., 1996; Hiemstra et al., 1999; Lützenkirchen, 2013; Lützenkirchen et al., 2015; Lützenkirchen et al., 2010) and have weak positional ordering of interfacial water (Catalano, 2011; Tuladhar et al., 2017). In contrast, (012) and (110) surfaces terminated by singly and triply coordinated functional groups are always charged even when the net surface charge is neutral (Chatman et al., 2013; Hiemstra et al., 1996; Hiemstra et al., 1999; Lützenkirchen, 2013; Rustad et al., 1999) and have strong ordering of interfacial water (Catalano, 2010; Catalano et al., 2007, 2009; Catalano et al., 2006; McBriarty et al., 2017; Tuladhar et al., 2016). The observed weak and strong ordering of interfacial water above distinct crystallographic planes thus appear to be correlated with the charge states of various surface functional groups on those minerals.

In addition to mineral surface structure, the charge state of surface sites also depends on pH and the adsorption of ions. Surface charge of metal oxide minerals varies with pH because of

the protonation and deprotonation of functional groups in multiple coordination states (Hiemstra et al., 1999). Surface site charge originating from functional group protonation or deprotonation may thus affect interfacial water structure. Several previous studies have investigated the response of interfacial water on corundum surfaces as a function of pH using sum-frequency vibrational spectroscopy (SFVS) (Sung et al., 2012; Sung et al., 2011; Zhang et al., 2008). SFVS spectra show that O-H bonds at the mineral-water interface reorient on corundum (001), (012), and (110) surfaces as pH and surface charge changes. However, SFVS experiments are highly surface sensitive and different sample pretreatments can cause substantial changes in SFVS spectra (Braunschweig et al., 2008), which has led to disagreements in the interpretation of the results (Lützenkirchen et al., 2010). In addition, it is difficult to determine if the structural changes responsible for the pH-dependent response of the resulting O-H vibrational bands observed in SFVS spectra originated from surface OH groups or interfacial water (Lützenkirchen et al., 2010; Tong et al., 2015). If the latter dominate SFVS spectra, this suggests that interfacial water molecules reorient at the interface as pH changes. However, SFVS cannot characterize the full rearrangement of interfacial water structure nor the spatial distributions of ions and molecules at the interfaces, as it is primarily sensitive to the orientation of bonds along the surface normal direction (Björneholm et al., 2016). Therefore, the effect of pH on the overall interfacial water structure currently remains unclear and complementary structural studies are needed.

Surface site charge will also be changed by ion adsorption, with a more negative or less positive charge after anion adsorption and a more positive or less negative surface charge after cation adsorption (Hiemstra and Van Riemsdijk, 1996, 1999). The local charge on adsorbates bound to surface groups will differ from that of uncomplexed surface sites, and adsorbates must

displace interfacial water molecules at the surface. Such interactions may perturb the arrangement of water molecules near the mineral surface. If this hypothesized adsorbate-induced restructuring of interfacial water occurs, then it may substantially affect the thermodynamics of interfacial reactions.

In this study, the effects of pH and ion adsorption on the interfacial water structure at corundum (001) surfaces were investigated using surface X-ray scattering methods. (001) surfaces are used because they have weak interfacial water ordering in pure water (Catalano, 2011). If water restructuring occurs following changes in pH or ion adsorption, then the response of interfacial water structure may be more extensive on such surfaces. Arsenate is used as the probe adsorbate due to its environmental importance (Jain and Ali, 2000; Smedley and Kinniburgh, 2002) and its well-established adsorption mechanisms on metal oxide surfaces (Arai et al., 2001; Catalano et al., 2008; Foster et al., 1998; Kappen and Webb, 2013; Ladeira et al., 2001), including substantial uptake over a wide pH range (unlike many cations). In aqueous systems, arsenate occurs as oxoanions $H_nAsO_4^{3-n}$ with pK_a values of 2.30, 6.99, and 11.80 (Nordstrom and Archer, 2003). These thus predict that $H_2AsO_4^-$ and $HAsO_4^{2-}$ are the predominant arsenate species in most natural waters at typical environmental pH values of 4 to 9. Non-resonant X-ray reflectivity (XR) on corundum (001) surface at pH 5, 7, and 9 was used to probe the effect of pH on the arrangement of interfacial water molecules. A combination of XR and resonant anomalous X-ray reflectivity (RAXR) were then used to determine interfacial water structure as a function of arsenate surface coverage at each pH. For the latter studies, RAXR was used to determine the interfacial distribution of adsorbed arsenate, which allowed the interfacial water structure to be isolated from the corresponding XR data.

4.3 MATERIALS AND METHODS

4.3.1 Sample Preparation

Approximately 1 cm^2 synthetic corundum crystals, cut and polished parallel to the (001) surface plane, were obtained from MTI Corporation (Richmond, CA, USA). The crystals were cleaned prior to use following the procedure described in previous work (Catalano, 2010; Catalano, 2011; Catalano et al., 2006). Briefly, the crystal surfaces were first cleaned by four cycles of HPLC-grade acetone, HPLC-grade methanol, and fresh deionized water (>18MΩ·cm) rinses, followed by soaking in 2% HF overnight for removal of possible silicon contamination, and finally rinsing with deionized water. This was followed by soaking in 0.1 M HCl (Trace metal grade) for 4 h, rinsing repeatedly with deionized water, soaking in deionized water for 2 h in Teflon jars, and then drying with compressed N_2 gas. These crystals were put into a boat crucible (99.8% Al_2O_3) and then transferred to a tube furnace with a 99.8% Al_2O_3 tube for annealing at 1000°C with a constant ramping rate of 4°C/min in air. After reaching the target temperature, a dwelling duration of 24 h was applied to guarantee a sufficient time. After cooling to room temperature, the crystals were soaked in 0.1 M HCl (Trace metal grade) again for 1 h, rinsed repeatedly with deionized water, and then dried with a jet of compressed N_2 gas. In the last step, the crystals were annealed at 450 °C using a tube furnace for 12 h and then stored dry in a sectioned plastic box lined with lint-free cloths for transport to the Advanced Photon Source (APS) for measurements. At the APS, the crystals were re-cleaned by Ultraviolet-Ozone surface treatment (BioForce UV/Ozone ProCleaner) for 0.5 h to remove possible organic surface contaminants taken up from air during sample transport. The crystals were then stored in deionized water in Teflon jars for less than 12 h before measurements. The surface composition was measured after cleaning via X-ray photoelectron spectroscopy (XPS) using a Physical

Electronics 5000 VersaProbe II Scanning ESCA Microprobe with Al Kα X-ray monochromatic X-ray source (1486.6 Ev) and a 200 μm beam size. The resulting spectrum reveals only Al, O, and adventitious C on the surface, with no evidence of F retention from the cleaning process (Figure A4.1). Atomic Force Microscopy imaging was conducted with the sample immersed in deionized water using an Agilent Technologies model 5500 AFM in contact mode using a silicon nitride probe (Veeco Instrument NP-S10, 0.58 N/m spring constant). The surface displays parallel terraces of 170±20 nm width with measured step heights of 2.0±0.4 Å (Figure A4.2), consistent with the 2.16 Å height of Al_2O_3 layers normal to the *c*-axis in the crystal structure.

4.3.2 X-ray Scattering Measurements and Analysis

Data Collection

Solutions of 0.01 M NaCl at pH 5, 7, and 9 as well as solutions of 10, 30, 60, and 100 μM $Na_2HAsO_4 \cdot 7H_2O$ in 0.01 M NaCl were prepared from reagent grade chemicals and deionized water. The pH was adjusted using 0.1 M HCl or 0.1 M NaOH. Three corundum crystals were used for data collection, with one crystal used for all measurements at each pH condition. Each corundum crystal was initially loaded into a thin-film geometry sample cell (Fenter, 2002) in deionized water and sealed with Kapton film. A 0.01 M NaCl solution at the specific pH was then flushed into the cell. The sample was reacted with the fluid for about 1 h, during which the fluid was exchanged repeatedly to stabilize the system. After the reaction time, excess fluid was drained from the sample cell by gravity while a thin (~2-5 μm) solution film was left between the crystal surface and the Kapton film. When the solution film above the crystal surface achieved a uniform thickness based on visual inspection (the thin water film produces iridescent interference fringes), the sample cell was sealed and then mounted on a diffractometer for data collection.

After measurements, the sample cell was removed from the diffractometer and an arsenate solution of the same pH was injected to the sample cell. A repeated cycle of fluid injections and measurements was repeated, sequentially stepping through the arsenate solutions from the lowest to highest concentration.

High resolution X-ray reflectivity (XR), arsenic K-edge resonant anomalous X-ray reflectivity (RAXR), and X-ray absorption near-edge spectroscopy (XANES) measurements were performed at the GeoSoilEnviroCARS beamline 13-ID-C at the APS at Argonne National Laboratory. All sample cells were mounted on a Newport Kappa six (4+2) circle diffractometer and the scattered beam intensity was measured using a Dectris PILATUS 100K pixel array detector (Eikenberry et al., 2003). All data were collected with the crystal aligned such that the miscut direction was perpendicular to the scattering plane; typical miscuts were ~0.1°. The incident beam energy was selected using a cryogenically cooled Si (111) double-crystal monochromator and the beam was then collimated using a pair of 1 m long Rh-coated Si mirrors in Kirkpatrick-Baez geometry, with a final beam size of 0.1 mm × 1.0 mm (horizontal × vertical) defined by slits. All data were normalized to the incident beam flux as monitored by a N_2-filled ionization chamber.

Detailed methodologies of XR and RAXR have been described elsewhere previously (Fenter, 2002; Fenter et al., 2007; Park et al., 2005). XR was measured as a function of momentum transfer Q ($Q = 4\pi sin(\theta)/\lambda$, where θ is the scattering angle and λ is the X-ray wavelength) at a fixed incident X-ray energy of 16.0 keV in this study. This energy was chosen because it was well separated from arsenic K-edge energy (11.87 keV) resulting in a negligible anomalous scattering component of the arsenic scattering factor. The XR data were collected for Q values between 0.3 and 6.3 $Å^{-1}$ with an experimental resolution (π/Q_{max}, where Q_{max} is the

maximum Q value measured) of ~0.50 Å for all XR data (Fenter, 2002). RAXR data were obtained by measuring the X-ray reflectivity as a function of X-ray energy at a selected series of fixed Q values near the arsenic K-edge (± 400 eV). A XANES spectrum of a 0.25 M $Na_2HAsO_4 \cdot 7H_2O$ solution at pH 5 was collected in transmission mode to provide the anomalous scattering factors for the arsenic component in the RAXR analysis as described in the following section. However, the strong beam intensity caused bubble formation and a drift in the absorbance spectrum with time. While the near-edge region was adequate for edge determination, the region away from the edge could not be used to obtain anomalous scattering factors. Instead, scattering factors derived from a XANES spectrum (Cross et al., 1998) collected on a 0.5 M sodium arsenate solution at 33-ID-D were used, as the fine-structure and white-line height of these data were the same as that in the present measurement. RAXR spectra were measured over a range of Q values from 0.53 up to 3.00 $Å^{-1}$ for samples reacted with 10 and 100 μM arsenate solutions at pH 5 and for samples reacted with 100 μM arsenate solution at pH 7 and 9. RAXR spectra at $Q = 0.53$ $Å^{-1}$ were measured for all other samples. Additional spectra at $Q = 0.77$ and 1.16 $Å^{-1}$ were also measured for samples reacted with 10 μM arsenate solutions at pH 7 and with 30 and 60 μM arsenate solutions at pH 9. For both XR and RAXR experiments, the stability of the experimental system was verified by periodically measuring the reflectivity at reference Q values. Repeated measurements have a standard deviation of ~1.3%, and this uncertainty was added in quadrature to the measurement uncertainty (derived from counting statistics) to obtain the final error on each measurement.

XR and RAXR Analysis

All XR data were analyzed following previously-described procedures (Catalano, 2011; Catalano et al., 2006; Fenter, 2002). The XR data were fit using a parameterized structural model, consisting of three components: the bulk structure of the corundum, the interfacial structure including four relaxable Al_2O_3 layers at the corundum (001) mineral surface and surface-adsorbed species (i.e., adsorbed water and, when present in the system, arsenate), and ordered water structure above the surface (see below). In a given model, the reflectivity $R(Q)$ is calculated by:

$$R(Q) = \left(\frac{4\pi r_e}{QA_{UC}}\right)^2 \left|F_{UC}F_{CTR} + F_{interface} + F_{water}\right|^2$$

Where Q is the momentum transfer oriented along the surface normal direction for the specular reflectivity condition; $r_e = 2.818 \times 10^{-5}$ Å is the classical electron radius; A_{UC} is the unit cell area in the *ab* plane; F_{UC}, F_{CTR}, $F_{interface}$, *and* F_{water} are the structure factors of the bulk unit cell, crystal truncation rod, interfacial region, and ordered water, respectively. The structure factor of each component is defined as:

$$F = \sum_j c_j f_j(Q) \exp(iQz_j)\, exp\left[-\frac{1}{2}(Qu_j)^2\right]$$

where $f_j(Q)$, c_j, z_j, and u_j are the atomic scattering factor, occupancy, position from the surface, and vibrational amplitude of the j_{th} atom described as a Gaussian distribution, respectively. The bulk crystal structure and vibrational amplitudes were taken from previously published data (Kirfel and Eichhorn, 1990). Corundum has a (001) spacing of 12.9877 Å and a surface unit cell area ($A_{UC} = absin60°$) of 19.60 Å^2 (a = 4.757 Å, b = 4.757 Å) (Kirfel and Eichhorn, 1990). In addition, parameters representing extrinsic factors of water film thickness (Fenter, 2002), surface roughness (Robinson, 1986), an alternate roughness model using only a single partial layer

(Catalano et al., 2008), and a scale factor were used to fit each dataset. A layered-water model (Cheng et al., 2001; Schlegel et al., 2006) was used to describe the structure of bulk water above the mineral surface in this study.

In this study, all XR data sets were modeled using a single termination surface structure with doubly coordinated oxygen groups (>Al_2O). The two aluminum sites in the surface layer in the models were fixed to full occupancies of unity during the analysis to reduce parameter correlations. In the preliminary fitting, the occupancy parameters of terminal oxygen sites (>Al_2O) were varied in the model, with full occupancies of 3.0 ± 0.1 obtained for most samples. Thus, the terminal oxygen occupancy was fixed to 3 to reduce parameter correlations and avoid undercoordination of underlying aluminum sites during the final analysis. The vibrational amplitudes of terminal oxygen sites were either allowed to vary or, when they refined in preliminary fits to values close to 0, fixed to the value of this site in the bulk structure. The adsorbed water was modeled by a single layer site with parameters describing its height relative to the surface structure, vibrational amplitude, and occupancy, which was sufficient to reproduce the XR features observed for each sample. The use of two distinct adsorbed water layers was previously unsuccessful in modeling interfacial structures on corundum (001) surfaces (Catalano, 2011). Attempts to include two sites in the present study were similarly unsuccessful, with the two sites either refining to the same position or the occupancy of one site refining to zero.

Arsenic-specific electron density profiles were determined by RAXR. The RAXR data were analyzed using a procedure similar to the fixed-arsenic model analysis described previously (Catalano et al., 2008). Briefly, under a resonant condition, the total structure factor $F_{tot}(Q,E)$ at a selected Q is the sum of non-resonant and resonant structure factors, $F_{NR}(Q)$ and $F_R(Q,E)$,

respectively. $F_{NR}(Q)$ is calculated from the best-fit model of the non-resonant XR as described above. $F_R(Q,E)$ is determined as follow:

$$F_R(Q,E) = [f'(E) + if''(E)] \times \sum_j c_j exp(iQz_j) exp\left[-\frac{1}{2}(Qu_j)^2\right]$$

where $f'(E)$ and $f''(E)$ are the anomalous scattering factors of the resonant element (arsenic in the present study) and the resonant atom geometry was constrained by z_j, c_j, and u_j (position, occupancy, and root-mean square (rms) distribution width of a Gaussian distribution for the j_{th} resonant atom, respectively). Specific to this study, structural models involving two adsorbed As species, inner- and outer-sphere arsenate, were used to describe the interfacial As distribution. The distribution width parameters for both inner- and outer-sphere arsenate components were fixed at the values determined in previous work (Catalano et al., 2008) to minimize correlations between parameters because of the limited *Q*-range of the RAXR data.

At a given pH condition, the full distributions (i.e., the height and occupancy) of two adsorbed As species were determined by fitting a series of RAXR spectra measured over a full range of *Q* values for the sample (reacted with the highest arsenate concentration) at each pH. The resulting positions of As species were then fixed in the analysis of single RAXR spectra collected at the same pH value but lower arsenate concentrations, with only the occupancy parameters allowed to vary in order to obtain the arsenate surface coverage. The phase and amplitude of the modulation in single RAXR spectra collected at low *Q* values depends on the average height and total surface coverage of arsenate (Park and Fenter, 2007). For multimodal systems with two As species, as in the present study, a single RAXR measurement cannot independently determine the full interfacial distribution of As, but if the positions of the two As species are known (and held constant) then occupancies of each species can be determined with the relative amount of each determining the phase of the RAXR spectrum and the sum

determining the amplitude. This fitting strategy reduced the number of free parameters required to construct the model and reduced parameter correlations due to limitations in available data, especially at low Q values.

After determining the distributions of As from the initial RAXR analysis, the XR data were refit with a structural model including fixed As positions, occupancies, and distribution widths as determined from RAXR. The resulting XR fits generated new non-resonant structure factors which were then used to reanalyze the RAXR data. Iterations of the XR and RAXR analysis were applied until convergence was reached so that the changes in the As distribution parameters were within the parameter uncertainties. All RAXR spectra and fits are shown in the Electronic Annex (Figure A4.3, A4.4, and A4.5).

For both XR and RAXR data, the fitting parameters were optimized using a nonlinear least-squares algorithm. The goodness-of-fit parameters, ${\chi_v}^2$ and R-factor, were calculated according to following equations:

$$ {\chi_v}^2 = \sum \left[(I - I_{calc}) / \sigma_{exp} \right]^2 / (N - N_p) $$

$$ R = \sum_k |(I - I_{calc}) / I| / N $$

where N and N_p are the number of data points and parameters in the model fit, respectively, I and I_{calc} are the measured and calculated intensities, and σ_{exp} is the experimental uncertainty on each measured intensity. Minimization of ${\chi_v}^2$ was used in the least-squares fitting of the data, and the resulting R values were also used to evaluate the quality of the fit. Fitting parameter uncertainties were obtained from the least-squares fitting procedure and are reported at the 95% (2σ) confidence level.

4.4 RESULTS

4.4.1 Variations of Interfacial Water Structure with pH

XR data were collected to investigate the effect of pH on interfacial water structure near the corundum (001) surface in 0.01 M NaCl solution in the absence of arsenate. No substantial changes were visually apparent among XR data at pH 5, 7, and 9 (Figure 4.1A). The surface relaxations were generally small (< 0.1 Å) regardless of different pH conditions (Table A4.1, A4.2, and A4.3). The best-fit structural models have adsorbed water layers with heights of 2.87 ± 0.01, 2.85 ± 0.01, 2.89 ± 0.04 Å and vibrational amplitudes of 0.38 ± 0.04, 0.38 ± 0.02, 0.36 ± 0.07 Å at pH 5, 7, and 9, respectively (Table A4.1, A4.2, and A4.3). The positional shifts of adsorbed water of only a few hundredths of an Ångstrom and the insignificant variations in the vibrational amplitudes of these water sites demonstrate that interfacial water structure was invariant across the pH range studied. In addition, interfacial water electron density profiles determined by XR showed a similar overall hydration structure along the surface normal direction on the (001) surface under all pH conditions explored (Figure 4.1B). This structure of a single layer of adsorbed water with a broad distribution (Figure 4.1B) is consistent with a previous XR study in deionized water (Catalano, 2011), revealing a less ordered interfacial water structure above the corundum (001) surface compared to the (012) and (110) (Catalano, 2010; Catalano et al., 2006). The XR data showed no substantial variations of interfacial water structure over the pH range of 5 to 9 in the absence of adsorbates, suggesting that the changes of pH studied here are insufficient to induce extensive structural changes in interfacial water on this surface.

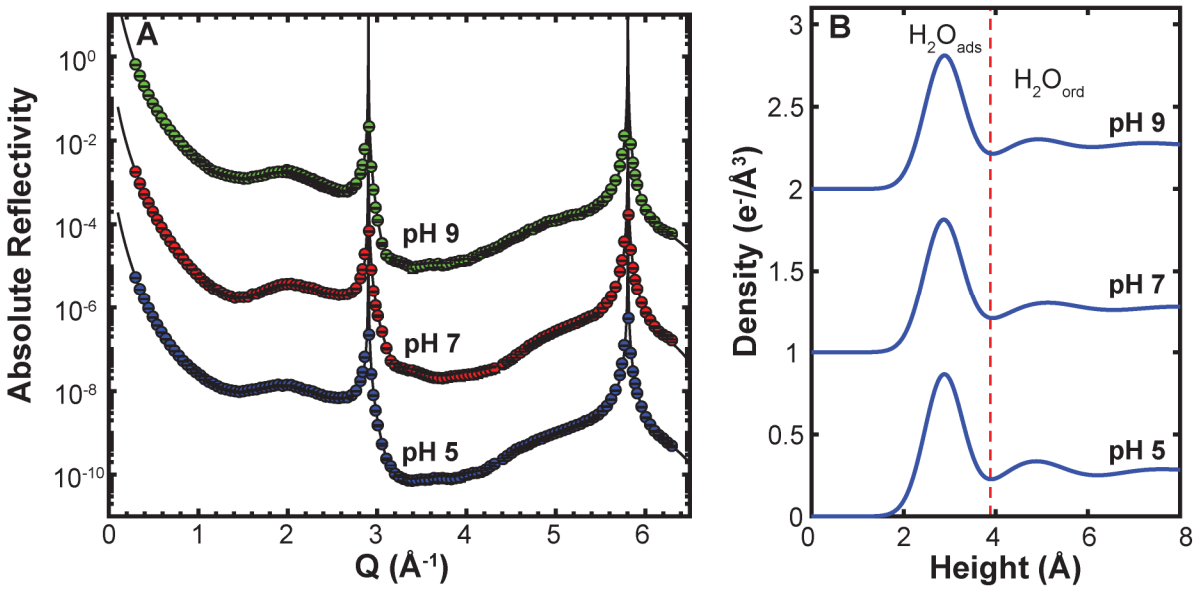

Figure 4.1. (A) Absolute X-ray reflectivity data (symbols) and calculated reflectivity from the best-fit model (lines) at corundum (001)-water interface in 0.01 M NaCl at pH 5, 7, and 9. (B) Resulting interfacial water electron density profiles above the corundum (001) surfaces. H_2O_{ads} and H_2O_{ord} represent the adsorbed water and extended ordered water (as modeled by a layered water profile), respectively. Each plot is offset vertically for clarity.

4.4.2 Arsenate Adsorption Mechanism on Corundum (001) Surfaces

In order to explore the effects of adsorbates on the structure of interfacial water on corundum (001) surfaces, the distribution of adsorbed arsenate under each experimental condition and the possible geometries of arsenate complexes on those surfaces were determined from the surface X-ray scattering data. Substantial changes in reflectivity data were observed at pH 5, 7, and 9 with increasing arsenate surface coverage (Figure 4.2A, 4.3A, and 4.4A). Differences between the five datasets at a given pH were most apparent near the minima in the reflectivity occurring near the anti-Bragg positions ($Q \approx 3.5$ Å^{-1}) where the reflectivity was most sensitive to the interfacial structure (Figure 4.2A, 4.3A, and 4.4A), indicating that the adsorption of arsenate significantly changed the total interfacial structure. XR and RAXR analyses were integrated to finalize arsenate distribution and the interfacial structure. The resulting models

revealed minor relaxations to the structure in the presence of arsenate except for the Al sites in the upper Al_2O_3 layer, which showed a general decrease in the separation of the two Al sites along the surface normal direction (Table A4.1, A4.2, and A4.3). This type of relaxation of Al sites, yielding a more gibbsite-like surface layer, has been noted in prior studies (Catalano, 2011; Eng et al., 2000). The displacements of these sites increased (up to 0.3 Å from the bulk positions) with increasing arsenate coverages at all pH values (Table A4.1, A4.2, and A4.3), indicating that arsenate adsorption perturbs the corundum (001) surface structure.

At each pH condition, the interfacial distribution of adsorbed As was determined using RAXR. Analysis of spectra for samples reacted with 100 μM total arsenate solutions refined both the arsenic position and occupancy (and thus surface coverage) because this condition generated the strongest RAXR signal at multiple Q values. The amplitude and phase variations of RAXR signals are well fit with As-specific density profiles consisting of two distinct adsorbate ion heights (Figure A4.3D, A4.4D, and A4.5D). The misfit to RAXR spectra at Q = 2.03, 2.32, and 2.52 $Å^{-1}$ at pH 5 (Figure A4.3D) is likely the result of measurement errors that produced a rise in reflectivity below the As K-edge; this was not reproduced in measurements at other pH values. Additional RAXR spectra at low Q values were collected as a function of arsenate solution concentration (10, 30, and 60 μM) at each pH condition to determine arsenate surface coverage (Figure A4.3, A4.4, and A4.5), as well as to evaluate whether the formation of two arsenate complexes only occurs at high arsenate concentration. All RAXR spectra for a given Q value had consistent phases for all concentrations explored (Figure A4.3, A4.4, and A4.5), indicating that the average height of adsorbed arsenate was similar at all surface coverages and thus a bimodal distribution is always present. Analysis of these RAXR spectra for lower arsenate concentrations (Table 4.2) reveals that two arsenate species coexist for all conditions explored in this study.

Different pH conditions did not produce any significant difference in the heights of the As species on corundum (001) surfaces (Figure 4.5), indicating uniform arsenate binding mechanisms. The first As position is around 0.77Å (Table 4.1) above the terminal oxygen groups under all pH conditions, indicating the formation of an inner-sphere arsenate complex on corundum (001) surfaces through a ligand exchange reaction. The second sites are around 3.2 Å (Table 4.1) above the terminal oxygen groups, which is too far for arsenate to directly bind to the surface and thus indicates the formation of an outer-sphere arsenate complex, a species that has been already observed on the (012) surfaces of corundum and hematite (Catalano et al., 2008).

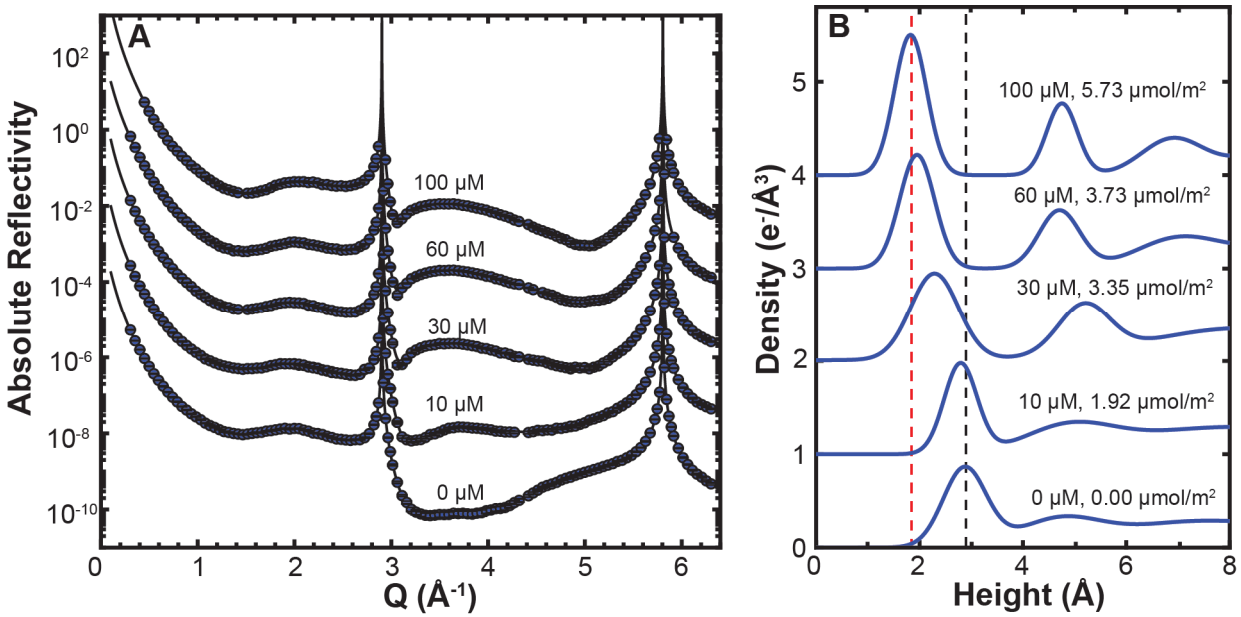

Figure 4.2. (A) Absolute X-ray reflectivity data (symbols) and calculated reflectivity from the best-fit model (lines) at corundum (001)-water interface in 0.01 M NaCl at pH 5 with increasing total arsenate concentration (C_{As}). (B) Changes in the interfacial water electron density profiles with increasing C_{As}. The corresponding arsenate surface coverage values (Γ_{As}) are from Table 4.2. The black and red dashed lines represent the adsorbed water height at 0 and 100 µM C_{As}, respectively. Each plot is offset vertically for clarity.

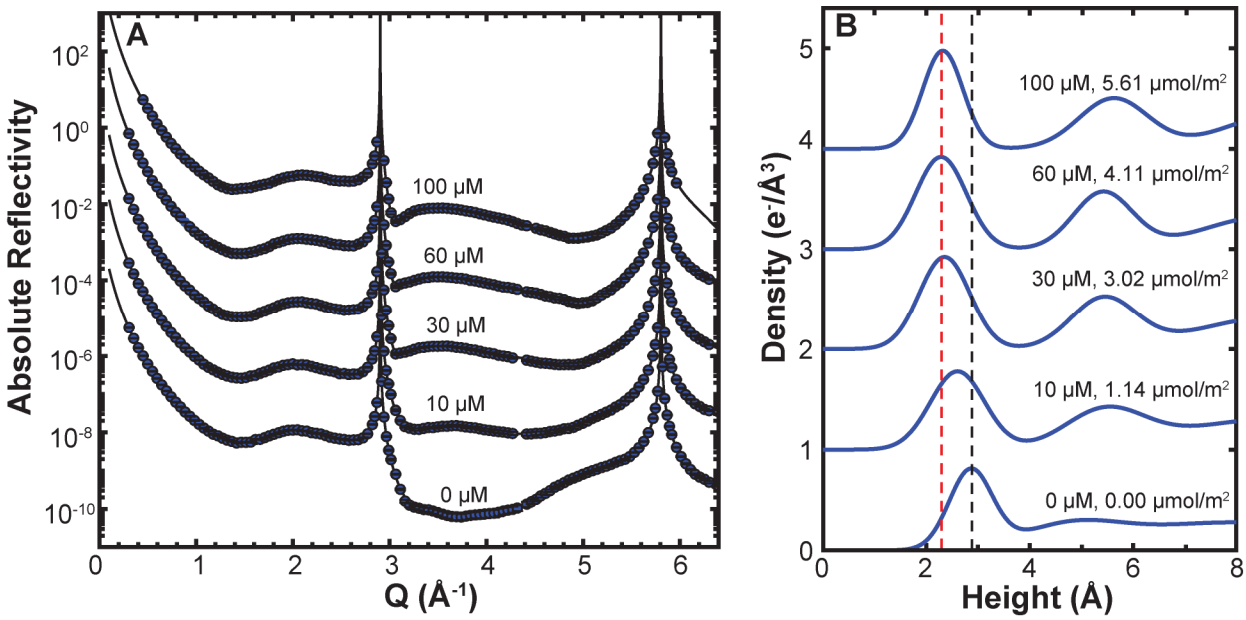

Figure 4.3. (A) Absolute X-ray reflectivity data (symbols) and calculated reflectivity from the best-fit model (lines) at corundum (001)-water interface in 0.01 M NaCl at pH 7 with increasing total arsenate concentration (C_{As}). (B) Changes in the interfacial water electron density profiles with increasing C_{As}. The corresponding arsenate surface coverage values (Γ_{As}) are from Table 4.2. The black and red dashed lines represent the adsorbed water height at 0 and 100 µM C_{As}, respectively. Each plot is offset vertically for clarity.

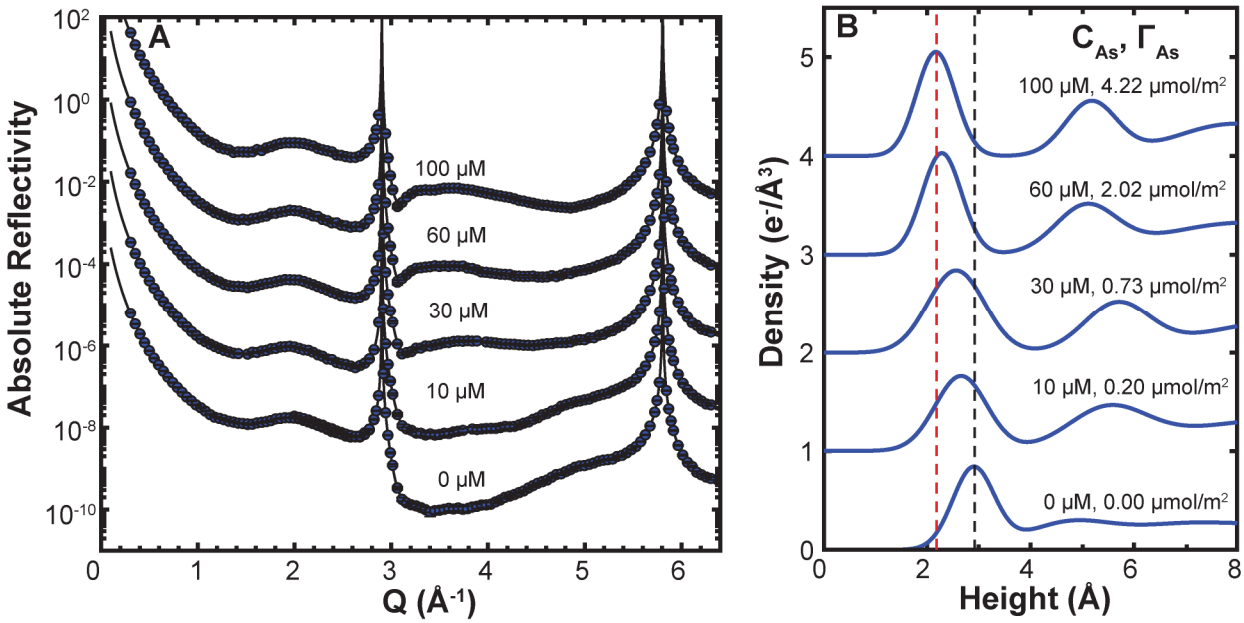

Figure 4.4. (A) Absolute X-ray reflectivity data (symbols) and calculated reflectivity from the best-fit model (lines) at corundum (001)-water interface in 0.01 M NaCl at pH 9 with increasing total arsenate concentration (C_{As}). (B) Changes in the interfacial water electron density profiles with increasing C_{As}. The corresponding arsenate surface coverage values (Γ_{As}) are from Table 4.2. The black and red dashed lines represent the adsorbed water height at 0 and 100 µM C_{As}, respectively. Each plot is offset vertically for clarity.

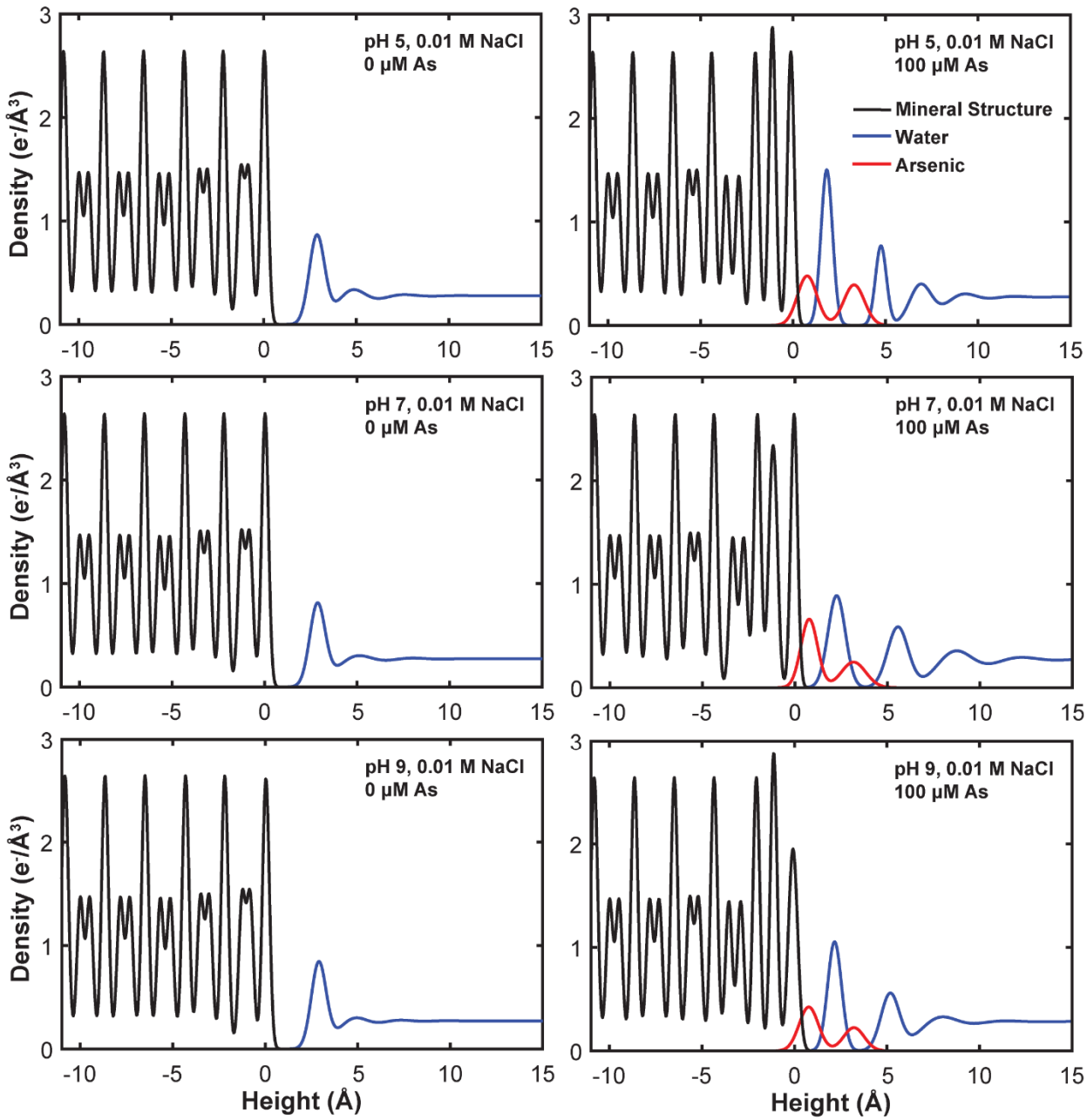

Figure 4.5. Interfacial electron density profiles of the refined structure of arsenate-free (left) and arsenate-sorbed (right) corundum (001)-water interface at pH 5, 7, and 9.

Table 4.1. RAXR-derived As positions and surface coverages (Γ_{As}) of inner-sphere (IS) and outer-sphere (OS) species for samples reacted with 100 μM total arsenate at pH 5, 7, and 9 in 0.01 M NaCl.

pH	Site	Height (Å)[a]		Γ_{As} (μmol/m^2)
5	IS	0.77(2)[b]		3.06(2)
	OS	3.30(5)		2.66(2)
			Total	5.73(2)
7	IS	0.77(8)		3.63(5)
	OS	3.17(3)		1.98(5)
			Total	5.61(7)
9	IS	0.77(2)		2.69(3)
	OS	3.21(2)		1.53(3)
			Total	4.22(5)

[a] Zero point set to the unrelaxed height of the terminal oxygen group on corundum (001) surfaces. [b] Uncertainties in the last digit are listed in parentheses.

Table 4.2. RAXR-derived arsenate surface coverages (Γ_{As}) for inner-sphere (IS) and outer-sphere (OS) species at pH 5, 7, and 9 in 0.01 M NaCl.

Concentration (μM)	Site		pH 5	pH 7	pH 9
			Γ_{As} (μmol/m^2)		
10	IS		1.54(2)[a]	0.97(2)	0.195(8)
	OS		0.38(2)	0.17(2)	0.002(8)
		Total	1.92(3)	1.14(2)	0.20(1)
30	IS		2.44(2)	2.26(7)	0.414(8)
	OS		0.90(2)	0.77(7)	0.317(8)
		Total	3.35(3)	3.02(9)	0.73(1)
60	IS		2.58(2)	2.82(5)	1.50(5)
	OS		1.15(2)	1.30(5)	0.52(5)
		Total	3.73(2)	4.11(7)	2.02(7)
100	IS		3.06(2)	3.91(5)	2.69(3)
	OS		2.66(2)	1.72(5)	1.53(3)
		Total	5.73(2)	5.63(7)	4.22(5)

[a] Uncertainties in the last digit are listed in parentheses.

4.4.3 Effect of Arsenate Adsorption on Interfacial Water Structure

The combined analysis of the XR and RAXR data allows changes in the structural arrangement of water near the surface to be identified separately from the interfacial As distribution. The interfacial water electron density profiles at all pH values experienced a substantial restructuring showing a positional shift of the adsorbed water layer towards the mineral surface and also the appearance of layered water (Figure 4.2B, 4.3B, and 4.4B) with increased arsenate adsorption. At pH 5, low arsenate surface coverages ($\Gamma_{As} < 1.92$ μmol/m^2) had little effect on interfacial water structure while high arsenate surface coverages ($\Gamma_{As} > 3.73$ μmol/m^2) showed a distinct water rearrangement; intermediate coverage ($\Gamma_{As} = 3.35$ μmol/m^2) produced a transitional water structure with relatively high disorder (Figure 4.2B). The same systematic change in interfacial water structure was also observed in both pH 7 and 9 systems (Figure 4.3B and 4.4B) but the onset of gradual structural transition occurred at lower arsenate surface coverage ($\Gamma_{As} = 3.02$ μmol/m^2 at pH 7, $\Gamma_{As} = 0.73$ μmol/m^2 at pH 9). This is a clear indication that a charged adsorbate (e.g., oxoanion arsenate) induces a substantial structural change in interfacial water, which does not occur in the absence of arsenate when pH alone is varied between 5 and 9.

For all pH conditions, the XR-derived average height for the adsorbed water varied proportionally with arsenate surface coverage, with these water sites shifting closer to the mineral surface as arsenate surface coverage increased (Figure 4.6). The XR-derived adsorbed water vibrational amplitudes show a generally similar trend across pH values as arsenate surface coverage increases, with an increase from arsenate-free to low/intermediate arsenate systems (30 μM total As at pH 5 and 9; 10 μM total As at pH 7), followed by a decrease from low/intermediate to high arsenate systems (Figure 4.6). The monotonic decrease in height

coupled with the increase and then decrease in vibrational amplitude for the adsorbed water layer is most consistent with two coexisting interfacial structures that vary in proportions with arsenate surface coverage. Adsorbed water layers in the absence of arsenate and at high arsenate coverage clearly occur at different heights. If a mixture of these two sites occurs, then the height obtained when modeled as a single site will approximately reflect the weighted mean position of the two adsorbed water positions. When mixed in roughly equal proportions, the single site will appear to have a wide distribution width, resulting in broadening of the vibrational amplitude in the model. No attempt was made to model the data with two adsorbed water layers because the structural model with a single site well reproduced the data (Table A4.1, A4.2, and A4.3), suggesting that additional fitting parameters may largely fit noise and systematic errors in the data rather than provide additional structural information.

In addition to the adsorbed water modifications described above, the structure of the layered water also changed upon arsenate adsorption, with the vibrational amplitudes of the beginning of the layered water (σ_o) decreasing monotonically with increasing arsenate surface coverage at all pH conditions studied (Table A4.1, A4.2, and A4.3). Even though the spatial arrangements of those sites differed among the pH values (Figure 4.6), the consistent trends in the vibrational amplitudes indicate a more ordered layered water profile above corundum (001) surfaces, regardless of changes in pH. This effect is readily seen in the sharpness of the first layered water peaks in Figures 4.2B, 4.3B, and 4.4B. These observations indicate that the adsorption of arsenate not only directly affects the structure of the adsorbed water layer but also the degree of order for the extended layering of interfacial water.

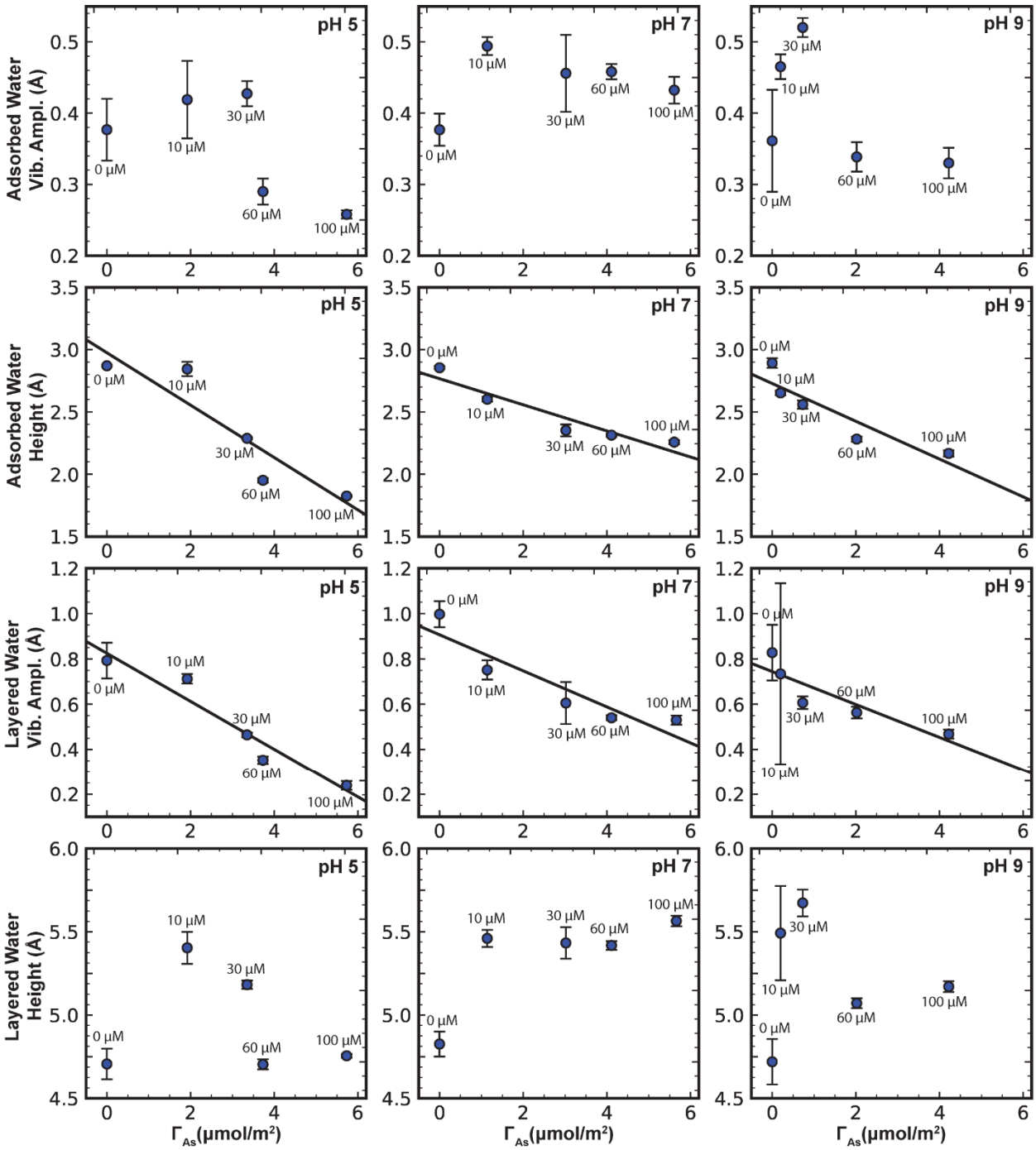

Figure 4.6. XR-derived parameters (vibrational amplitude and height) for the adsorbed and layered water profile versus increasing arsenate surface coverage (Γ_{As}) at pH 5, 7, and 9. The height and vibrational amplitude of the layered water profile refers to the position and degree of order of the first water layer. The black solid lines are linear regression fits for the data. Each data point is labeled with the corresponding total arsenate concentration. The full fitting parameters are summarized in Table A4.1, A4.2, and A4.3.

4.5 DISCUSSION

4.5.1 Factors Inducing Interfacial Water Restructuring on Corundum (001) Surfaces

The results of the present study taken together with previous studies of the interfacial water structure derived from a variety of methods provide further insight into the major factors controlling water ordering near corundum (001) surfaces. A previous study using SFVS suggests that reorientation of interfacial water molecules and variations in surface charge on corundum (001) surfaces occur as pH changes from 3 to 10 (Zhang et al., 2008). Two different OH stretching frequencies are observed at ~3200 and 3450 cm^{-1} and display amplitudes that change with pH. The amplitudes of the 3200 cm^{-1} band invert from negative to positive as pH increases from 3 to 10 but remains close to zero in the pH region from 5 to 7. This band is interpreted to originate from the first layer of water on the mineral surface (adsorbed water in the present study), with the amplitude change suggesting that this water reorients along the surface normal direction in response to a change in surface charge, with a near-zero surface charge between pH 5 and 7. However, SFVS measurements cannot quantify the spatial distributions of water molecules near the surface (Björneholm et al., 2016) and thus cannot determine the overall structural arrangement of interfacial water. Our current XR data show no evidence of substantial interfacial water restructuring from pH changes alone between pH 5 and 9. A broader pH range was not examined because corundum solubility increases at lower and higher pH values. This could potentially generate dissolved species which, if they readsorb as Al^{3+} adatoms, may alter the surface charge (Lützenkirchen et al., 2014) and thus the interfacial water structure. Such changes in surface charging after large pH fluctuations was observed an isostructural hematite (001) surface and attributed to Fe^{3+} adatoms (Boily et al., 2011). Over the pH range examined, the interfacial water structures on (001) surfaces were the same in 0.01 M NaCl solutions

(corresponding to an ionic strength of 0.01 M) as observed in DI water. It is unclear how interfacial water structure changes at high ionic strength because electrolyte ions like Na^+ may bind to mineral surfaces and are difficult to distinguish from water in surface scattering experiments.

Changes in pH and adsorbate surface coverage are the primary factors controlling the charge states for surface sites. The corundum (001) surface is dominated by doubly coordinated functional groups that are predicted to be neutrally charged in the circumneutral pH range (Hiemstra et al., 1989a; Hiemstra et al., Hiemstra et al., 1996). There is inconsistency in reported point of zero charge (PZC) or isoelectric points (IEP) for the corundum (001) surface, with the Multi-Site-Complexation (MUSIC) model (Hiemstra et al., 1989a; Hiemstra et al., Hiemstra et al., 1996), SFVS (Zhang el al., 2008), and streaming potential measurements (Kershner et al., 2004) indicating values around pH 6, whereas more recent streaming potential measurements and second harmonic generation suggesting a value closer to pH 4 (Lützenkirch et al., 2010; Fitts et al., 2005).

The structure of interfacial water near this surface varied little among pH 5, 7, and 9, suggesting that surface charging from protonation-deprotonation of functional groups under the conditions explored is inadequate to induce extensive restructuring of interfacial water structure. In contrast, the adsorption of arsenate produces a substantial change in interfacial water structure. The entire interfacial water structure shifts closer to the surface and stronger ordering is observed extending out toward the bulk fluid. This indicates that the formation of charged surface sites, i.e., adsorbed arsenate species, induces the rearrangement of interfacial water on corundum (001) surfaces. Such groups may generate local electrostatic fields that cause orientation of water

dipoles or may provide alternative sites for hydrogen bonding between water and the mineral surface.

4.5.2 Possible Nature of Water Structure Transition

The combined XR and RAXR observations reveal a structural transition of interfacial water upon arsenate adsorption on corundum (001) surfaces at all pH conditions studied. The changes in the adsorbed water positions appear to be continuous but the degree of order for such sites appears to pass through a more disordered state at intermediate arsenate surface coverages. As noted in section 4.4.3, this phenomenon is most likely caused by the coexistence of two distinct water structures near the surface that vary in proportions with arsenate surface coverage. In arsenate-free systems, the adsorbed water is dominated by weakly ordered water with relatively large vibrational amplitudes. With arsenate present at high coverages, the first adsorbed water is located closer to the mineral surface. In systems with intermediate arsenate surface coverage, the adsorbed water appears to be a mixture of these two end-member states, with overlapping of adsorbed water at two distinct heights causing an apparent increase in vibrational amplitude, consistent with that observed in the present study. Accompanying this transition, the extended layering of interfacial water showed a continuous transition to a more ordered state as arsenate surface coverage increased. The shift in position of this layering is smaller and more variable than for the adsorbed water layer, and also generally smaller than the spatial resolution of the data, and the start of this profile shows a substantial decrease in positional disorder (i.e., a substantially smaller vibrational amplitude). Mixing these two layered water profiles should thus manifest as a systematic shift in the σ_o value, as is observed (Figure 4.6).

These structural changes with increasing arsenate coverage are thus consistent with water locally having a different structure near sites of adsorbed arsenate than on the pristine surface. This suggests that the charge state of individual surface sites instead of net surface charge controls the observed interfacial water restructuring upon arsenate adsorption. If water structure depended on net surface charge, restructuring transitions would either display an abrupt change above some threshold charge once its magnitude could drive water dipole reorientation, which in the present system is primarily generated by arsenate adsorption, or both the positions and vibrational amplitudes of adsorbed water would show a systematic change with increasing surface coverage. Neither effect is observed in our experiments. This is further supported by interfacial water structure not changing substantially at pH 9 in the absence of arsenate despite some surface charge development from deprotonation reactions. While the arsenate-induced changes to interfacial water structure are observed at a lower As coverage at pH 9 than for lower pH, this may originate from the arsenate surface complex having a larger negative charge (Fukushi and Sverjensky, 2007). Such adsorbate-induced restructuring of interfacial water on corundum (001) surfaces suggests a feedback during ion uptake that is controlled by surface site charge behavior. Developing approaches to include the contribution of water restructuring to the thermodynamics of adsorption processes may help refine predictive models of adsorbate behavior in natural systems.

4.5.3 Relationship of Arsenate Adsorption Mechanisms and Interfacial Water Restructuring

In this study, arsenate adsorbs as a mixture of inner- and outer-sphere complexes on corundum (001) surfaces over a wide pH range. Based on the height (~0.77 Å) of the lower

arsenate species above the surface and steric constraints, inner-sphere arsenate complexes have tridentate adsorption geometry, with arsenate molecules sitting over the dioctahedral vacancies in the (001) plane (Figure 4.7). No configuration is possible with As in this position that does not involve bonding to the surface functional groups, and if arsenate were not located over the vacancy then this would cause substantial cation-cation repulsion between As and an underlying Al atom. This geometry was unexpected as bond valence analysis (Brese and O'Keeffe, 1991) for an arsenate group bound in an inner-sphere mode to an unrelaxed corundum (001) surface predicts the doubly coordinated oxygen surface site would be overbonded, yielding a bond valence sum of 2.23 to 2.27 v.u., assuming the range of As-O distances in example arsenate mineral structures (Harrison, 2000; Xu et al., 2007). However, arsenate adsorption is coupled with a downward relaxation of the uppermost Al site (Table A4.1, A4.2, and A4.3), which would lengthen the Al-O bond and lower the bond valence sum, suggesting that these Al displacements are a response to As adsorption. The structural models derived from the current XR analysis only reveal the laterally-averaged structure along the surface normal direction and a complete three-dimensional structural analysis is needed to fully test this possible bonding geometry.

Regardless of the exact binding geometry, the presence of inner-sphere arsenate on a surface terminated in doubly coordinated oxygen groups indicates that these sites can play a role in adsorption processes. At the highest arsenate coverage studied, ~30% of Al_2O sites on the surface are bound to arsenate, suggesting a substantial capacity for participating in ligand exchange reactions. Previous surface complexation models established to describe arsenate adsorption behavior have only included singly coordinated functional groups in complexing arsenate (Dixit and Hering, 2003; Fukushi and Sverjensky, 2007; Goldberg, 1986; Hiemstra and Van Riemsdijk, 1999). However, our recent extended X-ray absorption fine structure (EXAFS)

spectroscopy investigations of arsenate binding to gibbsite platelets (Xu and Catalano, 2016, 2018) suggested that inner-sphere complexes were forming on basal planes terminated in doubly coordinated oxygen groups, as is observed on corundum (001). The common assumption regarding the lack of reactivity of doubly coordinated surface functional groups towards oxoanions may thus underestimate the binding capacity of aluminum oxide and hydroxide surfaces. This assessment is in agreement with a previous study of Cm^{3+} adsorption to the corundum (001) surface (Rabung et al., 2004).

Outer-sphere arsenate species also exist on corundum (001) surfaces over a broad range of adsorbate concentrations, with the As in such groups located ~3.2 Å above the surface. The presence of such species is consistent with our recent study of arsenate adsorption on gibbsite particles (Xu and Catalano, 2018), which expose the same type of surface functional group as corundum (001) surfaces. EXAFS spectroscopy suggested a portion of the adsorbed arsenate occurred as outer-sphere complexes, and macroscopic arsenate uptake displayed a substantial dependence on ionic strength. In addition, a previous study of the (012) surfaces of corundum and hematite (Catalano et al., 2008) observed outer-sphere arsenate occurring at a similar height above the mineral surfaces as in the current work. This suggests that outer-sphere complexes may be stabilized through similar mechanisms on multiple corundum surfaces, and also on gibbsite, such as via the formation of H-bonds between arsenate oxoligands and surface functional groups or interfacial water. According to the location of the outer-sphere As, H-bonding between outer-sphere arsenate oxoligands and doubly coordinated oxygen functional groups on the surface may be the most plausible configuration. Doubly coordinated functional groups, as the dominant surface sites on the corundum (001) surface, are generally charge-neutral (Hiemstra et al., 1996; Hiemstra et al., 1999; Lützenkirchen, 2013; Lützenkirchen et al.,

2010) over the pH range examined, indicating that electrostatics are unlikely to contribute substantially to outer-sphere arsenate adsorption. In addition, these surface groups have a limited ability to form H-bonds with water molecules compared to singly or triply coordinated functional groups (Hass and Schneider, 2000; Hass et al., 1998; Kerisit, 2011). Thus, arsenate may be more effective in forming H-bonds with doubly coordinated surface functional groups, helping to bridge between surface sites and interfacial water molecules. Such linkages may be the origin of the observed structural transition of water near the surface.

The observed changes in interfacial water structure upon arsenate adsorption may also affect the stability of outer-sphere arsenate species. At low arsenate surface coverages, ~20 ± 1%, 15 ± 2%, and 1 ± 4% of arsenate is bound as outer-sphere species at pH 5, 7, and 9, respectively. In contrast, at high surface coverage, outer-sphere species represents ~47 ± 2%, 35 ± 1%, and 36 ± 1% of the total adsorbed arsenate (Table 4.2). The predominance of inner-sphere species at low surface coverage further suggests a connection between the degree of water ordering and the presence of these surface complexes. The adsorption of inner-sphere arsenate may be the dominant driver of water restructuring as it is present at all conditions studies. This restructuring may then facilitate outer-sphere binding, providing a mechanism to generate the formation of these coexisting adsorbed arsenate species.

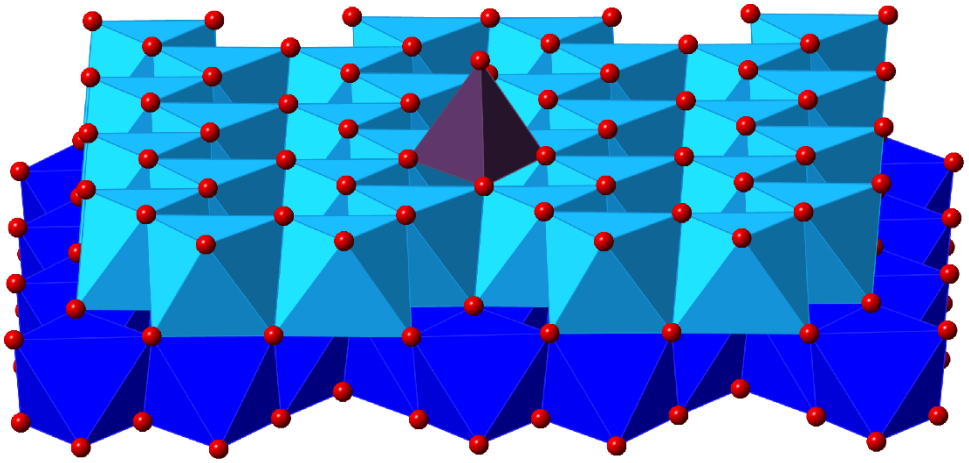

Figure 4.7. Proposed structural model of inner-sphere adsorbed AsO_4^{3-} bound to doubly coordinated functional groups of the corundum (001) surface, forming a tridentate surface complex. Red balls represent oxygen atoms. Purple, light blue, and dark blue polyhedra represent AsO_4 tetrahedron and the first and second layers of AlO_6 octahedra, respectively.

4.6 ACKNOWLEDGEMENTS

This research was supported by the U.S. National Science Foundation (NSF) Environmental Chemical Sciences Program (award no. CHE-1505532). The XR and RAXR data were collected at beamline 13-IDC (GeoSoilEnviroCARS) at the Advanced Photon Source, Argonne National Laboratory. GeoSoilEnviroCARS is supported by NSF Earth Sciences (EAR-1634415) and U.S. Department of Energy (DOE) Office Geosciences (DE-FG02-94ER14466). The APS is an Office of Science User Facility operated for the U.S. DOE Office of Science by Argonne National Laboratory under contract no. DE-AC02-06CH11357.

4.7 APPENDIX

Table A4.1. Optimized structural parameters for the best-fit models of the corundum (001)-water interface at pH 5 for increasing total arsenate concentrations.

Surface structure		Unrelaxed	Total arsenate concentration				
Atom		Structure[a]	No As	10 μM As	30 μM As	60 μM As	100 μM As
As	z (Å)[b]		0	3.30	3.30	3.30	3.30(5)
	θ[c]		0	0.046(3)	0.110(3)	0.141(1)	0.325(2)
As	z (Å)		0	0.77	0.77	0.77	0.77(2)
	θ		0	0.187(3)	0.299(2)	0.315(2)	0.374(2)
O	z (Å)		2.87(1)[j]	2.84(6)	2.288(7)	1.95(2)	1.825(8)
(H_2O_{ads})	θ		2.2(1)	2.2(1)	2.64(3)	2.54(7)	2.88(3)
	σ[d]		0.38(4)	0.42(5)	0.43(2)	0.29(2)	0.258(8)
O	z (Å)	0.000	0.003(4)	-0.005(4)	-0.169(3)	-0.087(5)	-0.168(3)
(>Al_2O)	σ		0.056	0.056	0.056	0.19(2)	0.056
Al	z (Å)	-0.837	-0.814(8)	-0.88(1)	-1.017(8)	-1.166(8)	-1.114(3)
Al	z (Å)	-1.327	-1.252(3)	-1.33(2)	-1.302(9)	-1.151(8)	-1.112(4)
O	z (Å)	-2.165	-2.195(6)	-2.172(9)	-2.063(5)	-2.062(6)	-2.038(3)
Al	z (Å)	-3.002	-3.033(7)	-3.037(6)	-2.930(6)	-2.964(7)	-2.926(9)
Al	z (Å)	-3.492	-3.503(6)	-3.480(7)	-3.462(8)	-3.599(6)	-3.614(9)
O	z (Å)	-4.329	-4.305(3)	-4.289(3)	-4.346(2)	-4.388(4)	-4.398(5)
Al	z (Å)	-5.167	-5.124(3)	-5.132(8)	-5.162(4)	-5.177(5)	-5.177(3)
Al	z (Å)	-5.657	-5.669(4)	-5.687(7)	-5.683(4)	-5.623(4)	-5.650(3)
O	z (Å)	-6.494	-6.498(2)	-6.501(2)	-6.483(2)	-6.475(2)	-6.486(3)
Al	z (Å)	-7.331	-7.315	-7.315	-7.316	-7.314	-7.314
Al	z (Å)	-7.821	-7.837	-7.837	-7.836	-7.838	-7.383
O	z (Å)	-8.659	-8.660(1)	-8.658(2)	-8.668(1)	-8.663(2)	-8.658(2)
Al	z (Å)	-9.496	-9.479	-9.480	-9.481	-9.479	-9.479
Al	z (Å)	-9.986	-10.0002(2)	-10.0020(2)	-10.0009(2)	-10.0024(3)	-10.0029(4)
O	z (Å)	-10.823	-10.823	-10.822(1)	-10.823	-10.823	-10.823
Layered water structure							
z (Å)			4.71(9)	5.40(1)	5.18(3)	4.70(3)	4.76(1)
σ_0(Å)[e]			0.79(8)	0.71(2)	0.46(1)	0.35(2)	0.24(2)
$\overline{\sigma}$ (Å)[f]			0.40(6)	0.50(6)	0.98(4)	0.44(2)	0.33(1)
d_w (Å)[g]			2.21(7)	2.45(4)	2.47(5)	2.29(2)	2.13(1)
Non-structural parameters							
Water film (μm)			40(1)	38(2)	36(2)	47(2)	29(5)
Roughness (Å)[h]			0.85(1)	1.59(5)	1.46(3)	1.49(3)	1.93(3)
Layer fraction[i]			0.23(1)	0	0	0	0
Goodness-of-fit parameters							
χ_v^2			1.49	1.45	2.01	2.36	3.55
R-factor			0.024	0.023	0.022	0.055	0.030

[a] Atom height for the unrelaxed structure. [b] Atom height from the best fit model. [c] Occupancy. [d] Vibrational amplitude. [e] Vibrational amplitude of the first water layer (Fenter, 2002). [f] A parameter describing how the vibrational amplitude of each water layer increases with distance from the surface (Fenter, 2002). [g] Spacing of layered water (Fenter, 2002). [h] Roughness parameter of Robinson (Robinson, 1986). [i] Fractional occupancy of partial layer accounting minor roughness (Catalano et al., 2008). [j] Uncertainties in the last digit are listed in parentheses,

reported at the 95% confidence level. Parameters with no listed uncertainties were not varied in the analysis.

Table A4.2. Optimized structural parameters for the best-fit models of the corundum (001)-water interface at pH 7 for increasing total arsenate concentrations.

Surface structure		Unrelaxed	Total arsenate concentration				
Atom		Structure	No As	10 μM As	30 μM As	60 μM As	100 μM As
As	z (Å)		0	3.17	3.17	3.17	3.17(3)
	θ		0	0.021(2)	0.093(8)	0.158(6)	0.210(6)
As	z (Å)		0	0.77	0.77	0.77	0.77(8)
	θ		0	0.118(2)	0.276(8)	0.343(6)	0.477(6)
O	z (Å)		2.85(1)	2.60(2)	2.35(5)	2.31(1)	2.26(2)
(H_2O_{ads})	θ		1.98(6)	2.50(5)	2.77(1)	2.77(4)	2.55(7)
	σ		0.38(2)	0.49(1)	0.46(5)	0.46(1)	0.43(2)
O	z (Å)	0.000	0.003(2)	-0.003(3)	-0.006(1)	-0.006(2)	-0.05(1)
(>Al_2O)	σ		0.056	0.046(2)	0.13(3)	0.056	0.056
Al	z (Å)	-0.837	-0.809(3)	-0.896(7)	-1.006(5)	-1.018(5)	-1.06(1)
Al	z (Å)	-1.327	-1.264(3)	-1.344(8)	-1.311(2)	-1.306(5)	-1.295(7)
O	z (Å)	-2.165	-2.20(1)	-2.16(1)	-2.11(3)	-2.067(3)	-2.03(1)
Al	z (Å)	-3.002	-3.039(7)	-3.009(8)	-2.90(1)	-2.867(7)	-2.77(3)
Al	z (Å)	-3.492	-3.503(6)	-3.469(6)	-3.43(3)	-3.417(8)	-3.36(2)
O	z (Å)	-4.329	-4.306(3)	-4.302(6)	-4.332(8)	-4.346(2)	-4.375(6)
Al	z (Å)	-5.167	-5.130(3)	-5.110(8)	-5.169(4)	-5.178(3)	-5.198(5)
Al	z (Å)	-5.657	-5.679(4)	-5.666(3)	-5.695(9)	-5.688(3)	-5.678(7)
O	z (Å)	-6.494	-6.494(2)	-6.501(2)	-6.494(2)	-6.481(2)	-6.470(3)
Al	z (Å)	-7.331	-7.315	-7.316	-7.318	-7.316	-7.316
Al	z (Å)	-7.821	-7.837	-7.837	-7.835	-7.837	-7.836
O	z (Å)	-8.659	-8.658(1)	-8.656(1)	-8.663(1)	-8.664(1)	-8.669(2)
Al	z (Å)	-9.496	-9.480	-9.480	-9.482	-9.480	-9.481
Al	z (Å)	-9.986	-10.0018(2)	-10.0014(1)	-9.9992(2)	-10.0014(2)	-10.0007(2)
O	z (Å)	-10.823	-10.823	-10.822(1)	-10.823	-10.823	-10.823
Layered water structure							
z (Å)			4.83(8)	5.46(5)	5.43(9)	5.42(3)	5.57(3)
σ_0 (Å)			0.99(6)	0.75(4)	0.61(9)	0.54(1)	0.53(2)
$\overline{\sigma}$ (Å)			0.33(4)	0.73(4)	0.72(2)	0.63(2)	0.45(3)
d_w (Å)			2.42(3)	2.71(7)	2.97(7)	3.00(2)	3.06(2)
Non-structural parameters							
Water film (μm)			40(2)	33(1)	34(3)	30(2)	27(8)
Roughness (Å)			0.85(1)	1.65(3)	1.57(4)	1.74(3)	2.25(6)
Layer fraction			0.28(1)	0	0	0	0
Goodness-of-fit parameters							
χ_v^2			1.10	0.51	1.70	1.29	1.93
R-factor			0.023	0.016	0.016	0.017	0.033

See Table A4.1 for description of the parameters.

Table A4.3. Optimized structural parameters for the best-fit models of the corundum (001)-water interface at pH 9 for increasing total arsenate concentrations.

Surface structure		Unrelaxed	Total arsenate concentration				
Atom		Structure	No As	10 μM As	30 μM As	60 μM As	100 μM As
As	z (Å)		0	3.21	3.21	3.21	3.21(2)
	θ		0	0.000(1)	0.039(1)	0.064(6)	0.187(4)
As	z (Å)		0	0.77	0.77	0.77	0.77(2)
	θ		0	0.024(1)	0.051(1)	0.183(6)	0.329(4)
O	z (Å)		2.89(4)	2.65(2)	2.56(3)	2.28(2)	2.17(3)
(H_2O_{ads})	θ		2.0(1)	2.3(2)	2.84(4)	2.41(4)	2.42(8)
	σ		0.36(7)	0.47(2)	0.52(1)	0.34(2)	0.33(2)
O	z (Å)	0.000	0.004(7)	-0.001(1)	-0.003(3)	-0.007(7)	-0.008(2)
(>Al_2O)	σ		0.062(6)	0.12(6)	0.174(6)	0.213(8)	0.18(1)
Al	z (Å)	-0.837	-0.813(5)	-0.90(3)	-1.02(2)	-1.19(1)	-1.123(4)
Al	z (Å)	-1.327	-1.252(6)	-1.26(4)	-1.25(2)	-1.05(1)	-1.333(3)
O	z (Å)	-2.165	-2.187(9)	-2.14(4)	-2.08(2)	-2.097(7)	-2.059(8)
Al	z (Å)	-3.002	-3.026(5)	-3.00(1)	-2.85(3)	-2.924(9)	-2.91(1)
Al	z (Å)	-3.492	-3.500(6)	-3.51(6)	-3.44(2)	-3.526(9)	-3.55(1)
O	z (Å)	-4.329	-4.304(3)	-4.33(3)	-4.327(2)	-4.336(7)	-4.350(6)
Al	z (Å)	-5.167	-5.131(4)	-5.13(2)	-5.166(6)	-5.160(4)	-5.188(6)
Al	z (Å)	-5.657	-5.673(3)	-5.665(4)	-5.686(4)	-5.657(4)	-5.667(3)
O	z (Å)	-6.494	-6.496(1)	-6.488(5)	-6.489(1)	-6.497(3)	-6.499(2)
Al	z (Å)	-7.331	-7.317	-7.317	-7.315	-7.315	-7.316
Al	z (Å)	-7.821	-7.835	-7.835	-7.837	-7.837	-7.386
O	z (Å)	-8.659	-8.660(1)	-8.658(1)	-8.662(1)	-8.655(1)	-8.651(3)
Al	z (Å)	-9.496	-9.482	-9.482	-9.480	-9.480	-9.480
Al	z (Å)	-9.986	-9.9996(2)	-9.9998(2)	-10.0016(1)	-10.0018(2)	-10.0010(2)
O	z (Å)	-10.823	-10.823	-10.823	-10.823	-10.823	-10.823
Layered water structure							
z (Å)			4.72(9)	5.49(3)	5.67(8)	5.07(3)	5.17(3)
σ_0 (Å)			0.8(1)	0.7(4)	0.61(3)	0.56(3)	0.47(2)
$\overline{\sigma}$ (Å)			0.24(5)	0.9(1)	0.81(5)	0.80(7)	0.56(2)
d_w (Å)			2.80(2)	2.7(3)	2.85(6)	2.54(3)	2.55(3)
Non-structural parameters							
Water film (μm)			34(2)	25(2)	27(2)	25(2)	30(2)
Roughness (Å)			0	1.26(7)	0	1.20(2)	1.15(1)
Layer fraction			0.25(1)	0.2(1)	0.26(3)	0	0
Goodness-of-fit parameters							
χ_v^2			1.80	0.89	0.89	1.31	2.06
R-factor			0.019	0.012	0.017	0.019	0.034

See Table A4.1 for description of the parameters.

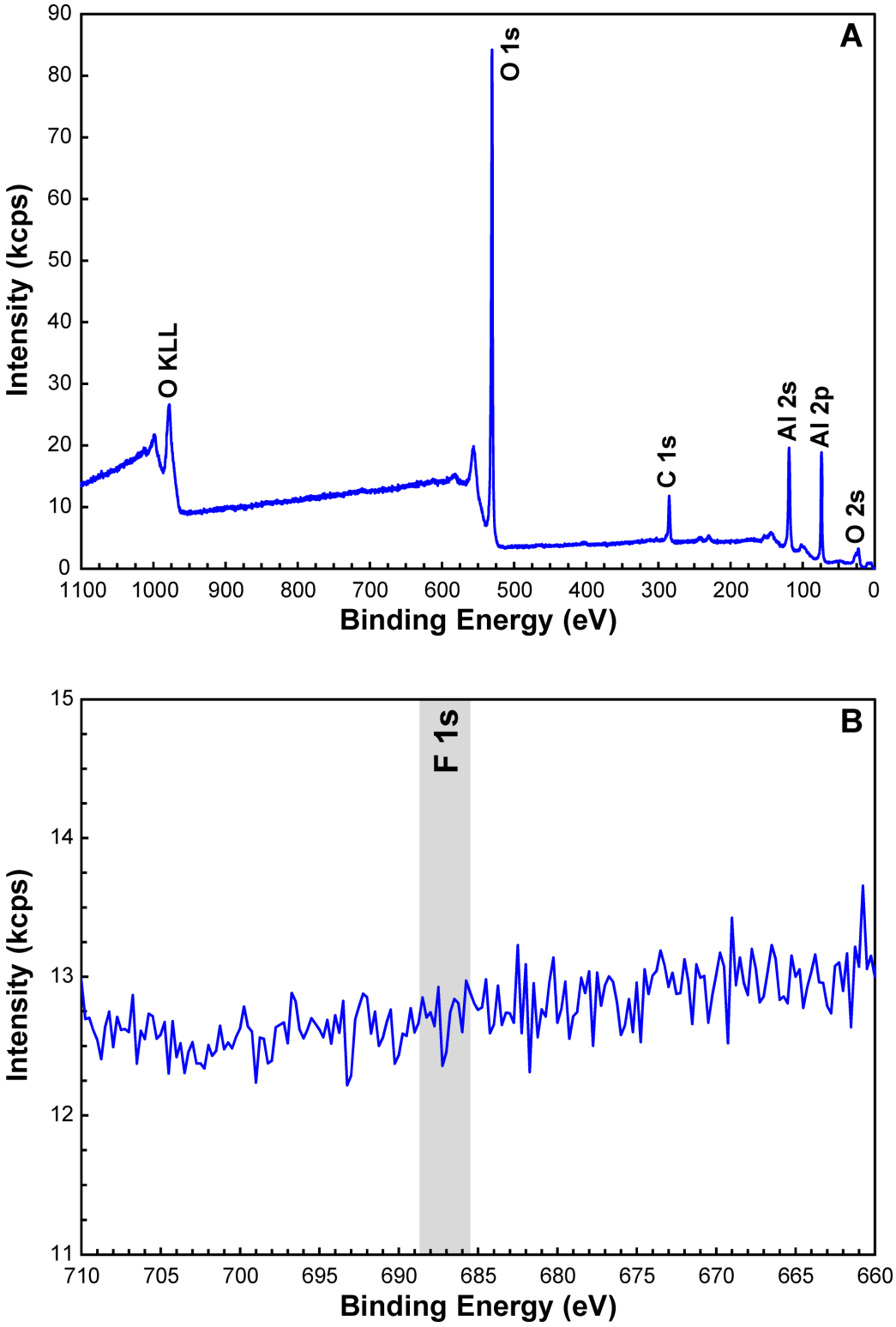

Figure A4.1. XPS spectrum of a corundum (001) single crystal surface after cleaning: (A) full survey scan, (B) region near the F 1s spectral line, with the shaded region outlining observed binding energies from aluminum fluoride phases (NIST, 2000).

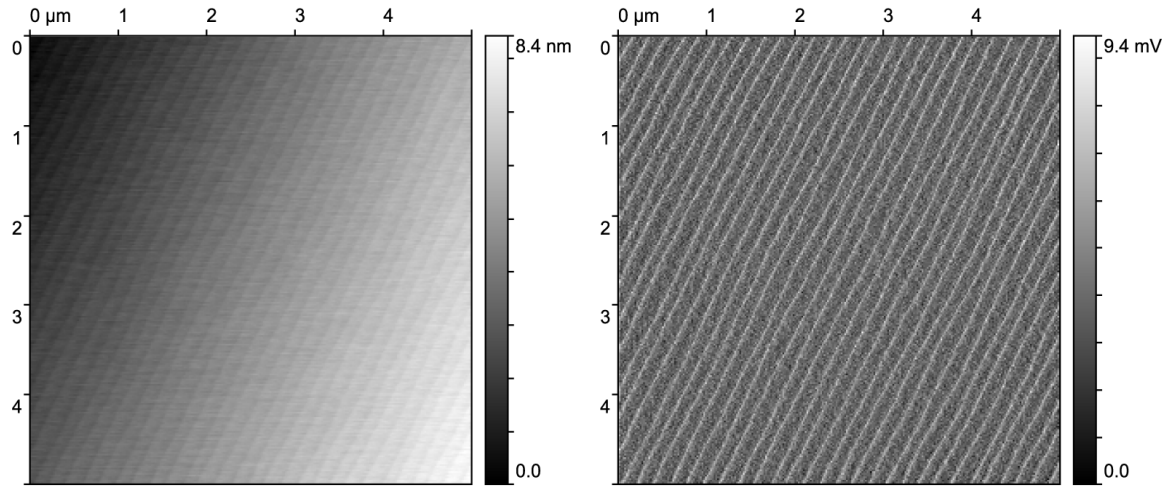

Figure A4.2. Atomic force microscopy topographic (left) and deflection (right) image of a corundum (001) single crystal surface after the full cleaning procedure, including UV ozone treatment.

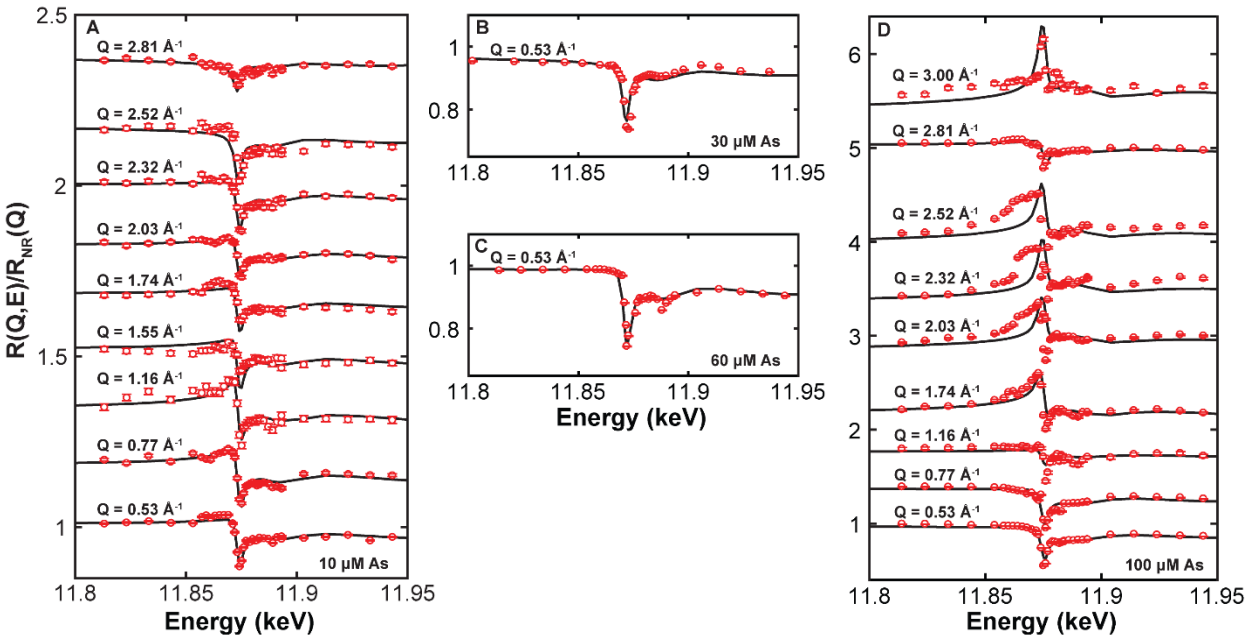

Figure A4.3. Arsenic K-edge RAXR spectra for arsenate adsorbed to corundum (001) in 0.01 M NaCl solution at pH 5 with 10 µM (A), 30 µM (B), 60 µM (C), and 100 µM (D) total arsenate concentration. Model-dependent (solid) fits to the data (circles) are shown. Spectra have been offset vertically for clarity.

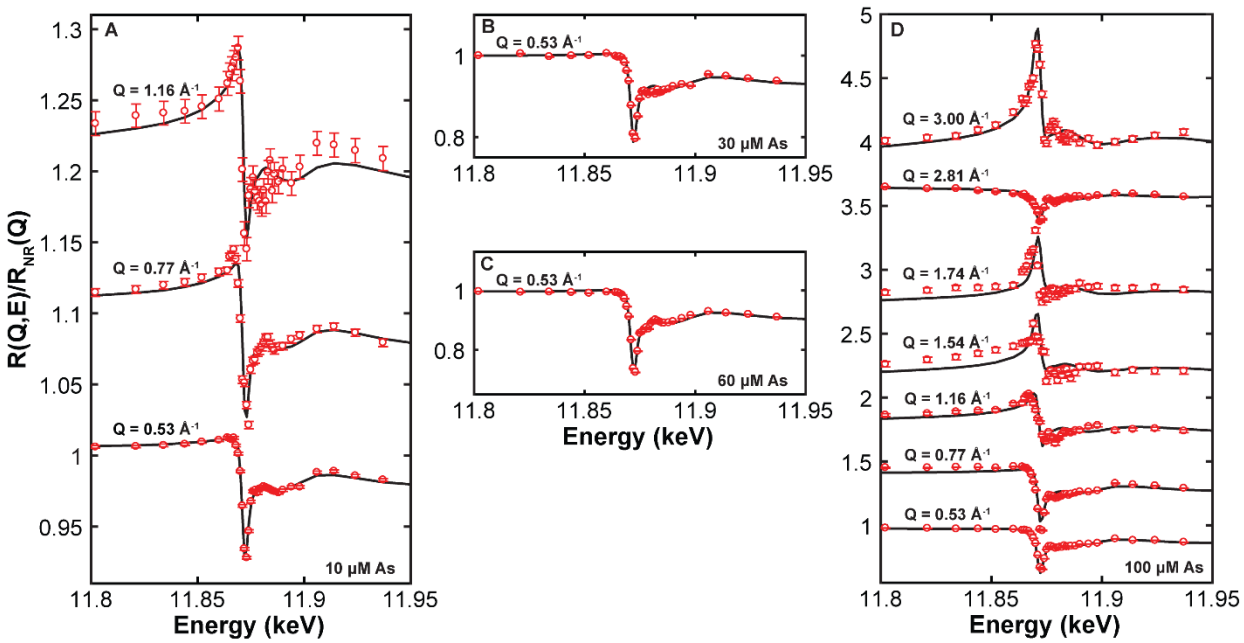

Figure A4.4. Arsenic K-edge RAXR spectra for arsenate adsorbed to corundum (001) in 0.01 M NaCl solution at pH 7 with 10 µM (A), 30 µM (B), 60 µM (C), and 100 Mm (D) total arsenate concentration. Model-dependent (solid) fits to the data (circles) are shown. Spectra have been offset vertically for clarity.

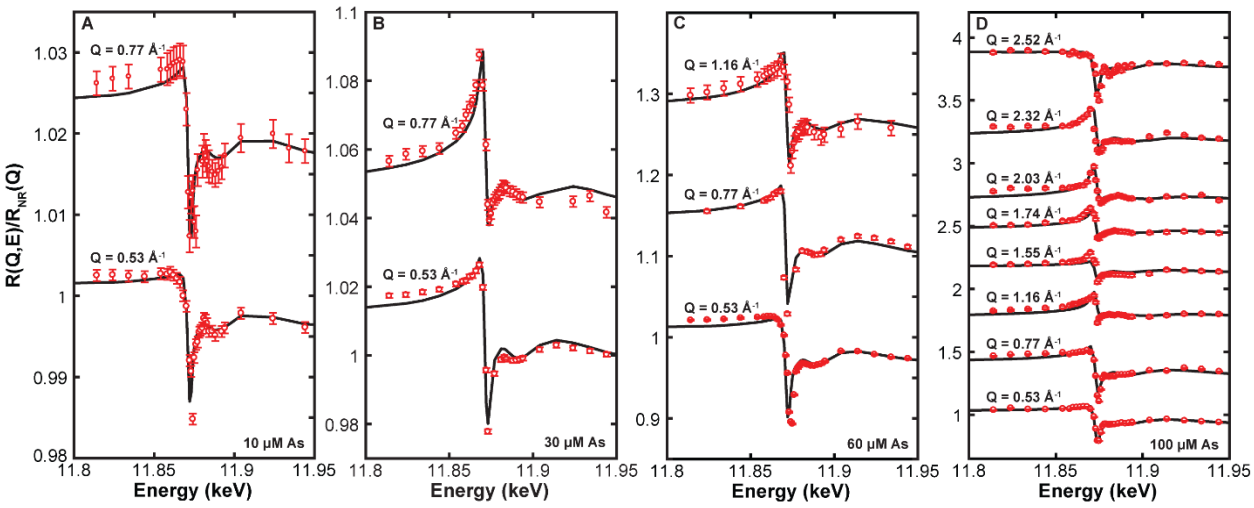

Figure A4.5. Arsenic K-edge RAXR spectra for arsenate adsorbed to corundum (001) in 0.01 M NaCl solution at pH 9 with 10 µM (A), 30 µM (B), 60 µM (C), and 100 Mm (D) total arsenate concentration. Model-dependent (solid) fits to the data (circles) are shown. Spectra have been offset vertically for clarity.

4.8 REFERENCES

Al-Abadleh, H.A. and Grassian, V.H. (2003) Oxide surfaces as environmental interfaces. *Surf. Sci. Rep.* **52**, 63-161.

Arai, Y., Elzinga, E.J. and Sparks, D.L. (2001) X-ray absorption spectroscopic investigation of arsenite and arsenate adsorption at the aluminum oxide-water interface. *J. Colloid Interface Sci.* **235**, 80-88.

Argyris, D., Ho, T.A., Cole, D.R. and Striolo, A. (2011) Molecular dynamics studies of interfacial water at the alumina surface. *J. Phys. Chem. C* **115**, 2038-2046.

Benning, L.G. and Waychunas, G.A. (2008) Nucleation, Growth, and Aggregation of Mineral Phases: Mechanisms and Kinetic, in: Brantley, S.L., Kubichi, J.D., White, A.F. (Eds.), *Kinetics of Water-Rock Interaction*. Springer, Newyork, pp. 259-333.

Björneholm, O., Hansen, M.H., Hodgson, A., Liu, L.-M., Limmer, D.T., Michaelides, A., Pedevilla, P., Rossmeisl, J., Shen, H., Tocci, G., Tyrode, E., Walz, M.-M., Werner, J. and Buhm, H. (2016) Water at interfaces. *Chem. Rev.* **116**, 7698-7726.

Boily, J.F., Chatman, S. and Rosso, K.M. (2011) Inner-Helmholtz potential development at the hematite (α-Fe_2O_3) (001) surface. *Geochim. Cosmochim. Acta* **75**, 4113-4124.

Braunschweig, B., Eissner, S. and Daum, W. (2008) Molecular structure of a mineral/water interface: Effects of surface nanoroughness of α-Al_2O_3 (0001). *J. Phys. Chem. C* **112**, 1751-1754.

Brese, N.E. and O'Keeffe, M. (1991) Bond-valence parameters for solids. *Acta Crystallographica Section B* **47**, 192-197.

Brown, G.E., Henrich, V.E., Casey, W.H., Clark, D.L., Eggleston, C., Felmy, A., Goodman, D.W., Gratzel, M., Maciel, G., McCarthy, M.I., Nealson, K.H., Sverjensky, D.A., Toney, M.F. and Zachara, J.M. (1999) Metal oxide surfaces and their interactions with aqueous solutions and microbial organisms. *Chem. Rev.* **99**, 77-174.

Brown, G.E. and Parks, G.A. (2001) Sorption of trace elements on mineral surfaces: Modern perspectives from spectroscopic studies, and comments on sorption in the marine environment. *Int. Geol. Rev.* **43**, 963-1073.

Catalano, J.G. (2010) Relaxations and interfacial water ordering at the corundum (110) surface. *J. Phys. Chem. C* **114**, 6624-6630.

Catalano, J.G. (2011) Weak interfacial water ordering on isostructural hematite and corundum (001) surfaces. *Geochim. Cosmochim. Acta* **75**, 2062-2071.

Catalano, J.G., Fenter, P. and Park, C. (2007) Interfacial water structure on the (012) surface of hematite: Ordering and reactivity in comparison with corundum. *Geochim. Cosmochim. Acta* **71**, 5313-5324.

Catalano, J.G., Fenter, P. and Park, C. (2009) Water ordering and surface relaxations at the hematite (110)–water interface. *Geochim. Cosmochim. Acta* **73**, 2242-2251.

Catalano, J.G., Park, C., Fenter, P. and Zhang, Z. (2008) Simultaneous inner- and outer-sphere arsenate complexation on corundum and hematite. *Geochim. Cosmochim. Acta* **72**, 1986-2004.

Catalano, J.G., Park, C., Zhang, Z. and Fenter, P. (2006) Termination and water adsorption at the α-Al_2O_3 (012)-aqueous solution interface. *Langmuir* **22**, 4668-4673.

Chatman, S., Zarzycki, P. and Rosso, K.M. (2013) Surface potentials of (001), (012), (113) hematite (α-Fe_2O_3) crystal faces in aqueous solution. *Phys. Chem. Chem. Phys.* **15**, 13911-13921.

Cheng, L., Fenter, P., Nagy, K.L., Schlegel, M.L. and Sturchio, N.C. (2001) Molecular-scale density oscillations in water adjacent to a mica surface. *Phys. Rev. Lett.* **87**, 156103.

Chorover, J. and Brusseau, M.L. (2008) Kinetics of Sorption–Desorption: Mechanisms and Kinetic, in: Brantley, S.L., Kubichi, J.D., White, A.F. (Eds.), *Kinetics of Water-Rock Interaction*. Springer, Newyork, pp. 109-149.

Cross, J.O., Newville, M., Rehr, J.J., Sorensen, L.B., Bouldin, C.E., Watson, G., Gouder, T., Lander, G.H. and Bell, M.I. (1998) Inclusion of local structure effects in theoretical X-ray resonant scattering amplitudes using ab initio X-ray-absorption spectra calculations. *Phys. Rev. B* **58**, 11215-11225.

Dixit, S. and Hering, J.G. (2003) Comparison of arsenic(V) and arsenic(III) sorption onto iron oxide minerals: implications for arsenic mobility. *Environ. Sci. Technol.* **37**, 4182-2189.

Eikenberry, E.F., Brönnimann, C., Hülsen, G., Toyokawa, H., Horisberger, R., Schmitt, B., Schulze-Briese, C. and Tomizaki, T. (2003) PILATUS: a two-dimensional X-ray detector for macromolecular crystallography. *Nucl. Instrum. Methods Phys. Res., Sect. A* **501**, 260-266.

Eng, P.J., Trainor, T.P., Brown, G.E., Waychunas, G.A., Newville, M., Sutton, S. and River, M.L. (2000) Structure of the hydrated α-Al_2O_3 (0001) surface. *Science* **288**, 1029-1033.

Fenter, P. (2002) X-ray reflectivity as a probe of mineral-fluid interfaces: a user guide. *Rev. Mineral. Geochem.* **49**, 149-220.

Fenter, P., Park, C., Nagy, K.L. and Sturchio, N.C. (2007) Resonant anomalous X-ray reflectivity as a probe of ion adsorption at solid-liquid interfaces. *Thin Solid Films* **515**, 5654-5659.

Fitts, J.P., Shang, X.M., Flynn, G.W., Heinz, T.F. and Eisenthal, K.B. (2005) Electrostatic surface charge at aqueous/α-Al_2O_3 single-crystal interfaces as probed by optical second-harmonic generation. *J. Phys. Chem. B* **109**, 7981-7986.

Flörsheimer, M., Kruse, K., Polly, R., Abdelmonem, A., Schimmelpfennig, B., Klenze, R. and Fanghänel, T. (2008) Hydration of mineral surfaces probed at the molecular level. *Langmuir* **34**, 13434-13439.

Foster, A.L., Brown, G.E., Tingle, T.N. and Parks, G.A. (1998) Quantitative arsenic speciation in mine tailings using X-ray absorption spectroscopy. *Am. Mineral.* **83**, 553-568.

Fukushi, K. and Sverjensky, D.A. (2007) A predictive model (ETLM) for arsenate adsorption and surface speciation on oxides consistent with spectroscopic and theoretical molecular evidence. *Geochim. Cosmochim. Acta* **71**, 3717-3745.

Gaigeot, M.P., Sprik, M. and Sulpizi, M. (2012) Oxide/water interfaces: How the surface chemistry modifies interfacial water properties. *J. Phys.: Condens. Matter* **24**, 11.

Goldberg, S. (1986) Chemical modeling of arsenate adsorption on aluminum and iron oxide minerals. *Soil Sci. Soc. Am. J.* **50**, 1154-1157.

Hamm, L.M., Bourg, I.C., Wallace, A.F. and Rotenberg, B. (2013) Molecular simulation of CO_2- and CO_3-brine-mineral systems. *Rev. Miner. Geochem.* **77**, 189-228.

Harrison, W.T.A. (2000) Synthetic mansfieldite, $AlAsO_4 \cdot 2H_2O$. *Acta Cryst.* **56**, 421.

Hass, K.C. and Schneider, W.F. (2000) First-principles molecular dynamics simulations of H_2O on α-Al_2O_3 (0001). *J. Phys. Chem. B* **104**, 5527-5540.

Hass, K.C., Schneider, W.F., Curioni, A. and Andreoni, W. (1998) The chemistry of water on alumina surfaces: Reaction dynamics from first principles. *Science* **282**, 265-268.

Hiemstra, T., Dewit, J.C.M, and Van Riemsdijk, W.H. (1989a) Multisite proton adsorption modeling at the solid/solution interface of (hydr)oxides: A new approach: II. Application to various important (hydr)oxides. *J. Colloid Interface Sci.* **133**, 105-117.

Hiemstra, T., Van Riemsdijk, W.H., and Bolt, G.H. (1989b) Multisite proton adsorption modeling at the solid/solution interface of (hydr)oxides: A new approach: I. Model description and evaluation of intrinsic reaction constant. *J. Colloid Interface Sci.* **133**, 91-104.

Hiemstra, T. and Van Riemsdijk, W.H. (1996) A surface structural approach to ion adsorption: the charge distribution (CD) model. *J. Colloid Interface Sci.* **179**, 488-508.

Hiemstra, T. and Van Riemsdijk, W.H. (1999) Surface structural ion adsorption modeling of competitive binding of oxyanions by metal (hydr)oxides. *J. Colloid Interface Sci.* **210**, 182-193.

Hiemstra, T., Venema, P. and Van Riemsdijk, W.H. (1996) Intrinsic proton affinity of reactive surface groups of metal (hydr)oxides: The bond valence principle. *J. Colloid Interface Sci.* **184**, 680-692.

Hiemstra, T., Yong, H. and Van Riemsdijk, W.H. (1999) Interfacial charging phenomena of aluminum (hydr)oxides. *Langmuir* **15**, 5942-5955.

Huang, P., Pham, T.A., Galli, G. and Schwegler, E. (2014) Alumina (0001)/water interface: Structural properties and infrared spectra from first-principles molecular dynamics simulations. *J. Phys. Chem. C* **118**, 8944-8951.

Jain, C.K. and Ali, I. (2000) Arsenic: occurrence, toxicity and speciation techniques. *Water Res.* **34**, 4304-4312.

Kappen, P. and Webb, J. (2013) An EXAFS study of arsenic bonding on amorphous aluminum hydroxide. *Appl. Geochem.* **31**, 79-83.

Kaszuba, J., Yardley, B. and Andreani, M. (2013) Experimental perspectives of mineral dissolution and precipitation due to carbon dioxide-water-rock interactions. *Rev. Miner. Geochem.* **77**, 153-188.

Kerisit, S. (2011) Water structure at hematite-water interfaces. *Geochim. Cosmochim. Acta* **75**, 2043-2061.

Kershner, R.J., Bullard, J.W. and Cima, M.J. (2004) Zeta potential orientation dependence of sapphire substrates. *Langmuir* **20**, 4101-4108.

Kirfel, A. and Eichhorn, K. (1990) Accurate structure analysis with synchrotron radiation. The electron density in Al_2O_3 and Cu_2O. *Acta Crystallogr. A* **46**, 271-284.

Ladeira, A.C.Q., Ciminelli, V.S.T., Duarte, H.A., Alives, M.C.M. and Ramos, A.Y. (2001) Mechanism of anion retention from EXAFS and density functional calculations: Arsenic(V) adsorbed on gibbsite. *Geochim. Cosmochim. Acta* **65**, 1211-1217.

Lützenkirchen, J. (2013) Specific ion effects at two single-crystal planes of sapphire. *Langmuir* **29**, 7726-7734.

Lützenkirchen, J., Abdelmonem, A., Weerasooriya, R., Heberling, F., Metz, V. and Marsac, R. (2014) Adsorption of dissolved aluminum on sapphire-c and kaolinite: implications for points of zero charge of clay minerals. *Geochemical Transactions* **15**, 9.

Lützenkirchen, J., Franks, G.V., Plaschke, M., Zimmermann, R., Herberling, F., Abdelmonem, A., Darbha, G., Schild, D., Filby, A., Eng, P.J., Catalano, J.G., Rosenqvist, J., Preocanin, T., Aytug, T., Zhang, D., Gan, Y. and Braunschweig, B. (2018) The surface chemistry of sapphire-c: A literature review and a study on various factors influencing its IEP. *Adv. Colloid Interface Sci.* **251**, 1-25.

Lützenkirchen, J., Heberling, F., Supljika, F., Preocanin, T., Kallay, N., Johann, F., Weisser, L. and Eng, P.J. (2015) Structure-charge relationship-the case of hematite (001). *Farady Discuss* **180**, 55-79.

Lützenkirchen, J., Zimmermann, R., Preocanin, T., Filby, A., Kupcik, T., Küttner, D., Abdelmonem, A., Schild, D., Rabung, T., Plaschke, M., Brandenstein, F., Werner, C. and Geckeis, H. (2010) An attempt to explain bimodal behaviour of the sapphire c-plane electrolyte interface. *Adv. Colloid Interface Sci.* **157**, 61-74.

Ma, S.Y., Liu, L.M. and Wang, S.Q. (2016) Water film adsorbed on the α-Al_2O_3(0001) surface: Structural properties and fynamical behaviors from first-principles molecular dynamics simulations. *J. Phys. Chem. C* **120**, 5398-5409.

NIST X-ray Photoelectron Spectroscopy Database, NIST Standard Reference Database Number 20, National Institute of Standards and Technology, Gaithersburg MD, 20899 (2000), doi:10.18434/T4T88K, (retrieved 26 June 2018).

McBriarty, M.E., von Rudorff, G.F., Stubbs, J.E., Eng, P.J., Blumberger, J. and Rosso, K.M. (2017) Dynamic stabilization of metal oxide-water interfaces. *J. Am. Chem. Soc.* **139**, 2581-2584.

Nordstrom, D.K. and Archer, D.G. (2003) Arsenic thermodynamic data and environmental geochemistry, in: Welch, A.H., Stollenwerk, K.G. (Eds.), *Arsenic in Ground Water: Geochemistry and Occurrence*. Kluwer Academic Publishers, Dordrecht.

Park, C. and Fenter, P. (2007) Phasing of resonant anomalous X-ray reflectivity spectra and direct fourier synthesis of elementspecific partial structures at buried interfaces. *J. Appl. Crystallogr.* **40**, 290-301.

Park, C., Fenter, P., Sturchio, N.C. and Regalbuto, J.R. (2005) Probing outer-sphere adsorption of aqueous metal complexes at the oxide-water interface with resonant anomalous X-Ray reflectivity. *Phys. Rev. Lett.*, 076104.

Robinson, I.K. (1986) Crystal truncation rods and surface roughness. *Phys. Rev. B* **33**, 3830-3836.

Rubasinghegea, G. and Grassian, V. (2013) Role(s) of adsorbed water in the surface chemistry of environmental interfaces. *Chem. Commun.* **49**, 3071-3094.

Rustad, J.R., Wasserman, E. and Felmy, A.R. (1999) Molecular modeling of the surface charging of hematite II. Optimal proton distribution and simulation of surface charge versus pH relationships *Surf. Sci.* **424**, 28-35.

Rabung T, Schild D, Geckeis H, Klenze R, and Fanghanel, T. (2004) Cm(III) sorption onto sapphire (α-Al_2O_3) single crystals. *J. Phys. Chem. B.* **108**, 17160-17165.

Schlegel, M.L., Nagy, K.L., Fenter, P., Cheng, L., Sturchio, N.C. and Jacobsen, S.D. (2006) Cation sorption on the muscovite (001) surface in chloride solutions using high-resolution X-ray reflectivity. *Geochim. Cosmochim. Acta* **70**, 3549-3565.

Smedley, P.L. and Kinniburgh, D.G. (2002) A review of the source, behavior and distribution of arsenic in natural waters. *Appl. Geochem.* **17**, 517-568.

Sung, J., Shen, Y.R. and Waychunas, G.A. (2012) The interfacial structure of water/protonated α-Al_2O_3 (11-20) as a function of pH. *Condens. Matter* **24**, 124101.

Sung, J., Zhang, L.N., Tian, C.S., Shen, Y.R. and Waychunas, G.A. (2011) Effect of pH on the water/α-Al_2O_3 (1-102) interface structure studied by sum-frequency vibrational spectroscopy. *J. Phys. Chem. C* **115**, 13887-13893.

Tong, Y., Wirth, J., Kirsch, H., Wolf, M., Saalfrank, P. and Campen, P.K. (2015) Optically probing Al-O and O-H vibrations to characterize water adsorption and surface reconstruction on α-alumina: An experimental and theoretical study. *J. Chem. Phys.* **142**, 054704.

Trainor, T.P., Eng, P.J., Brown, G.E., Robinson, I.K. and De Santis, M. (2002) Crystal truncation rod diffraction study of the α-Al_2O_3 (1-102) surface. *Surf. Sci.* **496**, 238-250.

Tuladhar, A., Dewan, S., Kubicki, J.D. and Borguet, E. (2016) Spectroscopy and ultrafast vibrational dynamics of strongly hydrogen bonded OH species at the α-Al_2O_3(11-20)/H_2O interface. *J. Phys. Chem. C* **120**, 16153-16161.

Tuladhar, A., Piontek, S. and Borguet, E. (2017) Insights on interfacial structure, dynamics, and proton transfer from ultrafast vibrational sum frequency generation spectroscopy of the alumina(0001)/water interface. *J. Phys. Chem. C* **121**, 5168-5177.

Xu, T. and Catalano, J.G. (2016) Impacts of surface site coordination on arsenate adsorption: Macroscopic uptake and binding mechanisms on aluminum hydroxide surfaces. *Langmuir* **32**, 13261-13269.

Xu, T. and Catalano, J.G. (2018) Effect of ionic strength on arsenate adsorption at aluminum hydroxide-water interface. *Soil. Syst.* **2**, 1.

Xu, Y., Zhou, G.-P. and Zheng, X.-F. (2007) Redetermination of iron(III) arsenate dihydrate. *Acta Crystallographica Section E* **63**, i67-i69.

Yanina, S.V. and Rosso, K.M. (2008) Linked reactivity at mineral-water interfaces through bulk crystal conduction. *Science* **320**, 218-222.

Zhang, L., Tian, C., Waychunas, G.A. and Shen, Y.R. (2008) Structures and charging of α-alumina (0001)/water interfaces studied by sum-frenqueny vibrational spectroscopy. *J. Am. Chem. Soc.* **130**, 7686-7694.

CHAPTER 5

COMPARATIVE RESPONSE OF INTERFACIAL WATER TO PH VARIATIONS AND ARSENATE ADSORPTION ON CORUNDUM (012) AND (001) SURFACES

To be submitted to *Geochimica et Cosmochimica Acta* as:
Xu, T., Stubbs, J.E., Eng, P.J., and Catalano, J.G. (2018) Comparative response of interfacial water to pH variations and arsenate adsorption on corundum (012) and (001) surfaces.

5.1 ABSTRACT

The atomic-scale structure of the interface between metal oxide minerals and aqueous solutions regulates chemical reactions that are fundamental to many geological and environmental processes. Reactions occur at surface sites having multiple possible coordination states, each of which display distinct pH-dependent charging behavior that affects interactions with adsorbates and interfacial water. Our previous work has shown that corundum (001) surfaces induce weak spatial ordering of interfacial water that varies little between pH 5 and 9 but is substantially altered by the adsorption of arsenate. The (001) surface is dominated by doubly coordinated functional groups that are largely uncharged over the pH range examined, but other surfaces have functional groups in different coordination states with distinct charging behavior. Corundum (012) surfaces are known to induce stronger interfacial water ordering than (001) surfaces, but how this is affected by pH changes or ion adsorption has not been investigated. In this study, surface X-ray scattering measurements have been used to determine the response of interfacial water structure on corundum (012) surfaces to pH variations and the surface coverage of adsorbed arsenate. Comparison of interfacial water properties on (012) surfaces to those observed for (001) surfaces is then used to systematically investigate how surface site coordination state affects ion adsorption mechanisms, interfacial water structure, and the feedback between them. In the absence of arsenate, interfacial water displays little variation in its arrangement near the (012) surface between pH 5 and 9. This general invariance is also observed for the (001) surface, suggesting that over the pH range of most natural waters, surface site protonation-deprotonation appears inadequate to induce extensive restructuring of interfacial water. The adsorption of arsenate weakly perturbs interfacial water structure near the (012) surface, with both the spatial arrangement and ordering of the adsorbed water sites independent

of arsenate surface coverage, in contrast to the substantial restructuring of interfacial water near the (001) surface. This suggest that on surfaces with initially weak water ordering [i.e., corundum (001) surfaces], the addition of a charged adsorbate species may induce water restructuring, but on surfaces with initially strong water ordering [i.e., corundum (012) surfaces], water structure is generally unperturbed. As arsenate forms coexisting inner- and outer-sphere complexes on both surfaces, adsorption mechanisms do not appear to control the resulting restructuring of interfacial water. Instead, the different surface functional groups present on the (012) and (001) surfaces, with their distinct charging behaviors, likely drive the response of interfacial water to arsenate adsorption. These observations suggest that on surfaces where water restructures upon ion adsorption, the dielectric constant, capacitances, and electrostatic activity corrections will all differ from the pristine surface. In contrast, on surfaces where water structure is unaltered by ion adsorption these parameters will be unperturbed. This should be considered during future refinements of surface complexation models to better predict adsorption behavior at environmental interfaces.

5.2 INTRODUCTION

Ion adsorption is of central importance to chemical reactions at mineral-water interfaces because it directly controls the mobility of contaminants and nutrients in soils and aquatic systems (Brown and Parks, 2001; Chorover et al., 2007), promotes the nucleation and growth of minerals (Benning and Waychunas, 2008), initiates surface redox reactions (Amstaetter et al., 2010; Boland et al., 2011; Elsner et al., 2004), and plays a role in microbial or ligand-promoted dissolution of metal oxide minerals (Kraemer, 2004, 2005; Rechard et al., 2007; Shi et al., 2013). Reactions on metal oxide mineral surfaces involve functional groups having multiple possible coordination states with distinct pH-dependent charging behaviors (Hiemstra and Van Riemsdijk, 1996; Hiemstra et al., 1989; Hiemstra et al., 1996; Venema et al., 1998). These sites interact with both adsorbates, (e.g., Brown et al., 1999; Brown and Parks, 2001) and interfacial water molecules, (e.g., Al-Abadleh and Grassian, 2003; Hass et al., 1998; Hiemstra and Van Riemsdijk, 2006; Thomas and Richardson, 2008). A molecular-level understanding of how water interacts with mineral surfaces in the presence and absence of adsorbates is thus crucial to providing insight into fundamental controls of adsorption processes.

Previous theoretical and experimental approaches have found that in pure water, the structure of interfacial water near metal oxide single crystal surfaces is directly controlled by the mineral surface structure (Argyris et al., 2011; Catalano, 2010; Catalano, 2011; Catalano et al., 2007, 2009; Catalano et al., 2006; Flörsheimer et al., 2008; Gaigeot et al., 2012; Hass et al., 1998; Huang et al., 2014; Kerisit, 2011; Ma et al., 2016; Sung et al., 2012; Sung et al., 2011; Tuladhar et al., 2016; Tuladhar et al., 2017; Zhang et al., 2008). Surfaces like corundum and hematite basal planes dominated by neutrally charged surface sites (i.e., doubly coordinated functional groups) over a wide pH range (Boily et al., 2011; Chatman et al., 2013; Hiemstra et

al., 1996; Hiemstra et al., 1999; Lützenkirchen, 2013; Lützenkirchen et al., 2015; Lützenkirchen et al., 2010) induce weak ordering of interfacial water (Catalano, 2011; Tuladhar et al., 2017). In contrast, surfaces like non-basal planes of corundum and hematite have singly and triply coordinated functional groups that are always charged even when the net surface charge is zero (Chatman et al., 2013; Hiemstra et al., 1996; Hiemstra et al., 1999; Lützenkirchen, 2013; Rustad et al., 1999), and induce strong ordering of interfacial water (Catalano, 2010; Catalano et al., 2007, 2009; Catalano et al., 2006; McBriarty et al., 2017; Tuladhar et al., 2016). The structure of interfacial water on these surfaces is thus correlated with surface site charge states.

Our recent work has shown that on corundum (001) surfaces, weakly ordered interfacial water is largely unaffected by pH variations but is substantially restructured by the adsorption of arsenate (Chapter 4). However, the response of interfacial water structure to chemical conditions, especially to varying pH and adsorbate concentrations, may differ on surfaces having charging behavior distinct from (001) surfaces. The corundum (012) surface is an ideal substrate for such a comparison because it is terminated in singly and triply coordinated functional groups that are always charged with their pK_a values within the pH range for most natural waters. Thus, a different response of interfacial water structure to pH changes and adsorbate surface coverages is expected on corundum (012) than on (001) surfaces. In addition, the surface and interfacial water structures at the pristine corundum (012)-water interface have been determined previously (Catalano et al., 2006), and arsenate adsorption mechanisms at pH 5 have also been established (Catalano et al., 2008). This prior work can thus serve as a structural basis for investigating the effects of pH and arsenate adsorption on interfacial water structure on this surface.

In this study, surface X-ray scattering measurements were performed on corundum (012) surfaces in the absence and presence of arsenate over a range of pH conditions to determine the

response of interfacial water structure to protonation-deprotonation of surface sites and ion adsorption. In situ non-resonant X-ray reflectivity (XR) measurements on corundum (012) surfaces at pH 5, 7, and 9 in 0.01 M NaCl solutions were applied to investigate the effect of pH on interfacial water structure. Under similar experimental conditions, resonant anomalous X-ray reflectivity (RAXR) analyses were used to determine the arsenic distribution (i.e., surface coverage and location) as a function of increasing total arsenate concentrations. This was then combined with XR measurements to isolate the interfacial water structure. These results were then compared to water properties previously observed on the corundum (001) surface to gain a systematic understanding of the fundamental controls on water structure at corundum-water interfaces.

5.3 MATERIALS AND METHODS

5.3.1 Sample Preparation

Synthetic corundum single crystals (10 × 10 × 0.5 mm) oriented, cut, and polished to expose the (012) surface, were purchased from MTI Corporation (Richmond, CA, USA). The crystals were cleaned prior to each experiment following previously described procedures (Catalano, 2011; Catalano et al., 2006). This included four cycles of alternating rinses with acetone (HPLC-grade), methanol (HPLC-grade), and deionized water (>18.2 MΩ·cm), followed by an overnight soak in 2% HF, multiple rinses with deionized water, an acid wash (0.1 M Trace metal grade HCl), further repeated deionized water rinses, and then drying in a flow of ultrahigh purity N_2 gas. After cleaning, the crystals were annealed at 1000 °C for 24 h and after cooling were soaked in 0.1 M HCl for 1 h. Following this final acid step, the crystals were thoroughly rinsed with deionized water, dried with compressed N_2 gas, and annealed at 450 °C for 12 h.

After cooling to room temperature, the crystals were stored dry in a sectioned polypropylene box lined with lint-free cloths for transport to the Advanced Photon Source (APS). At the APS, the crystals underwent a 0.5 h Ultraviolet-Ozone surface treatment (BioForce UV/Ozone ProCleaner) to remove hydrocarbons accumulated during transport and then stored in deionized water in PTFE jars until data collection. Reaction solutions containing 0, 10, 30, 60, or 100 μM $Na_2HAsO_4 \cdot 7H_2O$ in 0.01 M NaCl were prepared at pH 5, 7, and 9 from reagent grade chemicals and deionized water. The pH of each solution was adjusted using NaOH or HCl. One corundum (012) crystal was used for all XR and RAXR measurements at an individual pH condition.

5.3.2 XR and RAXR Measurements and Analysis

Data Collection

Reflectivity data were collected following similar procedures to those described previously (Chapter 4). These experiments were designed to collect two complimentary sets of data, with XR determining the total electron density (Fenter, 2002) and RAXR determining the arsenic specific electron density (Fenter et al., 2007). For samples reacting with pure NaCl solutions, only XR data were collected; for samples reacting with arsenate solutions, both XR and RAXR data were collected. Each sample was prepared by placing a clean corundum (012) crystal into a thin-film geometry sample cell (Fenter, 2002) in deionized water and sealed with Kapton film. At each pH, the sample was initially reacted with 0.01 M NaCl for about 1 h by flushing the solution into the sample cell. The fluid was exchanged repeatedly to stabilize the system during the reaction period. Then excess solution was drained from the sample cell to minimize the amount of solution on the crystal surface and achieve a uniform fluid film thickness above the surface. The sample cell was mounted on the diffractometer and the crystal

was aligned to the surface normal direction for data collection. After measurements, each sample was reacted with an arsenate solution of the same pH. The As-bearing solutions were injected sequentially from lowest to highest arsenate concentrations, with XR and RAXR data collected at each concentration.

All XR and RAXR experiments were performed in situ at the GeoSoilEnviroCARS beamline 13-ID-C at the APS at Argonne National Laboratory. Measurements were made using a Newport Kappa six (4+2)-circle diffractometer. The incident X-ray beam energy was selected by a Si (111) double-crystal monochromator. The beam was collimated by a pair of Rh-coated Kirkpatrick-Baez-type Si mirrors, with slits defining beam size to 0.1 mm × 1.0 mm (horizontal × vertical). The reflected X-ray beam intensity was measured using a Dectris PILATUS 100K pixel array detector (Eikenberry et al., 2003). XR data were measured in the specular geometry as a function of vertical momentum transfer Q (0.2 - 5.6 $Å^{-1}$) at a fixed incident X-ray energy (E = 16.0 keV) well separated from arsenic K-edge (11.87 keV). The spatial resolutions (π/Q_{max}, where Q_{max} is the maximum Q value measured) of the datasets were 0.56 Å (Fenter, 2002). RAXR data were collected by measuring the reflected X-ray intensity as a function of energy near the arsenic K-edge (±0.4 keV) at a series of fixed Q values. For the analysis of arsenic distribution at each experimental condition, RAXR spectra were collected at a series of Q values from 0.45 up to 4.06 $Å^{-1}$ for samples reacted with 10, 30, and 100 μM total arsenate solutions at pH 5; 10, 100 μM total arsenate solutions at pH 7, and 100 μM total arsenate solutions at pH 9. RAXR spectra at Q = 0.45 and 0.63 $Å^{-1}$ were measured for samples reacted with 30 and 10 μM total arsenate solution at pH 7 and 9, respectively. RAXR spectra at Q = 0.45, 0.63, and 0.81 $Å^{-1}$ were measured for all other conditions. For both XR and RAXR measurements, system stability was monitored by collecting data at reference Q values periodically, which yielded an estimated

systematic uncertainty of ~1.8%. This was added in quadrature to the measurement uncertainty to obtain the final uncertainty for each data point.

XR and RAXR Analysis

All XR data were analyzed following previously described procedures (Catalano et al., 2008; Catalano et al., 2006; Fenter, 2002). Each dataset was fit with a structural model consisting of the bulk structure of corundum, the interfacial region including the relaxed corundum (012) surface and the surface adsorbed species (i.e., arsenate and adsorbed water layers in this study), and the water above the interfacial region. In addition, the fit was coupled with sample specific extrinsic parameters including water film thickness (Fenter, 2002), surface roughness (Robinson, 1986), an alternate roughness model using only a single partial layer (Catalano et al., 2008), and an intensity scale factor to account for imperfect normalization of the data to the incident X-ray flux. The structural model used in this study was based on the structure of corundum (012)-water interfaces determined in a previous study (Catalano et al., 2006) with the surface terminated by two different kinds of oxygen sites bonded to one and three underlying aluminum atoms with a ratio of 1:1 (Figure 5.1). This model allowed for atom relaxations in the top three layers of the corundum structure and included two sites of adsorbed water and a layered water model to describe extended ordering through the transition to bulk water (Cheng et al., 2001; Schlegel et al., 2006). The bulk crystal structure and vibrational amplitudes were taken from previously published data (Kirfel and Eichhorn, 1990). A (012) spacing of 3.481 Å (Catalano et al., 2006) and a surface unit cell area of 24.39 $Å^2$ (Trainor et al., 2002) were used from previous studies. To reduce parameter correlations, the occupancies of the surface aluminum sites and the surface oxygen sites (i.e., triply and singly coordinated functional groups) were fixed to 2 during the analysis. The occupancy of the terminal, singly coordinated oxygen site was initially varied in

the preliminary fit with full occupancies of 2.00 ± 0.06 obtained for most samples and was thus fixed to 2 during the final analysis. The adsorbed water was modeled by two water sites with the same vibrational amplitudes (Catalano et al., 2006) but different heights and occupancies; these parameters were allowed to vary during the fitting process.

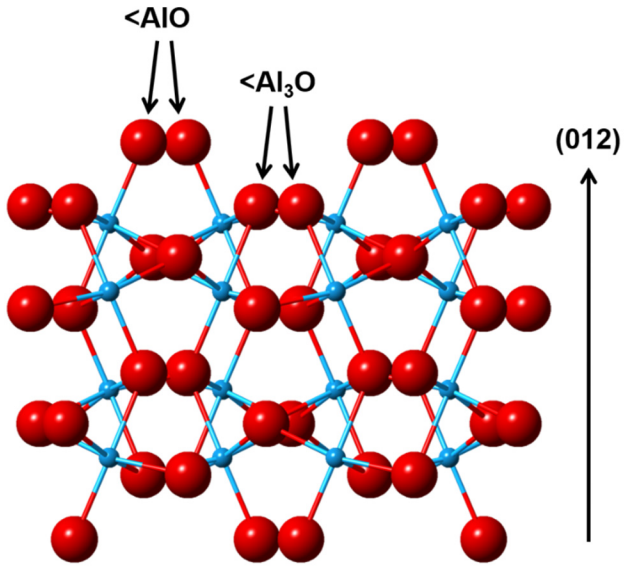

Figure 5.1. Structural model of the corundum (012) termination used in this study. The small and large spheres represent Al and O atoms, respectively. H atoms on surface sites are not included in the model. Also shown are the singly (<AlO) and triply (<Al3O) coordinated functional groups exposed on the (012) surface.

In this study, the RAXR data were analyzed using a fixed-arsenic model as described previously (Catalano et al., 2008). This model considered two adsorbed arsenic species, inner-sphere (IS) and outer-sphere (OS) arsenate complexes, to describe the arsenic density profile at the interface. The vibrational amplitudes for both IS and OS arsenic components were fixed to 0.35 and 0.53 Å, taken from Catalano et al. (2008). The detailed fitting strategy followed the procedure described in our previous study on corundum (001) surfaces (Chapter 4). Briefly, at each pH condition, the full distribution of IS and OS arsenic species were determined by varying

the height and occupancy in RAXR fitting to the sample reacted in 100 μM total arsenate solution where RAXR spectra over a full range of Q values were collected. Then the RAXR spectra of samples reacted with lower arsenate concentrations were fitted with fixed arsenic position and vibrational amplitudes, only allowing the surface coverage (i.e., occupancy) of each site to vary.

After determining the interfacial distribution profiles of arsenic, the corresponding XR data were refined with a structural model including arsenic positions, vibrational amplitudes, and occupancies obtained from the initial RAXR fitting. The resulting XR fits provided new non-resonant structure factors that were then input to refit the RAXR data. Iterations of the XR and RAXR analysis were performed until convergence was reached. All RAXR spectra and fits are reported in the Electronic Annex (Figure A5.1, A5.2, and A5.3). For both XR and RAXR analysis, a nonlinear least-squares algorithm was used to optimize the fitting parameters by minimizing the goodness-of-fit parameters $\chi_v{}^2$; both $\chi_v{}^2$ and an R-factor are reported (Geissbuhler et al., 2004). All fitting uncertainties were based on the standard deviations obtained from the least-squares fitting procedures and are reported at the 95% (2σ) confidence level.

5.4 RESULTS

5.4.1 Effects of pH on Interfacial Water Structure

Non-resonant XR measurements (Figure 5.2A) were performed at pH 5, 7, and 9 on corundum (012) surfaces in 0.01 M NaCl solutions. The optimized structure and resulting goodness-of-fit parameters are summarized in the Electronic Annex (Table A5.1, A5.2, and A5.3). XR datasets were well modeled ($\chi_v{}^2$ < 1.8 and R-factor < 0.04) using the previously-

identified corrugated surface structure terminated by equal proportions of singly and triply coordinated oxygen groups (Figure 5.1) (Catalano et al., 2006), with the surface atoms displaying only minor (< 0.1 Å) relaxations. XR data showed no systematic variations among pH 5, 7, and 9 (Figure 5.2A). The best-fit structural models had two adsorbed water sites whose positions did not vary with pH (Table A5.1, A5.2, and A5.3). The two adsorbed water sites had vibrational amplitudes of 0.12 ± 0.01 Å at pH 5, 0.12 ± 0.02 Å at pH 7, and 0.20 ± 0.01 Å at pH 9, consistent with the values obtained in the previous study (Catalano et al., 2006), indicating a strongly ordered interfacial water structure (Catalano, 2011). The XR data in the current study showed no substantial variations of interfacial water structure in terms of spatial arrangement (i.e., adsorbed water heights) and degree of ordering (i.e., vibrational amplitudes) over the pH range explored in NaCl solutions.

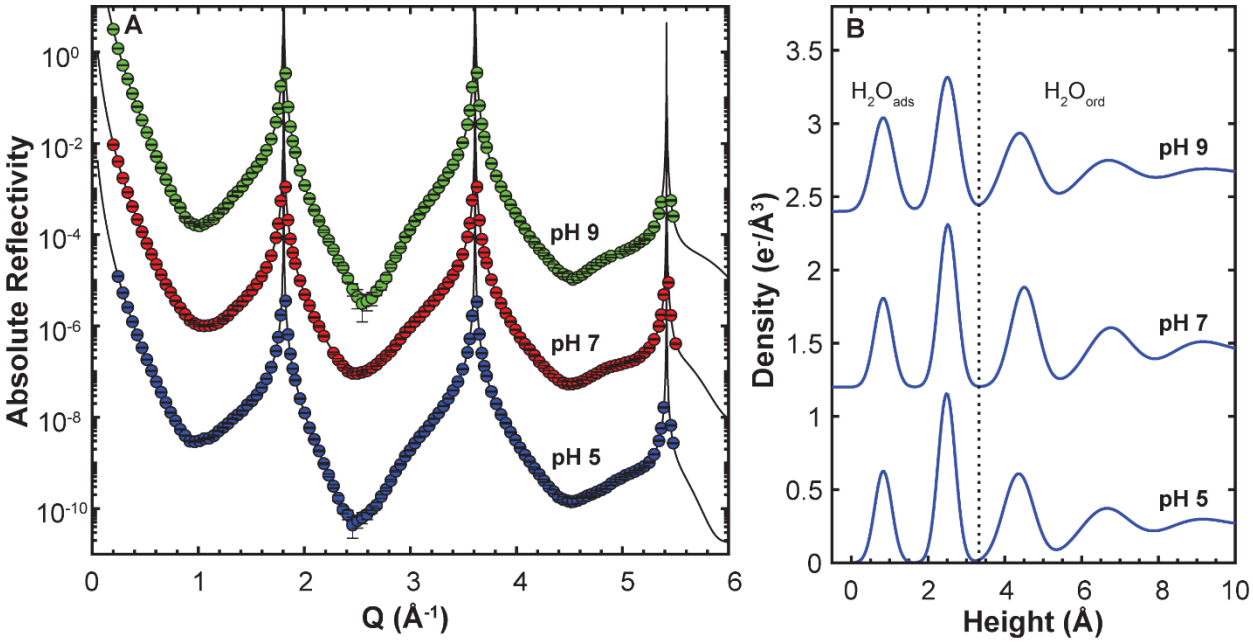

Figure 5.2. (A) Absolute X-ray reflectivity data (symbols) and calculated reflectivity from the best-fit model (lines) at corundum (012)-water interface in 0.01 M NaCl at pH 5, 7, and 9. (B) Resulting interfacial water electron density profiles above the corundum (012) surfaces. H_2O_{ads} and H_2O_{ord} represent the adsorbed water and extended ordered water (as modeled by a layered water profile), respectively. The black dotted line delineates the approximated boundary between the adsorbed and extended ordered water. Each plot is offset vertically for clarity.

5.4.2 Arsenate Distribution at Corundum (012)-Water Interfaces

In the presence of arsenate, non-resonant XR (Figure 5.3A, 5.4A, and 5.5A) and RAXR (Figure A5.1, A5.2, and A5.3) measurements were performed on corundum (012) surfaces with varying total arsenate concentration, and thus surface coverage, at pH 5, 7, and 9 in 0.01 M NaCl. Model-dependent RAXR analyses (Park et al., 2006) were used to determine the distribution of interfacial arsenate species. This provides structural constraints needed to isolate the effects of adsorbates on interfacial water structure on corundum (012) surfaces, as described in detail in section 5.4.3. Beyond the primary purpose of this study, the measurements also explore higher pH conditions than in Catalano et al. (2008), evaluating whether the co-occurrence of inner- and outer-sphere species extends to neutral and weakly alkaline fluids. The resulting optimized structural models reveal relaxations to the structure are small, regardless of different arsenate surface coverage and pH, consistent with our prior work (Catalano et al., 2008). At each pH, the interfacial arsenic distribution, including the height above terminal oxygen groups and the surface coverage, was determined by RAXR for samples reacted with 100 μM total arsenate. A bimodal arsenic distribution (Table 5.1), consisting of inner- and outer-sphere arsenate species, well reproduced the RAXR data at all pH conditions (Figure A5.1D, A5.2D, and A5.3D). The average heights of both arsenate species were invariant within experimental error among the pH conditions studied (Figure 5.6, Table 5.1). Additional RAXR spectra collected for samples reacted with 10, 30, and 60 μM total arsenate solutions at all pH conditions had consistent phases (Figure A5.1, A5.2, and A5.3), indicating the coexistence of two distinct types of adsorbed arsenate species above corundum (012) surfaces over a broad range of solution concentrations and pH. At each pH condition, the surface coverages of the two arsenate species and the total arsenate coverage generally increased with increasing arsenate solution concentrations. The only

exceptions were at pH 7, where the inner-sphere coverage determined by model fitting decreased between 30 to 60 μM total arsenate concentration and the outer-sphere coverage decreased between 10 to 30 μM total arsenate. Time limitations resulted in RAXR spectra being collected at only two *Q* values for 30 μM total arsenate at pH 7, likely reducing the accuracy of the arsenate distribution determined at this condition.

The arsenic distribution derived from RAXR at corundum (012)-water interface showed a bimodal behavior of the co-occurrence of inner- and outer-sphere arsenate species. The position of the inner-sphere As ~1 Å above the surface (as defined by the bulk terminal oxygen positions) under all pH conditions studied was consistent with that observed in Catalano et al. (2008). However, the position of outer-sphere As ~2.8 Å above the surface was closer to the surface by ~0.5 Å compared to our prior work (Catalano et al., 2008). This difference might originate from the present study refining interfacial structure to XR datasets with larger *Q*-ranges, providing improved spatial resolution and better constrained atom positions. This would affect the structure factors calculated at each *Q* value used in the RAXR analyses, which might affect the resulting As positions. Alternatively, a systematic error in energy calibration would shift the effective phase of the RAXR spectra and also change the resulting As positions, but this should also affect the inner-sphere position. Except for this discrepancy in the location of outer-sphere As position, the current and previous (Catalano et al., 2008) studies provide a consistent picture of arsenate adsorption behavior above corundum (012) surfaces.

5.4.3 Effect of Arsenate Adsorption on Interfacial Water Structure

In order to explore the response of interfacial water structure to increasing arsenate surface coverages, the arsenate distribution determined by RAXR analysis was used to isolate the

interfacial water structure from the corresponding XR analysis. Only slight changes were observed in the XR data at all pH conditions in the presence and absence of arsenate (Figure 5.3A, 5.4A, and 5.5A), indicating that arsenate adsorption did not substantially change the total interfacial structure. The interfacial water profiles at all pH conditions showed a similar hydration structure near the surface that is characterized by two adsorbed water sites, each of which has similar heights above the terminal oxygens (Figure 5.3B, 5.4B, and 5.5B). In addition, the heights and vibrational amplitudes of these two adsorbed water sites above corundum (012) surfaces did not vary significantly with increasing arsenate surface coverage at each pH condition (Table A5.1, A5.2, and A5.3), suggesting that both the spatial arrangement and ordering of these water molecules were independent of arsenate surface coverage. The occupancies of the adsorbed water sites generally decreased as arsenate adsorption increased (Table A5.1, A5.2, and A5.3), consistent with arsenate partially displacing interfacial water molecules. In addition, the properties of the extended ordered water changed upon arsenate adsorption at pH 5 and 7, with the vibrational amplitudes of the beginning of the layered water profile (σ_0) increasing with increasing arsenate surface coverage at pH 5 and 7 (Figure 5.2B and 5.3B; Table A5.1 and A5.2), indicating a more disordered structure. In contrast, no systematic trend in the structure of the extended ordered water was observed as arsenate surface coverage increased in the pH 9 system, with consistent vibrational amplitudes obtained for all experimental conditions studied (Figure 5.4B and Table A5.3).

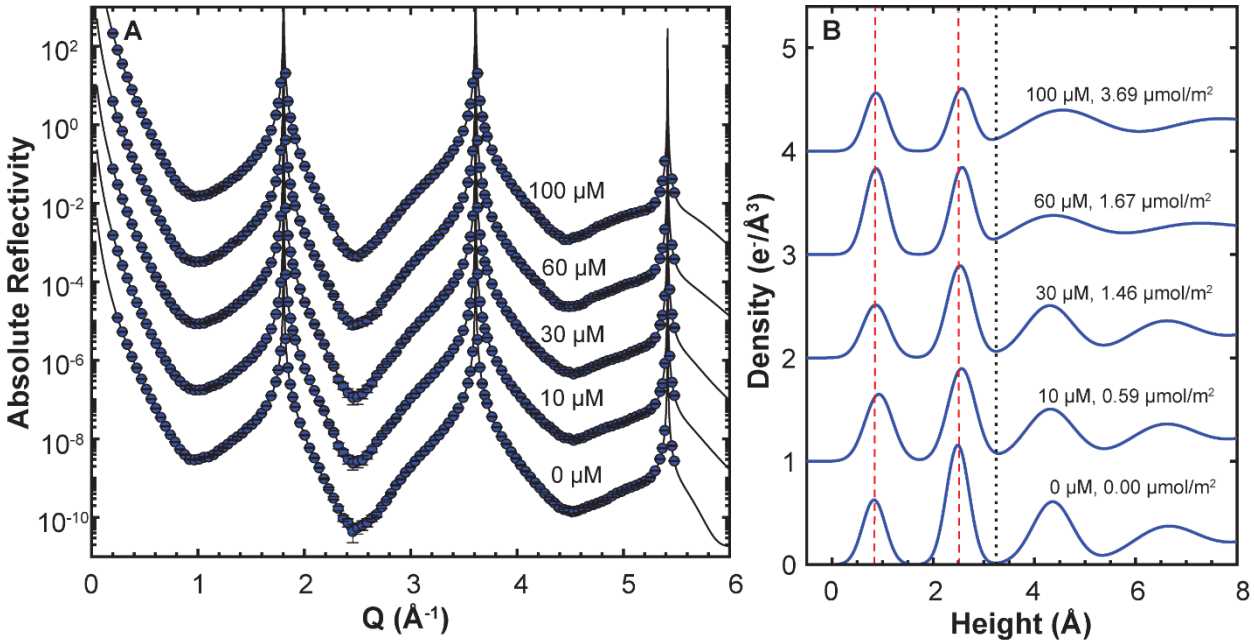

Figure 5.3. (A) Absolute X-ray reflectivity data (symbols) and calculated reflectivity from the best-fit model (lines) at corundum (012)-water interface in 0.01 M NaCl at pH 5 with increasing total arsenate concentration (C_{As}). (B) Changes in the interfacial water electron density profiles with increasing C_{As}. The corresponding arsenate surface coverage values (Γ_{As}) are from Table 5.2. The red dashed lines represent the adsorbed water heights in the As-free system. The black dotted line delineates the approximated boundary between the adsorbed and extended ordered water. Each plot is offset vertically for clarity.

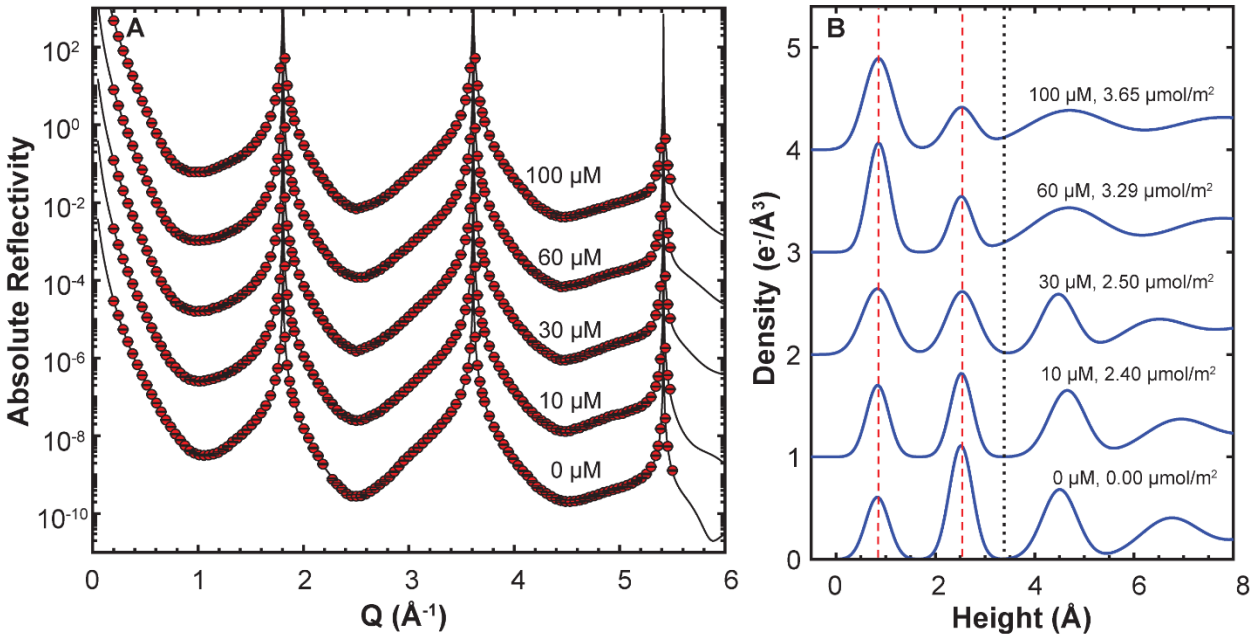

Figure 5.4. (A) Absolute X-ray reflectivity data (symbols) and calculated reflectivity from the best-fit model (lines) at corundum (012)-water interface in 0.01 M NaCl at pH 7 with increasing total arsenate concentration (C_{As}). (B) Changes in the interfacial water electron density profiles with increasing C_{As}. The corresponding arsenate surface coverage values (Γ_{As}) are from Table 5.2. The red dashed lines represent the adsorbed water heights in the As-free system. The black dotted line delineates the approximated boundary between the adsorbed and extended ordered water. Each plot is offset vertically for clarity.

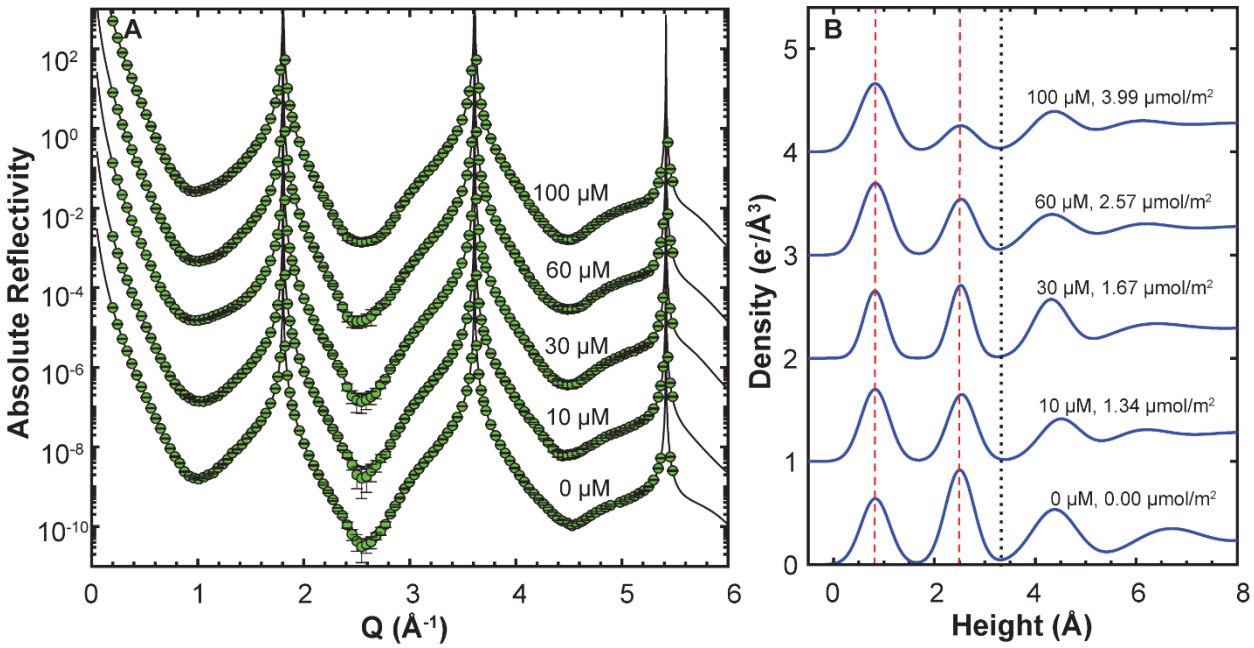

Figure 5.5. (A) Absolute X-ray reflectivity data (symbols) and calculated reflectivity from the best-fit model (lines) at corundum (012)-water interface in 0.01 M NaCl at pH 9 with increasing total arsenate concentration (C_{As}). (B) Changes in the interfacial water electron density profiles with increasing C_{As}. The corresponding arsenate surface coverage values (Γ_{As}) are from Table 5.2. The red dashed lines represent the adsorbed water heights in the As-free system. The black dotted line delineates the approximated boundary between the adsorbed and extended ordered water. Each plot is offset vertically for clarity.

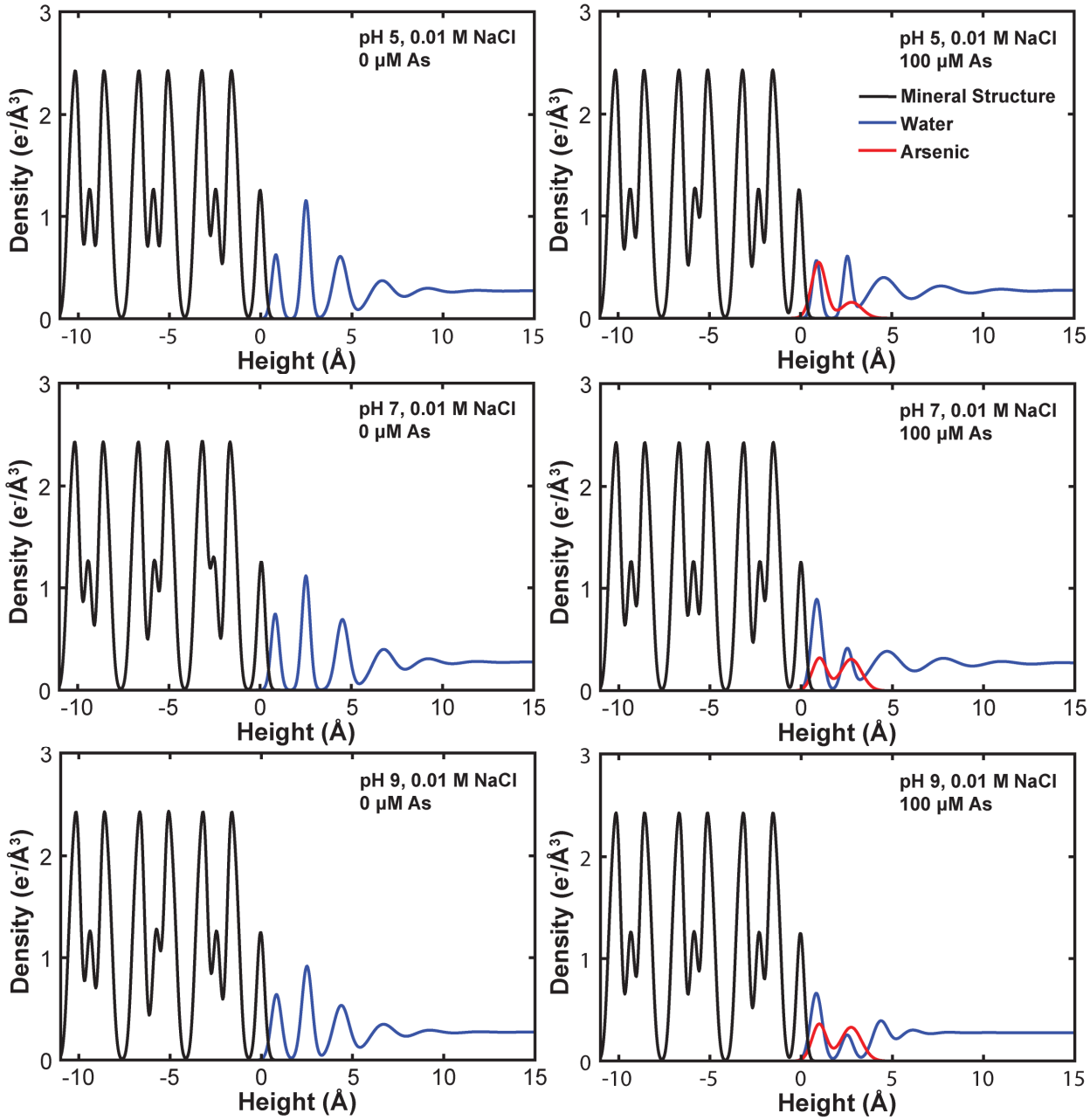

Figure 5.6. Interfacial electron density profiles of the refined structure of arsenate-free (left) and arsenate-sorbed (right) corundum (012)-water interfaces at pH 5, 7, and 9.

Table 5.1. RAXR-derived As positions and surface coverages (Γ_{As}) of inner-sphere (IS) and outer-sphere (OS) species for samples reacted with 100 μM total arsenate at pH 5, 7, and 9 in 0.01 M NaCl.

pH	Site	Height (Å) [a]		Γ_{As} (μmol/m^2)
5	IS	0.99(2)[b]		2.61(5)
	OS	2.79(2)		1.07(5)
			Total	3.69(7)
7	IS	1.00(2)		1.53(6)
	OS	2.74(5)		2.12(5)
			Total	3.65(8)
9	IS	1.03(1)		1.72(3)
	OS	2.81(2)		2.27(3)
			Total	3.99(4)

[a] Zero point set to the unrelaxed height of the terminal oxygen group (>AlO) on unrelaxed corundum (012) surfaces. [b] Uncertainties in the last digit are listed in parentheses.

Table 5.2. RAXR-derived arsenate surface coverages (Γ_{As}) for inner-sphere (IS) and outer-sphere (OS) species at pH 5, 7, and 9 in 0.01 M NaCl.

Concentration (μM)	Site		pH 5	pH 7	pH 9
			Γ_{As} (μmol/m^2)		
10	IS		0.53(1)[a]	1.09(3)	0.81(4)
	OS		0.07(1)	1.31(3)	0.53(3)
		Total	0.59(2)	2.40(4)	1.34(5)
30	IS		1.12(3)	1.58(7)	1.13(6)
	OS		0.34(2)	0.92(7)	0.54(1)
		Total	1.46(3)	2.50(9)	1.67(6)
60	IS		1.21(6)	1.38(7)	1.32(7)
	OS		0.46(4)	1.91(7)	1.25(7)
		Total	1.67(7)	3.29(9)	2.57(9)
100	IS		2.61(5)	1.53(6)	1.72(3)
	OS		1.07(5)	2.12(5)	2.27(3)
		Total	3.69(7)	3.65(7)	3.99(4)

[a] Uncertainties in the last digit are listed in parentheses.

5.5 DISCUSSION

5.5.1 Effects of pH on Water Structure near Corundum (001) and (012) Surfaces

Previous studies have investigated the interfacial hydration structure near (001) and (012) surfaces of corundum in adsorbate-free systems (Catalano, 2011; Catalano et al., 2006; Xu et al., 2018). In both prior studies and the current work, adsorbed water molecules fully coat the surface and gradually transition to bulk water. In deionized water, corundum (001) surfaces have a single adsorbed water layer with a broad distribution (i.e., vibrational amplitude ranging from 0.4 to 0.6 Å), corresponding to a weakly ordered structure (Catalano, 2011), whereas corundum (012) surfaces have two adsorbed water sites with a narrow distribution (i.e., vibrational amplitude ranging from 0.1 to 0.2 Å), corresponding to a strongly ordered structure (Catalano et al., 2006). The distinct water structures on (001) and (012) also occur over the pH range of 5 to 9 in NaCl solutions, as observed in our current and prior studies (Chapter 4).

Previous studies have suggested that the weak and strong ordering of interfacial water above (001) and (012) surfaces is correlated to the charge states of various surface functional groups on those minerals (Catalano, 2011; Catalano et al., 2006). Three types of surface functional groups in singly, doubly, and triply coordinated states are expected at the corundum (001)/(012)-water interface and those groups display protonation states controlled by pH. In a Multi-Site-Complexation (MUSIC) model framework (Hiemstra et al., 1989a; Hiemstra et al., Hiemstra et al., 1996) the dominant surface sites on the corundum (001) surface, doubly coordinated functional groups (>Al_2OH), undergo protonation or deprotonation at low and high pH conditions (pK_a values of ~0 and ~12), which results in predominantly charge-neutral surface sites over a wide pH range. Experimental studies have observed limited surface charge over pH range from 4 to 8 (Kershner et al., 2004; Zhang el al., 2008; Lützenkirchen, 2013; Lützenkirchen

et al., 2010). Negative zeta potentials observed in some studies above pH 4 have been attributed to protolysis behavior of the adsorbed water layer (Lützenkirchen, 2013; Lützenkirchen et al., 2010; Lützenkirchen et al., 2018) and not surface functional group. In contrast, the (012) surface is terminated by singly and triply coordinated groups, which can protonate or deprotonate to have +0.5 or -0.5 charges with pK_a values of ~9 and ~5, respectively (Bickmore et al., 2004; Hiemstra et al., 1999; Sung et al., 2011). Functional groups on this surface always exist in a charged state and undergo protonation-deprotonation in the pH range of natural waters. Under the conditions of our present and prior studies (Xu et al., 2018), surface site protonation-deprotonation results in net surface charge that varies little with pH on (001) surfaces but changes substantially with pH and crosses through the point of zero charge (PZC) for (012) surfaces (Franks and Meagher, 2003; Lützenkirchen et al., 2018; Sung et al., 2011). These distinct, pH-dependent charge behaviors of surface sites may thus induce the different structures of interfacial water near (001) and (012) surfaces.

Two past studies have investigated the response of interfacial water structure at corundum (001)/(012)-water interfaces as a function of pH using sum-frequency vibrational spectroscopy (SFVS) (Sung et al., 2011; Zhang et al., 2008). The OH stretch at lower frequencies (at ~3200 cm^{-1}) in SFVS spectra have been interpreted to originate from interfacial water molecules with the sign of its amplitude inverting from negative to positive around pH 6 - 7 for both (001) and (012) systems. These observations may indicate a net dipolar reorientation of interfacial water molecules as pH varies due to protonation and deprotonation of functional groups on these surfaces. However, our XR measurements on both (001) (Chapter 4) and (012) surfaces clearly show that the overall interfacial water structure varies little between pH 5 and 9 on both surfaces, with positional shifts of < 0.1 Å and insignificant change in vibrational

amplitudes of the adsorbed water sites. This indicates that either interfacial water reorientation suggested by SFVS spectra has little effect on the overall spatial distributions of water molecules or that only a small portion of interfacial water actually reorients. Our observations together with the distinct charging behaviors on the (001) and (012) surfaces suggest that surface site protonation-deprotonation appears inadequate on its own to induce extensive structural changes in interfacial water over the pH range of most natural waters.

5.5.2 Effects of Arsenate Adsorption on Water Structure near Corundum Surfaces

In addition to surface site protonation-deprotonation, the charge states of surface sites can also be altered by ion adsorption. The binding of a charged species to a surface functional group will result in a different local charge on surface sites compared to those that remain uncomplexed, which may affect water structure near these sites. The charge states of functional groups on a corundum surface thus depend on the crystallographic termination as well as the adsorbate. This is reflected in the response of interfacial water structure to arsenate adsorption on (001) surfaces differing from that of (012) surfaces. The adsorption of arsenate to the (001) surface induces a substantial restructuring of interfacial water with a dependence on arsenate surface coverage. This includes a substantial decrease in the heights of the adsorbed water layer and in the positional disorder of the extended layering of interfacial water (Fig. 7) (Xu et al., 2018), indicating that the overall interfacial water structure shifts closer to the surface and a more ordered layered water extends toward the bulk fluid. In contrast, the adsorption of arsenate only weakly perturbs the water structure above the (012) surface, especially the adsorbed water layers, with consistent heights and vibrational amplitudes of such sites obtained for all pH conditions and arsenate surface coverages (Fig. 7; Table EA1, EA2, and EA3). The distinct interfacial water

restructuring induced by arsenate adsorption on the (001) and (012) surface is observed over the full pH range studied. This suggests that on surfaces with initially weak water ordering, such as corundum (001), the addition of a charged adsorbate may induce interfacial water restructuring, but on surfaces with initially strong water ordering, such as corundum (012), water structure is generally unperturbed by charged adsorbates like arsenate.

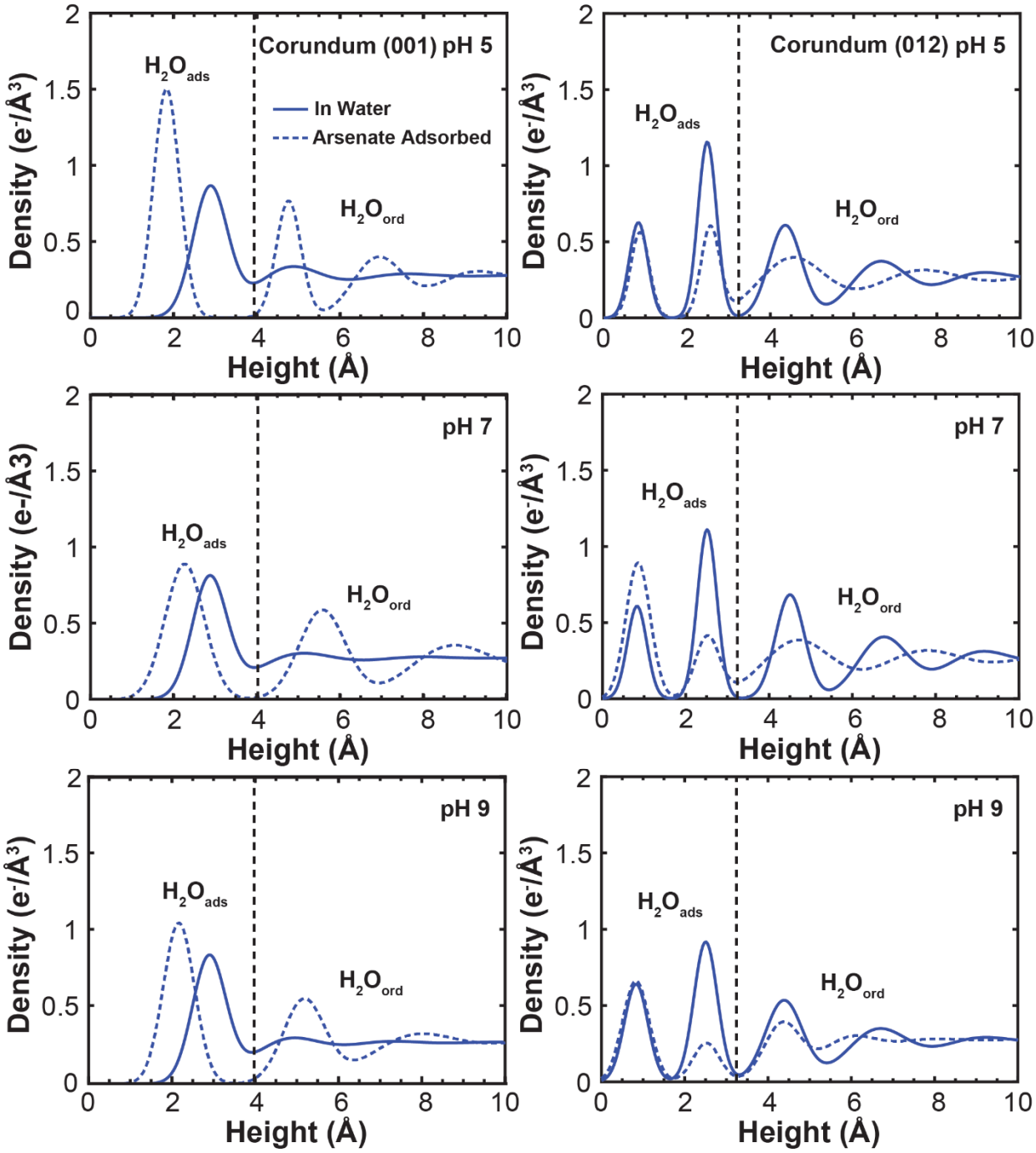

Figure 5.7. Comparison of interfacial water density profiles above corundum (001) (left) and (012) surfaces (right) in the absence and presence of 100 µM arsenate at pH 5, 7, and 9. H_2O_{ads} and H_2O_{ord} represent the adsorbed water and extended ordered water, respectively. The black dashed lines delineate the approximated boundary between the adsorbed and extended ordered water. The height scale is set to zero at the position of the terminal oxygen, $>Al_2O$ and >AlO for the (001) and (012) surfaces, respectively. It should be noted that on the (012) surface, structure is corrugated with $>Al_3O$ at -1.348 Å, and the lower adsorbed water is interpreted to be above $>Al_3O$ sites, not the higher >AlO site at 0.

5.5.3 Possible Mechanisms of Adsorbate-Induced Water Restructuring

On both corundum (001) and (012) surfaces, arsenate adsorbs as a mixture of inner- and outer-sphere complexes over a range of arsenate surface coverages and pH conditions (Catalano et al., 2008; Chapter 4), indicating that adsorption mechanisms may not be the primary control on the resulting restructuring of interfacial water. Instead, the different surface functional groups present on the (001) and (012) surfaces, with their distinct charging behaviors, likely drive the response of interfacial water to arsenate adsorption. The dominant surface sites on the (001) surface, doubly coordinated functional groups, are usually charge-neutral over the pH range explored (Hiemstra et al., 1996; Hiemstra et al., 1999; Lützenkirchen et al., 2010). These groups also have a limited ability to form hydrogen bonds with water molecules and thus weakly orient water dipoles compared to singly and triply coordinated functional groups on the (012) surface (Hass and Schneider, 2000; Hass et al., 1998). We have observed a structural transition of interfacial water above the (001) surface with a dependence on arsenate surface coverage that is most consistent with the coexistence of two distinct water structures, one near the pristine surface and the other in regions near adsorbed arsenate (Chapter 4). Arsenate adsorbed to doubly coordinated functional groups on the (001) surface adds charge to such sites by forming inner-sphere surface complexes (Chapter 4). The distal oxoligands in such an arsenate surface species may serve as a new site that is more favorable for hydrogen bonding to interfacial water, and may thus result in a different water structure. In contrast, the only substantial change to interfacial water on the (012) surface is a decrease in the occupancy of adsorbed water as arsenate surface coverage increases. These results are most consistent with a mechanism where arsenate does not alter the overall interfacial water structure on the (012) surface, only causing displacement of some water molecules near the surface. Our observations on the (001) and (012)

surfaces further support the hypothesis that charge states of individual surface sites, including those binding adsorbates, serve as the ultimate control on water restructuring at the corundum-water interface.

5.5.4 Implications for Interfacial Reactions

Dynamic responses of interfacial water to the addition of arsenate have broader implications for reactivity at mineral-water interfaces. Surfaces with initial weak water ordering, like corundum (001), have limited ability to form H-bonds and orient water dipoles (Hass and Schneider, 2000; Hass et al., 1998; Kerisit, 2011), and are thus expected to have interfacial dielectric constants similar to bulk water and larger capacitances than surfaces with strongly ordered water (Sverjensky, 2001). The change in water structure on the (001) surface upon adsorption of inner-sphere arsenate should thus alter the interfacial capacitance, variation in surface potential with distance from the surface, and electrostatic activity corrections. However, surfaces with intrinsically strong water ordering that is unaltered by arsenate adsorption, like the corundum (012) surface, will not display such changes in capacitances, potential distributions, and activity corrections. Additional work is needed to evaluate whether water restructuring, and resulting changes in interfacial properties, occurs for other adsorbates to determine if this is a general phenomenon.

Both corundum (001) and (012) surfaces can react with arsenate through inner- and outer-sphere adsorption mechanisms (Catalano et al., 2008; Chapter 4). While inner-sphere adsorption involves direct binding to surface functional groups through ligand exchange, the mechanism(s) to stabilize outer-sphere species is less clear. The locations of outer-sphere species above both the (001) and (012) surfaces suggest that hydrogen bonding between arsenate

oxoligands and surface functional groups or interfacial water molecules has a key role in such surface complexation (Catalano et al., 2008; Chapter 4). These interactions may be strongly affected by interfacial water structure. The distinct water restructuring on (001) and (012) surfaces upon arsenate adsorption suggests that calculation of activity corrections for outer-sphere complexes may require different approaches for these two surfaces. On (001), these would require using capacitances associated with the interfacial water structure induced by inner-sphere arsenate adsorption, whereas on (012) a single capacitance value would be needed for the clean and arsenate-adsorbed surface. This highlights the need to refine surface complexation models to account for conditions where water restructuring generates interfacial capacitances that differ for surface functional group protonation-deprotonation compares to adsorption reactions.

5.6 ACKNOWLEDGEMENTS

This research was supported by the U.S. National Science Foundation (NSF) Environmental Chemical Sciences program through award no. CHE-1505532. The XR and RAXR data were collected at beamline 13-ID-C (GeoSoilEnviroCARS) at the Advanced Photon Source, Argonne National Laboratory. GeoSoilEnviroCARS is supported by NSF Earth Sciences (EAR-1634415) and U.S. Department of Energy (DOE) Office Geosciences (DE-FG02-94ER14466). The APS is an Office of Science User Facility operated for the U.S. DOE Office of Science by Argonne National Laboratory under contract no. DE-AC02-06CH11357.

5.7 APPENDIX

Table A5.1. Optimized structural parameters for the best-fit models for the corundum (012)-water interface at pH 5 for increasing total arsenate concentrations.

Surface structure		Unrelaxed	Total arsenate concentration				
Atom		Structure[a]	No As	10 μM As	30 μM As	60 μM As	100 μM As
As	z (Å)[b]		0	2.79	2.79	2.79	2.79(2)
	θ[c]		0	0.006(2)	0.052(3)	0.070(6)	0.163(8)
As	z (Å)		0	0.99	0.99	0.99	0.99(2)
	θ		0	0.080(2)	0.170(4)	0.184(9)	0.397(8)
O	z (Å)		2.49(5)[j]	2.49(6)	2.53(7)	2.57(6)	2.56(4)
(H_2O_{ads})	θ		1.98(7)	1.86(9)	1.8(1)	1.40(9)	1.00(2)
	σ[d]		0.12(1)	0.19(4)	0.17(9)	0.11(3)	0.11(2)
O	z (Å)		0.83(8)	0.87(5)	0.87(9)	0.87(6)	0.87(2)
(H_2O_{ads})	θ		1.1(2)	1.3(1)	1.0(2)	1.43(9)	0.97(5)
	σ		0.12(1)	0.19(4)	0.17(9)	0.11(3)	0.11(2)
O(>AlO)	z (Å)	0.000	-0.03(4)	-0.12(2)	-0.04(5)	-0.05(2)	-0.08(1)
O(>Al_3O)	z (Å)	-1.348	-1.32(3)	-1.28(2)	-1.29(2)	-1.26(1)	-1.25(5)
Al	z (Å)	-1.703	-1.68(3)	-1.66(2)	-1.65(2)	-1.62(1)	-1.60(5)
O	z (Å)	-2.414	-2.46(5)	-2.36(3)	-2.40(5)	-2.35(3)	-2.31(2)
Al	z (Å)	-3.126	-3.15(1)	-3.10(1)	-3.13(1)	-3.13(1)	-3.105(5)
O	z (Å)	-3.480	-3.50(1)	-3.46(1)	-3.48(1)	-3.48(1)	-3.460(5)
O	z (Å)	-4.829	-4.809(6)	-4.827(7)	-4.809(8)	-4.812(5)	-4.812(3)
Al	z (Å)	-5.184	-5.163(6)	-5.181(7)	-5.163(8)	-5.167(5)	-5.166(3)
O	z (Å)	-5.895	-5.882(9)	-5.878(8)	-5.827(9)	-5.816(9)	-5.801(9)
Al	z (Å)	-6.606	-6.603(4)	-6.614(2)	-6.606(4)	-6.601(3)	-6.594(3)
O	z (Å)	-6.961	-6.958(4)	-6.969(2)	-6.960(4)	-6.956(3)	-6.948(3)
O	z (Å)	-8.309	-8.306(5)	-8.310(2)	-8.305(3)	-8.300(2)	-8.298(2)
Al	z (Å)	-8.664	-8.661(5)	-8.665(2)	-8.660(3)	-8.655(2)	-8.653(2)
O	z (Å)	-9.376	-9.38(1)	-9.37(5)	-9.365(9)	-9.356(5)	-9.347(4)
Al	z (Å)	-10.087	-10.094(3)	-10.083(2)	-10.084(3)	-10.082(2)	-10.079(2)
O	z (Å)	-10.442	-10.448	-10.438	-10.439	-10.437	-10.433
Layered water structure							
z (Å)			4.36(6)	4.42(7)	4.30(7)	4.32(3)	4.52(5)
σ_0 (Å)[e]			0.34(7)	0.44(6)	0.44(7)	0.76(6)	0.79(3)
$\overline{\sigma}$ (Å)[f]			0.31(3)	0.23(3)	0.24(3)	0.32(4)	0.30(3)
d_w (Å)[g]			2.24(4)	2.25(4)	2.26(5)	2.69(7)	2.97(7)
Non-structural parameters							
Water film (μm)			16(3)	15(1)	17(1)	17(2)	12(1)
Roughness (Å)[h]			5.48(4)	5.23(3)	5.19(4)	4.78(2)	4.87(2)
Layer fraction[i]			0.34(1)	0.297(4)	0.296(5)	0.303(6)	0.296(5)
Goodness-of-fit parameters							
χ_v^2			1.81	1.29	1.99	1.45	1.50
R-factor			0.021	0.013	0.008	0.017	0.011

[a] Atom height for the unrelaxed structure. [b] Atom height from the best fit model. [c] Occupancy. [d] Vibrational amplitude. [e] Vibrational amplitude of the first water layer (Fenter, 2002). [f] A parameter describing how the vibrational amplitude of each water layer increases with distance from the surface (Fenter, 2002). [g] Spacing of layered water (Fenter, 2002). [h] Roughness

parameter of Robinson (Robinson, 1986). [i] Fractional occupancy of partial layer accounting minor roughness (Catalano et al., 2008). [j] Uncertainties in the last digit are listed in parentheses, reported at the 95% confidence level. Parameters with no listed uncertainties were not varied in the analysis.

Table A5.2. Optimized structural parameters for the best-fit models of the corundum (012)-water interface at pH 7 for increasing total arsenate concentrations.

Surface structure		Unrelaxed	Total arsenate concentration				
Atom		Structure[a]	No As	10 μM As	30 μM As	60 μM As	100 μM As
As	z (Å)		0	2.74	2.74	2.74	2.74(5)
	θ		0	0.199(4)	0.14(1)	0.29(1)	0.322(8)
As	z (Å)		0	1.00	1.00	1.00	1.00(2)
	θ		0	0.166(4)	0.24(1)	0.21(1)	0.232(9)
O	z (Å)		2.51(3)	2.53(3)	2.54(4)	2.52(4)	2.52(3)
(H_2O_{ads})	θ		1.98(5)	1.40(2)	1.46(8)	0.92(2)	0.90(3)
	σ		0.12(2)	0.11(4)	0.24(6)	0.11(2)	0.22(3)
O	z (Å)		0.83(2)	0.84(3)	0.83(3)	0.86(5)	0.86(1)
(H_2O_{ads})	θ		1.09(3)	1.20(9)	1.53(2)	1.83(3)	2.00(9)
	σ		0.12(2)	0.11(4)	0.24(6)	0.11(2)	0.22(3)
O(>AlO)	z (Å)	0.000	0.007(5)	0.008(4)	0.003(9)	-0.005(4)	-0.012(1)
O(>Al_3O)	z (Å)	-1.348	-1.367(3)	-1.368(3)	-1.262(5)	-1.250(3)	-0.249(3)
Al	z (Å)	-1.703	-1.72(3)	-1.723(3)	-1.616(5)	-1.604(3)	-1.604(3)
O	z (Å)	-2.414	-2.518(4)	-2.480(6)	-2.378(1)	-2.253(8)	-2.269(1)
Al	z (Å)	-3.126	-3.096(3)	-3.068(3)	-3.121(9)	-3.082(3)	-3.082(4)
O	z (Å)	-3.48	-3.450(3)	-3.422(3)	-3.475(9)	-3.437(3)	-3.437(4)
O	z (Å)	-4.829	-4.803(3)	-4.815(2)	-4.909(6)	-4.840(3)	-4.844(3)
Al	z (Å)	-5.184	-5.157(3)	-5.170(2)	-5.263(6)	-5.195(3)	-5.199(3)
O	z (Å)	-5.895	-5.797(6)	-5.869(7)	-5.948(9)	-5.882(7)	-5.904(9)
Al	z (Å)	-6.606	-6.600(3)	-6.611(3)	-6.670(4)	-6.610(2)	-6.616(2)
O	z (Å)	-6.961	-6.954(3)	-6.966(3)	-6.925(4)	-6.964(2)	-6.971(2)
O	z (Å)	-8.309	-8.317(2)	-8.303(2)	-8.279(4)	-8.295(2)	-8.293(2)
Al	z (Å)	-8.664	-8.672(2)	-8.658(2)	-8.634(4)	-8.650(2)	-8.647(2)
O	z (Å)	-9.376	9.419(5)	-9.366(5)	-9.335(7)	-9.332(4)	-9.328(4)
Al	z (Å)	-10.087	-10.089(2)	-10.078(2)	-10.085(4)	-10.072(2)	-10.073(1)
O	z (Å)	-10.442	-10.444	-10.432	-10.439	-10.426	-10.428
Layered water structure							
z (Å)			4.51(1)	4.65(1)	4.47(2)	4.67(3)	4.67(2)
σ_0 (Å)			0.28(1)	0.31(1)	0.29(3)	0.72(3)	0.82(3)
$\overline{\sigma}$ (Å)			0.306(6)	0.35(1)	0.35(2)	0.29(2)	0.24(2)
d_w (Å)			2.228(5)	2.22(1)	1.92(1)	2.10(2)	2.97(3)
Non-structural parameters							
Water film (μm)			18(1)	12(1)	13(2)	13(1)	17(1)
Roughness (Å)			5.50(2)	5.40(3)	6.45(5)	5.06(2)	4.72(2)
Layer fraction			0.317(4)	0.277(6)	0.14(2)	0.236(7)	0.241(5)
Goodness-of-fit parameters							
χ_v^2			1.27	1.48	1.96	2.07	1.56
R-factor			0.039	0.020	0.013	0.021	0.014

See Table A5.1 for description of the parameters.

Table A5.3. Optimized structural parameters for the best-fit models of the corundum (012)-water interface at pH 9 for increasing total arsenate concentrations.

Surface structure		Unrelaxed	Total arsenate concentration				
Atom		Structure[a]	No As	10 μM As	30 μM As	60 μM As	100 μM As
As	z (Å)		0	2.81	2.81	2.81	2.81(1)
	θ		0	0.080(5)	0.082(2)	0.19(1)	0.345(4)
As	z (Å)		0	1.03	1.03	1.03	1.03(1)
	θ		0	0.123(6)	0.172(9)	0.20(1)	0.262(4)
O	z (Å)		2.50(4)	2.54(2)	2.52(5)	2.53(5)	2.52(6)
(H_2O_{ads})	θ		1.98(6)	1.40(5)	1.22(7)	1.18(5)	0.62(4)
	σ		0.20(1)	0.20(2)	0.11(9)	0.20(3)	0.25(2)
O	z (Å)		0.83(4)	0.83(2)	0.82(2)	0.83(3)	0.83(3)
(H_2O_{ads})	θ		1.39(2)	1.50(7)	1.12(8)	1.51(9)	1.62(7)
	σ		0.20(1)	0.20(2)	0.11(9)	0.20(3)	0.25(2)
O(>AlO)	z (Å)	0.000	-0.004(5)	-0.001(8)	-0.002(7)	-0.002(7)	-0.004(6)
O(>Al_3O)	z (Å)	-1.348	-1.336(4)	-1.281(4)	-1.263(4)	-1.276(4)	-1.262(4)
Al	z (Å)	-1.703	-1.691(4)	-1.636(4)	-1.618(4)	-1.631(4)	-1.617(4)
O	z (Å)	-2.414	-2.452(4)	-2.36(1)	-2.40(2)	-2.37(2)	-2.31(2)
Al	z (Å)	-3.126	-3.128(4)	-3.118(8)	-3.155(8)	-3.117(8)	-3.098(5)
O	z (Å)	-3.48	-3.482(4)	-3.473(8)	-3.510(8)	-3.472(8)	-3.453(5)
O	z (Å)	-4.829	-4.794(3)	-4.850(5)	-4.855(9)	-4.849(4)	-4.856(3)
Al	z (Å)	-5.184	-5.149(3)	-5.205(5)	-5.210(9)	-5.204(4)	-5.211(3)
O	z (Å)	-5.895	-5.760(7)	-5.899(6)	-5.850(9)	-5.855(6)	-5.876(6)
Al	z (Å)	-6.606	-6.588(3)	-6.621(4)	-6.600(5)	-6.612(2)	-6.617(2)
O	z (Å)	-6.961	-6.943(3)	-6.976(4)	-6.954(5)	-6.966(2)	-6.972(2)
O	z (Å)	-8.309	-8.313(2)	-8.313(3)	-8.288(4)	-8.307(2)	-8.303(2)
Al	z (Å)	-8.664	-8.668(2)	-8.668(3)	-8.642(4)	-8.662(2)	-8.658(2)
O	z (Å)	-9.376	-9.389(5)	-9.369(6)	-9.309(4)	-9.354(4)	-9.340(5)
Al	z (Å)	-10.087	-10.088(2)	-10.086(3)	-10.076(2)	-10.081(2)	-10.079(2)
O	z (Å)	-10.442	-10.443	-10.441	-10.431	-10.436	-10.434
Layered water structure							
z (Å)			4.38(2)	4.49(2)	4.30(2)	4.30(2)	4.34(3)
σ_0 (Å)			0.40(2)	0.36(4)	0.29(4)	0.43(2)	0.39(4)
$\overline{\sigma}$ (Å)			0.30(1)	0.25(4)	0.53(4)	0.26(3)	0.27(3)
d_w (Å)			2.23(1)	1.53(2)	1.77(9)	1.68(2)	1.53(2)
Non-structural parameters							
Water film (μm)			14(1)	17(2)	11(1)	14(1)	15(1)
Roughness (Å)			5.65(2)	5.73(3)	6.02(3)	5.41(2)	5.10(2)
Layer fraction			0.369(3)	0.318(6)	0.285(8)	0.317(6)	0.343(7)
Goodness-of-fit parameters							
χ_v^2			1.14	2.01	1.91	1.03	1.76
R-factor			0.022	0.015	0.013	0.013	0.014

See Table A5.1 for description of the parameters.

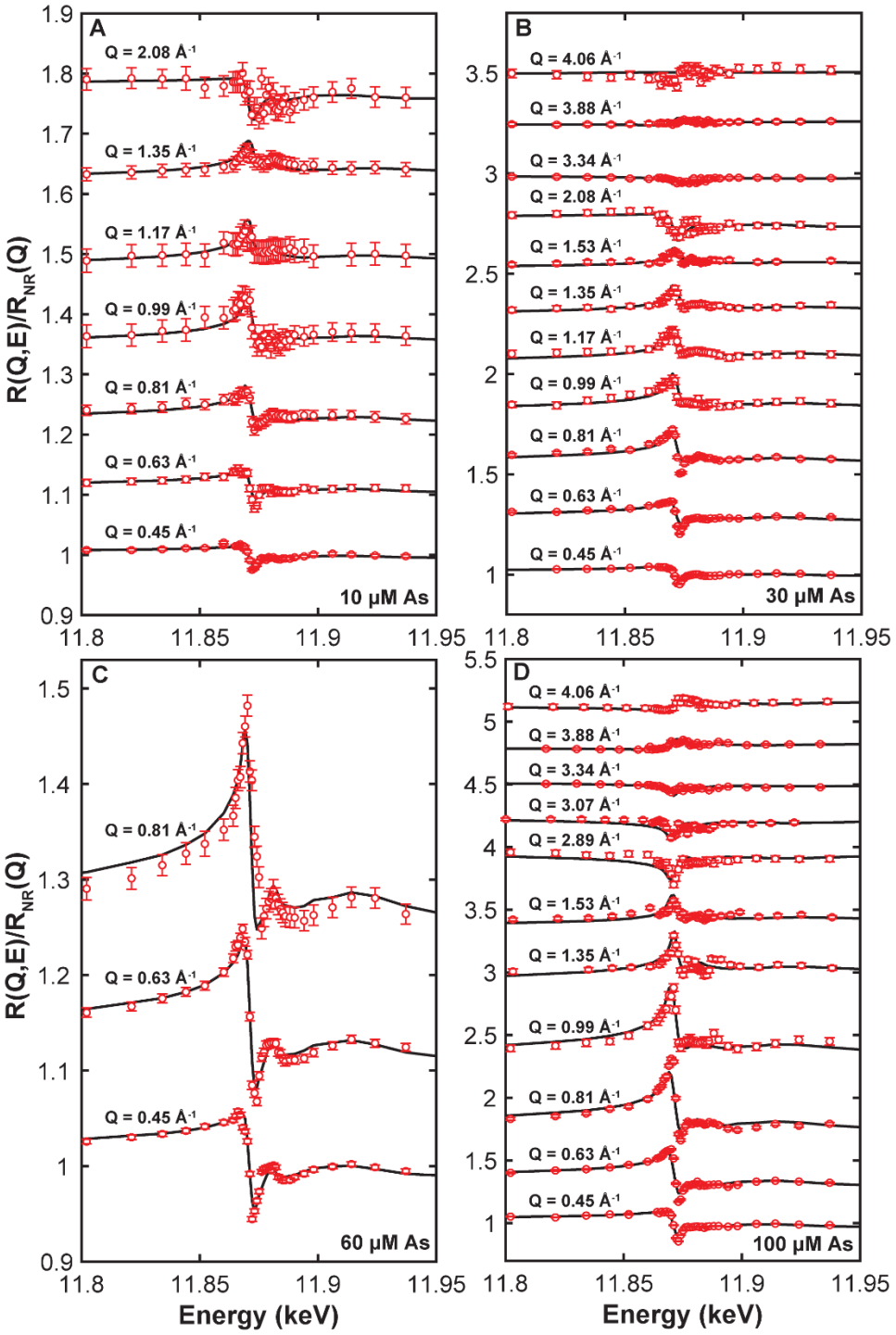

Figure A5.1. Arsenic K-edge RAXR spectra for arsenate adsorbed to corundum (012) in 0.01 M NaCl solution at pH 5 with 10 µM (A), 30 µM (B), 60 µM (C), and 100 µM (D) total arsenate concentration. Model-dependent (solid) fits to the data (circles) are shown. Spectra have been offset vertically for clarity.

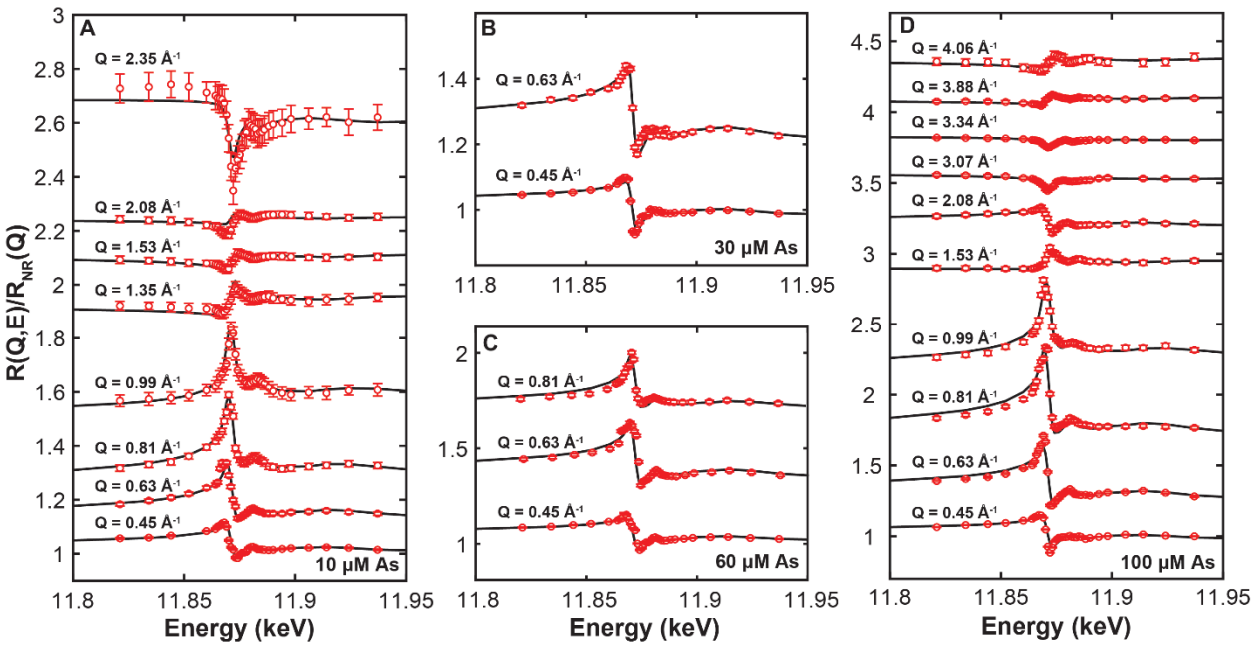

Figure A5.2. Arsenic K-edge RAXR spectra for arsenate adsorbed to corundum (012) in 0.01 M NaCl solution at pH 7 with 10 µM (A), 30 µM (B), 60 µM (C), and 100 µM (D) total arsenate concentration. Model-dependent (solid) fits to the data (circles) are shown. Spectra have been offset vertically for clarity.

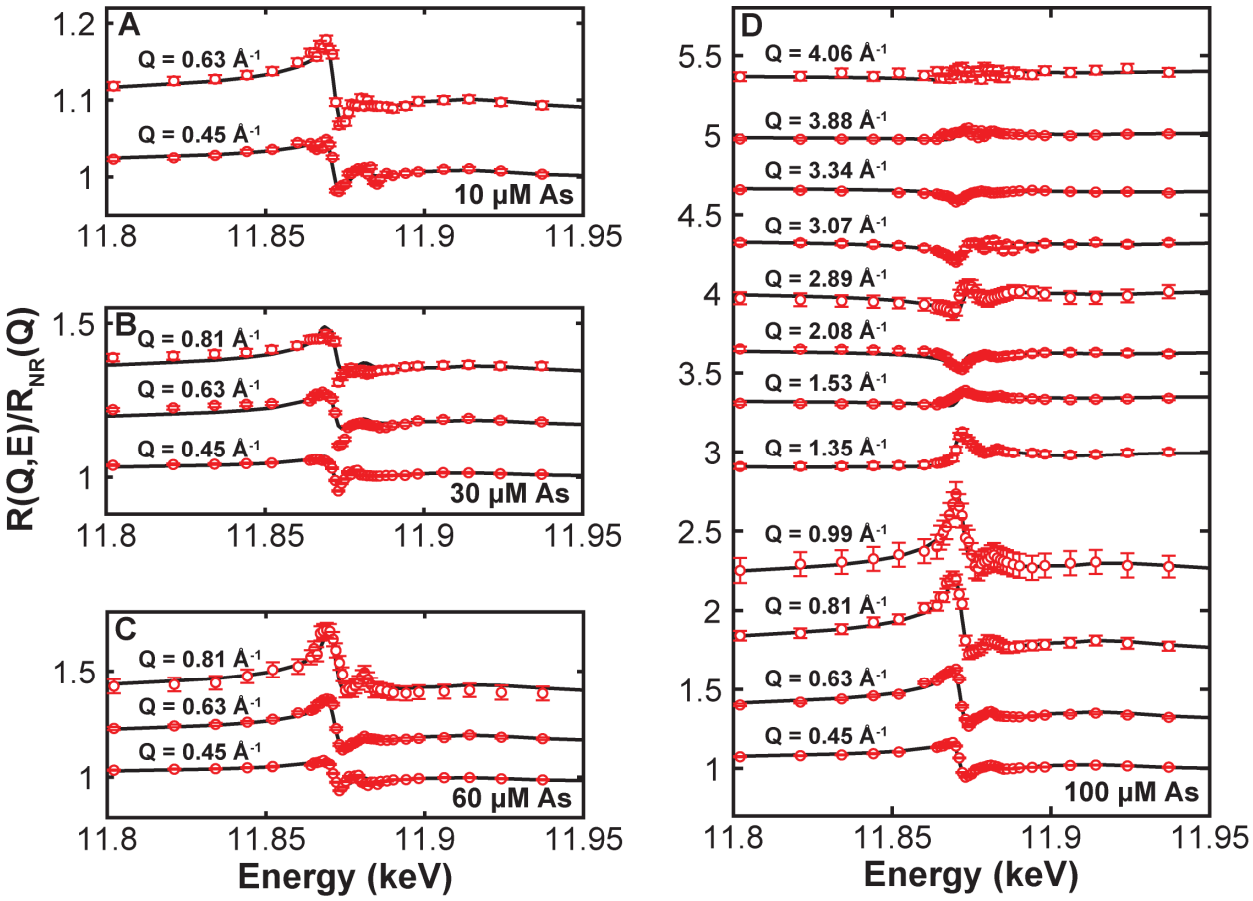

Figure A5.3. Arsenic K-edge RAXR spectra for arsenate adsorbed to corundum (012) in 0.01 M NaCl solution at pH 9 with 10 µM (A), 30 µM (B), 60 µM (C), and 100 µM (D) total arsenate concentration. Model-dependent (solid) fits to the data (circles) are shown. Spectra have been offset vertically for clarity.

5.8 REFERENCES

Al-Abadleh, H.A. and Grassian, V. (2003) FT-IR study of water adsorption on aluminum oxide surfaces. *Langmuir* **19**, 341-347.

Amstaetter, K., Borch, T., Larese-Casanova, P. and Kappler, A. (2010) Redox transformation of arsenic by Fe(II)-activated goethite (α-FeOOH). *Environ. Sci. Technol.* **44**, 102-108.

Argyris, D., Ho, T.A., Cole, D.R. and Striolo, A. (2011) Molecular dynamics studies of interfacial water at the alumina surface. *J. Phys. Chem. C* **115**, 2038-2046.

Benning, L.G. and Waychunas, G.A. (2008) Nucleation, Growth, and Aggregation of Mineral Phases: Mechanisms and Kinetic, in: Brantley, S.L., Kubichi, J.D., White, A.F. (Eds.), *Kinetics of Water-Rock Interaction*. Springer, Newyork, pp. 259-333.

Bickmore, B.R., Tadanier, C.J., Rosso, K.M., Monn, W.D. and Eggett, D.L. (2004) Bond-valence methods for pKa prediction: critical reanalysis and a new approach. *Geochim. Cosmochim. Acta* **68**, 2025-2042.

Boily, J.F., Chatman, S. and Rosso, K.M. (2011) Inner-Helmholtz potential development at the hematite (α-Fe_2O_3) (001) surface. *Geochim. Cosmochim. Acta* **75**, 4113-4124.

Boland, D.D., Collins, R.N., Payne, T.E. and Waite, T.D. (2011) Effect of amorphous Fe(III) oxide transformation on the Fe(II)-mediated reduction of U(VI). *Environ. Sci. Technol.* **45**, 1327-1333.

Brown, G.E., Henrich, V.E., Casey, W.H., Clark, D.L., Eggleston, C., Felmy, A., Goodman, D.W., Gratzel, M., Maciel, G., McCarthy, M.I., Nealson, K.H., Sverjensky, D.A., Toney, M.F. and Zachara, J.M. (1999) Metal oxide surfaces and their interactions with aqueous solutions and microbial organisms. *Chem. Rev.* **99**, 77-174.

Brown, G.E. and Parks, G.A. (2001) Sorption of trace elements on mineral surfaces: Modern perspectives from spectroscopic studies, and comments on sorption in the marine environment. *Int. Geol. Rev.* **43**, 963-1073.

Catalano, J.G. (2010) Relaxations and interfacial water ordering at the corundum (110) surface. *J. Phys. Chem. C* **114**, 6624-6630.

Catalano, J.G. (2011) Weak interfacial water ordering on isostructural hematite and corundum (001) surfaces. *Geochim. Cosmochim. Acta* **75**, 2062-2071.

Catalano, J.G., Fenter, P. and Park, C. (2007) Interfacial water structure on the (012) surface of hematite: Ordering and reactivity in comparison with corundum. *Geochim. Cosmochim. Acta* **71**, 5313-5324.

Catalano, J.G., Fenter, P. and Park, C. (2009) Water ordering and surface relaxations at the hematite (110)–water interface. *Geochim. Cosmochim. Acta* **73**, 2242-2251.

Catalano, J.G., Park, C., Fenter, P. and Zhang, Z. (2008) Simultaneous inner- and outer-sphere arsenate complexation on corundum and hematite. *Geochim. Cosmochim. Acta* **72**, 1986-2004.

Catalano, J.G., Park, C., Zhang, Z. and Fenter, P. (2006) Termination and water adsorption at the α-Al_2O_3 (012)-aqueous solution interface. *Langmuir* **22**, 4668-4673.

Chatman, S., Zarzycki, P. and Rosso, K.M. (2013) Surface potentials of (001), (012), (113) hematite (α-Fe_2O_3) crystal faces in aqueous solution. *Phys. Chem. Chem. Phys.* **15**, 13911-13921.

Cheng, L., Fenter, P., Nagy, K.L., Schlegel, M.L. and Sturchio, N.C. (2001) Molecular-scale density oscillations in water adjacent to a mica surface. *Phys. Rev. Lett.* **87**, 156103.

Chorover, J., Kretzschmar, R., Garcia-Pichel, F. and Sparks, D.L. (2007) Soil biogeochemical processes within the Critical Zone. *ELEMENTS* **3**, 321-326.

Eikenberry, E.F., Brönnimann, C., Hülsen, G., Toyokawa, H., Horisberger, R., Schmitt, B., Schulze-Briese, C. and Tomizaki, T. (2003) PILATUS: a two-dimensional X-ray detector for macromolecular crystallography. *Nucl. Instrum. Methods Phys. Res., Sect. A* **501**, 260-266.

Elsner, M., Schwarzenbach, R.P. and Haderlein, S.B. (2004) Reactivity of Fe(II)-bearing minerals toward reductive transformation of organic contaminants. *Environ. Sci. Technol.* **38**, 799-807.

Fenter, P. (2002) X-ray reflectivity as a probe of mineral-fluid interfaces: a user guide. *Rev. Mineral. Geochem.* **49**, 149-220.

Fenter, P., Park, C., Nagy, K.L. and Sturchio, N.C. (2007) Resonant anomalous X-ray reflectivity as a probe of ion adsorption at solid-liquid interfaces. *Thin Solid Films* **515**, 5654-5659.

Fitts, J.P., Shang, X.M., Flynn, G.W., Heinz, T.F. and Eisenthal, K.B. (2005) Electrostatic surface charge at aqueous/α-Al_2O_3 single-crystal interfaces as probed by optical second-harmonic generation. *J. Phys. Chem. B* **109**, 7981-7986.

Flörsheimer, M., Kruse, K., Polly, R., Abdelmonem, A., Schimmelpfennig, B., Klenze, R. and Fanghänel, T. (2008) Hydration of mineral surfaces probed at the molecular level. *Langmuir* **34**, 13434-13439.

Franks, G.V. and Meagher, L. (2003) The isoelectric points of sapphire crystals and α-alumina powder. *Colloids Surf. A: Physicochem. Eng. Aspects* **214**, 99-110.

Gaigeot, M.P., Sprik, M. and Sulpizi, M. (2012) Oxide/water interfaces: How the surface chemistry modifies interfacial water properties. *J. Phys.: Condens. Matter* **24**, 11.

Geissbuhler, P., Fenter, P., DiMasi, E., Srajer, G., Sorensen, L.B. and Sturchio, N.C. (2004) Three-dimensional structure of the calcite–water interface by surface X-ray scattering. *Surf. Sci.* **573**, 191-203.

Hass, K.C. and Schneider, W.F. (2000) First-principles molecular dynamics simulations of H_2O on α-Al_2O_3 (0001). *J. Phys. Chem. B* **104**, 5527-5540.

Hass, K.C., Schneider, W.F., Curioni, A. and Andreoni, W. (1998) The chemistry of water on alumina surfaces: Reaction dynamics from first principles. *Science* **282**, 265-268.

Hiemstra, T. and Van Riemsdijk, W.H. (1996) A surface structural approach to ion adsorption: the charge distribution (CD) model. *J. Colloid Interface Sci.* **179**, 488-508.

Hiemstra, T. and Van Riemsdijk, W.H. (2006) On the relationship between charge distribution, surface hydration, and the structure of the interface of metal hydroxides. *J. Colloid Interface Sci.* **301**, 1-18.

Hiemstra, T., Van Riemsdijk, W.H. and Bolt, G.H. (1989) Multisite proton adsorption modeling at the solid/solution interface of (hydr)oxides: a new approach I. Model description and evaluation of intrinsic reaction constants. *J. Colloid Interface Sci.* **133**, 91-104.

Hiemstra, T., Venema, P. and Van Riemsdijk, W.H. (1996) Intrinsic proton affinity of reactive surface groups of metal (hydr)oxides: The bond valence principle. *J. Colloid Interface Sci.* **184**, 680-692.

Hiemstra, T., Yong, H. and Van Riemsdijk, W.H. (1999) Interfacial charging phenomena of aluminum (hydr)oxides. *Langmuir* **15**, 5942-5955.

Huang, P., Pham, T.A., Galli, G. and Schwegler, E. (2014) Alumina (0001)/water interface: Structural properties and infrared spectra from first-principles molecular dynamics simulations. *J. Phys. Chem. C* **118**, 8944-8951.

Kerisit, S. (2011) Water structure at hematite-water interfaces. *Geochim. Cosmochim. Acta* **75**, 2043-2061.

Kershner, R.J., Bullard, J.W. and Cima, M.J. (2004) Zeta potential orientation dependence of sapphire substrates. *Langmuir* **20**, 4101-4108.

Kirfel, A. and Eichhorn, K. (1990) Accurate structure analysis with synchrotron radiation. The electron density in Al_2O_3 and Cu_2O. *Acta Crystallogr. A* **46**, 271-284.

Kraemer, S.M. (2004) Iron oxide dissolution and solubility in the presence of siderophores. *Aquat. Sci.* **66**, 3-18.

Kraemer, S.M. (2005) Siderophores and the dissolution of iron-bearing minerals in marine systems. *Rev. Mineral. Geochem.* **59**, 53-84.

Lützenkirchen, J. (2013) Specific ion effects at two single-crystal planes of sapphire. *Langmuir* **29**, 7726-7734.

Lützenkirchen, J., Franks, G.V., Plaschke, M., Zimmermann, R., Herberling, F., Abdelmonem, A., Darbha, G., Schild, D., Filby, A., Eng, P.J., Catalano, J.G., Rosenqvist, J., Preocanin, T., Aytug, T., Zhang, D., Gan, Y. and Braunschweig, B. (2018) The surface chemistry of sapphire-c: A literature review and a study on various factors influencing its IEP. *Adv. Colloid Interface Sci.* **251**, 1-25.

Lützenkirchen, J., Heberling, F., Supljika, F., Preocanin, T., Kallay, N., Johann, F., Weisser, L. and Eng, P.J. (2015) Structure-charge relationship-the case of hematite (001). *Farady Discuss* **180**, 55-79.

Lützenkirchen, J., Zimmermann, R., Preocanin, T., Filby, A., Kupcik, T., Küttner, D., Abdelmonem, A., Schild, D., Rabung, T., Plaschke, M., Brandenstein, F., Werner, C. and Geckeis, H. (2010) An attempt to explain bimodal behaviour of the sapphire c-plane electrolyte interface. *Adv. Colloid Interface Sci.* **157**, 61-74.

Ma, S.Y., Liu, L.M. and Wang, S.Q. (2016) Water film adsorbed on the α-Al_2O_3(0001) surface: Structural properties and fynamical behaviors from first-principles molecular dynamics simulations. *J. Phys. Chem. C* **120**, 5398-5409.

McBriarty, M.E., von Rudorff, G.F., Stubbs, J.E., Eng, P.J., Blumberger, J. and Rosso, K.M. (2017) Dynamic stabilization of metal oxide-water interfaces. *J. Am. Chem. Soc.* **139**, 2581-2584.

Park, C., Fenter, P., Nagy, K.L. and Sturchio, N.C. (2006) Hydration and distribution of ions at the mica-water interface. *Phys. Rev. Lett.* **97**, 016101.

Rechard, P., Kretzchmar, R. and Kraemer, S.M. (2007) Dissolution mechanisms of goethite in the presence of siderophores and organic acids. *Geochim. Cosmochim. Acta* **71**, 5635-5650.

Robinson, I.K. (1986) Crystal truncation rods and surface roughness. *Phys. Rev. B* **33**, 3830-3836.

Rustad, J.R., Wasserman, E. and Felmy, A.R. (1999) Molecular modeling of the surface charging of hematite II. Optimal proton distribution and simulation of surface charge versus pH relationships *Surf. Sci.* **424**, 28-35.

Schlegel, M.L., Nagy, K.L., Fenter, P., Cheng, L., Sturchio, N.C. and Jacobsen, S.D. (2006) Cation sorption on the muscovite (001) surface in chloride solutions using high-resolution X-ray reflectivity. *Geochim. Cosmochim. Acta* **70**, 3549-3565.

Shi, Z., Zachara, J.M., Wang, Z., Shi, L. and Fredrickson, J.K. (2013) Reductive dissolution of goethite and hematite by reduced flavins. *Geochim. Cosmochim. Acta* **121**, 139-154.

Sung, J., Shen, Y.R. and Waychunas, G.A. (2012) The interfacial structure of water/protonated α-Al_2O_3 (11-20) as a function of pH. *Condens. Matter* **24**, 124101.

Sung, J., Zhang, L.N., Tian, C.S., Shen, Y.R. and Waychunas, G.A. (2011) Effect of pH on the water/α-Al_2O_3 (1-102) interface structure studied by sum-frequency vibrational spectroscopy. *J. Phys. Chem. C* **115**, 13887-13893.

Sverjensky, D.A. (2001) Interpretation and prediction of triplelayer model capacitances and the structure of the oxide-electrolyte-water interface. *Geochim. Cosmochim. Acta* **65**, 3643-3655.

Thomas, A.C. and Richardson, H.H. (2008) Growth of thin film water on α-Al_2O_3 (0001): An FTIR study. *J. Phys. Chem. C* **112**, 20033-20037.

Trainor, T.P., Eng, P.J., Brown, G.E., Robinson, I.K. and De Santis, M. (2002) Crystal truncation rod diffraction study of the α-Al_2O_3 (1-102) surface. *Surf. Sci.* **496**, 238-250.

Tuladhar, A., Dewan, S., Kubicki, J.D. and Borguet, E. (2016) Spectroscopy and ultrafast vibrational dynamics of strongly hydrogen bonded OH species at the α-Al_2O_3(11-20)/H_2O interface. *J. Phys. Chem. C* **120**, 16153-16161.

Tuladhar, A., Piontek, S. and Borguet, E. (2017) Insights on interfacial structure, dynamics, and proton transfer from ultrafast vibrational sum frequency generation spectroscopy of the alumina(0001)/water interface. *J. Phys. Chem. C* **121**, 5168-5177.

Venema, P., Hiemstra, T., Weidler, P.G. and van Riemsdijk, W.H. (1998) Intrinsic proton affinity of reactive surface groups of metal (hydr)oxides: Application to iron (hydr)oxides. *J. Colloid Interface Sci.* **198**, 282-295.

Zhang, L., Tian, C., Waychunas, G.A. and Shen, Y.R. (2008) Structures and charging of α-alumina (0001)/water interfaces studied by sum-frenqueny vibrational spectroscopy. *J. Am. Chem. Soc.* **130**, 7686-7694.

APPENDIX A

ADDITIONAL EXPERIMENT DATA

A.1 INTRODUCTION

Beyond the main focus of this dissertation, additional experimental data were collected that include phosphate adsorption isotherms on gibbsite and bayerite, arsenate adsorption isotherms in the presence of different amount of phosphate on gibbsite and bayerite, and EXAFS spectra of arsenate adsorbed gibbsite and bayerite in the presence of phosphate. These results are reported below.

A.2 MATERIALS AND METHODS

Mineral and Reagent Preparation

Gibbsite and bayerite were prepared following the synthesis methods described in Chapters 2 and 3. After synthesis, gibbsite and bayerite were washed repeatedly in deionized water (>18.2 MΩ cm) to remove excess electrolytes. Both minerals were resuspended in deionized water and stored in polypropylene bottles. The concentrations of the gibbsite and bayerite mineral suspensions were determined through gravimetric analysis. Both gibbsite and bayerite particles have been previously characterized by Brunauer-Emmett-Teller (BET) analysis, powder X-ray diffraction (XRD), and scanning electron microscope (SEM).

Sodium nitrate ($NaNO_3$; Sigma Aldrich, 99%), 3-(N-morpholino) propanesulfonic acid hemisodium salt (MOPS; Sigma Aldrich, 99%), sodium arsenate ($Na_2HAsO_4 \cdot 7H_2O$; Sigma Aldrich, 98%), and sodium phosphate (Na_2HPO_4; Sigma Aldrich, 98%) stock solutions were prepared using deionized water. Two 20 g L^{-1} suspensions of gibbsite and bayerite were prepared. Experiments conducted at pH 7 used a MOPS solution to buffer pH. All pH adjustments were made using HNO_3 or NaOH solutions.

Macroscopic Phosphate Adsorption Isotherms

Phosphate adsorption isotherms were measured at pH 4 and 7 on gibbsite and bayerite. All samples are prepared in the similar way as the batch arsenate adsorption samples described in Chapter 2. Briefly, these samples contained 4 g L^{-1} of gibbsite or bayerite reacted in a solution with an initial phosphate concentration from 10 to 500 μM, a 0.01 M $NaNO_3$ to buffer ionic strength, and a pH buffer of 0.001 M 3-(N-morpholino) propanesulfonic acid (MOPS) at pH 7 (no buffer was used at pH 4). The pH value of each sample was adjusted to 4 or 7 with NaOH or HNO_3. The samples were rotated on end-over-end rotators for 24 hours at room temperature. At the end of experiment, the samples were centrifuged, filtered (0.22 μm, MCE; Ultra Cruz), and acidified to 2% HNO_3 (trace metal grade; OmniTrace Ultra). Dissolved phosphate concentrations were determined by inductively coupled-plasma mass spectrometry (ICP-MS, PerkinElmer ELAN DRCII).

Macroscopic Arsenate Adsorption Isotherms in the Presence of Phosphate

Arsenate adsorption isotherms in the presence of phosphate were measured at pH 4 and 7 on gibbsite and bayerite. All samples are prepared in the similar way as the batch arsenate adsorption samples described in Chapter 2 but with different amount of phosphate present. For gibbsite system, 51 or 102 μM phosphate was added from a Na_2HPO_4 stock solution. For bayerite system, 72.5 or 145 μM phosphate was added from a Na_2HPO_4 stock solution. This amount of phosphate was selected based on that phosphate can take up half or entire surface sites of gibbsite or bayerite.

EXAFS Spectroscopic Measurements

The coordination environment of arsenate adsorbed to gibbsite and bayerite in the presence of phosphate was investigated with extended X-ray absorption fine structure (EXAFS) spectroscopy. Separate batch adsorption experiments were conducted to prepare fresh samples before beamline measurements. Scaled-up reactors (50 mL total volume) were used to prepare samples with sufficient solid mass for EXAFS measurements. Two adsorbed arsenate samples for each mineral with certain amount of phosphate at each pH were prepared with initial low (40 μM) and high (400 μM) loading of arsenate (Table A.1). All samples were centrifuged to separate the supernatant and solid (wet paste). The solids were packed as wet paste into polycarbonate sample holders, sealed with 25 μm Kapton tape, and heat sealed in a polyethylene bag with a damp Kimwipe to prevent drying. Samples were prepared within 3 days of transport to the Advanced Photon Source (APS) at Argonne National Laboratory for measurements of As K-edge EXAFS spectra at APS beamline 20-BM-B. Beamline optics and details regarding EXAFS data analysis procedures are described in Chapter 2.

Table A.1. Conditions for the adsorption samples analyzed by EXAFS spectroscopy

Sample	Mineral	pH	$[PO_4^{3-}]$ (μM)	$[AsO_4^{3-}]_{init}$ (μM)	$[AsO_4^{3-}]_{final}$ (μM)	Γ_{As} (μmol/m^2)
GP1	4 g/L gibbsite	7.0	51	40	13	0.31
GP2	4 g/L gibbsite	7.0	51	400	380	0.87
GP3	4 g/L gibbsite	7.0	102	40	25	0.24
GP4	4 g/L gibbsite	7.0	102	400	388	0.76
GP5	4 g/L gibbsite	4.0	51	40	12	0.39
GP6	4 g/L gibbsite	4.0	51	400	375	0.95
GP7	4 g/L gibbsite	4.0	102	40	20	0.29
GP8	4 g/L gibbsite	4.0	102	400	374	0.84
BP1	4 g/L bayerite	7.0	72.5	40	6	0.68
BP2	4 g/L bayerite	7.0	72.5	400	352	1.78
BP3	4 g/L bayerite	7.0	145	40	23	0.39
BP4	4 g/L bayerite	7.0	145	400	371	1.42
BP5	4 g/L bayerite	4.0	72.5	40	2	0.75
BP6	4 g/L bayerite	4.0	72.5	400	290	2.72
BP7	4 g/L bayerite	4.0	145	40	8	0.65
BP8	4 g/L bayerite	4.0	145	400	315	2.29

A.3 RESULTS

Macroscopic Phosphate Adsorption Isotherms

The macroscopic adsorption of phosphate onto gibbsite and bayerite at pH 4 and 7 shows similar trended as arsenate adsorption behavior on both minerals observed in Chapter 2, with both oxoanions displaying greater adsorption at low pH and on bayerite (Figure A.1). The macroscopic phosphate adsorption data are then fitted using a dual Langmuir isotherm model considering two adsorption sites with co-optimized maximum adsorption capacity parameters ($\Gamma_{max,1}$ *and* $\Gamma_{max,2}$) and affinity constants (K_1 *and* K_2):

$$\Gamma_{ads} = \frac{K_1 \Gamma_{max,1} C_{(ads)}}{1 + K_1 C_{(ads)}} + \frac{K_2 \Gamma_{max,2} C_{(ads)}}{1 + K_2 C_{(ads)}}$$

where Γ_{ads} is the amount of adsorbate adsorbed, $C_{(ads)}$ is the final adsorbate concentration in solution. The adsorption data are well fitted using the dual Langmuir isotherm model for both gibbsite and bayerite (Figure A.1). Comparing the fitting parameters in the dual Langmuir model, the total Γ_{max} values ($\Gamma_{max,1} + \Gamma_{max,2}$) of bayerite are larger than those of gibbsite at same experimental condition (Table A.2), which could be attributed to the abundance of edge surface sites on bayerite particles displaying stronger adsorption capacity. However, under the same experimental condition, the two components $\Gamma_{max,1}$ and $\Gamma_{max,2}$ do not vary in proportion to the relative areas of basal and edge surface sites on both minerals, suggesting that dual Langmuir behavior is not related to particle morphology but the presence of two different surface complexes (e.g., inner- and outer-sphere species) on both minerals. These macroscopic phosphate adsorption behaviors have also been observed in individual arsenate adsorption on gibbsite and bayerite in Chapter 2 and 3.

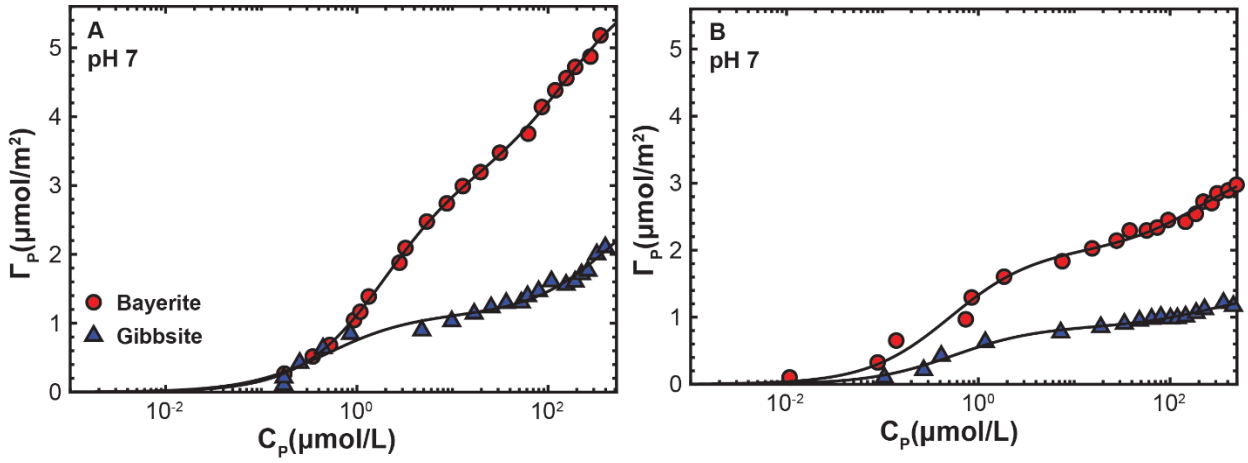

Figure A.1. Phosphate adsorption isotherm on gibbsite and bayerite at (A) pH 7 and (B) pH 4. Lines represent dual Langmuir isotherm fits to the data.

Table A.2. Fitting parameters for phosphate dual Langmuir isotherms

Mineral	Γ_{max} (µmol/m²)	K (L/µmol)	R-factor [a]
Gibbsite pH 4			
Langmuir_1	1.12 ± 0.07	2.0 ± 0.5	
Langmuir_2	2.1 ± 0.1	0.002 ± 0.002	
Total	3.2 ± 0.1		0.032
Gibbsite pH 7			
Langmuir_1	0.85 ± 0.04	1.8 ± 0.3	
Langmuir_2	0.6 ± 0.2	0.004 ± 0.003	
Total	1.2 ± 0.2		0.036
Bayerite pH 4			
Langmuir_1	3.17 ± 0.08	0.53 ± 0.03	
Langmuir_2	2.9 ± 0.2	0.006 ± 0.001	
Total	6.1 ± 0.2		0.013
Bayerite pH 7			
Langmuir_1	2.0 ± 0.1	2.0 ± 0.4	
Langmuir_2	1.4 ± 0.3	0.005 ± 0.003	
Total	3.4 ± 0.3		0.032

[a] Goodness-of-fit parameter. The R-factor is the sum of the differences between the data and the model fit at each data point divided by the sum of the data at each corresponding point. It represents the mean misfit between the data and the fit. Smaller R-factor values reflect better fits.

Macroscopic Arsenate Adsorption Isotherms with the Presence of Phosphate

To better understand the reactivity of surface sites, how the addition of other oxoanions such as phosphate affects arsenate adsorption on both minerals is investigated. In these competitive adsorption experiments, the initial arsenate loading is the same as the phosphate-free system. The addition of phosphate is observed to suppress arsenate adsorption on both mineral through competitive adsorption (Figure A.2 and A.3). Phosphate has a greater effect on arsenate adsorption onto gibbsite than that onto bayerite, indicating that the relative affinities for arsenate and phosphate adsorption differ between >AlOH and >Al_2OH. Arsenate adsorption data with and without phosphate are all well fitted using the dual Langmuir isotherm model for both gibbsite and bayerite (Figure A.2 and A.3), indicating the similar dual Langmuir adsorption behaviors as observed in individual arsenate and phosphate adsorption isotherms. The detailed fitting parameters for dual Langmuir isotherms are summarized in Table A.3.

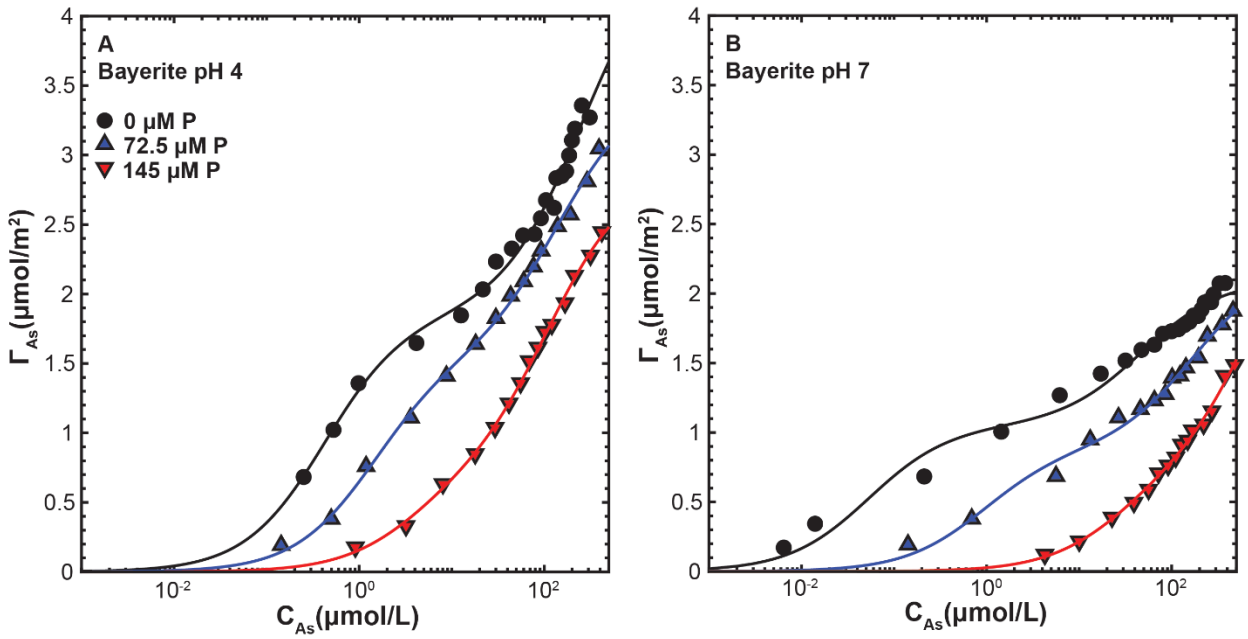

Figure A.2. Arsenate adsorption isotherms on bayerite with 0, 72.5, and 145 µM phosphate present at (A) pH 4 and (B) pH 7. Lines represent dual Langmuir isotherm fits to the data.

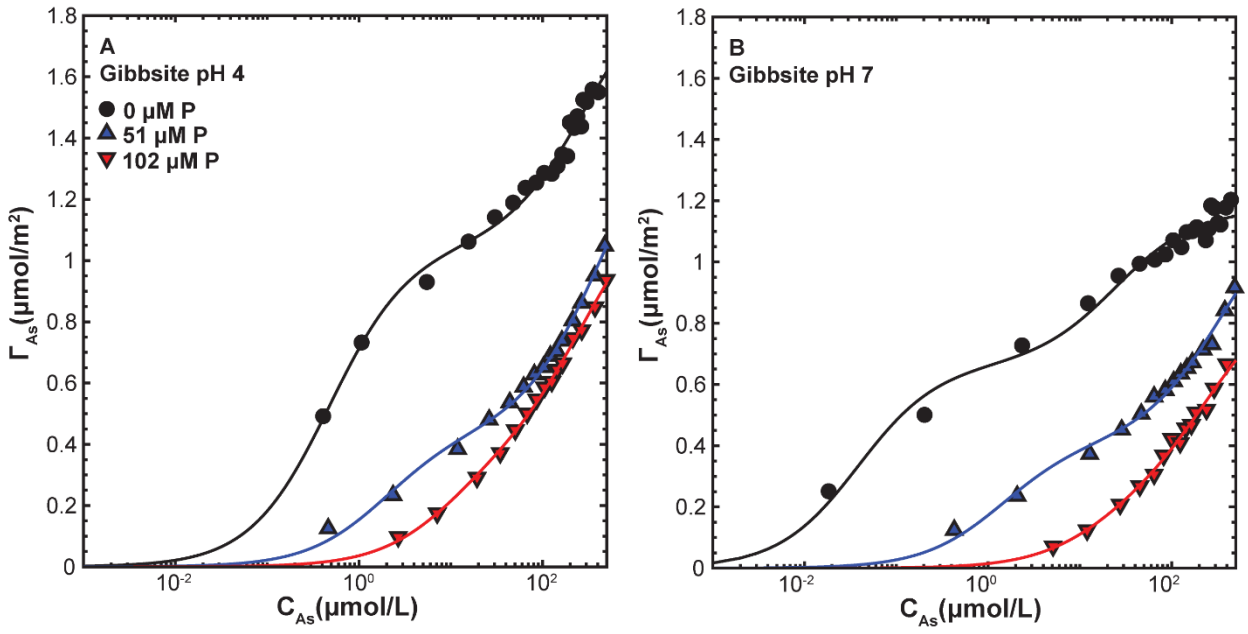

Figure A.3. Arsenate adsorption isotherms on gibbsite with 0, 51, and 102 µM phosphate present at (A) pH 4 and (B) pH 7. Lines represent dual Langmuir isotherm fits to the data.

Table A.3. Fitting parameters for dual Langmuir isotherms

Mineral	pH	[P] (μM)	$\Gamma_{max,1}$ (μmol/m^2)	K_1 (L/μmol)	$\Gamma_{max,2}$ (μmol/m^2)	K_2 (L/μmol)	R-factor [a]
Bayerite	4	0	1.85 ± 0.08	2.4 ± 0.4	2.7 ± 0.4	0.004 ± 0.001	0.025
		72.5	1.54 ± 0.08	0.7 ± 0.1	2.0 ± 0.1	0.007 ± 0.002	0.018
		145	0.7 ± 0.1	0.25 ± 0.09	2.22 ± 0.09	0.02 ± 0.007	0.017
Bayerite	7	0	1.05 ± 0.07	19 ± 7	1.05 ± 0.08	0.021 ± 0.007	0.034
		72.5	0.88 ± 0.08	1.1 ± 0.4	1.4 ± 0.1	0.006 ± 0.002	0.029
		145	0.7 ± 0.2	0.04 ± 0.02	2 ± 1	0.001 ± 0.001	0.027
Gibbsite	4	0	1.05 ± 0.03	2.1 ± 0.3	0.9 ± 0.1	0.003 ± 0.001	0.019
		51	0.44 ± 0.03	0.5 ± 0.1	1.1 ± 0.1	0.023 ± 0.001	0.021
		102	0.38 ± 0.05	0.10 ± 0.03	0.89 ± 0.05	0.003 ± 0.001	0.017
Gibbsite	7	0	0.67 ± 0.05	26 ± 8	0.51 ± 0.04	0.04 ± 0.01	0.028
		51	0.41 ± 0.03	0.7 ± 0.2	0.8 ± 0.1	0.003 ± 0.001	0.027
		102	0.2 ± 0.2	0.05 ± 0.01	0.7 ± 0.1	0.004 ± 0.003	0.031

[a] Goodness-of-fit parameter. The R-factor is the sum of the differences between the data and the model fit at each data point, divided by the sum of the data at each corresponding point. It represents the mean misfit between the data and the fit. Smaller R-factor values reflect better fits.

Arsenate Adsorption Mechanisms in the Presence of Phosphate

Arsenic surface speciation for a series of adsorption samples (Table A.1) was characterized using EXAFS spectroscopy to determine if the presence of phosphate affects arsenate binding mechanisms. Conditions are chosen to explore low (40 μM) and high (400 μM) arsenate surface loading with low (72.5 and 51 μM phosphate for bayerite and gibbsite, respectively) and high concentrations (145 and 102 μM phosphate for bayerite and gibbsite, respectively) of phosphate present. Different experimental conditions, such as pH variation, arsenate coverage, the addition of different amount of phosphate, and mineral adsorbents, did not produce any distinctive patterns in EXAFS spectra (Figure A.4), indicating the similar arsenate adsorption mechanisms on all samples explored.

Table A.4. As K-edge EXAFS fitting parameters

Sample	Path	CN[a]	R (Å)[b]	σ^2 (Å^2)[c]	ΔE_0 (eV)[d]	R-Factor[e]	χ_v^2 [e]
GP1	As-O	4	1.696(3)	0.0019(2)	6(1)	0.016	13.91
	As-Al	0.9(5)[f]	3.18(3)	0.006			
GP2	As-O	4	1.693(3)	0.0018(1)	6(1)	0.012	7.12
	As-Al	0.7(4)	3.20(4)	0.006			
GP3	As-O	4	1.696(3)	0.0021(2)	5(1)	0.016	13.19
	As-Al	0.9(5)	3.08(3)	0.006			
GP4	As-O	4	1.692(3)	0.0021(2)	5(1)	0.020	5.16
	As-Al	0.8(5)	3.20(4)	0.006			
GP5	As-O	4	1.695(3)	0.0019(2)	6(1)	0.017	15.15
	As-Al	1.1(5)	3.19(3)	0.006			
GP6	As-O	4	1.697(3)	0.0023(2)	7(1)	0.019	9.64
	As-Al	1.2(5)	3.22(3)	0.006			
GP7	As-O	4	1.694(3)	0.0019 (1)	5(1)	0.014	16.37
	As-Al	1.2(4)	3.21(4)	0.006			
GP8	As-O	4	1.688(3)	0.0019(2)	5(1)	0.020	20.33
	As-Al	1.2(5)	3.19(3)	0.006			
BP1	As-O	4	1.693(3)	0.0018(1)	5(1)	0.014	13.04
	As-Al	1.4(4)	3.18(3)	0.006			
BP2	As-O	4	1.694(3)	0.0019(2)	5(1)	0.018	22.54
	As-Al	1.3(5)	3.19(3)	0.006			
BP3	As-O	4	1.692(3)	0.0019 (2)	4(1)	0.017	19.71
	As-Al	1.4(5)	3.19(2)	0.006			
BP4	As-O	4	1.691(3)	0.0018(1)	5(1)	0.015	8.56
	As-Al	1.5(4)	3.19(2)	0.006			
BP5	As-O	4	1.694(3)	0.0017(2)	6(1)	0.016	15.85
	As-Al	1.5(6)	3.19(2)	0.006			
BP6	As-O	4	1.696(3)	0.0018(2)	7(1)	0.017	17.75
	As-Al	1.3(5)	3.20(2)	0.006			
BP7	As-O	4	1.693(3)	0.0019(2)	5(1)	0.016	11.06
	As-Al	1.3(5)	3.19(2)	0.006			
BP8	As-O	4	1.691(3)	0.0018(2)	5(1)	0.019	14.72
	As-Al	1.3(5)	3.19(3)	0.006			

[a] Coordination number. [b] Interatomic distance. [c] Debye-Waller factor. [d] Difference in the threshold Fermi level between the data and theory. [e] Goodness-of-fit parameters (Kelly et al., 2008). [f] The estimated standard deviations are listed in parentheses, representing the errors in the last digit.

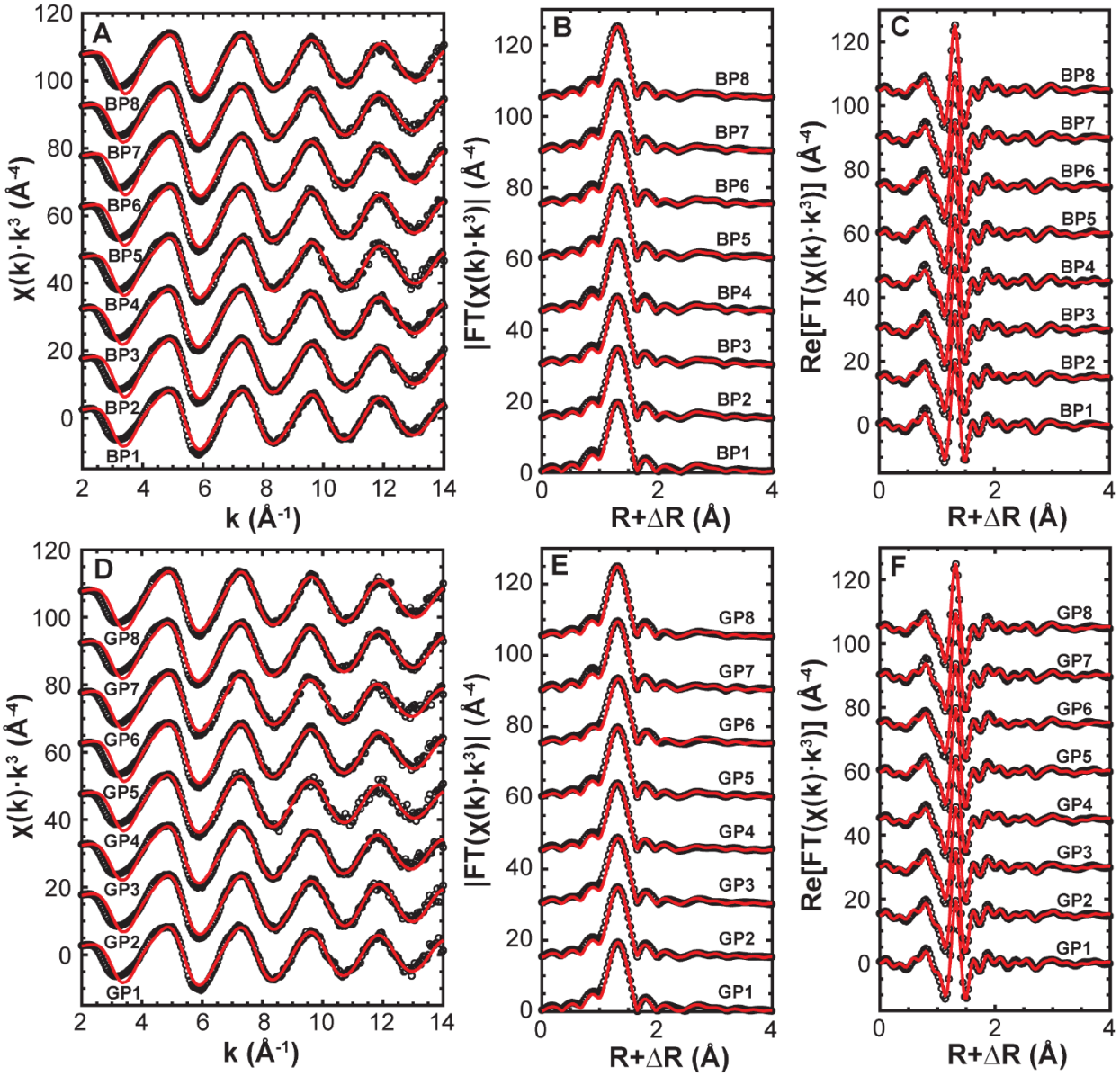

Figure A.4. Data (dotted) and structural fits (solid) to the As K-edge spectra (A, D), Fourier transform magnitudes (B, E), and real components of the Fourier transforms (C, F) of the series of adsorption samples. Detailed sample information is provided in Table A.1.

A.4 REFERENCE

Kelly, S.D., Hesterberg, D. and Ravel, B. (2008) Analysis of soils and minerals using X-ray absorption spectroscopy. *Methods of Soil Analysis Part 5 - Mineralogical Methods*, 387-463.